SINGLE-PRESSURE ABSORPTION REFRIGERATION SYSTEMS FOR LOW-SOURCE-TEMPERATURE APPLICATIONS

A Dissertation
Presented to
The Academic Faculty

by

Alexander S Rattner

In Partial Fulfillment
of the Requirements for the Degree
Doctor of Philosophy in Mechanical Engineering

Georgia Institute of Technology

August 2015

SINGLE-PRESSURE ABSORPTION REFRIGERATION SYSTEMS FOR LOW-SOURCE-TEMPERATURE APPLICATIONS

Approved by:

Dr. Srinivas Garimella, Advisor
G.W. Woodruff School of Mechanical Engineering
Georgia Institute of Technology

Dr. Edmond Chow
School of Computational Science and Engineering
Georgia Institute of Technology

Dr. S. Mostafa Ghiaasiaan
G.W. Woodruff School of Mechanical Engineering
Georgia Institute of Technology

Dr. Gershon Grossman
Department of Mechanical Engineering
Technion Israel Institute of Technology

Dr. Alexander Alexeev
G.W. Woodruff School of Mechanical Engineering
Georgia Institute of Technology

Date Approved: [June 10, 2015]

ACKNOWLEDGEMENTS

I wish to express my sincere gratitude to my advisor, Dr. Srinivas Garimella. He has supported me greatly throughout my graduate education at Georgia Tech, and has pushed me to grow both technically and professionally. Without his mentorship, this body of work would not have been possible. I would also like to thank the other members of my Ph.D. committee: Dr. Mostafa Ghiaasiaan, Dr. Alexander Alexeev, Dr. Edmond Chow, and Dr. Gershon Grossman. Their guidance has helped me significantly improve this dissertation and solve key engineering challenges.

The members of the Sustainable Thermal Systems Laboratory have been an incredible support network, both as friends and as technical advisors. While I have benefited greatly from the advice of almost every member of the lab, I would like to express thanks in particular to Dr. Ananda Krishna Nagavarapu, Dr. Jeffrey Milkie, Dr. Brian Fronk, Dr. John Bustamante, Adrienne Little, Jared Delahanty, Chris Keinath, Malcolm Macdonald, and Hannah Oermann.

Finally, I would like to thank my family. My parents have instilled in me a strong work ethic from an early age and taught me never to shrink from a challenge. My wife has been an endless source of support (and helped with some statistics).

TABLE OF CONTENTS

LIST OF TABLES

Page

LIST OF FIGURES

Page

NOMENCLATURE

A	area (m^2) or momentum matrix equation coefficients (kg m^{-3} s^{-2})
a	correction factor in model of Liu and Winterton (1991)
AAD	average absolute deviation
AR	aspect ratio (unit-cell height / diameter)
CAVP	closest approach vapor pressure (kPa)
CAT	closest approach temperature (K)
C_r	fluid stream thermal capacity rate ratio
C_0	distribution parameter (in bubble rise velocity model)
c_p	specific heat at constant pressure (kJ kg K^{-1})
D	diameter (m)
D_{ab}	binary diffusion coefficient (m^2 s^{-1})
E	error (various units)
f	friction factor, or body force (N m^{-3})
f_s	surface tension body force (N m^{-3})
f_{LS}	blending factor (capillary-to-large diameter)
Flow	image with two-phase flow
g	gravitational acceleration (9.81 m s^{-2})
G^*	image analysis heuristic
H	height (m)
h	convection heat transfer coefficient (W m^{-2} K^{-1})
h'	adjusted convection coefficient (W m^{-2} K^{-1})
h^*	mass transfer convection coefficient (kg m^{-2} s^{-1} Pa^{-1})
i	enthalpy (kJ kg^{-1})
ID	inner diameter (m)
j	superficial velocity (m s^{-1})
k	thermal conductivity (W m^{-1} K^{-1})
L	length (m)
L^*	dimensionless length (for developing flow)
l	time step limiting scaling factor
Liq	liquid-only image
LMPD	log-mean vapor pressure difference (kPa)
LMTD	log-mean temperature difference (K)
m	mass (kg) or parameter in correlation of White and Beardmore (1962)
$\dot{m}$	mass flow rate (kg s^{-1})
M_G	parameter in interface oscillation damping model
MW	molar mass (kg $kmol^{-1}$)
n	number of measurements, or segment / cell count
$\hat{n}$	normal vector
$\hat{n}_{int}$	interface normal vector
NTU	heat exchanger number of transfer units

OD	outer diameter (m)
P^*	dimensionless dynamic pressure change
p	pressure (Pa), or tube pitch
p_v	vapor pressure (kPa)
per	perimeter (m)
Q	heat transfer rate (W)
q	heat flux (W m^{-2})
$\dot{q}_{pc}$	volumetric phase change heating rate (W m^{-3})
R	radial dimension (m), or thermal resistance (K W^{-1})
R'	thermal resistance × unit length (m K W^{-1})
R''	thermal resistance × unit area (m^2 K W^{-1})
R^*	universal gas constant (8.314 kJ $kmol^{-1}$ K^{-1})
$R^{*'}$	mass transfer resistance × unit length (m^2 s^{-1}, or kmol s kg^{-1})
r	phase change rate parameter (s^{-1})
S	volumetric phase change rate in model of Yang *et al.* (2008) (kg m^{-3} s^{-1})
r	radial coordinate (m)
s	under-relaxation parameter
seg	segment value in axially discretized models
S_r	submergence ratio (reservoir height / bubble pump height)
t	time (s)
T	temperature (°C)
$\overline{T}$	average temperature (°C)
U	velocity (m s^{-1})
u	velocity field (m s^{-1})
UA	overall heat transfer conductance (W K^{-1})
UA*	overall mass transfer conductance (kg Pa^{-1} s^{-1})
u^*	modified velocity field (m s^{-1})
V	volumetric flow rate (ml min^{-1})
$\dot{v}_{pc}$	volumetric phase change rate (s^{-1})
WF	wetting factor (liquid film coverage of surface)
x	position vector (m)
x,y	radial, axial coordinates (px, m)
y^+	dimensionless wall distance
z	axial position (m)

Greek characters

α	void fraction
α_1	liquid phase-fraction field
$\dot{\alpha}_{1,pc}$	volumetric liquid-phase phase-change generation rate (s^{-1})
β	length fraction of unit cell occupied by Taylor bubble
Γ	drift flux parameter in bubble velocity model, or mass flow per unit width in liquid film (kg m^{-1} s^{-1})
Δ	finite difference, or mesh cell dimension (m)
ε	heat exchanger effectiveness
δ	thickness (of liquid film)

η	fin efficiency
θ	contact angle (deg), or generic material property
κ	curvature (m^{-1})
μ	dynamic viscosity (kg m^{-1} s^{-1})
ξ	auxiliary gas (He) mass fraction in gas mixture
ξ*	auxiliary gas (He) mole fraction in gas mixture
ρ	mass density (kg m^{-3})
ρ*	molar density (kmol m^{-3})
σ	surface tension (kg s^{-2}), or Stefan-Boltzmann constant (5.67×10^{-8} W m^{-2} K^{-4})
τ	shear stress (N m^{-2}), or time scale (s)
ϕ	cell face volume flux (m^3 s^{-1})
ψ	absorbent mass fraction in solution

Subscripts

0	static contact angle, or non-limited value
1,2,3…	segment or node number
a	annulus
a, r	advancing and receding contact angle
abs	absorber component
acc	fluid acceleration (pressure change)
air	ambient air value
amb	ambient value
aux	auxiliary gas mixture
avg	average value
B	buoyancy (force)
b	bubble
BPG	bubble-pump generator
Bretherton	from Bretherton (1961)
c	capillary (pressure), interface compressive field, or combined quantity
Ca	capillary parameter
cell	mesh cell value
CF	coupling fluid
cl	contact line
col	collected liquid in a reservoir
cool	cool stream value, or cooling delivery temperature
cond	value for condensation phase-change, or condenser component
cryst	solute crystallization point
CS	absorbent-concentrated solution stream
D	diagonal entry of matrix equation (self-contribution)
d	hydrodynamic quantity
DEV	developing flow quantity
DevSlug	developing slug-flow heat transfer model
DS	absorbent-dilute solution stream
Dukler	from Dukler and Hubbard (1975)

eff	effective value
ent	entrance region of tube
evap	value for evaporation phase change, or evaporator
exp	value from experiment
ext	external value
Extended	extended transition pressure drop model
f	liquid film, or frictional value, mesh cell face quantity, final value, or fin value
FD	fully developed
forced	forced flow
Fukano	from Fukano *et al.* (1989)
G	gas phase
GHX	gas heat exchanger
gauge	gauge pressure
H	Hoffman function
hs	hydrostatic (pressure change)
i	inner value, or initial value
i, *j*, *k*	indices
in	inlet value, or inner fin channel
int	liquid-to-gas interface, or internal value
Kreutzer	from Kreutzer *et al.* (2005)
L	liquid phase
L0	all-liquid-flow value
lim,CFL	value limited for Courant-Friedrichs-Lewy condition
lim,mass	value limited by mass availability
log	log-scale quantity
loss	heat loss (to surroundings)
LS	large-scale channels
LV	liquid-to-vapor change
LW	value from the model of Liu and Winterton (1991)
max, min	maximum and minimum values
mod	value from model
n	interface normal value
nat	natural convection value
NB	nucleate boiling value
net	total value
NH_3	pure ammonia value
NH_3-NaSCN	sodium thiocyanate
o	outer value, or overall surface value
out	outlet value, or outer fin value
pc	phase change
PH	electric pre-heater
prs	location of pressure transducer
rad	radiation heat transfer
ref	refrigerant flow value
res	value in liquid reservoir

ρgh	pressure field less hydrostatic contribution
row	tube row
run	duration of experimental run
s	liquid slug
sat	saturation conditions
set	set-point value
shell	shell around test section
SHX	solution heat exchanger
sim	simulation value
sol	solution flow value
source	heat source
st	steam tube (cross-section area)
sub	subcooled value, or subcooler component
sys	system value (pressure)
θ	contact-line-velocity to contact-angle slope
tot	total value
trans	Taylor bubble to liquid slug transition
tube	per-tube value
turb	turbulent quantity
Uni	universal (laminar-to-turbulent) model
V	vapor phase
wall	channel wall
WK	evaporation model of Wadekar and Kenning (1990)

Dimensionless parameters

Bo	Bond number $\left(\rho_{\mathrm{L}}-\rho_{\mathrm{G}}\right) gD^2/\sigma$
Ca	capillary number $\mu_{\mathrm{L}} j/\sigma$, or $\mu u/\sigma$
$\mathrm{Ca_b}$	bubble capillary number $\mu_{\mathrm{L}} U_{\mathrm{b}}/\sigma$
COP	coefficient of performance $Q_{\mathrm{evap}}/Q_{\mathrm{BPG}}$
Gz	Graetz number $D\,\mathrm{Re}\,\mathrm{Pr}/L$
Ja	Jakob number $c_{\mathrm{p}}\left(T-T_{\mathrm{sat}}\right)/i_{\mathrm{LV}}$
Mo	Morton number $g\mu^4\rho^{-1}\sigma^{-3}$
$\mathrm{N_f}$	viscous number $\sqrt{\rho_{\mathrm{L}}\left(\rho_{\mathrm{L}}-\rho_{\mathrm{G}}\right) gD^3/\mu_{\mathrm{L}}^2}$
Nu	Nusselt number hD/k
Pr	Prandtl number $\mu c_{\mathrm{p}}/k$
$\mathrm{Re_b}$	bubble-to-film Reynolds number $\rho_{\mathrm{G}}\left(U_{\mathrm{b}}+U_{\mathrm{f}}\right)\left(D-2\delta_{\mathrm{f}}\right)/\mu_{\mathrm{G}}$
$\mathrm{Re_f}$	liquid film Reynolds number $4\rho_{\mathrm{L}} U_{\mathrm{f}}\delta_{\mathrm{f}}/\mu_{\mathrm{L}}$
Re_j	superficial velocity Reynolds number $\rho_{\mathrm{L}} jD/\mu_{\mathrm{L}}$
$\mathrm{Re}_{j,\mathrm{L}}$	superficial liquid velocity Reynolds number $\rho_{\mathrm{L}} j_{\mathrm{L}} D/\mu_{\mathrm{L}}$
$\mathrm{Re_G}$	gas Reynolds number (Liu *et al.*, 2005) $\rho_{\mathrm{G}} j_{\mathrm{G}} D/\mu_{\mathrm{G}}$

Re'_G	alternate gas Reynolds number (Laborie *et al.*, 1999) $\rho_L U_b D/\mu_L$
Re_L	liquid Reynolds number $\rho_L j_L D/\mu_L$ (Liu *et al.*, 2005)
Re_{Ub}	bubble velocity Reynolds number $\rho_L U_b D/\mu_L$ (Liu *et al.*, 2005)
Sc	Schmidt number $\mu/\rho D_{ab}$
Sh	Sherwood number $h^* D/D_{ab}$

SUMMARY

The diffusion absorption refrigeration (DAR) cycle is a promising technology for fully thermally driven cooling. It is well suited to applications in medicine refrigeration and air-conditioning in off-grid settings. However, design and engineering knowhow for the technology is limited; therefore, system development has historically been an iterative and expensive process. Additionally, conventional system designs require high-grade energy input for operation, and are unsuitable for low-temperature solar- or waste-heat activated applications.

In the present effort, component- and system-level DAR engineering analyses are performed. Detailed bubble-pump generator (BPG) component models are developed, and are validated experimentally and with direct simulations. Investigations into the BPG focus on the Taylor flow pattern in the intermediate Bond number regime, which has not yet been thoroughly characterized in the literature, and has numerous industry applications, including nuclear fuel processing and well dewatering. A coupling-fluid heated BPG design is also investigated experimentally for low-source-temperature operation. Phase-change simulation methodologies are developed to rigorously study the continuously developing flow pattern in this BPG configuration. Detailed component-level models are also formulated for all of the other DAR heat and mass exchangers, and are integrated to yield a complete system-level model. Results from these modeling studies are applied to develop a novel fully passive low-source-temperature (110 - 130°C) DAR system that delivers refrigeration grade cooling. This design achieves operation at target conditions through the use of alternate working fluids (NH3-NaSCN-He), the

coupling-fluid heated BPG, and a novel absorber configuration. The complete DAR system is demonstrated experimentally, and evaluated over a range of operating conditions. Experimental results are applied to assess and refine component- and system-level models.

CHAPTER 1. INTRODUCTION

1.1 Background

Of the approximately 98 EJ yr^{-1} of primary energy consumption in the USA, 48 EJ yr^{-1} (49%) is exhausted as waste heat to the surroundings (Rattner and Garimella, 2011b). With careful matching of source temperatures and appropriate end uses, there is the potential to reuse approximately 24 EJ yr^{-1} of these waste heat streams, and thus reduce primary energy demand by 15%. Thermally activated refrigeration systems represent a particularly attractive avenue for harnessing such heat sources. Assuming representative multi-effect absorption thermal system performance (coefficient of performance COP_{cool} = cooling/thermal input rates ~ 1.2 (Herold *et al.*, 1996)), there is sufficient waste heat availability to meet 65% of USA air conditioning demand. However, designing practical thermally activated refrigeration systems to harness such abundant, yet diffuse and low-grade, heat sources remains a persistent challenge.

The principles of absorption refrigeration have been applied since the 18^{th} century, and large scale installations were common prior to the maturation of vapor-compression based technologies (Srikhirin *et al.*, 2001). Absorption systems have received renewed interest in recent years as energy-efficient and potentially low-operating-cost alternatives to vapor-compression refrigeration. Additionally, absorption systems can employ environmentally benign working fluids (e.g., water, ammonia) rather than high global warming potential (GWP) synthetic refrigerants (Garimella, 2003). The key defining feature of absorption systems is the use of a sorption process rather than mechanical compression to bring low pressure vapor refrigerant to a high pressure state. In conventional two-pressure absorption systems (Figure 1.1), low pressure refrigerant is

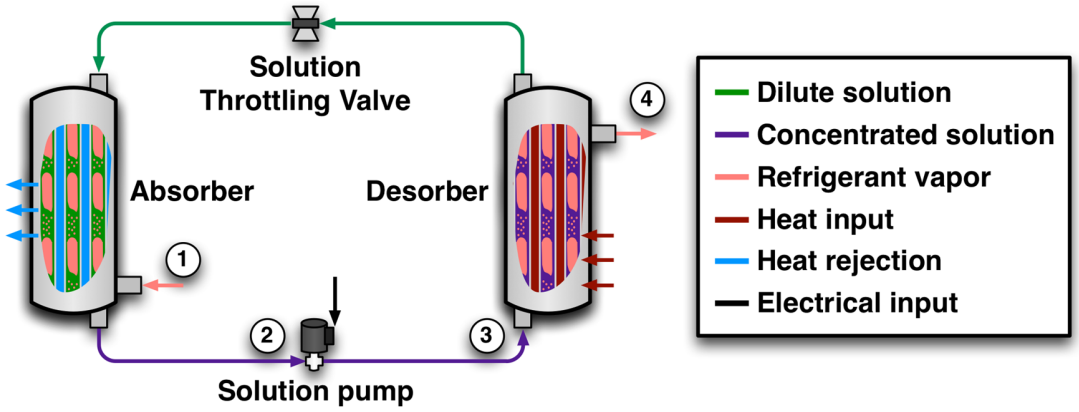

Figure 1.1 – Schematic of the two-pressure vapor sorption compression process

absorbed into a liquid solvent (points 1 → 2), rejecting heat to the surroundings. The high-refrigerant concentration solution is pumped to high pressure (2 → 3), which requires minimal mechanical work because the liquid is effectively incompressible. Finally, thermal input is supplied to the pressurized stream, desorbing (boiling off) vapor refrigerant (3 → 4). Following this approach, minimal mechanical input is required because pressure rise is effected in the liquid phase rather than through the compression of refrigerant vapor, and the process is primarily driven by thermal input, which may be abundant and comparatively inexpensive.

These two-pressure absorption systems are promising for recovering low-grade thermal energy with substantially reduced electrical demand. However, the fundamental need for a solution pump limits implementation to sites with electrical infrastructure or available mechanical input. Furthermore, the solution pump accounts for an appreciable portion of the system fabrication cost and is regarded as one of the primary points of failure (Rattner and Garimella, 2011a).

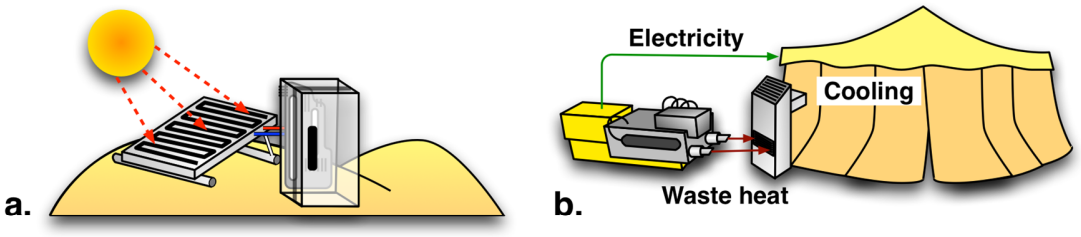

Figure 1.2 – Potential applications of single pressure absorption refrigeration for (**a**) solar-thermal activated medicine refrigeration in developing countries, and (**b**) waste-heat activated cooling in forward operating military bases

Single-pressure absorption refrigeration represents an alternate technology that operates using solely thermal energy input. As such, systems using this principle generally have no moving parts, and are fully passively operated. This enables new possibilities for off-grid applications. For example, such systems could be used for medicine and vaccine refrigeration in developing countries where electricity is unavailable or unreliable (Figure 1.2a). In such applications, heat could be supplied by a passive solar thermosyphon. Similarly, this technology could be attractive for stationary generator waste-heat activated refrigeration or air-conditioning in forward operating military bases where electricity use must be carefully budgeted (Figure 1.2b). This increased mechanical simplicity and flexibility comes at a cost: single pressure absorption systems generally achieve lower cooling COPs (~0.1 – 0.2) than conventional single-effect absorption systems with similar heat input temperatures (~0.5 – 0.7) (Srikhirin and Aphornratana, 2002).

1.2 Single Pressure Absorption Refrigeration

Single-pressure absorption refrigeration was first proposed by von Platen and Munters (1928) in the diffusion absorption refrigeration (DAR) cycle. A number of commercial products have been developed based on this design, including early residential refrigerators. Implementations have also been developed for camping or RV use – cases where propane or other thermal energy sources can be employed, but electricity availability is limited. These quiet, fully passive, systems are also commonly installed in hotel rooms where conventional compressor-driven VC cycles may be unacceptably noisy (Chen *et al.*, 1996). In such applications, electrical heating is usually employed as the thermal source, rather than a gas flame.

The present investigation focuses on the family of single-pressure absorption refrigeration technologies first proposed by von Platen and Munters (1928). A related thermodynamic cycle was patented by Einstein and Szilard (1930), but has not found commercial adoption. It was first demonstrated experimentally by Delano (1998), and a number of modeling-based studies of the cycle have since been conducted (Mejbri *et al.*, 2006; Shelton *et al.*, 1999).

1.3 Principles of Diffusion Absorption Refrigeration

Because, the DAR cycle operates in a fully passive, thermally activated fashion, mechanical means of circulating working fluid between components (e.g., electrically driven compressors or pumps) cannot be employed. Rather, fluid is transported through passive mechanisms. In the bubble-pump generator (BPG), liquid solution is lifted by the buoyancy of rising desorbed refrigerant-vapor bubbles. This process establishes the

hydrostatic head that drives liquid flow through other components in the system (e.g., absorber and solution heat exchanger (SHX)).

DAR systems are pressurized with an inert low-density non-condensable/non-absorbable auxiliary gas, usually helium or hydrogen (Zohar *et al.*, 2005). Net gas circulation is effected through the density difference between warm, refrigerant-poor, gas mixture rising out of the absorber and cool, refrigerant-rich, gas sinking from the evaporator. Thus, the cycle can be idealized as two passively circulating fluid loops (liquid and gas), which interact in the absorber.

The DAR cycle operates at nearly a single total pressure, with only slight (~1%) differences due to hydrostatic variations and frictional losses. Thus, the conventional throttling mechanism for refrigerant expansion and cooling employed in vapor-compression and conventional two-pressure absorption systems cannot be employed. Rather, the liquid refrigerant stream flowing out of the condenser is contacted with refrigerant-poor (low vapor pressure) gas flowing from the absorber. The vapor pressure difference between these two streams causes refrigerant evaporation, and thus, the cooling effect. This evaporative cooling process is similar to that employed in open-cycle absorption refrigeration technologies, which have been reviewed in detail by Kaushik and Kauinya (1989), Grossman (2002), and Enteria *et al.* (2013).

The DAR cycle is typically configured with ammonia refrigerant, water absorbent, and helium or hydrogen auxiliary gas (Zohar *et al.*, 2005). Other refrigerant-absorbent pairs have been considered, including Water-LiBr (Saravanan and Maiya, 2003), organic working fluids (Ben Ezzine *et al.*, 2010b), and Ammonia-$LiNO_3$ (Wang, 2012).

The basic DAR cycle flow process is presented schematically in Figure 1.3a (Rattner and Garimella, 2011a). In this cycle, refrigerant-rich solution flows from the reservoir to the generator (1), where it is heated to desorb refrigerant vapor. The refrigerant vapor and refrigerant-poor solution flow up the bubble pump (BP) (2) lifted by the buoyancy of the vapor bubbles. Refrigerant vapor separates from the solution flow at the BP outlet, and continues to the condenser (4). The refrigerant flows through the condenser, rejecting heat to the surroundings as it condenses, and exits as subcooled liquid (5). The liquid refrigerant partially flashes in the presence of the refrigerant-poor gas mixture at the evaporator inlet. The two-phase mixture continues to evaporate and cools the conditioned space as it flows through the evaporator towards the absorber vapor inlet (6). Refrigerant-poor solution overflowing from the BPG (3) flows into the absorber solution inlet, and contacts the gas stream from the evaporator in a counter-flow fashion (3 → 1). Refrigerant is absorbed from the gas mixture into the solution, rejecting heat to the surroundings and regenerating both the refrigerant-rich solution (1) and refrigerant-poor gas streams (7). The refrigerant-rich solution continues to the reservoir and the refrigerant-poor gas rises to the evaporator inlet, completing the cycle.

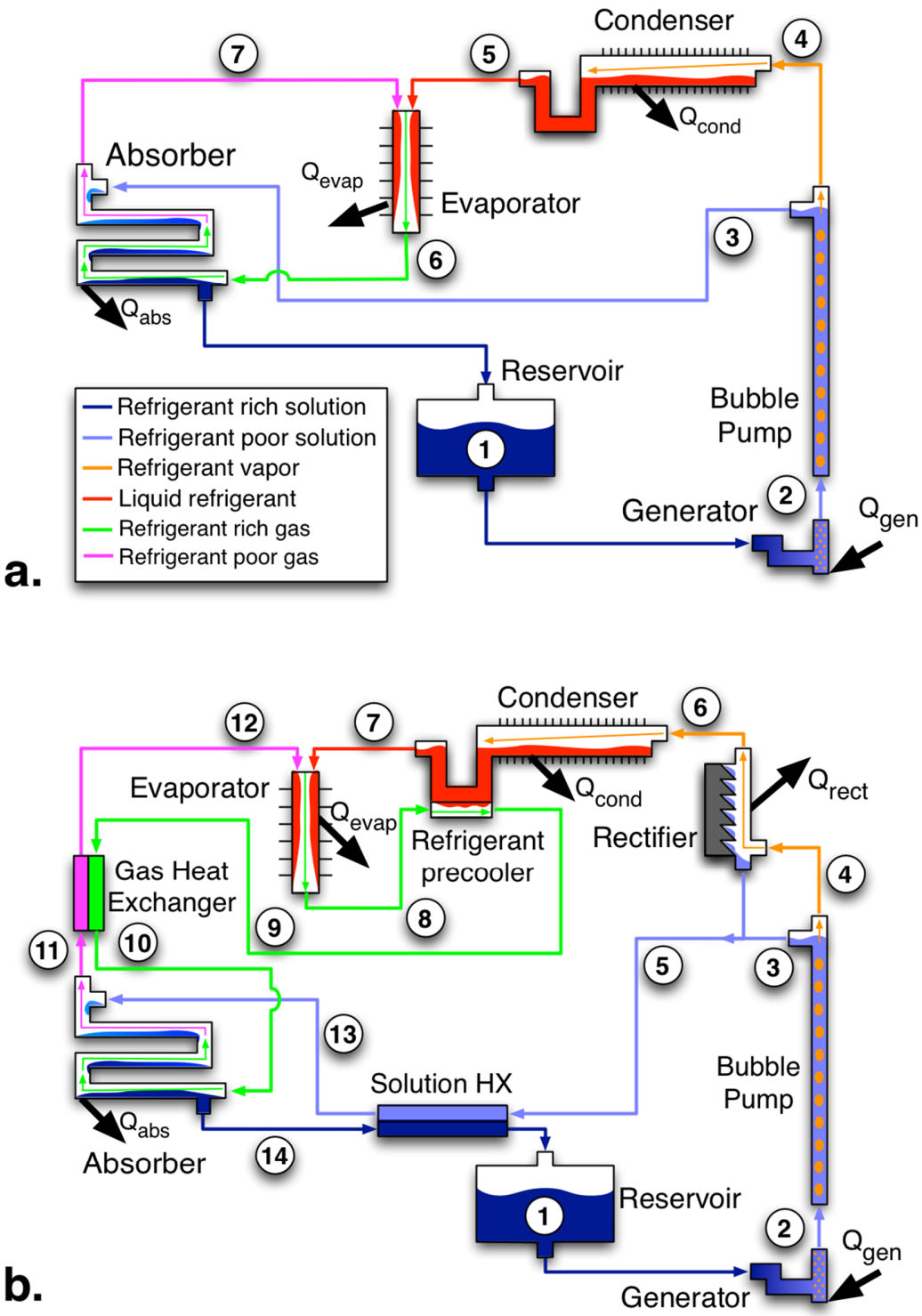

Figure 1.3 – Flow diagrams of the (**a**) basic and (**b**) advanced, recuperative, diffusion absorption refrigeration cycles

In advanced cycles, additional components are incorporated to improve overall system efficiency (Figure 1.3b) (Zohar *et al.*, 2007). A solution heat exchanger (SHX) is employed to recover heat from the high-temperature solution flow exiting the BPG, preheating the cool solution flowing out of the reservoir. A gas heat exchanger (GHX) is similarly incorporated for recuperation between the cool evaporator and warm absorber gas outlet streams. A refrigerant pre-cooler (RPC) can also be employed to precool liquid refrigerant entering the evaporator. A rectifier component may also be necessary if a relatively volatile absorbent, such as water, is employed. This component cools the vapor stream flowing out of the bubble-pump generator (BPG), condensing and separating the absorbent, and increasing the refrigerant purity. This process can lower the minimum evaporator temperature, but also reduces the cooling capacity because some refrigerant will be condensed and removed with the rectifier reflux. Unlike conventional pumped solution absorption cycles, the introduction of such recuperative components must be done judiciously, considering the fluid circulation penalty due to the frictional losses resulting from these additional components in a cycle in which buoyancy head is the sole driving force.

1.4 State of DAR Technology

The use of passive circulation mechanisms and solely thermal input enables mechanically simple and robust refrigeration systems. However, DAR device performance can be challenging to predict a priori, and the ability to tune the device is limited because all flow rates are fully coupled to the heat input rate (Rattner and Garimella, 2011a). Cycle-level modeling studies have been published; however, most assume flow rates and operating conditions based on results from specific experimental

systems. Device design and optimization for new DAR systems can thus be an iterative and expensive process (Jakob *et al.*, 2008). As such, there is a critical need for single-pressure absorption refrigeration design resources that account for both overall system-level behavior as well as the local fluid-mechanics and heat- and mass-transfer processes that govern the flow rates of the different fluid streams.

Conventional DAR systems require high source temperatures of 150 – 200°C (Jakob *et al.*, 2008; Srikhirin *et al.*, 2001), but can achieve relatively high COPs (approaching 0.30 (Chen *et al.*, 1996)) while delivering cooling at temperatures suitable for freezing or refrigeration. Additionally, overall package sizes can be competitive with commercially available vapor compression based refrigerators. However, this source temperature range necessitates relatively high grade energy inputs, usually from natural gas or electricity, which limits off-grid applications. A number of investigations have been conducted to develop alternate system configurations and working fluids that can operate with reduced input temperatures, which could be delivered from waste-heat or solar-thermal sources. However, such low-source-temperature experimental systems have either operated at elevated evaporator temperatures ($\gtrsim$5°C) unsuitable for refrigeration, or incorporated forced internal fluid circulation and/or coupling fluid loops for heat rejection, preventing fully passive applications. A graphical summary of reported source temperatures and COPs from these studies is presented in Figure 1.4. There is thus a need for DAR system designs that can achieve fully passive cooling with low- temperature ($\lesssim$ 130°C) sources at evaporator temperatures suitable for refrigeration ($\lesssim$ 5°C).

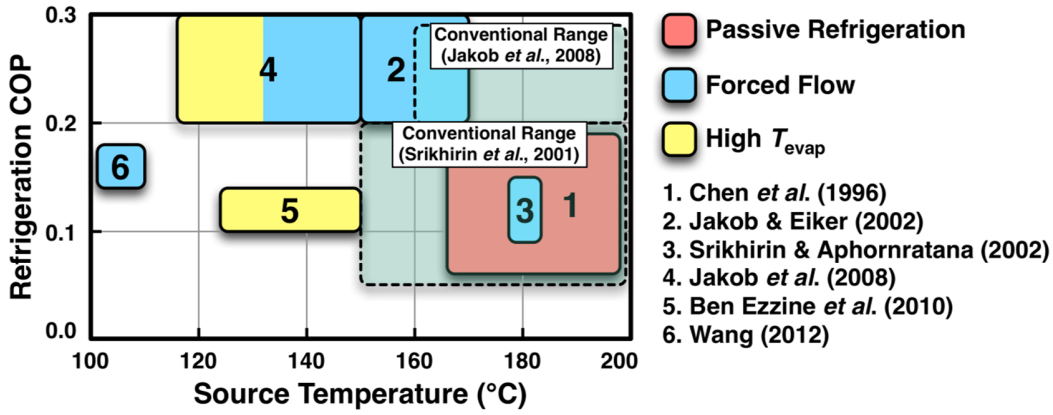

Figure 1.4 – COPs and source temperatures of experimentally investigated DAR systems

While there have been extensive component-level investigations of two-pressure absorption technologies, single pressure system components have received comparatively limited attention. Single-pressure absorption system components must operate under strict constraints, with minimal internal pressure drop allowances (passive fluid circulation) and relatively high thermal resistances to the surroundings (passive heat transfer). These design challenges are exacerbated at low-source-temperature conditions due to reduced driving buoyancy forces in the gas loop and low temperature differences available for heat transfer.

The bubble-pump generator is a critical candidate for detailed investigation and enhancement because it establishes both solution and refrigerant flow rates, and thus dramatically affects overall system performance (Zohar *et al.*, 2008). Relevant mechanistic models have been reported (de Cachard and Delhaye, 1996; Delano, 1998; Reinemann *et al.*, 1990; White, 2001), but robust predictive capabilities have not been achieved.

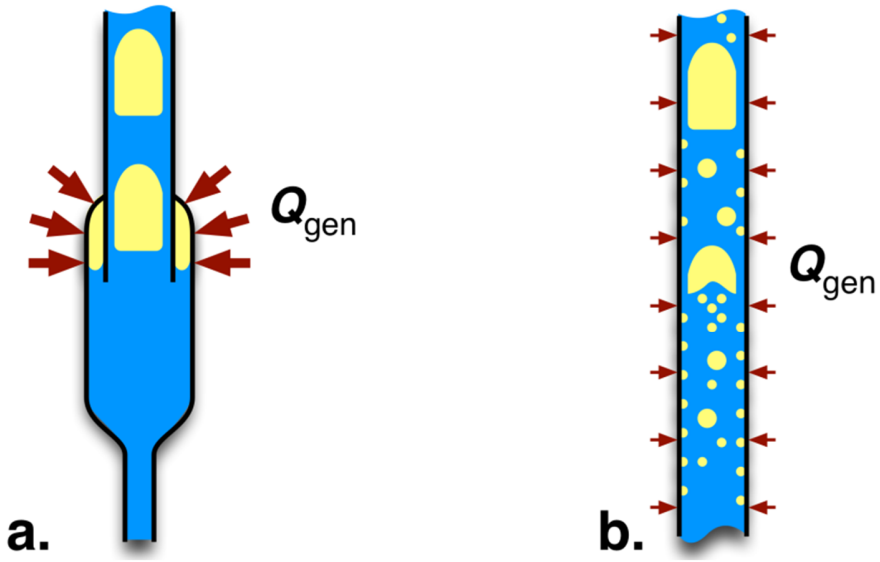

Figure 1.5 – Schematics of (**a**) spot heated and (**b**) distributed heated bubble pump generators

Conventional BPG generator designs employ "spot heating" (Figure 1.5a), wherein all input heat is delivered to a small localized portion at the base of the component. This approach can yield high pumping rates and simplifies component analysis because liquid and vapor flow rates are constant along a major portion of the component length. However, it also necessitates high source temperatures for given heating rates due to the limited heat-transfer area. A number of recent studies have proposed an alternate distributed heating approach (Figure 1.5b) (Benhimidene *et al.*, 2011; Dammak *et al.*, 2010; Jakob *et al.*, 2008; Rattner and Garimella, 2015a). This configuration could enable operation with low-temperature thermal sources, such as solar-heat or stationary generator coolant. However, this BPG design is significantly more difficult to analyze because liquid and vapor flow rates vary continuously along the component length. Some

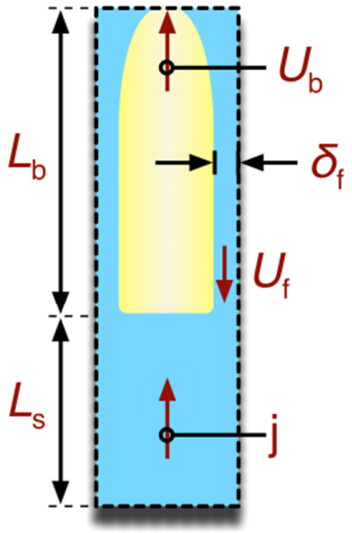

Figure 1.6 – Schematic of Taylor flow unit cell

distributed heating BPG models have been reported in the literature, but validation has not yet been demonstrated.

BPGs are usually designed to operate in the Taylor flow regime (Delano, 1998), indicated schematically in Figure 1.6, in which elongated (Taylor) bubbles are separated by liquid slugs in quasi-periodic unit cells (Gao and Jin, 2012). This flow pattern is desirable for bubble pump operation because liquid only flows downward in the thin films (thickness δ_f) around the rising elongated bubbles. BPGs have been found to operate most efficiently in the intermediate Bond number range (Bo = $\rho g D^2/\sigma$, $5 \lesssim \text{Bo} \lesssim 40$) where inter-phase slip is relatively low (increases with Bo), but frictional flow resistance is also acceptable (decreases with Bo). Here, the Bond number (Bo) is a measure of relative buoyancy to surface tension force strengths, and has been highlighted as a key parameter for identifying important forces governing two-phase flow mechanisms (Funada *et al.*, 2005; Khandekar *et al.*, 2010; Viana *et al.*, 2003). While the

Taylor flow pattern has been extensively studied in the large diameter channel ($\mathrm{Bo} \gtrsim 40$) and capillary/microchannel ($\mathrm{Bo} \lesssim 5$) limits, the intermediate-scale transition region has not yet been thoroughly characterized (Rattner and Garimella, 2015b). Additionally, for the most commonly used refrigerants in DAR systems (e.g., ammonia or water), this intermediate Bond number range also corresponds to the transition between laminar and turbulent flow in the liquid slugs, further complicating the flow analysis. As a result, substantial discrepancies in predicted pumping rates can be found between published BPG flow models that incorporate sub-models that are only valid at the high or low Bond number and laminar or turbulent flow limits (Figure 1.7). Thus, there is a need for improved understanding and characterization of the underlying two-phase Taylor flow at conditions applicable to BPG operation.

A wide variety of experimental and simulation based techniques have been applied to investigate two-phase Taylor flow phenomena. High speed photography has been successfully applied to measure kinematic parameters including bubble rise velocity (U_b) (Bendiksen, 1984; Davies and Taylor, 1950; White and Beardmore, 1962), liquid film thickness (δ_f) (Funada *et al.*, 2005; Thulasidas *et al.*, 1995), and Taylor bubble (L_b) and liquid slug (L_s) lengths (Pinto *et al.*, 2001; Shao *et al.*, 2011; van Hout *et al.*, 2001; Wang *et al.*, 2009). However, such detailed data are relatively sparse for intermediate Bond number flows.

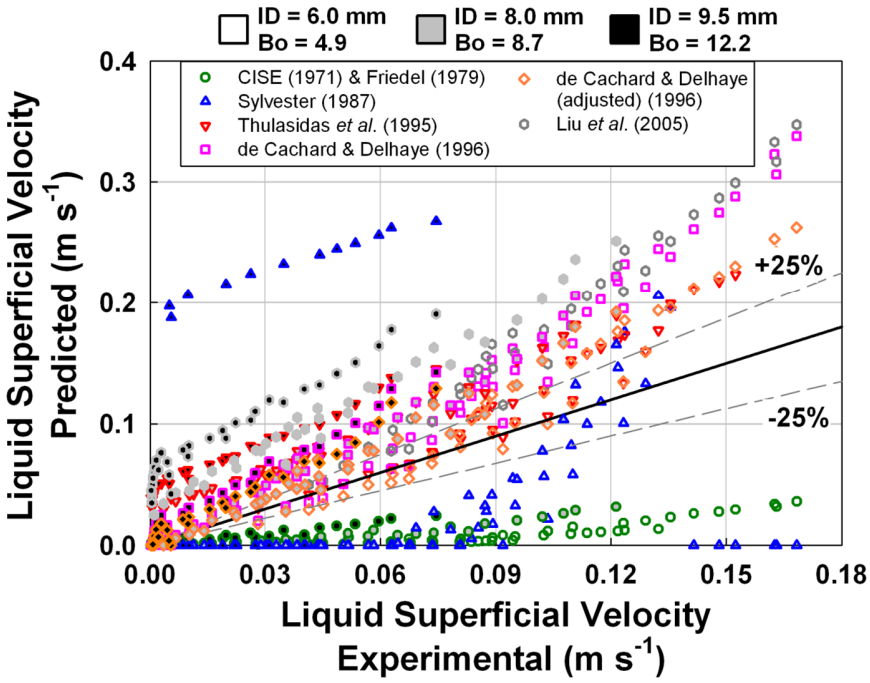

Figure 1.7 – Comparison of predicted liquid pumping rates using various Taylor flow models and the experimental data of Rattner and Garimella (2015b) (air-water flow in 6.0 – 9.5 mm ID tubes, T = 22°C, P = 101 kPa)

Relatively mature two-phase flow simulation approaches, such as the level-set and volume-of-fluid (VOF) methods, have also been applied to study adiabatic Taylor flows (Akbar and Ghiaasiaan, 2006; Figueroa-Espinoza and Fabre, 2011; Kawaji *et al.*, 1997; Marschall *et al.*, 2014). These simulation studies have proven particularly useful for evaluating pressure fields (hydrodynamics), which can be difficult to measure experimentally. For example, in the study by Kreutzer *et al.* (2005), computational results were applied to develop correlations for the flow-transition pressure drop in the wake behind Taylor bubbles. However, simulation techniques for two-phase flows with phase-change heat transfer are still in their infancy (Rattner and Garimella, 2014). Thus, new

approaches must be developed to analyze the distributed heating boiling flow pattern that would be found in enhanced BPG designs.

1.5 Present Investigation

The objective of the present investigation is to develop a fundamental understanding of single-pressure diffusion absorption refrigeration technology, from the underlying fluid flow and transport phenomena to the full system scale, concentrating on low-source-temperature applications. This study attempts to address limitations in the literature that have led to an iterative and empirical design process for DAR systems and poor predictive capabilities for DAR component behavior, particularly the BPG. By addressing these research needs, this effort will also lead to the development of a fully passive low-source-temperature ($T_{source} \lesssim 130°C$) DAR system suitable for refrigeration applications ($T_{evap} \lesssim 5°C$). To these ends, the following studies are conducted:

- Detailed complementary experimental and simulation studies are performed to gain improved insights into Taylor flow phenomena in the intermediate Bond number regime. This approach integrates local kinematic measurements obtained using high-speed photography and hydrodynamic data (i.e., pressure field) from simulations.
- A comprehensive two-phase Taylor flow model for the intermediate Bond number regime is formulated. This model integrates sub-models that have been independently validated with experimental and simulation data.
- A novel coupling-fluid (distributed) heated BPG design is developed and experimentally evaluated. A mechanistically consistent model is developed for the coupling-fluid heated BPG design, and is validated using detailed results from the experimental and simulation based component studies. New simulation techniques are

formulated to model the phase-change heat transfer along the length of the component.

- Detailed DAR BPG, condenser, evaporator, and absorber design models are formulated to enable prediction of flow rates and heat and mass transfer rates from first principles. Results from these models are integrated to inform a system-level DAR design model.
- This DAR model is applied to develop a fully passive low-source-temperature (110 – 130°C) refrigeration system. This system integrates the novel coupling-fluid heated BPG design, a new enhanced absorber configuration, and an alternate working fluid set (NH_3-NaSCN-He) suitable for low-source-temperature operation. This system is experimentally evaluated over a range of representative operating conditions.

1.6 Structure of this Dissertation

The structure of this dissertation is as follows.

- **Ch. 2: Adiabatic Taylor flow experiments and kinematic closure in the intermediate Bond number regime** – Detailed experimental high-speed photography studies are conducted of Taylor flow at intermediate Bond numbers. Sub-models are formulated for bubble rise velocity, liquid film thickness, void fraction, and Taylor bubble and liquid slug lengths. These results enable kinematic closure of Taylor flow in the intermediate Bond number regime.
- **Ch. 3: Taylor flow simulation and hydrodynamic closure in the intermediate Bond number regime** – VOF based simulations are conducted for Taylor flow in the intermediate Bond number regime. Experimental results reported in Chapter 2 are

applied to validate results. Simulation data are applied to inform and formulate sub-models for pressure drop in the film flow around Taylor bubbles, bulk liquid slug flow, and transition regions between Taylor bubbles and liquid slugs. These hydrodynamic sub-models are integrated with kinematic sub-models from Chapter 2 to formulate a comprehensive, experimentally validated, Taylor flow and bubble pump model.

- **Ch. 4: Coupling-fluid heated bubble pump generators: experiments and model development** – A novel coupling-fluid heated BPG design is experimentally investigated with boiling steam-water flow over a range of conditions representative of DAR operation. A physically consistent coupled fluid-flow and heat-transfer model is developed for this design, incorporating the Taylor flow submodel developed in Chapter 3. Experimental validation for overall flow rates, heat transfer, and pressure drop is demonstrated.
- **Ch. 5: Simulation of flow boiling and distributed heated bubble-pump generator model assessment** – A first-principles based phase-change simulation approach is developed and validated with established phase-change heat-transfer results. This formulation is applied to validate predictions from the coupling-fluid heated BPG model formulated in Chapter 4.
- **Ch. 6: Low-source-temperature diffusion absorption refrigeration: modeling and cycle analysis** – Detailed DAR design models are formulated to enable integrated component and overall system design from first principles. This model is applied to design a low-source-temperature passive DAR system.

- **Ch. 7: Low-source-temperature diffusion absorption refrigeration: experiments and model assessment** – A full experimental DAR system is developed based on results from the model formulated in Chapter 6. This system integrates the coupling-fluid heated BPG design proposed in Chapter 4, a novel enhanced absorber design, and an alternate working fluid set (NH_3-NaSCN-He). System performance is evaluated over a range of source temperatures, evaporator temperatures, heating rates, and ambient conditions. Refrigeration (T_{cool} = 6 → 3°C) is achieved with source temperatures as low as 110°C.
- **Ch. 8: Conclusions and Recommendations** – Results and contributions from these investigations are summarized. Potential avenues for future research are discussed.

CHAPTER 2. ADIABATIC TAYLOR FLOW EXPERIMENTS AND KINEMATIC CLOSURE IN THE INTERMEDIATE BOND NUMBER REGIME

2.1 Introduction

2.1.1 Background

At intermediate liquid and gas flow rates in channels, elongated relatively large diameter bubbles translate, separated by full-diameter *liquid slugs* (Taitel and Barnea, 1990). At high velocities, turbulent shear at the elongated bubble tails can entrain small bubbles in, or *aerate*, the liquid slugs (Fernandes *et al.*, 1983). Turbulent dispersion may prevent agglomeration of these small *slug bubbles* (Barnea and Brauner, 1985). At lower velocities, bubbles are not present in the liquid slugs, and the flow pattern is sometimes referred to specifically as *elongated bubble* or *plug flow*. In small diameter (capillary) channels, the elongated bubbles tend to be symmetric with rounded *noses* and *tails*. Sometimes this configuration is specifically referred to as *bubble-train flow* (Thulasidas *et al.*, 1995). In the vertical upward (co-flow) configuration, the flow pattern is referred to as *Taylor flow*, after the bullet shaped bubbles studied by Davies and Taylor (1950).

In vertical upward Taylor flow, elongated rising bubbles fill a major portion of the channel cross-section, and are surrounded by downward flowing (gravitationally driven) annular liquid films on the walls. The interspersed cylindrical liquid slugs rise at the bulk superficial velocity (j), which is slower than the velocity of the Taylor bubbles ($U_b > j$). This flow pattern arises in, and is employed in, many engineering applications, including:

- **Airlift and bubble pumps** – In these devices, rising Taylor bubbles lift liquid, enabling mechanically simple pumping. Relatively high pumping efficiencies can be

This chapter adapted from: Rattner, A.S., Garimella, S., 2015. Vertical upward intermediate scale Taylor flow: experiments and kinematic closure, International Journal of Multiphase Flow (in press).

obtained in the Taylor-flow pattern because liquid only drains downwards in the thin films around elongated bubbles (Delano, 1998). End uses include well dewatering, nuclear fuel reprocessing (de Cachard and Delhaye, 1996), and solution circulation in single-pressure refrigeration systems (using bubble-pump generators) (von Platen and Munters, 1928). This last case represents the primary application of interest in the present investigation.

- **Miniaturized heat and mass exchangers** – The Taylor-flow pattern has been targeted for monolithic catalytic reactors as a high-interfacial area density, relatively low pressure drop, operating mode (Thulasidas *et al.*, 1995). Additionally, in microchannels, Taylor flow can occur for a large portion of the flow length during phase change processes, such as evaporation and condensation (Garimella, 2004).
- **Petrochemical processes** – Taylor flow of hydrocarbon gases and liquids occurs in oil-well bores (Fernandes *et al.*, 1983), and it is often necessary to employ "slug catchers" in petrochemical processes to dampen the effects of intermittent flow.

Considering these examples, Taylor flow can occur over a large span of channel diameters (μms to cms), flow rates, and fluid properties (water to heavy oils). Forces due to inertia (fluid acceleration, turbulence), gravity (buoyancy), friction (within the fluid medium and at the tube wall), and surface tension may thus significantly affect flow behavior. However, comprehensive investigations have thus far been available only at the asymptotic limits where some of these forces are negligible.

Extensive literature is available for Taylor flows in large scale channels. This regime has been defined using criteria based on the Bond number ($\mathrm{Bo} = \left(\rho_\mathrm{L} - \rho_\mathrm{G}\right) g D^2 / \sigma$), a measure of relative gravitational-to-surface tension force strengths. Here, ρ_L and ρ_G

represent the liquid and gas densities, respectively, g is the gravitational acceleration, D is the channel diameter, and σ is the fluid surface tension. Viana *et al.* (2003) identified the following criterion for large-scale flows: $\mathrm{Bo} = (\rho_L - \rho_G) g D^2 / \sigma \gtrsim 40$ ($D \gtrsim 17$ mm for ambient gas-water flow). For such cases, surface tension forces are negligible, leaving flows governed by inertial, viscous, and gravitational forces. Such configurations are of particular interest for petrochemical extraction and separation, and have generally been studied in either the viscous limit (for heavy products) or the inertial (turbulent) limit for high flow rates in large scale channels. Comprehensive flow models for these configurations have been reported by Fernandes *et al.* (1983), Sylvester (1987), and Taitel and Barnea (1990). Detailed shadowgraphy and particle image velocimetry studies have also been conducted to measure Taylor bubble profiles and near-bubble liquid velocity fields in the large scale regime (Bugg and Saad, 2002; Nogueira *et al.*, 2006a, b).

Many investigations have also been performed for Taylor flows at the capillary or microchannel scale. Several criteria have been proposed for defining this regime, ranging from $\mathrm{Bo} \lesssim 0.9$ to $\mathrm{Bo} \lesssim 19.7$ (Khandekar *et al.*, 2010)). This study adopts the condition of $\mathrm{Bo} \lesssim 5$, the minimum Bond number for which a Taylor bubble will rise in a stagnant liquid medium (Bendiksen, 1985). In such cases, inertial and gravitational forces are small or negligible compared to viscous and surface tension forces. Applications of interest include monolithic catalytic reactors (Thulasidas *et al.*, 1995), microchannel heat and mass exchangers (Garimella, 2000), and fuel cells (Anderson *et al.*, 2010; Argyropoulos *et al.*, 1999; Hussaini and Wang, 2009). Flow models and literature reviews for Taylor flows at this scale can be found in Thulasidas *et al.* (1995), Garimella (2004), Liu *et al.* (2005), and Angeli and Gavriilidis (2008).

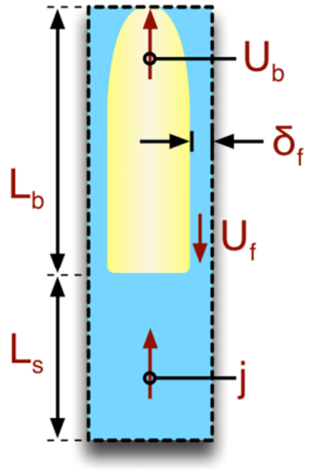

Figure 2.1 – Repeating unit cell model for Taylor flow

In contrast, vertical upward Taylor flows in the intermediate scale regime ($5 \lesssim \mathrm{Bo} \lesssim 40$) where all four classes of forces are relevant, have not yet been well characterized (Reinemann *et al.*, 1990). At this scale, the Taylor-flow pattern is particularly attractive for gas-lift-pump and bubble-pump applications (de Cachard and Delhaye, 1996).

Analytical or *mechanistic* Taylor-flow models have been proposed in the literature in which the flow pattern is modeled as identical repeating *unit cells* of liquid slugs and elongated Taylor bubbles (Figure 2.1). Appropriate closure models can then be applied for parameters including bubble rise velocity (U_b), slug or bubble length (L_s and L_b), and frictional resistances (Fernandes *et al.*, 1983; Sylvester, 1987; Taitel and Barnea, 1990; Thulasidas *et al.*, 1995). Many correlations have been reported for such closure models, but few are applicable in the intermediate scale regime where all four aforementioned classes of forces can be significant. Additionally, intermediate scale Taylor flows tend to

span the laminar-to-turbulent transition, indicating strong sensitivity to Reynolds numbers. This investigation focuses on measurement and prediction of the Taylor bubble rise velocity, liquid film thickness, void fraction, Taylor bubble length, and liquid slug length in intermediate scale flows.

2.1.2 Prior Work

2.1.2.1 Taylor bubble rise velocity prediction

In large scale flows, the rise velocity of Taylor bubbles has generally been modeled in a drift flux fashion:

$$U_b = C_0 j + \Gamma\sqrt{gD} \tag{2.1}$$

The Γ term corresponds to the rise velocity of a bubble in a quiescent liquid medium (no net liquid flow). C_0 is referred to as the distribution parameter, and accounts for the fact that Taylor bubbles rise faster than the bulk flow because the surrounding liquid film drains downward. While the governing fluid mechanics equations are non-linear, this superposition approach for bubble velocity has proven successful in the literature. In general, these models assume that individual Taylor bubbles are long, sufficiently far apart (no drafting, (Barnea and Taitel, 1993)), and that liquid transport properties are dominant ($\rho_G/\rho_L \ll 1$, $\mu_G/\mu_L \ll 1$, where μ is the dynamic viscosity).

The Γ parameter is assumed independent of total flow rate (j); therefore, dimensional analysis indicates that it can be correlated in terms of the Bond number (Bo) and viscous number (N_f) (White and Beardmore, 1962).

$$\mathrm{Bo} = \frac{(\rho_L - \rho_G) g D^2}{\sigma} \qquad \mathrm{N_f} = \sqrt{\frac{\rho_L (\rho_L - \rho_G) g D^3}{\mu_L^2}} \tag{2.2}$$

In the limit of negligible surface tension and viscous forces, Γ approaches approximately 0.35 (Davies and Taylor, 1950; Dumetriscu, 1943).

White and Beardmore (1962) found that surface tension effects on Γ are negligible for Bo > 70. They proposed the following correlation:

$$\Gamma = 0.345\left[1-\exp\left(\frac{-0.01\mathrm{N_f}}{0.345}\right)\right]\left[1-\exp\left(\frac{3.37-\mathrm{Bo}}{m}\right)\right] \tag{2.3}$$

$$m = \begin{cases} 10 & \mathrm{N_f} > 250 \\ 69\mathrm{N_f}^{-0.35} & 18 < \mathrm{N_f} < 250 \\ 25 & \mathrm{N_f} < 18 \end{cases} \tag{2.4}$$

Bendiksen (1985) modeled the Taylor bubble rise in the limit of negligible viscous forces and relatively small surface tension forces, and proposed the curve fit:

$$\Gamma = 0.486\sqrt{1+\frac{20}{\mathrm{Bo}}\left(1-\frac{6.8}{\mathrm{Bo}}\right)}\,\frac{1-0.96\exp\left(-0.0165\mathrm{Bo}\right)}{1-0.52\exp\left(-0.0165\mathrm{Bo}\right)} \tag{2.5}$$

This fit was reported to be valid for Bo > 5.7. Bendiksen (1985) also reported that Γ = 0 for Bo < 4.5; i.e., for low Bo (capillary) flow, individual elongated bubbles cannot rise without also effecting a net flow (j > 0). Bretherton (1961) found a slightly lower critical Bond number of 3.37. Studies on capillary flows generally assume Γ = 0.

Viana *et al.* (2003) conducted a survey of experimental studies of Taylor bubble rise velocities in quiescent liquid-filled tubes, and developed a universal empirical correlation for Γ. The authors found that Γ is independent of Bo for Bo > 40 and that Γ rapidly approaches 0 for Bo < 10. Funada *et al.* (2005) applied the results of Viana *et al.* (2003)

to predict the rise velocity of elongated ellipsoidal bubbles, and thus estimate Taylor bubble nose profiles.

Mandal *et al.* (2007) investigated the rise velocity of liquid Taylor bubbles in quiescent higher-density liquid-filled tubes. The authors developed a correlation for Γ accounting for the effects of reduced buoyancy forces.

Results from dimensional analysis indicate that the distribution parameter is a function of the Reynolds number (Re_j), Bond number (Bo), and capillary number (Ca).

$$\mathrm{Re}_j = \frac{\rho_L j D}{\mu_L} \qquad \mathrm{Ca} = \frac{\mu_L j}{\sigma} \tag{2.6}$$

In the limit of high Re_j and $\mathrm{Bo} \to 0$ (i.e. large scale channels), $C_0 = 1.20$ (Nicklin *et al.*, 1962). For low Re with $\mathrm{Bo} \to 0$, Taylor (1961) found that $C_0 = 2.29$. For turbulent flow and $\mathrm{Bo} \gtrsim 40$, Bendiksen (1985) proposed the fit:

$$C_0 = \frac{\log_{10}\left(\mathrm{Re}_j\right) + 0.309}{\log_{10}\left(\mathrm{Re}_j\right) - 0.743}\left\{1 - \frac{2}{\mathrm{Bo}}\left[3 - \log_{10}\left(\mathrm{Re}_j\right)\exp\left(-0.025\mathrm{Bo}\right)\right]\right\} \tag{2.7}$$

However, this fit does not approach appropriate limits outside the window of applicability, falling below 1.20 for large Re_j, and ranging from $-\infty$ to ∞ for small Bo. Bendiksen recommended a separate laminar fit for $\mathrm{Bo} \lesssim 40$, but the transition between the laminar and turbulent regimes remains an open problem.

$$C_0 = 2.29\left\{1 - \frac{20}{\mathrm{Bo}}\left[1 - \exp\left(-0.0125\mathrm{Bo}\right)\right]\right\} \tag{2.8}$$

In the capillary limit (Bo → 0), C_0 is generally assumed to only be a function of Ca. Fairbrother and Stubbs (1935) developed the implicit correlation:

$$\frac{\left(1-1/C_0\right)^2}{C_0} = \mathrm{Ca} \qquad 7.75\cdot 10^{-5} < \mathrm{Ca} < 0.014 \tag{2.9}$$

Liu *et al.* (2005) developed the following correlation with an extended range of applicability.

$$C_0 = \frac{1}{1-0.61\mathrm{Ca}^{-0.33}} \qquad 0.0002 < \mathrm{Ca} < 0.39 \tag{2.10}$$

Additional capillary-scale rise velocity correlations can be found in the review of Angeli and Gavriilidis (2008). In summary, the Taylor bubble rise velocity is well characterized at the asymptotic limits of N_f, Bo, and Re_j, but predictive models validated for intermediate Bond numbers and transitional Reynolds numbers are limited.

2.1.2.2 Liquid-film thickness prediction

In large scale flow models, the thickness of the falling liquid film around Taylor bubbles (δ_f) is usually predicted using correlations and analytical results for flat-plate falling-films with no-shear stress interface conditions. This approach is valid in the fully developed film region around long Taylor bubbles. For short bubbles, it may be important to account for the thicker film near the bubble-nose by applying profile models such as those by Dumetriscu (1943), Bendiksen (1985), Funada *et al.* (2005).

Fernandes *et al.* (1983) recommended the Brotz (1952) correlation for the turbulent falling-film thickness around long Taylor bubbles. Here, U_f is the average liquid film velocity.

$$\delta_f \left(\frac{g\rho_L^2}{\mu_L^2} \right)^{1/3} = \left(\frac{3\mathrm{Re}_f^2}{590} \right)^{1/3} \qquad \mathrm{Re}_f = \frac{\rho_L U_f \delta_f}{\mu_L} \tag{2.11}$$

Llewellin *et al.* (2011) investigated the falling liquid-film thickness around Taylor bubbles in large scale flows (Bo > 40), and developed a correlation for δ_f as a function of the viscous number N_f. Llewellin *et al.* (2011) also proposed an approach to predict film thickness for intermediate scale Taylor flows, but no experimental data was available for validation.

de Cachard and Delhaye (1996) developed models for Taylor flow in slightly smaller diameter tubes (10 – 40 mm). In these cases, the falling films may be laminar or turbulent; thus, a piecewise implicit correlation was recommended:

$$U_f = \begin{cases} 0.333 \dfrac{g\rho_L \delta_f^2}{\mu_L} & \mathrm{Re}_f < 750 \\ 15.8\left(g\delta_f\right)^{1/2} & \mathrm{Re}_f > 750 \end{cases} \tag{2.12}$$

At the capillary scale, the liquid film still flows downward due to gravity, but its thickness is usually modeled in terms of capillary effects only (independent of channel orientation). Fairbrother and Stubbs (1935) proposed a correlation for liquid film thickness in capillary tubes, which is independent of gravitational forces.

$$\frac{\delta_f}{D} = 0.25\mathrm{Ca}_b^{1/2} \qquad \mathrm{Ca}_b = \frac{\mu_L U_b}{\sigma} \tag{2.13}$$

Angeli and Gavriilidis (2008) detail a number of other correlations for liquid films in capillary tubes, which are all functions only of Ca. However, Thulasidas *et al.* (1995)

demonstrated that the film thickness in capillary flows is sensitive to orientation. Different trends in δ_f with orientation were reported at different ranges of Ca.

It is unlikely that these capillary-number-only correlations apply for intermediate scale flows where inertial forces are significant. The approach of de Cachard and Delhaye (1996) is promising, but has not been validated independently of their overall flow model.

2.1.2.3 Void fraction prediction

Void fraction (α) is a critical parameter for predicting Taylor-flow behavior, particularly in intermediate-to-large scale flows where hydrostatic forces are large relative to frictional forces. In most Taylor-flow models, void fraction is inferred from conservation equations and specified parameters including: liquid and gas flow rates (j_L, j_G), bubble rise velocity (U_b), and liquid film thickness (δ_f) (Fernandes *et al.*, 1983; Sylvester, 1987; Thulasidas *et al.*, 1995). Prediction of void fraction following this approach requires constitutive models valid for intermediate scale flows.

For large scale flows, dispersed gas bubbles in the liquid slugs can account for a significant portion of the void fraction. Barnea and Brauner (1985) developed a model to predict the gas fraction in liquid slugs, but it is specific to turbulent flows. It is not known whether dispersed bubbles can persist in liquid slugs in intermediate scale flows, where Reynolds numbers typically range from laminar to transitional values.

Many general purpose (flow-regime independent) two-phase void fraction correlations have been reported in the literature. Woldesemayat and Ghajar (2007)

performed a rigorous validation study of 68 of these models, but only 4% of the considered experimental data were from intermediate scale flows.

Small flow-passage-specific investigations of void fraction were performed by Triplett *et al.* (1999) (microchannels), Kawahara *et al.* (2002) (microchannels), and Winkler *et al.* (2012) (horizontal minichannels). It is unclear whether any of these correlations apply for vertical upward intermediate scale Taylor flows.

2.1.2.4 Taylor bubble and liquid slug length prediction

The Taylor-flow pattern is often referred to as quasi-periodic (Gao and Jin, 2012) in the sense that there is a repeating series of elongated bubbles and liquid slugs, but individual feature lengths are widely distributed. Even careful injection of identical-size bubbles can lead to downstream bubble trains of widely varying length scales (Nguen *et al.*, 1996). Barnea and Taitel (1993) performed simulations of developing slug flow, and found that the statistical distributions of bubble and slug lengths stabilize sufficiently far downstream. However, general prediction of entrance lengths for slug flow has proven difficult.

In large scale turbulent Taylor flows, liquid slugs are typically many tube diameters (D) in length. Varied representative values are reported in the literature: 4D (Wang *et al.*, 2009), 6 – 8D (Moissis and Griffith, 1962), ~16D (Taitel *et al.*, 1980), ~21.7D (Fernandes, 1981), and 30 – 48D (Schmidt, 1977). Dukler *et al.* (1985) developed a model to predict the minimum stable liquid slug length as a function of the decaying liquid jet generated at the falling film-to-slug transition. The fact that there is only an apparent physical mechanism for determining the *minimum* stable slug length may help explain the wide ranges reported in the literature. Taylor bubble lengths are typically not

correlated in the large scale tube literature, but rather are inferred from specified liquid-slug lengths and appropriate conservation equations.

Laborie *et al.* (1999) (Equation 2.14) and Liu *et al.* (2005) (Equation 2.15) proposed correlations for liquid slug lengths in capillaries in terms of superficial phase velocities and other relevant non-dimensional parameters. Laborie *et al.* (1999) (Equation 2.16) also proposed a correlation for bubble lengths at the same scale.

$$\frac{L_s}{D} = 3451\left(\mathrm{Re}'_G\,\mathrm{Bo}\right)^{-1.2688} \qquad \mathrm{Re}'_G = \frac{\rho_L U_b D}{\mu_L} \tag{2.14}$$

$$\frac{j_L}{\sqrt{L_s}} = 0.088\,\mathrm{Re}_G^{0.72}\,\mathrm{Re}_L^{0.19} \qquad \mathrm{Re}_G = \frac{\rho_G j_G D}{\mu_G} \quad \mathrm{Re}_L = \frac{\rho_L j_L D}{\mu_L} \tag{2.15}$$

$$\frac{L_b}{D} = 0.0878\left(\frac{\mathrm{Re}'_{U_b}}{\mathrm{Bo}^2}\right)^{0.63} \qquad \mathrm{Re}'_{U_b} = \frac{\rho_L U_b D}{\mu_L} \tag{2.16}$$

In all three correlations, relative feature lengths scale with Reynolds number, leading to extreme predictions outside the capillary regime where fitting data were obtained. Additionally, the model of (Liu *et al.*, 2005) is dimensionally inconsistent; therefore, its applicability to general Taylor flows is unclear.

Kreutzer *et al.* (2003) proposed a capillary-scale liquid slug length correlation in terms of void fraction (α).

$$\frac{L_s}{D} = \frac{1-\alpha}{-0.00141 - 1.556\left(1-\alpha\right)^2 \ln\left(1-\alpha\right)} \tag{2.17}$$

While void fraction is generally not known apriori in Taylor-flow models, it is a convenient parameter for predicting liquid slug length because: $\lim_{\alpha\to 1} L_s = 0$ (gas-only

flow) and $\lim_{\alpha \to 0} L_s = \infty$ (liquid-only flow). However, the correlation of Kreutzer *et al.* (2003) does not approach the second limit.

Additional correlations for liquid slug, Taylor bubble, and unit cell lengths are discussed by Angeli and Gavriilidis (2008). In general, information about Taylor bubble and liquid slug lengths is not available for intermediate scale flows.

2.1.3 Present investigation

In the present investigation, vertical upward air-water Taylor-flow experiments are conducted in intermediate scale tubes (D = 6.0, 8.0, 9.5 mm, Bo = 4.9, 8.7, 12.2) for a range of laminar-to-turbulent flow rates ($480 \le \mathrm{Re}_j \le 4460$). High speed videos are captured to measure flow parameters including: bubble rise velocity (U_b), falling film thickness (δ_f), void fraction (α), and bubble and slug lengths (L_b, L_s). Flow models and correlations are developed to predict these parameters for intermediate scale Taylor flows. Additionally, a universal upward-flow Taylor bubble rise velocity correlation is proposed for microchannel-to-large scale flows. These *kinematic* sub-models are integrated with *dynamic* (i.e., pressure drop) sub-models in Chapter 3 to formulate a comprehensive description of Taylor flow in the intermediate Bond number regime.

2.2 Experimental Facility and Procedure

2.2.1 Facility overview

An air-water flow and visualization facility was developed to investigate vertical upward Taylor flows in 6.0, 8.0, and 9.5 mm ID rounds tubes. A schematic of the experimental facility and photographic configuration is presented in Figure 2.2a-b. Tap water at approximately 22°C was supplied from a large open reservoir to an inlet port at each tube base. A large diameter (360 mm) primary reservoir was employed to maintain

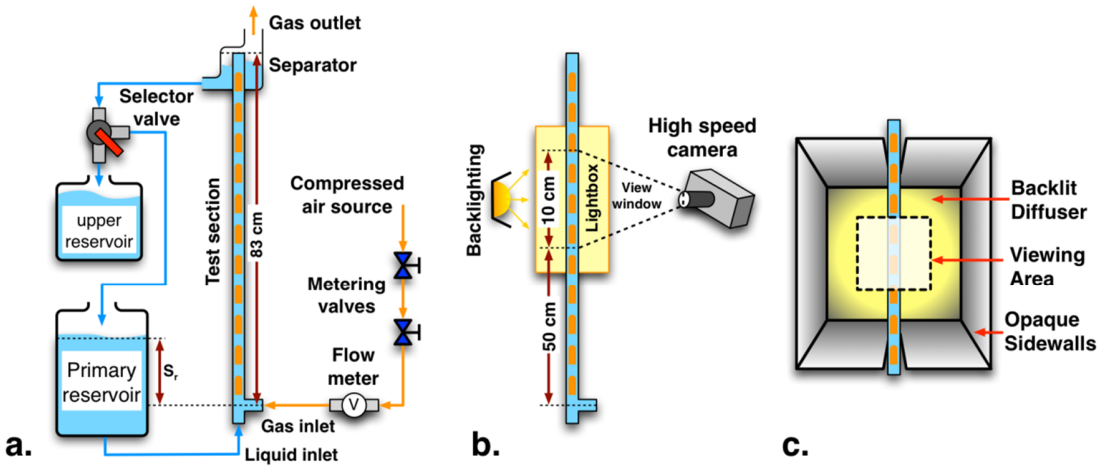

Figure 2.2 – **a**. Schematic of experimental facility, **b**. Photographic and lighting configuration, **c**. Detail view of lightbox and viewing area

nearly constant liquid levels and inlet pressures (± 22 mm, ± 220 Pa) during the experiments.

Compressed air was metered through two needle valves (coarse and fine control), and injected into each tube through a horizontal port 40 mm above the liquid inlet. Volumetric air flow rates were measured using a Dwyer® rotameter (± 38 ml min^{-1}).

The flow tubes were fabricated from glass to permit visual access, and were approximately 830 mm in length above the gas inlet. Each flow tube opened to a larger diameter (22 mm) settling section. Water flow from the settling section was diverted to an upper reservoir, which could be weighed to determine average liquid pumping rates during operation. A high speed camera was employed to record flow phenomena during experiments. The camera focus was centered approximately 550 mm above the gas inlet ports, and the viewing area included approximately 100 mm of tube length. A small *lightbox* enclosure was installed around the visualized portions of the test sections. This

lightbox was an approximately 0.15 m cube with an open front for optical access, opaque diffuse side- and top/bottom- walls to prevent glare from outside lighting, and a translucent diffuser-sheet back wall to provide uniform backlighting in the viewing window (Figure 2.2c). Distortion due to refraction in the fluid and curved glass tube has been highlighted as a potential source of error in two-phase visualization studies (Bugg and Saad, 2002; Milkie, 2014). Therefore, an optical analysis of this configuration was conducted to assess refraction effects.

2.2.2 Optical refraction analysis of visualization configuration

In the high-speed image analysis procedure (described in detail in Section 2.3), Taylor bubble liquid-gas interface positions are determined as the minimum intensity pixels on both sides of the tube axis for each row in collected photographs. A photorealistic ray-tracing simulation was conducted in the PhotoView 360 software package (Dassault Systems, 2013) to evaluate this approach and determine the potential for optical distortion due to refraction effects. This analysis focused on the 6.0 mm ID test section (8.0 mm OD) because it has the greatest relative wall thickness and smallest predicted liquid film thickness (~0.2 mm), and thus the greatest potential for distortion. The test section and lightbox were modeled with representative indices of refraction (Figure 2.3). Uniform diffuse luminosity was specified on the rear wall of the lightbox, representative of the backlit diffuser sheet employed in the experimental facility. Renderings were produced for a simulated small-angle-lens camera (3.6° view angle) 0.50 meters from the test section.

High-resolution (4 MPx) renderings were generated for the 6.0 mm ID tube with air fill (gas-only), water fill (liquid-only), and a 0.2 mm thick uniform water film on the

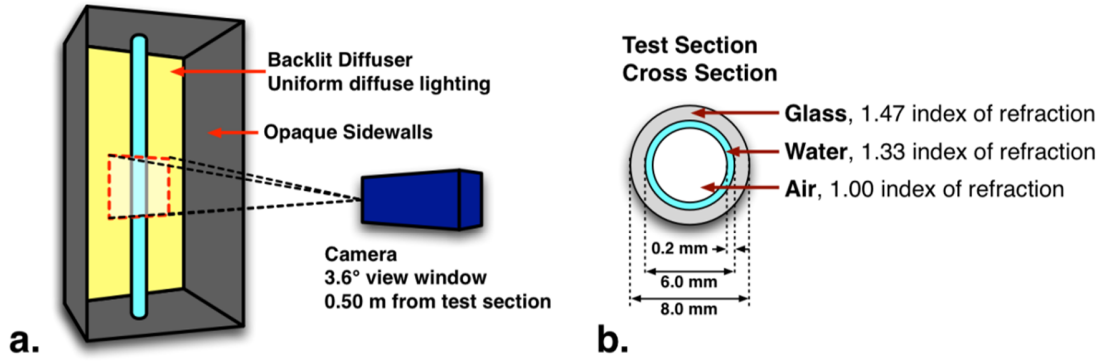

Figure 2.3 – **a**. Geometry for ray-tracing simulation, **b**. Geometry of test section and material indices of refraction

inside tube wall. The first two images correspond to calibration conditions that are employed in the experimental image analysis procedure. The last case is representative of the predicted liquid film around Taylor bubbles for this test section. Experimentally collected photographs and renderings are presented side-by-side for these cases in Figure 2.4. These images appear qualitatively similar, except that the texture of the diffuser sheet was not incorporated in the simulation cases and the liquid film is wavy in the experimental case. Representative normalized pixel-row intensity profiles are presented

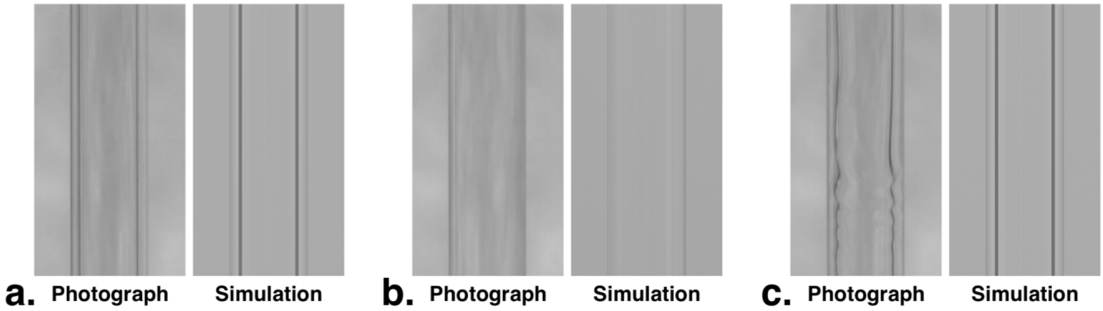

Figure 2.4 – Comparison of experimental photographs and ray tracing simulations for: **a**. air-filled tube (gas only), **b**. liquid-filled tube (liquid-only), **c**. annular water film around an elongated air bubble

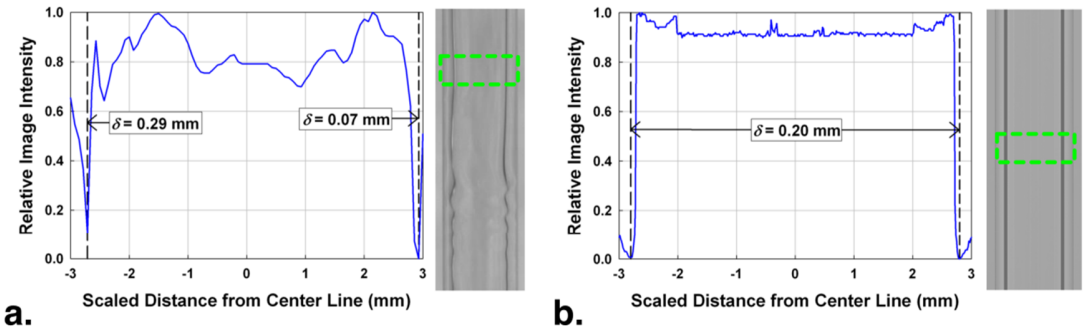

Figure 2.5 – Comparison of pixel intensities in indicated image regions and identified interface locations for: **a**. experimental photograph, **b**. Ray-tracing simulation

for the experimental and simulation liquid-film cases in Figure 2.5. These profiles display similar characteristics, although the wavy film is asymmetric for this row of the experimental image. Additionally, the experimental intensity profile is somewhat noisier, possibly due to the texture of the backlit diffuser sheet in the lightbox.

The apparent liquid-gas interface positions on each row were evaluated as the minimum intensity pixels on both sides of the tube axis. For the simulation case, the row-averaged measured film thickness was 0.204 mm with a standard deviation of 0.009 mm, assuming uniform pixel spacing scaled to the tube outer diameter. The resulting error in film thickness (0.004 mm) is insignificant compared to the experimental pixel pitch of 0.07 – 0.09 mm. Thus, this analysis indicates that optical distortion effects can be neglected in the experimental image analysis process.

2.2.3 Experimental procedure

Flow experiments were conducted for all tubes at submergence ratios (ratio of reservoir level to tube length, S_r) of 0.3, 0.4, and 0.5. For each of these conditions, the air

flow rate was varied from 142 – 940 ml min^{-1}, although net liquid flow was only achieved above threshold air flow rates in the 8.0 and 9.5 mm ID tubes at lower S_r values. Measurements were collected for 108 different conditions of tube diameter, S_r, and air flow-rate.

For each test condition, the flow was allowed to stabilize, and the settling section liquid outlet was then diverted to the upper reservoir. Air flow was maintained for 4 – 15 minutes (± 3 s estimated uncertainty), and the average liquid pumping rate was determined from the change in upper reservoir mass (measured with a scale with ± 1 g uncertainty). Shorter experimental durations were employed for high liquid flow rate cases in order to maintain the main reservoir level within 22 mm (± 0.027 S_r, or ± 220 Pa in hydrostatic inlet pressure). The resulting uncertainties in the average liquid flow rates were slightly higher for the shorter duration experiments, but were maintained below ± 4 ml min^{-1}. The relative uncertainties were less than 1%, except for unsteady very low flow rate cases (< 15 ml min^{-1} liquid flow). Measured volumetric liquid pumping rates (V_L) for all tested tube diameters, submergence ratios, and volumetric air flow rates (V_G) are presented in Figure 2.6.

Three 5 s duration high-speed videos (125 FPS) were collected during each experiment to enable evaluation of quantities including bubble rise velocity, liquid film thickness, void fraction, Taylor bubble length, and liquid-slug length.

2.3 High Speed Video Analysis

2.3.1 Bubble rise velocity measurement

For each set of recorded flow videos, brief (1 s) no-flow reference videos were collected with the test section entirely filled with air (*gas-only*) and with water (*liquid-*

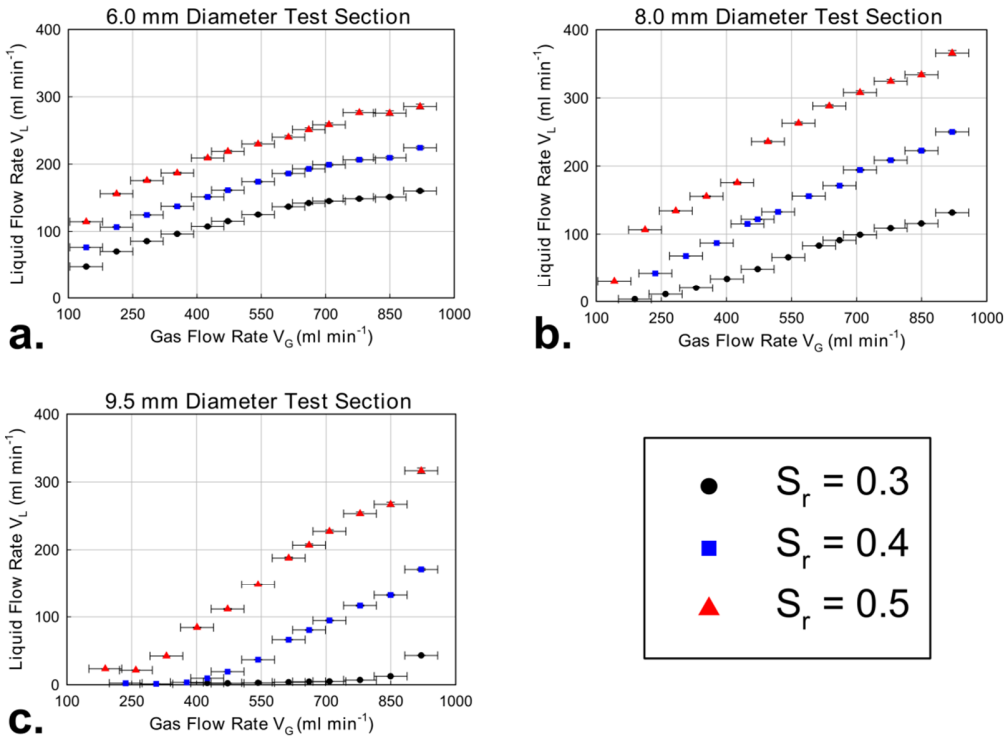

Figure 2.6 – Measured flow rates at submergence ratios of 0.3, 0.4, and 0.5 for: **a**. 6.0 mm, **b**. 8.0 mm, **c**. 9.5 mm diameter test sections

only). The glass-tube inside wall edges appear sharp in the gas-only videos, enabling automated image cropping and rotation correction. The liquid-only reference images were compared with flow images to assist in identifying all-liquid pixel rows and thus, liquid slugs. The following automated procedure was employed to determine the average Taylor bubble rise velocity for each flow experiment.

First, the all-gas reference image series was averaged to correct for camera vibration and lighting variation, and cropped horizontally to the middle 50%. The top and bottom 100 pixel rows were summed vertically, yielding two horizontal signals with sharp minima at the inner tube edges. Midpoints were determined between these upper and

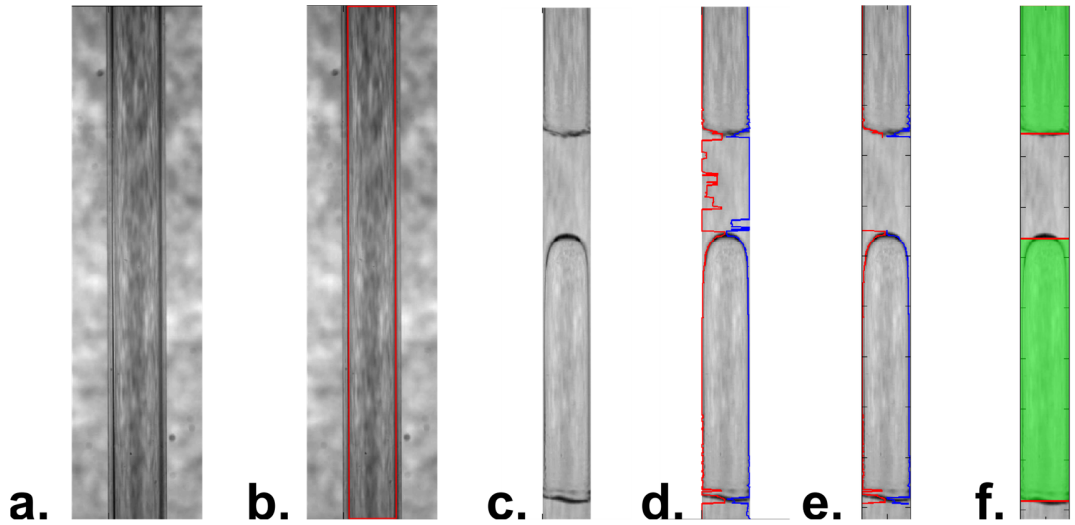

Figure 2.7 – Automated flow image analysis process: **a**. Raw calibration image, **b**. Rotation and cropping window, **c**. Corrected flow image, **d**. Interface identification, **e**. Liquid layer detection and interface closing, **f**. Bubble and slug segment identification

lower minima, and the resulting offset was used to rotate the tube images to be vertical. Typical corrective rotation angles were less than 1 degree, but even slight image misalignment could cause tube edges to be included in the search window for liquid-gas interfaces. Tube inside wall positions were then identified as the minimum average intensity image columns in the rotated gas-only images. The average gas-only and liquid-only reference images were then rotated and cropped to these inner tube extents (Figures. 2.7a, 2.7b).

Ten flow images were then loaded, averaged, rotated, and cropped for each flow condition. Correlations (i.e. inner products) were evaluated between these flow and gas-only images with slight horizontal shifts applied. This step enabled automated correction of slight changes in camera orientation during experiments. The optimal (maximum-correlation value) horizontal corrections were generally less than 2 pixels. Finally the full

set of images for each flow case was rotated, shifted, and cropped to the inside tube diameter (Figure 2.7c).

For each flow image, the left- and right- bubble-interface locations were determined for each row as the minimum intensity pixels on either side of the tube central axis (Figure 2.7d). Slug bubbles were rarely observed in this experimental study; therefore, image rows were classified to be either containing a Taylor bubble or all liquid.

All-liquid rows were identified by comparison with the liquid-only calibration images. This stage was also performed in an automated fashion by evaluating the following heuristic.

$$G^* = \left| \frac{\Delta(\text{Flow} - \text{Liq})}{\Delta x} \right| + \left| \frac{\Delta(\text{Flow} - \text{Liq})}{\Delta y} \right| \tag{2.18}$$

Here, "Flow" and "Liq" refer to the current flow image and averaged liquid-only calibration image, respectively. The $\Delta()/\Delta x$ and $\Delta()/\Delta y$ operations are the finite differences in the horizontal and vertical directions, respectively. The number of G^* values more than one standard deviation from the mean of G^* was then counted for each row. Image rows with fewer than five such pixels were empirically classified as *all liquid*. This process sometimes generated mislabeled rows; therefore, a multi-pass interface closing routine (based on neighbor row liquid/gas states) was then applied (Figure 2.7e).

This approach still occasionally mislabeled liquid and bubble rows; therefore, an additional heuristic was applied to identify the vertical end positions of Taylor bubble and liquid slug regions. The middle horizontal 50% of flow images were summed across

rows, and the resulting vertical 1-D signal was smoothed. Entries in this signal sufficiently far from the mean (more than 750 in this study) were found to correspond to bubble-slug transition regions. Single row transition regions were discarded as they almost always resulted from image noise. The center points of each remaining transition region were then reported as bubble/slug region ends (Figure 2.7f). Intermediate regions with majority all-liquid rows were then recorded as liquid slugs, and remaining regions as containing Taylor bubbles. Observed bubbles were found to almost always be elongated; thus, short regions ($L/D < 0.5$) were always classified as liquid slugs. Occasionally, Taylor bubbles where observed to rise with head-to-tail nearly touching. These were considered to represent single Taylor bubbles in this study as the intermediate slugs probably too short to affect the flow dynamics.

Bubble rise velocities were then measured using the following automated process. In a first pass, closest bubble nose positions in consecutive video frames were paired. The average instantaneous bubble velocity was then evaluated based on the displacement between these paired positions. This average velocity was then used to extrapolate expected bubble nose positions around which to search in a second pass. This approach was employed to minimize aliasing, wherein trains of consecutive short bubbles could be incorrectly tracked at low video frame rates. Bubbles with noses above the lower 85% of the camera window were ignored because of the difficulty of estimating the velocity of bubbles that partially exit the view between frames.

Only every 15 – 100^{th} frame pair was analyzed (18 – 125 frames per test case), depending on the average flow rate. This *striding* (only evaluating every n^{th} frame) was performed in order to avoid double counting the velocities of individual bubbles. The

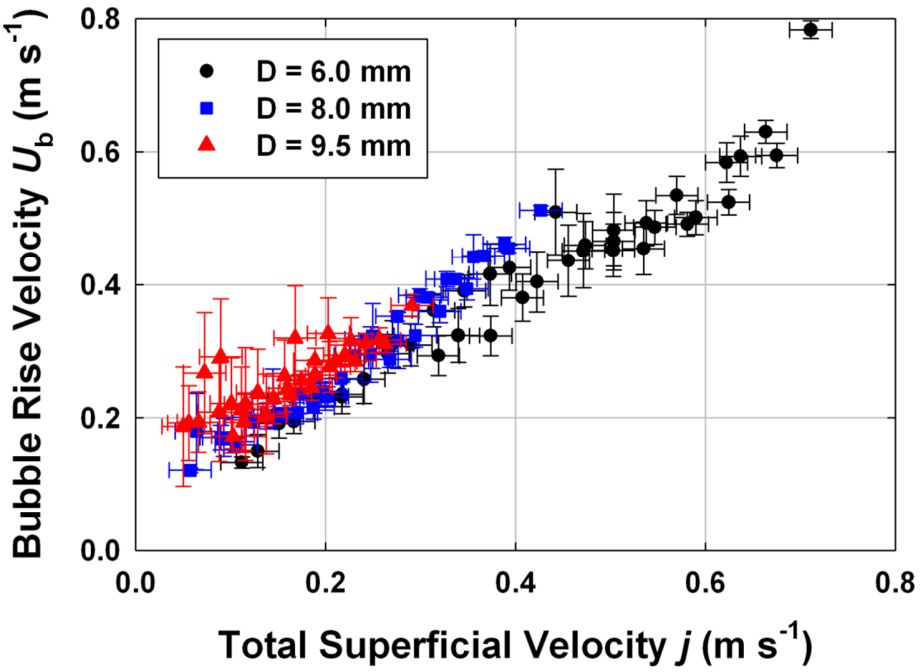

Figure 2.8 Average measured Taylor bubble rise velocities

–

reported average velocities were limited such that $U_b \geq j$. This limiting was primarily performed for 6 mm tube diameter cases where the expected bubble velocities are close to total superficial velocities, and measured values were occasionally less than j (within the measurement uncertainty). Uncertainties are reported as 95% confidence intervals, and are estimated as 1.96 standard deviations from the mean of the discrete bubble velocity measurements. It should be noted that the reported velocities are *number-averaged* (i.e., $\overline{U_b} = \sum_{i=1}^{n} U_{b,i} \Big/ n$), and might not correspond to the *dynamic averages* for which uniform-velocity bubbles would yield equivalent flow mechanics (e.g., $\overline{U_b}$ for pressure drop such that $\nabla p_{mod}\left(\overline{U_b}, ...\right) = \nabla p_{exp}$). Average bubble velocities for all test conditions are presented in Figure 2.8.

The observed Taylor-bubble rise-velocity trends are relatively intuitive, with U_b increasing nearly linearly with superficial velocity (j). Additionally, larger diameter tubes permit more inter-phase slip, and thus yield greater bubble rise-velocities for fixed superficial velocities.

An instability was observed in the 6 mm tube at lower flow rates when successive rising short bubbles periodically merged. The merged-bubble velocity was greater than that of the constitutive bubbles, leading to a runaway process of capture of slower leading bubbles and acceleration until the flow tube was nearly emptied of gas. The resulting high velocity bubbles were longer than the camera window (~12D); therefore, velocities could not be determined by nose tracking. As a result, reported average rise velocities might be skewed low in these cases, because no values could be obtained for these high-velocity bubbles. This phenomenon was not considered an *entrance-effect* because it was only observed in the 6 mm ID flow tube (L/D = 139), and not in the relatively shorter 8 mm (L/D = 103) and 9.5 mm (L/D = 89) flow tubes. A comparison of average instantaneous bubble velocities (for each video frame) is presented for one such unstable case and a similar 8 mm diameter case in Figure 2.9 (both at V_G = 708 ml min^{-1} and S_r = 0.4). The mechanics of this flow instability are beyond the scope of the present investigation, and represent an open area for future research in two-phase flow.

2.3.2 Liquid-film thickness measurement

The process for measuring liquid film thickness began using discrete bubbles and interface positions identified from strided images, following the approach of Section 2.3.1. The top 1D and bottom 0.5D of each Taylor bubble were cropped to prevent nose and tail sections from skewing average film thicknesses. Reported film thicknesses are

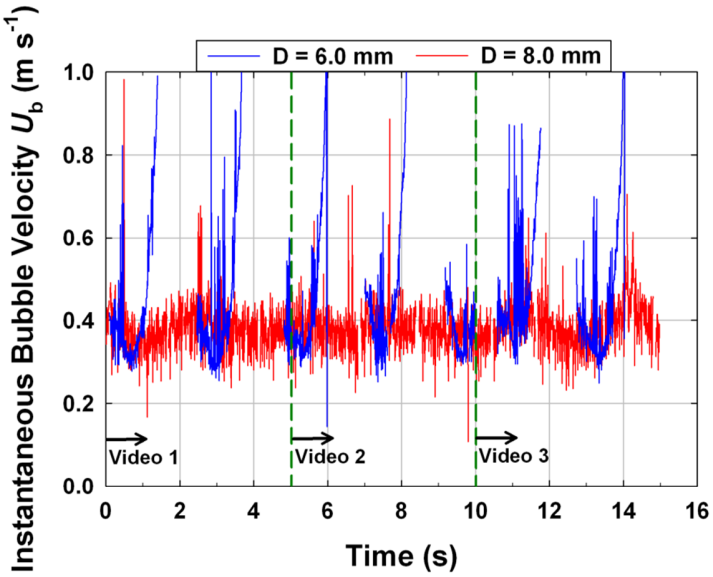

Figure 2.9 – Instantaneous average bubble velocity measurements for similar conditions in 6.0 and 8.0 mm diameter tubes (V_G = 708 ml min^{-1}, S_r = 0.4). The bubble rise-velocity instability is apparent for the 6.0 mm case.

total-length-averaged from Taylor bubbles in the strided image series. The experimental facility was not originally optimized for film thickness measurements, so the interface identification uncertainty (± 1 px for 2 – 5 px thick films) leads to relatively high film thickness uncertainties (~20 – 60%). Measured films thicknesses are presented in Figure 2.10.

Measured film thickness values appear to be nearly independent of flow rates and submergence ratios, and depend primarily on tube diameter. This result supports the gravity-driven falling-film model of de Cachard and Delhaye (1996) rather than the flow-rate (capillary number) dependence typically assumed in capillary-scale flows.

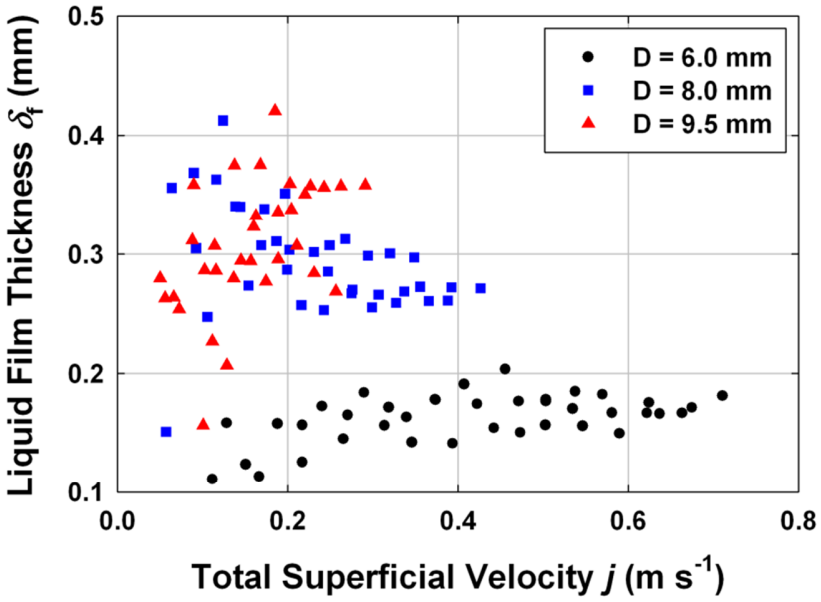

Figure 2.10 – Average measured liquid-film thickness (±0.07 mm for D = 6.0 mm, ±0.09 mm for D = 8.0 mm, ±0.08 mm for D = 9.5 mm)

2.3.3 Void fraction measurement

The void fraction measurement process began using discrete bubbles and interface positions obtained following the approach in Section 3.1. Unlike bubble velocity or film thickness, void fraction can meaningfully be *time and space averaged*. Therefore, data from every video frame and for the full height of each frame was considered. The gas volume on each bubble-pixel row was evaluated assuming cylindrical sections with diameter equal to the left-to-right interface position differences. Averaged void fraction values were obtained for 15 s of video data (1875 frames) for each test condition. In the recorded videos, the liquid-gas interfaces appear to span ~2 pixels. Upper and lower void-fraction bounds were obtained by offsetting the interface locations on each row by one pixel outward and inward, respectively. The resulting uncertainties are typically 3 –

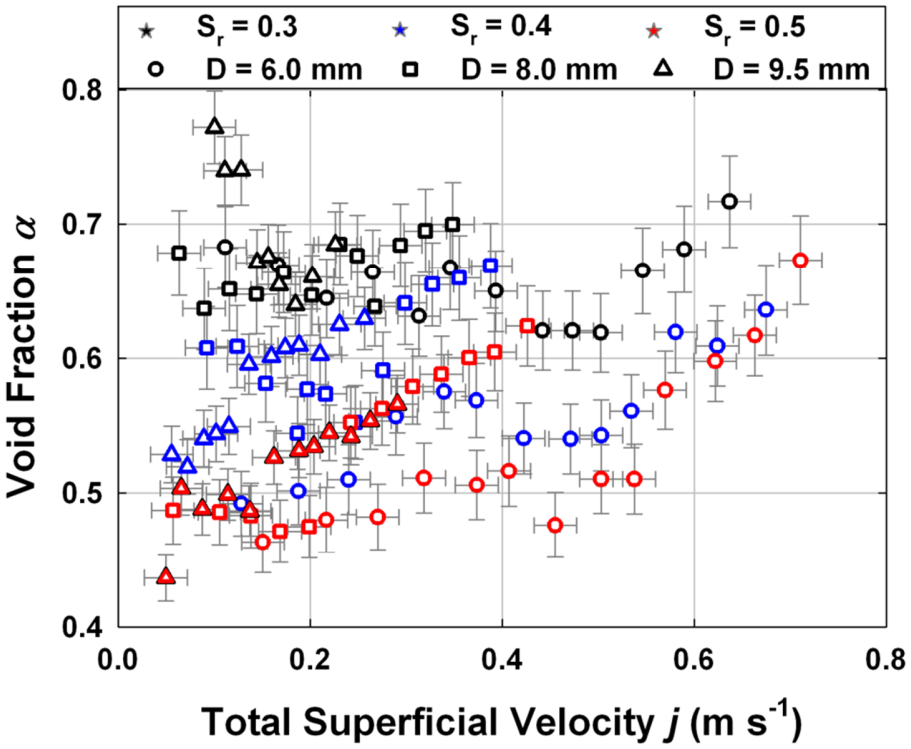

Figure 2.11 – Time- and space- averaged measured void fractions

6% (± 0.02 – 0.03) of the averaged void fraction values, which range from 0.44 – 0.77. Evaluated average void fractions for all experimental conditions are presented in Figure 2.11.

It is difficult to discern overall trends in void fraction from inspection of these experimental results. This is because the void fraction is a composite result of multiple factors including: Taylor-bubble rise velocity, liquid-film thickness, and liquid and gas flow rates. Thus, in Section 2.4.3, a comprehensive kinematic flow model is employed to predict void fraction as a function of these parameters.

2.3.4 Taylor bubble and liquid slug length measurement

The feature length measurement process begins by collecting discrete bubble and slug data from strided images following the approach in Section 2.3.1. Only bubbles and slugs at least partially inside the vertical middle 70% of the camera window were considered, reducing the need to extrapolate the length of features extending outside the camera window. Some long features were still observed extending from the middle window to outside the overall camera window. In particular, some very long Taylor bubbles were observed in the 6 mm ID tube flows. Such features were assumed to be twice as long as their extents within the camera window, or potentially four times as long if they extended beyond the top and bottom of the camera window. This approach can be considered *unbiased*, because long features should be equally likely to be x% or (100-x)% within the camera window at a given time.

Measured bubble and slug lengths were observed to follow an approximately log-normal statistical distribution, in agreement with the results of Brill *et al.* (1981), Barnea and Taitel (1993), and Wang *et al.* (2009). Representative length histograms for an 8.0 mm diameter tube flow case are presented in Figure 2.12. These histograms incorporate data for 78 Taylor bubbles (Figure 2.12a) and 43 liquid slugs (Figure 2.12b).

Average bubble and slug length measurements for all cases are presented in Figure 2.13. Uncertainties are reported as 95% confidence intervals, which are evaluated as 1.96 standard deviations from the mean of the discrete length measurements. Bubble length trends are apparent, but slug lengths of 1 – 6D are found for nearly all cases.

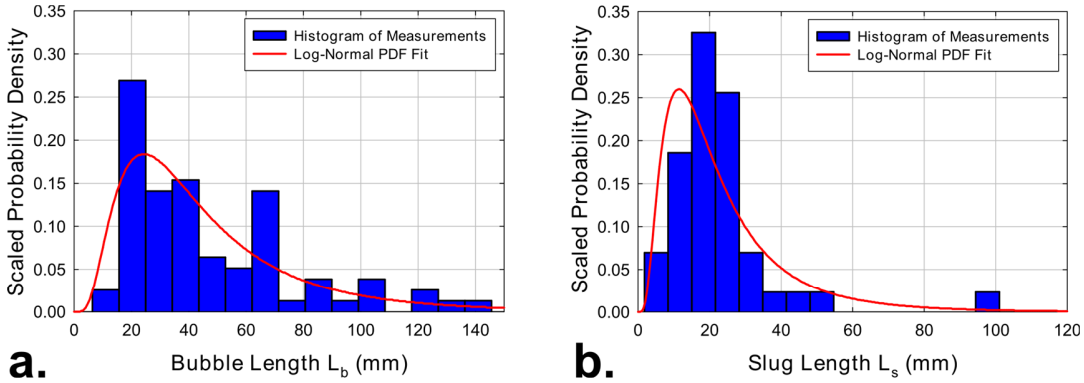

Figure 2.12 – Representative feature length distributions and best-fit log-normal PDF fits scaled by histogram bin size (D = 8.0 mm, V_G = 708 ml min^{-1}, S_r = 0.4). **a**. Taylor bubble length distributions (9.3 mm bins), **b**. Slug length distributions (6.6 mm bins)

2.4 Flow parameter modeling and correlation

2.4.1 Bubble rise velocity prediction

The Taylor bubble rise velocity model proposed in this study follows the drift-flux approach employed in previous investigations in which:

$$U_b = C_0\left(\mathrm{Re}_j,\ \mathrm{Bo},\ \mathrm{Ca}\right) j + \Gamma\left(\mathrm{Bo},\ \mathrm{N_f}\right)\sqrt{gD} \tag{2.19}$$

At the low-viscosity limit, Bendiksen (1985) reported a curve fit to an exact solution for Γ(Bo) valid for $\mathrm{Bo} \gtrsim 5.7$. Here, this curve fit is extended to the limit of $\mathrm{Bo} \geq 4.55$, below which it is 0 (no bubble rise without net flow). Additionally, the low-viscosity limit ($\mathrm{N_f} > 250$) exponential correction factor from White and Beardmore (1962) is applied. However, this term could not be independently validated in this study because this viscous effect was found to be negligible for all considered cases except for capillary flow cases where Bo < 4.55, setting $\Gamma = 0$.

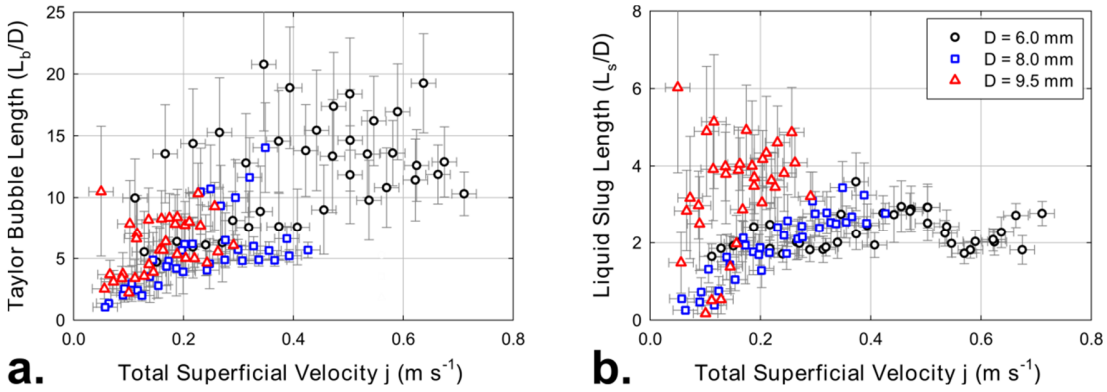

Figure 2.13 – Average measured Taylor bubble (**a**) and liquid slug (**b**) lengths

$$\Gamma = \begin{cases} 0.344\left[1-\exp\left(\dfrac{-0.01N_f}{0.345}\right)\right]\sqrt{1+\dfrac{20}{Bo}-\dfrac{93.7}{Bo^2}-\dfrac{676.5}{Bo^3}+\dfrac{2706}{Bo^4}\dfrac{1-0.96\exp(-0.0165Bo)}{1-0.52\exp(-0.0165Bo)}} & Bo>4.55 \\ 0 & Bo\le 4.55 \end{cases} \quad (2.20)$$

At low N_f (< 250) and Bo > 4.55, the correlation of White and Beardmore (1962) for Γ (Eqns. 3 – 4) is recommended. This low-Reynolds number large scale flow regime is never encountered for room-temperature air-water, but can be reached with more viscous fluids.

A blended capillary-to-large scale distribution parameter (C_0) is proposed in this investigation. For the capillary contribution, the explicit correlation of Liu *et al.* (2005) is adopted.

$$C_{0,Ca} = \frac{1}{1-0.61Ca^{0.33}} \quad (2.21)$$

For large scale flows, Bendiksen (1985) proposed a curve fit for C_0 (Equation 2.7) that decays from 2.29 (laminar, (Taylor, 1961)) at Re_j = 36, to 1.20 (turbulent, (Nicklin *et al.*, 1962)) at Re_j = 10^6 (for Bo → ∞). However, this curve fit diverges from these

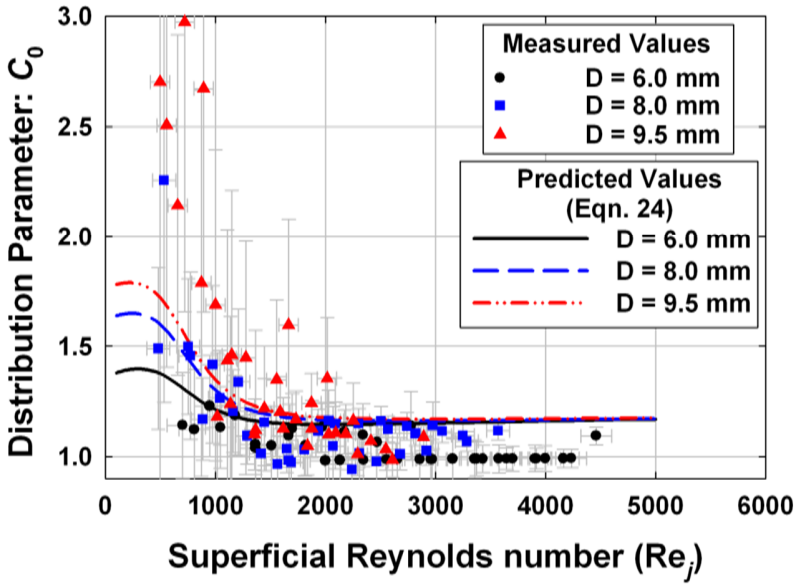

Figure 2.14 – Inferred C_0 from measurements (evaluating Γ using Eqn. 20, assuming 25% uncertainty) and predicted C_0 (Equation 2.24)

asymptotic limits outside of this range of Re_j. A laminar counterpart (Equation 2.8) was also developed, but the laminar-to-turbulent transition was not addressed. In the present investigation, inferred laminar values of C_0 (> 2) were found for $Re_j \lesssim 800$, and fully converged turbulent values were found for $Re_j \gtrsim 2500$ (Figure 2.14).

Based on the above findings and considerations, the following large scale contribution is proposed. This transitional model reaches 99% of the laminar value of C_0 (2.29) at $Re_j = 312$, and 101% of the turbulent value (1.20) at $Re_j = 2500$.

$$C_{0,LS} = 1.20 + \frac{1.09}{1 + \left(Re_j/805\right)^4} \tag{2.22}$$

Bendiksen (1985) highlighted the competing effects of inertial (Re) and capillary (Bo) forces in his turbulent model for C_0. This approach is adopted here to blend the capillary and large scale contributions:

$$f_{LS} = \left(\frac{1}{1 + 4840\,\mathrm{Re}_j^{-0.163}} \right)^{0.816/\mathrm{Bo}} \tag{2.23}$$

$$C_0 = f_{LS} C_{0,LS} + \left(1 - f_{LS}\right) C_{0,Ca} \tag{2.24}$$

The large scale fraction (f_{LS}) blending factor was fit to yield approximately 0.3 for the D = 6.0 mm cases, 0.5 for the D = 8.0 mm cases, and 0.6 for the D = 9.5 mm cases. These values were empirically found to deliver close agreement with experimental results for U_b from the present investigation. Future investigations over continuous ranges of Bo and wider ranges of Re_j could enable more rigorous fitting of this blending factor.

Predicted distribution parameter trends are presented for air-water flow in Figure 2.14. At low Re_j, measured values of C_0 for the 8.0 and 9.5 mm diameter tube flows exceed the established large scale laminar value of 2.29. However, the propagated uncertainty is very large for these conditions, primarily due to the high uncertainty in the measured Taylor bubble rise velocities relative to the low superficial velocities. The proposed correlation for C_0 slightly exceeds measured values in the 6.0 mm diameter tube at high Re_j. This trend is deemed acceptable due to the flow instability discussed in Section 3.1, which may skew measured velocities low. Further investigation into this phenomenon could enable improved prediction of bubble rise velocities for these lower Bond-number flows.

Table 2.1 – Comparison of average absolute relative deviation in Taylor bubble rise velocity using proposed and previously published models

Data set	Proposed Model	Bendiksen (1985)	de Cachard & Delhaye (1996)	Liu et al. (2005)
Present study	10%	22%	15%	19%
Liu et al. (2005)	8%	276%	12%	8%
Thulasidas et al (1995)	12%	255%	15%	12%
van Hout et al. (2002)	13%	12%	14%	35%
Legius et al. (1997)	9%	10%	9%	19%
Collins et al. (1978)	4%	3%	7%	74%

The performance of the overall proposed bubble rise velocity correlation is evaluated using:

- Intermediate scale results from the present investigation
- Capillary results from Liu *et al.* (2005) and Thulasidas *et al.* (1995)
- Large scale measurements for turbulent flow (Legius *et al.*, 1997; van Hout *et al.*, 2002) and with laminar-to-transitional flow (Collins *et al.*, 1978).

Average absolute relative deviations $\left(\sum_{i=1}^{n}\left|\left(U_{b,mod}-U_{b,exp}\right)/U_{b,exp}\right|/n\right)$ between predicted and measured bubble translation velocities for these data sets are summarized in Table 2.1. Results from the proposed correlation are compared with those obtained using the models of Bendiksen (1985), de Cachard and Delhaye (1996), and Liu *et al.* (2005).

Based on these results, the proposed correlation achieves the best agreement among the models considered with experimentally measured bubble velocities in intermediate

scale flows from the present investigation. Additionally, this model achieves comparable or better agreement than the other considered correlations for capillary and large scale flows. The correlation of Bendiksen (1985) yields excellent agreement with large scale flow results, but fails for capillary flows (Liu *et al.*, 2005; Thulasidas *et al.*, 1995). The model of de Cachard and Delhaye (1996) achieves good agreement in general, but assumes a fixed C_0 value of 1.2. Average errors are about 50% higher than with the proposed correlation for data sets where C_0 varied significantly (present study, (Collins *et al.*, 1978; Liu *et al.*, 2005)). The Liu *et al.* (2005) correlation is incorporated into the proposed model at the low-Bo limit, and achieves very good agreement at those scales. However, agreement is only fair for intermediate- and large-diameter tube flows. Capillary to large scale bubble rise velocity predictions using the proposed correlation are summarized in Figure 2.15.

2.4.2 Liquid-film thickness prediction

Kinematic closure for a unit-cell based Taylor-flow model requires an additional parameter in addition to the bubble-rise velocity (U_b) and phase superficial velocities (j_L, j_G). The continuity constraint requires that the average liquid slug velocity equals the total superficial velocity ($j = j_L + j_G$). Additionally, the net volumetric flow rate through cross-sections of a tube containing a liquid slug or a Taylor bubble and falling-film pair must be equal (Thulasidas *et al.*, 1995).

$$\alpha_b U_b - (1-\alpha_b) U_f = j \tag{2.25}$$

Here, α_b is the fraction of tube cross-section occupied by Taylor bubbles, and U_f is the average liquid film velocity (positive downward). The average liquid film thickness around Taylor bubbles can be obtained as:

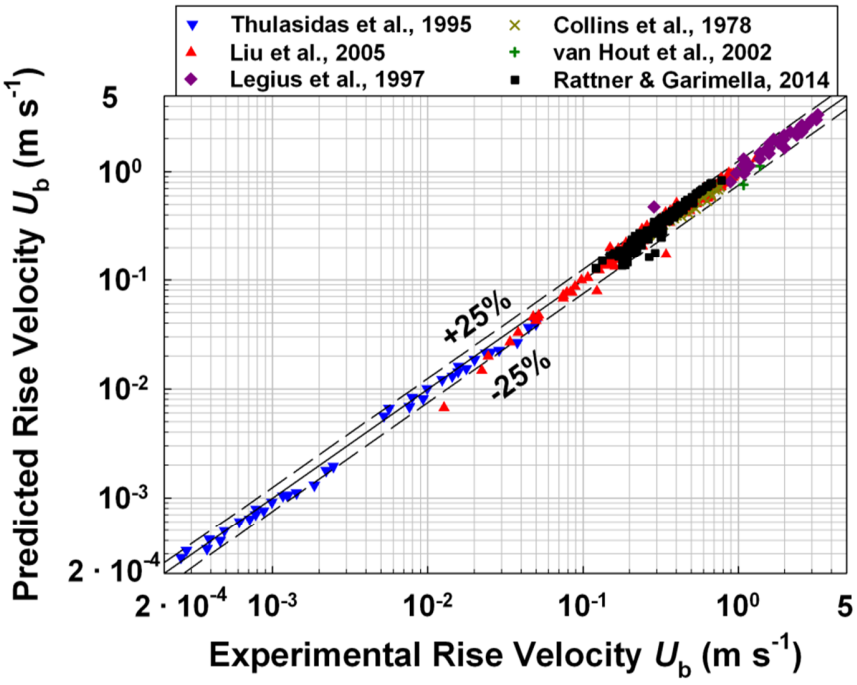

Figure 2.15 – Comparison of proposed Taylor bubble rise velocity model with measurements and values from the literature

$$\delta_f = \frac{D}{2}\left(1-\alpha_b^{1/2}\right) \tag{2.26}$$

Based on these conservation equations and experimental results, $Re_f < 180$ for all measured cases. This is well below the turbulent transition criterion of $Re_f > 750$ suggested by de Cachard and Delhaye (1996); therefore, laminar falling films are assumed. The gas flow in rising bubbles is also assumed to be laminar because the bubble Reynolds number ($Re_b = \rho_G (D-2\delta_f)(U_b+U_f)/\mu_G$) was found to be < 450 for all measured cases.

Force balances were performed on the falling films accounting for bubble-to-film shear (assuming a laminar developing flow friction factor in the bubble), wall shear

stress, and gravitational forces. For all considered cases, the bubble-to-film shear component was found to be insignificant ($\tau_{int} < 0.04$ N m^{-2}, $\tau_{wall} > 1.61$ N m^{-2}, and $\tau_{int} / \tau_{wall} < 0.019$ for all cases). Thus, the liquid film in intermediate scale Taylor flows can be assumed to travel down the tube wall with negligible interfacial shear. The laminar falling-film velocity result suggested by de Cachard and Delhaye (1996) (Equation 2.27) and Equations 2.25 – 2.26 (closure equations above) can thus be used to implicitly determine the film thickness in intermediate scale Taylor flows.

$$U_f = 0.333 g \frac{\rho_L \delta_f^2}{\mu_L} \tag{2.27}$$

Predicted and measured film thicknesses (using correlated U_b from Section 4.1) from this investigation are compared in Figure 2.16. An average absolute relative deviation ($\sum_{i=1}^{n} \left| \left(\delta_{f,mod} - \delta_{f,exp} \right) / \delta_{f,exp} \right| / n$) of 16% was found between measured and predicted values, and 86% of predictions were within 25% of measured values. Still, relatively wide scatter can be observed between predicted and measured values in Figure 2.16. This can be attributed primarily to the large experimental uncertainty in measuring film thicknesses typically 2 – 5 pixels wide. Additionally, measured thicknesses may be skewed slightly low in cases where shading near the inner tube wall may be difficult to distinguish from the liquid-to-gas interface.

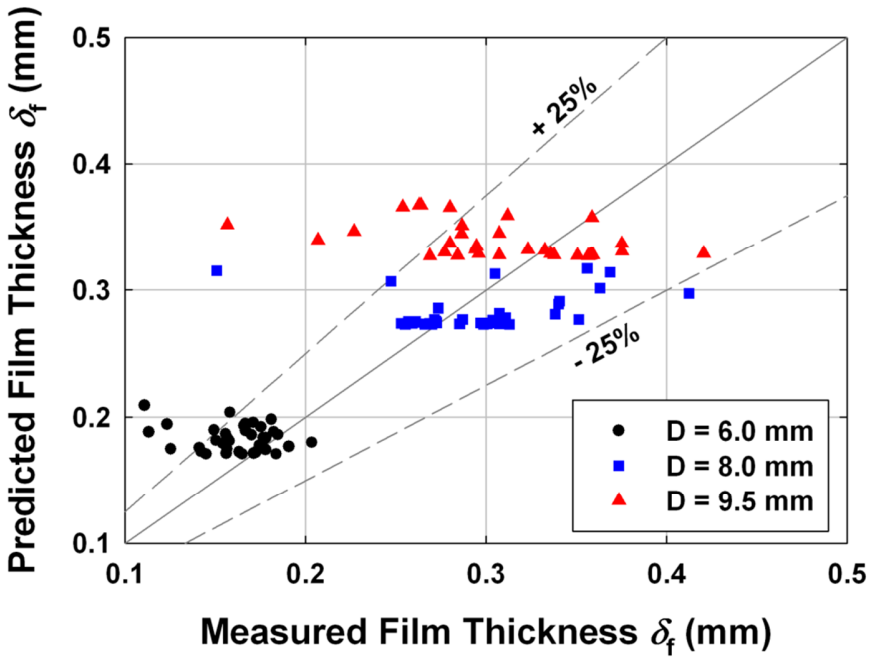

Figure 2.16 – Comparison of measured and predicted liquid-film thickness values

2.4.3 Void fraction prediction

The continuity constraint for gas-flow in a unit cell can be applied to determine the relative Taylor bubble length ($\beta = L_b/(L_b + L_s)$). If the liquid slug is not aerated, as was generally found to be the case for the studied intermediate scale Taylor flows, then:

$$\beta = \frac{j_G}{\alpha_b U_b} \tag{2.28}$$

The overall void fraction can then be determined as:

$$\alpha = \alpha_b \beta \tag{2.29}$$

This approach only requires knowledge of the superficial flow rates, the bubble rise velocity (correlated in Section 2.4.1), and the liquid film thickness (modeled in Section 2.4.2). Additionally, this method automatically satisfies the continuity constraint for the

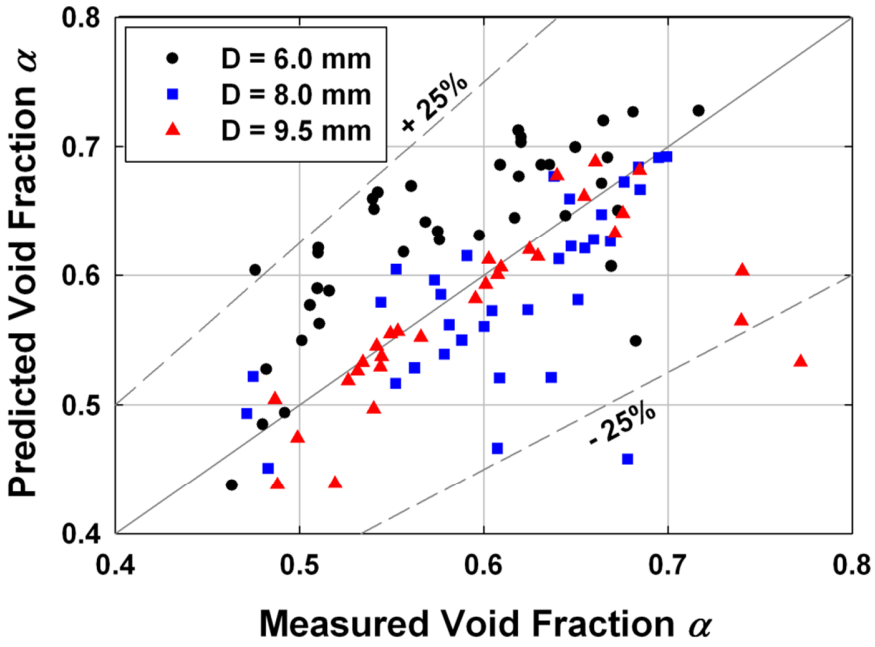

Figure 2.17 – Comparison of measured and predicted void fraction values

simplified unit-cell model, and is therefore preferable to application of a "general purpose" void fraction correlation. Predicted and measured void fraction values from this study are presented in Figure 2.17. In these results, U_b and δ_f are evaluated following the approaches presented in Sections 2.4.1 and 2.4.2, respectively. An average deviation of 9% in void fraction is seen, and 95% of data points are predicted within 25% of the measured values.

2.4.4 Taylor bubble and liquid slug length prediction

Taylor bubble and liquid slug length values are primarily employed in models for predicting the frequency of transitional pressure drops between bubble and slug segments. For large scale flows, the average relative liquid slug length (L_s/D) has been reported to be constant and universal, but widely varying values (6 – 48) have been published. This substantial difference between the results from different investigations

has not proved to be a significant issue in large scale flow models because bubbles and slugs are typically many tube diameters in length; thus, fully developed frictional pressure gradients dominate transitional pressure drops (Sylvester, 1987). In contrast, average liquid slug lengths of 1 – 6D were seen in the present study for intermediate tube-diameter flows. As such, the relative effect of transitional pressure drops can be expected to be much greater in these cases, and more accurate prediction of segment lengths is warranted.

In this study, video data were obtained approximately 500 – 600 mm (55 – 100D) above the inlet ports. It is thus possible that the short measured slugs and bubbles could be due to entrance effects. However, there are no clear trends of measured slug lengths varying with Reynolds number (Re_j) as might be expected for entrance effects. Additionally, measured relative slug lengths (L_s/D) are actually greater in the larger diameter tubes where measurements are collected relatively closer to the inlets (in dimensionless length: x/D). Future investigations with longer test sections could help verify whether these short segment lengths persist further downstream.

In the present investigation, Taylor bubbles were generally found to be much longer than liquid slugs ($L_b/D \sim 2 - 18$). Therefore, for known β, more accurate predictions of unit-cell length and frequency of transitional pressure drops can be obtained by correlating L_b rather than L_s. Additionally, trends of L_b/D with flow rate were more apparent than for L_s.

Laborie *et al.* (1999) proposed a capillary-scale power-law correlation for L_b/D in terms of Bond number and a bubble Reynolds number (Eqn. 16). However, this approach

might not apply at other scales where similar relative bubble lengths are observed, but Re and Bo vary by orders of magnitude. Kreutzer *et al.* (2003) proposed a correlation for slug length in terms of void fraction (Equation 2.17). This approach holds promise at all scales because relative bubble and slug lengths and void fractions are of similar order for Taylor flow at all length scales.

Here, a correlation for relative Taylor bubble length in intermediate scale flows is proposed based on image analysis results from Section 2.3.4.

$$\frac{L_b}{D} = 1.813\left\{\exp\left[1.815 - 0.866\left(\frac{U_b}{j}\right)^{2.176}\right]\left(\frac{\alpha}{1-\alpha}\right)^{1.637} + 1\right\} \tag{2.30}$$

This correlation yields a minimum bubble length of $L_b/D = 1.813$, and thus predicts *elongated* ($L_b/D > 1$) bubbles for all cases of Taylor flow. Additionally, predicted bubble lengths scale to ∞ as $\alpha \rightarrow 1$. As such, very long bubbles are predicted at the Taylor flow-to-annular flow transition. In the large Bond number limit, this correlation converges to $L_b/D = 1.813$, which is generally smaller than the first order approximation (assuming $\alpha_b = 1$, $L_s/D = 16$):

$$\left(\frac{L_b}{D}\right)_{Bo\rightarrow\infty} \approx \frac{16}{U_b/j_G - 1} \tag{2.31}$$

In future models, this limit could be incorporated, perhaps with a Bond-number based blending between intermediate and large scale flow bubble length predictions. At present, there is insufficient information about the transition from the intermediate- to large scale regimes to develop such a correlation.

Table 2.2 – Comparison of average absolute deviation (and order of magnitude error) in Taylor bubble lengths using proposed and previously published models

Data set	Proposed Model	Laborie et al. (1999)	Kreutzer et al. (2003)	Taitel et al. (1980)
Present study	22% (0.11)	85% (0.87)	44% (0.27)	453% (0.70)
Pinto et al. (2001)	73% (0.58)	99% (2.06)	83% (0.78)	12% (0.05)
Shao et al (2011)	140% (0.45)	1748% (0.99)	58% (0.45)	437% (0.61)

A comparison of the performance of bubble/slug-length models is presented in Table 2.2. The considered models include:

- The proposed correlation (Equation 2.30)
- The capillary scale correlation of Laborie *et al.* (1999) (Equation 2.16)
- The capillary scale correlation of Kreutzer *et al.* (2003) (Equation 2.17)
- The large scale (high Bo) result of Taitel *et al.* (1980) ($L_s/D = 16$)

These models are evaluated with experimental data, including:

- Measurements from this study – closure for U_b, δ_f, α, β obtained using models from the preceding sections)
- Large scale results from Pinto *et al.* (2001) – U_b, L_s, L_b available from experimental data, we assume $\alpha \sim \beta$
- Capillary data from Shao *et al.* (2011) – U_b estimated using the correlation of Liu *et al.* (2005) (Equation 2.10), δ_f estimated using the Fairbrother and Stubbs (1935) correlation (Equation 2.13), α and β obtained from continuity equations

Average absolute deviations (AAD) from experimental values are summarized in Table 2.2. Average logarithmic-scale errors are also reported in parentheses ($\left|\log_{10}\left(\text{Exp}/\text{Pred}\right)\right|$) to indicate prediction errors in terms of orders of magnitude.

Based on these results, there are no generally valid Taylor bubble length models available in the literature. The proposed correlation achieves good agreement with the present data (22% AAD), and predicts capillary and large scale results from the literature to within approximately 0.5 orders of magnitude. The Kreutzer *et al.* (2003) correlation achieves reasonable accuracy for the present data set (44% AAD), and similar logarithmic-scale accuracy to the present correlation at other scales. The Taitel *et al.* (1980) result is very accurate (12% AAD) for the large scale data of Pinto *et al.* (2001), but significantly over-predicts bubble lengths at the capillary and intermediate scales.

Using the proposed correlation, 66% of average bubble lengths from the present study are predicted within 25% of the measured values (91% within 50%). Slug lengths are also predicted using this correlation and closure models described in the previous sections. Only 17% of average slug length values are predicted within 25% of measured values (AAD = 74%, 52% within 50%). This limited agreement is unsurprising considering the wide range of average slug lengths reported in the large scale flow literature. Taylor bubbles were generally found to be much longer than liquid slugs in the present study; measured values of β ranged from $0.6 \lesssim \beta \lesssim 0.9$. Thus, unit cell lengths, and frequency of transition pressure drops, should be predicted reasonably well even with large uncertainty in L_s. Predicted and average measured bubble and slug lengths from this investigation are presented in Figure 2.18.

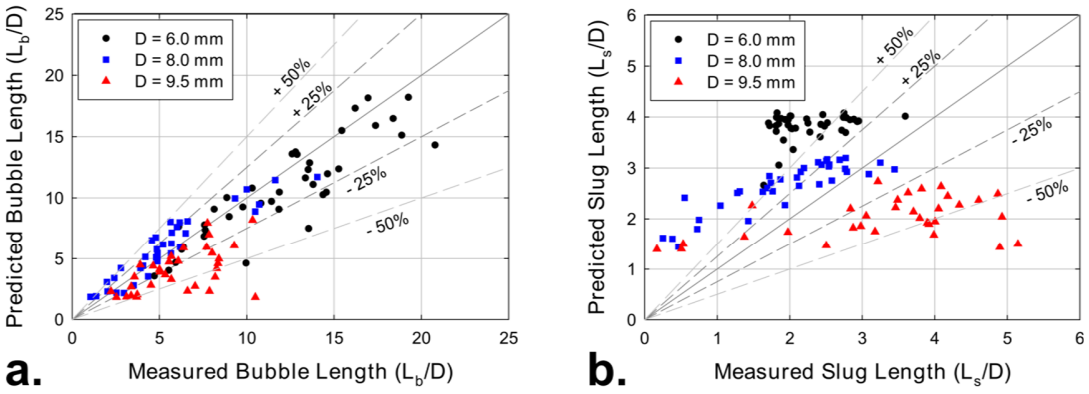

Figure 2.18 – Comparison of measured and predicted (**a**) Taylor bubble lengths, and (**b**) liquid slug lengths

2.5 Discussion

This investigation demonstrated experimentally that intermediate scale Taylor flows ($5 \lesssim \mathrm{Bo} \lesssim 40$) are significantly different from those at the capillary and large scales. In particular, Taylor bubble rise velocity and bubble and slug length trends differ from those found at other scales. These findings help explain why mechanistic bubble-pump models that incorporate results for capillary or high Bond number conditions often have poor predictive capabilities for liquid pumping rates, as was found by Schaefer (2000) and White (2001).

New correlations have thus been proposed to predict intermediate scale bubble rise velocity (also validated at other scales) and average Taylor bubble length. Laminar falling film results were demonstrated to apply for the liquid-films around Taylor bubbles at this scale. Closure models based on conservation laws and the simplified unit-cell model were employed to predict α, β, and L_s. This study thus provides sufficient information for *kinematic* closure of Taylor flows. Sample calculations for this kinematic Taylor flow model are presented in Appendix Section A.2. Pressure-drop models for the

liquid slugs, bubble regions, and bubble-to-slug transitions are required for *dynamic* closure, and are formulated using a simulation-based approach in Chapter 3.

One open question raised in this investigation is the effective entry length for intermediate scale Taylor flows. This is particularly relevant for measurement and prediction of bubble and slug lengths. Average bubble and slug lengths increase in the flow direction, up to stable values, as trailing bubbles merge with leading ones (Dukler *et al.*, 1985). It is therefore possible that short measured liquid slugs had not reached *fully developed* lengths. Taitel *et al.* (1980) proposed the following entrance length correlation for slug flow:

$$\frac{L_{ent}}{D} = 40.6\left(\frac{j}{\sqrt{gD}} + 0.22\right) \tag{2.32}$$

In this study, the camera recording window (~500 – 600 mm above the inlet) was above this point except for some of the highest flow rate D = 6.0 and 8.0 mm cases. However, this entrance length model was developed for large scale turbulent flows, and may not apply for intermediate scale conditions. Future investigations focusing on Taylor-flow entrance lengths are therefore warranted.

In this investigation, a capillary-to-large scale blending model was proposed for predicting Taylor bubble rise velocity (Equation 2.23). A similar approach could assist in developing a universal Taylor bubble length model. However, insufficient data were available in the literature to fit such a blending model at this point. Additionally, the blending model for Taylor bubble velocity was fit empirically, because measurements from the present study were only collected for three distinct values of Bo. Future

investigations focusing on the transition from the capillary-to-large scale limits would thus be of great value. The governing regime scale is primarily a function of Bond number ($\mathrm{Bo} = (\rho_L - \rho_G) g D^2 / \sigma$), which only depends on tube diameter and fluid properties. Thus, it is more difficult to perform experiments over a continuous range of Bond numbers than other parameters, which can be varied simply with flow rate. However, this is an attractive avenue for simulation-based studies.

2.6 Conclusions

In this investigation, experimental air-water studies were performed for vertical upward intermediate scale Taylor flows. High speed photography was employed to enable measurement of flow parameters including Taylor bubble velocity, liquid film thickness, void fraction, and bubble and slug length.

Correlations were developed for Taylor bubble rise velocities at all scales, and for Taylor bubble lengths in intermediate scale flows. Laminar falling-film results were demonstrated to apply for liquid films around Taylor bubbles in intermediate scale flows. Additionally, the continuity constraint and simplified unit-cell model were employed to predict void fraction and average liquid slug length. This study thus provides models for kinematic closure of intermediate scale Taylor flows. Dynamic closure sub-models (for pressure drop) are needed to formulate a comprehensive description for Taylor flow in the intermediate Bond number regime. These are developed using simulation-based studies in Chapter 3.

This investigation demonstrated that intermediate scale Taylor flows ($5 \lesssim \mathrm{Bo} \lesssim 40$) are fundamentally different from those found at the capillary and large scales. Additional

classes of forces and phenomena must be considered as compared with flows at either limit. This study identified a number of open topics for future Taylor flow investigations including the nature of the strong flow intermittency measured at Bo = 4.9 (Section 2.3.1), the trends of bubble and liquid slug lengths in the transition from capillary to large scale flows (Section 2.4.4), and prediction of entrance lengths for intermediate scale flows.

CHAPTER 3. TAYLOR FLOW SIMULATION AND HYDRODYNAMIC CLOSURE IN THE INTERMEDIATE BOND NUMBER REGIME

3.1 Introduction

3.1.1 Background

The vertical-upward Taylor flow pattern is a quasi-periodic two-phase flow pattern (Gao and Jin, 2012) that occurs over a broad range of flow scales (μm to cm channel diameters). In Taylor flow, elongated large diameter (Taylor) bubbles are separated by full-channel cross-section liquid *slugs*. Thin annular liquid films drain downward around the rising bubbles. This flow pattern is encountered in a variety of geometries and applications including miniaturized heat and mass exchangers (Garimella, 2004), monolithic catalytic reactors (Thulasidas *et al.*, 1995), fuel cells (Anderson *et al.*, 2010), petrochemical extraction equipment (Fernandes *et al.*, 1983), and gas-lift and bubble pumps (Reinemann *et al.*, 1990).

The Taylor flow pattern has been extensively studied at the capillary/microchannel ($\mathrm{Bo}=\left(\rho_{\mathrm{L}}-\rho_{\mathrm{G}}\right) gD^{2}/\sigma \lesssim 5$, see Section 2.1.1) and large Bond number ($\mathrm{Bo} \gtrsim 40$ (Viana *et al.*, 2003)) limits. The present study focuses on Taylor flow in the intermediate Bond number regime, which has been comparatively poorly characterized. These operating conditions span a transition regime in which forces due to buoyancy, inertia, surface tension, and viscosity are all significant. Additionally, for many liquids (e.g., water and ammonia), the intermediate Bond number Taylor flow regime also spans the transition from laminar to turbulent flow, further complicating analysis.

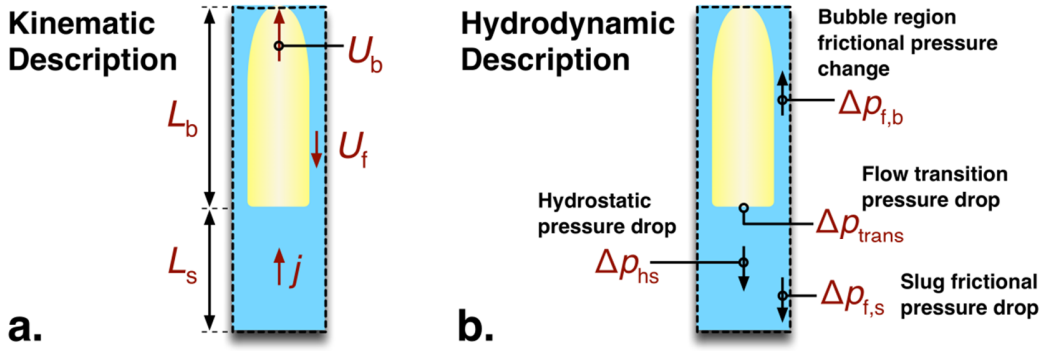

Figure 3.1 – Repeating unit cell model for Taylor flow: **a**. Kinematic and **b**. Hydrodynamic descriptions

The Taylor flow pattern is often idealized as being composed of repeating *unit cells* (Fig. 3.1), which can be analytically modeled in a piecewise and mechanistic fashion. This approach has been applied in the high Bond number limit (e.g., for large diameter channels) by Fernandes *et al.* (1983), Sylvester (1987), and Taitel and Barnea (1990). Similar approaches have also been developed for capillary and microchannel Taylor flow (Garimella, 2004; Thulasidas *et al.*, 1995). Such models generally describe the flow pattern with two coupled systems of equations for *kinematic* (flow rates and fluid structure dimensions) and *hydrodynamic* (momentum balances) closure.

The kinematic specification of Taylor flow can be formulated by first applying continuity balances between representative liquid-slug and Taylor-bubble cross-sections.

$$U_s = \alpha_b U_b + (1-\alpha_b) U_f \tag{3.1}$$

Here, U_s is the average slug velocity, α_b is the fraction of the bubble-region channel cross-section occupied by the gas-phase (assuming prismatic bubble shape), U_b is the

average bubble velocity, and U_f is the average liquid film velocity. The total volumetric flow rate must be conserved across each channel cross-section for incompressible flow; therefore, the slug velocity (U_s) must equal the total superficial velocity (j).

$$U_s = j = j_L + j_G \tag{3.2}$$

Here, the phase superficial velocities (j_L, j_G) are defined as the phase volumetric flow rates divided by the channel flow area ($j_L = V_L/A$, $j_G = V_G/A$). Similarly, by averaging over the whole unit cell, the bubble velocity can be related to the gas superficial velocity.

$$j_G = U_b \alpha_b \beta \tag{3.3}$$

Here, β is the ratio of the bubble length to the total unit-cell length $\left(\beta = L_b / \left(L_b + L_s\right)\right)$. In the case of negligible gas volume fraction in the liquid slug, as has been found for intermediate Bond number Taylor flow (see Section 2.3.1 and Ros (1961)), the total void fraction (α, gas-phase volume fraction) is thus:

$$\alpha = \alpha_b \beta \tag{3.4}$$

For a circular cross-section channel, the liquid film thickness and bubble diameter are:

$$\delta_f = \frac{D}{2}\left(1 - \alpha_b^2\right) \tag{3.5}$$

$$D_b = D - 2\delta_f \tag{3.6}$$

Equations 3.1-3.6 summarize the continuity constraints for the idealized repeating unit-cell description of Taylor flow. Kinematic closure is usually obtained by specifying

constituitive relations for bubble velocity (U_b), liquid film velocity (U_f) or thickness (δ_f), and bubble or liquid slug length (L_b, L_s). Sets of kinematic closure models for intermediate Bond number Taylor flows have been proposed by Reinemann *et al.* (1990), by de Cachard and Delhaye (1996), and in Chapter 2 of this thesis.

The hydrodynamic description of Taylor flow can be formulated by applying a momentum balance over the fluid in the unit cell. Here, incompressible flow is assumed.

$$-\frac{dp}{dz} = \left[\alpha\rho_G + (1-\alpha)\rho_L\right] g + \beta\nabla p_{f,b} + (1-\beta)\nabla p_{f,s} + \frac{\Delta p_{trans}}{L_b + L_s} \tag{3.7}$$

dp/dz is the total average pressure drop gradient in the flow direction (upward). The first term on the right hand side of Equation 3.7 represents the hydrostatic pressure drop (∇p_{hs}). $\nabla p_{f,b}$ and $\nabla p_{f,s}$ represent the frictional pressure change gradients in the Taylor bubble and liquid slug regions, respectively. Finally, Δp_{trans} represents the irreversible pressure drop (pressure loss) due to flow transitions between the Taylor bubble and liquid slug regions. Reversible pressure changes also occur due to liquid acceleration and deceleration in the bubble-to-slug transitions, but there is no net effect over a unit cell. Representative pressure change contributions from these terms are presented schematically in Figure 3.2. Here, the dynamic pressure field (p_d) is defined as $p - p_{hs}$. Hydrodynamic closure is obtained by specifying constitutive relations for $\nabla p_{f,b}$, $\nabla p_{f,s}$, and Δp_{trans}. The objective of this investigation is to formulate and validate hydrodynamic closure models for Taylor flow in the intermediate Bond number regime.

Taylor flow is generally predicted to occur at low-to-moderate flow rates, for which fluid velocities are not sufficient to disrupt large scale flow structures (i.e., Taylor

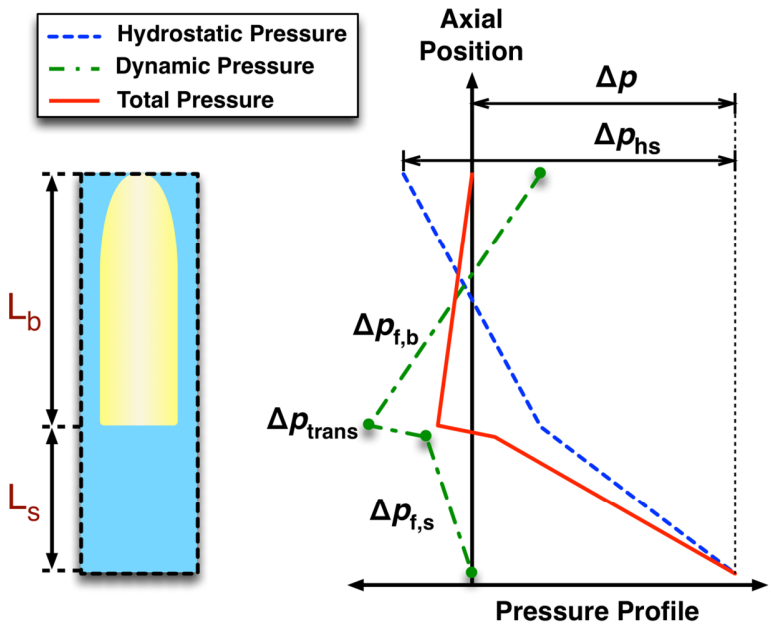

Figure 3.2 – Hydrostatic, dynamic, and total pressure profiles in a Taylor-flow unit cell

bubbles and liquid slugs) and cause transition to the annular (Taitel *et al.*, 1980) or churn (Jayanti and Hewitt, 1992) flow patterns. Under such conditions, hydrodynamic pressure drops are relatively minor (~10 – 20%) compared to hydrostatic pressure drops. Thus, large errors in frictional and transition pressure drop predictions can often be tolerated in applications where gas and liquid flow rates are specified. In such cases, general purpose flow-regime-independent two-phase flow hydrodynamic pressure drop correlations could be employed, such as those of Chisholm (1967), Friedel (1979), Müller-Steinhagen and Heck (1986), and Mishima and Hibiki (1996) (for microchannels).

In contrast, for air-lift- and bubble-pump applications, where gas flow rates and total pressure drops are specified, relatively small errors in hydrodynamic pressure drop prediction can lead to dramatic changes in liquid pumping rates – the primary quantity of

interest. The high sensitivity of liquid flow rate to pressure drop, wherein relatively small $\left(\partial\left(\partial p_{\mathrm{d}}/\partial z\right)/\partial j_{\mathrm{L}}\right)_{j_{\mathrm{G}}}$ indicates large $\left(\partial j_{\mathrm{L}}/\partial\left(\partial p_{\mathrm{d}}/\partial z\right)\right)_{j_{\mathrm{G}}}$, has been reported in previous studies (Delano, 1998; Schaefer, 2000). In fact, for many of the conditions considered in the present investigation, net hydrodynamic pressure forces actually act *in the flow direction*. This occurs because upward wall shear stress in the relatively long draining liquid-film regions exceeds downward shear stress in the shorter liquid slugs and transition pressure loss. This negative hydrodynamic pressure drop result would not be predicted using any of the general purpose two-phase flow pressure drop correlations. Thus, an accurate mechanistic description of intermediate Bond number Taylor flow hydrodynamics must be developed to formulate robust air-lift and bubble pump design models.

Of the existing mechanistic descriptions of two-phase Taylor flow, including those of (de Cachard and Delhaye, 1996; Delano, 1998; Fernandes *et al.*, 1983; Garimella, 2004; Schaefer, 2000; Sylvester, 1987; White, 2001), hydrodynamic models have almost always been assessed *globally*. Total predicted pressure drops and flow rates were compared to experimentally measured values, but pressure-drop sub-models were not assessed individually. Thus, sources of error and individual sub-model ranges of validity could not be identified. Experimental validation of Taylor-flow pressure-drop sub-models is challenging due to the random nature of the flow structure, as variations in L_{b} and L_{s} warrant different locations of pressure transducers for each unit cell. Transient pressure traces from fixed pressure transducers have been applied to qualitatively assess hydrodynamic sub-models (Dukler and Hubbard, 1975), but unsteady upstream and downstream effects can affect measurements, and high precision instruments are needed

to resolve small pressure changes in single unit cells. Therefore, this study adopts a simulation-based approach, which directly solves the unsteady governing equations to determine velocity, pressure, and fluid-phase fields ($u_i(x, t)$, $p(x, t)$, $\alpha_1(x, t)$) to facilitate evaluation of individual sub-models. In the following section, reviews of prior work in mechanistic Taylor flow modeling (3.1.2.1), approaches for simulating two-phase flows (3.1.2.2), and simulation of Taylor flows (3.1.2.2) are presented.

3.1.2 Prior work

3.1.2.1 Mechanistic Taylor flow models

Fernandes *et al.* (1983) proposed one of the earliest detailed mechanistic hydrodynamic models of Taylor flow in the large Bond number regime, assuming turbulent flow in the liquid films and slugs. Sylvester (1987) extended the model of Fernandes *et al.* (1983), proposing specific models for frictional pressure drop in the Taylor bubble (Taitel *et al.*, 1980), liquid slug (Zigrang and Sylvester, 1982), and the bubble-to-slug transition (Dukler and Hubbard, 1975). Total pressure drop predictions were validated using oil-gas and water-gas experimental data. Sylvester (1987) found that transition pressure loss effects were relatively insignificant because of the long unit-cells found for large Bond number flows ($L_s \sim 6 - 48D$). However, such effects may be important for intermediate Bond number flows, which often have short unit cells ($L_s + L_b < 10D$ for most cases, see Section 2.3.4).

Taitel and Barnea (1990) presented an extensive review of two-phase slug flow, and proposed various laminar and turbulent flow models for frictional shear in the liquid slug, liquid film, and bubble-to-film interface. Approaches for predicting transitional pressure drop were also discussed. Their review presented models that span all channel

inclinations and focused on large Bond number flows, although some bubble rise velocity results for intermediate Bond numbers were included.

Reinemann *et al.* (1990) proposed a mechanistic model for Taylor flow in intermediate Bond number airlift pumps ($5 < Bo < 50$). Their model incorporates a turbulent frictional pressure drop model for liquid slugs, and assumes a freely draining liquid film in bubble regions ($\nabla p_{f,b}$). Transitional pressure drops were neglected in their study. Reinemann *et al.* (1990) validated predicted liquid flow rates with experimental air-lift pump data.

de Cachard and Delhaye (1996) developed mechanistic models for Taylor and churn flow in the intermediate Bond number regime. Liquid films were modeled assuming negligible interfacial shear, and liquid slug frictional pressure drops were modeled assuming fully developed turbulent channel flow. Transition pressure drops were neglected in their study, and liquid pumping rate predictions were validated with experimental air-water flow data for $1 < Bo < 14$.

Delano (1998) developed a bubble-pump model for the design of Einstein-Sziliard refrigeration systems, and applied the fully developed laminar single-phase pressure drop result to model frictional flow resistance ($f_s = 64/Re_j$, $Re_j = \rho_L j D/\mu_L$). Predicted liquid pumping rates were compared with experimental steam-water bubble-pump data at ambient pressure ($Bo = 9.3$). A large empirical frictional pressure drop correction (+65%) was applied to the model to achieve agreement with experimentally measured liquid pumping rates. Schaefer (2000) modified the model of Delano (1998) by applying a turbulent channel flow frictional pressure drop model. White (2001) further modified the

model by applying the Beattie and Whalley (1982) two-phase frictional pressure drop correlation, and evaluated a variety of Taylor bubble rise velocity models. White (2001) validated the model with experimental air-water flow rate measurements.

A number of bubble-pump Taylor-flow models have been proposed recently for design of diffusion absorption refrigeration systems (Belman-Flores *et al.*, 2014; Benhimidene *et al.*, 2014; Benhimidene *et al.*, 2011; Dammak *et al.*, 2010). These models incorporate a variety of kinematic and hydrodynamic sub-models. However, limited validation studies have been performed.

Thulasidas *et al.* (1995) developed a kinematic model for Taylor flow in capillary channels. However, pressure drop and hydrodynamic effects were not investigated.

Garimella *et al.* (2002) developed a comprehensive model of intermittent flows in microchannels. Liquid slug frictional pressure gradients were predicted assuming fully developed channel flow. Film-region frictional pressure gradients were modeled accounting for interfacial shear, assuming turbulent flow in the bubbles. Transitional pressure drops were modeled using the approach of Dukler and Hubbard (1975). Garimella *et al.* (2002) proposed a closure correlation for unit-cell length that led to close total pressure drop agreement with experimental (R-134a) flow data over a range of channel sizes and flow rates.

Liu *et al.* (2005) experimentally investigated capillary-scale Taylor flow over a wide range of Capillary (Ca $=\mu_L j/\sigma$) and Reynolds (Re_j) numbers. They found that laminar fully developed slug frictional pressure drop results were valid for homogeneous two-phase flow conditions (at the limit of $U_b \rightarrow U_s$), and proposed an empirical correlation for

non-homogeneous flows. Transitional pressure drops were not considered explicitly, but may be captured in their correlation.

A number of mechanistic Taylor flow models have been reported in the literature. However, relatively few have been validated for flows in the intermediate Bond number regime, almost all of which have been included in this literature review. Most studies incorporate multiple closure relations to describe hydrodynamic effects. However, independent hydrodynamic sub-model validation is rarely performed. Thus, sources of error and sub-model ranges of validity cannot be identified.

Liquid slug frictional pressure drops have been commonly modeled using fully developed single-phase laminar or turbulent results. However, developing flow corrections may be important for cases with relatively short liquid-slugs, as has been found in the intermediate Bond number regime ($L_s / D \sim 1 - 5$, Section 2.3.4). Bubble-region frictional pressure changes have generally been modeled assuming negligible interfacial shear or by applying fully developed single-phase channel flow results to the bubble. Again, developing flow effects may be important for relatively short bubbles.

While many Taylor flow modeling approaches neglect transitional pressure losses, such effects may be important for cases with relatively short unit cells. Bretherton (1961) proposed the first model for transitional pressure drop, accounting for the surface tension force difference between rounded bubble noses and flat bubble tails in capillary flows. Kreutzer *et al.* (2005) performed a simulation-based study of capillary scale Taylor flow, and extended this result with a correlation that accounts for hydrodynamic effects up to $\mathrm{Re}_j = 900$. Dukler and Hubbard (1975) modeled the transition pressure loss in large Bond

number turbulent flows as the pressure change needed to cause flow reversal from the draining liquid film to rising liquid slug. Fukano *et al.* (1989) proposed a related model that predicts the transition pressure loss as the dynamic pressure change from the liquid film to liquid slug ($\rho_L (U_s - U_f)^2 / 2$). All of these models lead to significantly different transition pressure loss predictions for intermediate Bond number Taylor flows, and none have been independently evaluated at such conditions.

3.1.2.2 Simulation of two-phase flow

Two main categories of approaches have been developed for simulating two-phase flows. *Two-fluid* Eulerian-Eulerian formulations solve separate sets of governing equations for each phase, and apply sub-grid-scale (SGS) transport models to describe inter-phase interactions. These SGS models generally employ empirical results (e.g., for bubble drag coefficient or droplet-turbulence interactions), and are not strictly consistent with the underlying continuum-scale mechanics (e.g., by applying bubbly flow SGS models in mesh cells that could be smaller than individual bubbles). *One-fluid* approaches solve a single set of governing conservation equations, eliminating the need for SGS closure models and enabling numerical consistency with the underlying physics. However, such formulations require special care to account for the large variations in fluid properties in two-phase flow, the presence of sharp liquid-vapor interfaces, and discontinuous pressure across interfaces due to surface tension forces. Simulations of Taylor flow in the intermediate Bond number regime necessitate one-fluid based approaches because the main flow features (Taylor bubbles and liquid slugs) are of the same scales as channels, and thus cannot be described using SGS models.

The most commonly employed one-fluid multiphase flow simulation techniques can be classified as either *interface tracking* or *interface capturing*. Interface tracking schemes explicitly define the fluid interface position, and advect it with the velocity field. Common approaches include *level-set*, which defines a scalar field representing the distance to the interface (Sussman *et al.*, 1994), and direct interface front tracking (Unverdi and Tryggvason, 1992). Such techniques maintain sharp interfaces, but care must be taken to ensure that the interpolation of velocity near the interface conserves the volume of each phase (Sethian and Smereka, 2003). Additionally, front-tracking approaches may necessitate complex algorithms to account for interface topology changes (e.g., bubble coalescence or breakup).

The interface tracking approach is also adopted in *body-fitted mesh* frameworks. In these techniques, the mesh is dynamically adjusted such that liquid-to-gas interfaces coincide with cell boundaries. This allows for natural determination of fluid properties in each cell and application of surface tension forces on cell faces. In some implementations, governing equations are only solved in the liquid phase, reducing the range of scales that must be resolved. While the body-fitted mesh framework is intuitive, it is not well suited to flows with large interface deformations or topology changes.

This study adopts the volume-of-fluid (VOF) interface capturing approach, first proposed by Hirt and Nichols (1981). In this methodology, the volumetric phase fraction of fluid (α_1 – the liquid fraction) is tracked in each mesh cell and advected with the velocity field. Fluid properties in each cell are weighted based on the local phase fraction. Provided that the underlying velocity field and advection schemes are conservative, the volumes of each phase will also be conserved. Two major numerical challenges arise in

the VOF method. First, numerical diffusion in the advection algorithm can cause the interface to smear out, leading to non-physical behavior. Second, care must be taken in the application of surface tension forces because the interface may be spread over several cells.

Geometric interface reconstruction (Youngs, 1982) or *interface triangulation* is performed in many VOF formulations to enable conservative and sharp advection of the interface (Deshpande *et al.*, 2012). Additionally, reconstruction enables precise evaluation of local interface area and curvature for applying surface tension forces. However, geometric reconstruction introduces substantial program complexity, especially for unstructured meshes, and increases communication costs in parallelized domain-decomposed simulations. Reconstruction-free or *pseudo-VOF* schemes (Marschall *et al.*, 2012) have thus been widely employed in two-phase flow simulations. Such approaches apply compressive velocity fields in the vicinity of interfaces to counteract numerical diffusion. This approach can lead to slightly distorted velocity fields near interfaces, but the magnitude of such errors decreases with increasing mesh resolution (Rusche, 2002).

Most pseudo-VOF schemes model the effects of surface tension with the continuum surface tension force (CSF) model, originally formulated by Brackbill *et al.* (1992). While this model is relatively simple to implement and is consistent with the governing fluid mechanics, it can also lead to spurious currents near the interface due to the diffuse nature of the phase fraction field (Raeini *et al.*, 2012). The relative magnitude of such spurious currents increases at reduced spatial scales where surface-tension forces are large compared to viscous forces. Thus individual surface tension force models are only valid above characteristic Capillary numbers ($Ca = \mu u/\sigma$). Therefore, it is important to

carefully consider the nature of a simulated two-phase flow and assess its sensitivity to interface modeling approaches to arrive at a numerical scheme that is both valid and of acceptable computational cost. In the following section, prior simulation-based studies of Taylor flow will be reviewed and assessed to arrive at approaches that are suitable for studying the intermediate Bond number flows of interest.

3.1.2.3 Simulation of two-phase Taylor flow

The earliest simulation-based studies of two-phase Taylor flow only modeled flow in liquid-phase regions (i.e., films and slugs) using body-fitted meshes. Irandoust and Andersson (1989) pioneered this technique, and investigated mass transfer in capillary scale Taylor flow with symmetric hemispherically capped bubbles with fixed interfaces. The liquid-gas interface was modeled as a no-shear uniform pressure boundary. This technique is suitable for cases where inter-phase shear is negligible in the liquid domain and the interface profile is known *a priori*. Mao and Dukler (1990) extended the approach of Irandoust and Andersson (1989) by dynamically refining the bubble profile to maintain the uniform gas-phase pressure condition. Bubble profiles were evaluated for a range of laminar flow conditions and surface tension values. Clarke and Issa (1997) employed a similar dynamic mesh adaptation approach to that of Mao and Dukler (1990) for steady turbulent Taylor flows. The two-equation standard k-ε eddy viscosity model was employed. They assumed flat bubble tails because iterative solutions for tail profiles were unstable, although they noted that this instability was consistent with experimental findings. They found agreement with established results for bubble velocity, bubble nose profile, and pressure drop.

Kawaji *et al.* (1997) performed experimental and numerical studies of Taylor bubble profiles and liquid-phase velocity fields. Their numerical approach employed the VOF-based RIPPLE solution algorithm of Kothe and Mjolsness (1992), which applies continuum surface tension forces on interface cells, but does not solve the momentum equation in the gas-bulk. Kawaji *et al.* (1997) focused on quantifying bubble and film wake lengths, and investigating the mechanisms of Taylor bubble coalescence. Bugg *et al.* (1998) adopted a similar approach to investigate laminar flow around rising Taylor bubbles in quiescent liquid mediums for a range of Bond (10 – 100) and Morton (10^{-12} – 1, Mo = $g\mu^4\rho^{-1}\sigma^{-3}$) numbers. They focused on predicting bubble shape profiles, rise velocities, and separation effects behind bubble tails.

Anglart and Podowski (2002) performed one of the first 3D VOF-based numerical studies of Taylor flow, and obtained the velocity field in both the liquid and gas regions. They employed the commercial CFX 4 solver (ANSYS Inc.), which applies the Brackbill *et al.* (1992) CSF model and employs a compressive velocity field in the vicinity of the interface to counteract numerical diffusion of α_1. Their study focused on bubble rise velocities, bubble profiles, and 3D flow effects that may contribute to bubble coalescence.

Kreutzer *et al.* (2005) performed one of the few simulation-based studies focused on pressure drop in Taylor flow. They developed a liquid-region-only flow solver that iteratively corrected the interface profile to maintain the uniform gas-phase pressure condition, similar to the approach of Mao and Dukler (1990). Kreutzer *et al.* (2005) focused on capillary scale flows, and extended the transition pressure loss model of Bretherton (1961) to higher Reynolds numbers ($Re_j < 900$).

Taha and Cui (2006) investigated vertical turbulent Taylor flow using the VOF approach with PLIC geometric interface reconstruction (Youngs, 1982) as implemented in the Fluent software package (ANSYS Inc.). This study focused on Taylor bubble profiles and rise velocities, and good agreement with experimental results was found. Taha and Cui (2006) also qualitatively explored wall shear stress profiles and Taylor flow in inclined tubes.

Akbar and Ghiaasiaan (2006) applied VOF simulations in Fluent (ANSYS Inc.) to investigate Taylor flow in capillaries. They found good agreement with experimental results and models for Taylor bubble length and rise velocity, and proposed improved correlations for liquid slug length and pressure drop. Wörner *et al.* (2007) applied the TURBIT-VOF (Ghidersa *et al.*, 2004) solver with interface reconstruction to study Taylor flow in square capillaries. Their study focused on measuring liquid residence time in Taylor flow. They found that the gas-phase density and viscosity could be artificially increased (10×) to improve numerical stability with minimal effects on overall results. Guo and Chen (2009) performed VOF simulations of vapor injection into microchannel T-junctions, and investigated the development of the Taylor flow pattern. Their study focused on the effects of surface tension, viscosity, and wall contact angles on bubble and slug lengths.

Özkan and Wörner (2007) evaluated the performance of a number of different simulation approaches and solvers for predicting capillary Taylor flow. The considered solvers include: STAR-CD V4 (CD-Adapco) : VOF with interface compression, CFX 10 (ANSYS Inc.) : VOF with high-order velocity interpolation, TURBIT-VOF (Ghidersa *et al.*, 2004): VOF with EPIRA interface reconstruction (Sabisch *et al.*, 2001), and Fluent

(ANSYS Inc.) : VOF with geometric interface reconstruction (PLIC, (Youngs, 1982)). Close agreement was found between all approaches for bubble rise velocity, but bubble shapes varied between some solvers. They reported that geometric-reconstruction based VOF schemes are more accurate than pseudo-VOF solvers, and that surface tension force related errors are amplified in smaller spatial scale flows. Gupta *et al.* (2009) performed a broad study of the feasibility and challenges of simulating Taylor flow in microchannels. They found that accurate evaluation of surface tension forces is critical at this scale, and poor implementations of the CSF formulation can lead to strong spurious currents, as indicated for more general two-phase flows by Lafaurie *et al.* (1994) and Harvie *et al.* (2006). Gupta *et al.* (2009) also investigated the effects of mesh resolution, and determined that liquid films should be resolved with at least five mesh cells for accurate simulations.

Lu and Prosperetti (2009) performed liquid-phase simulations of co-current upward and downward laminar Taylor flow for moderate to high Bond numbers ($Bo \geq 15$). They found good agreement with established results for bubble rise velocities and shapes. Lu and Prosperetti (2009) proposed a new correlation for the transition from concave to convex bubble tails, and found that oscillations can occur in the liquid film and bubble tail with even very viscous liquid. Quan (2011) also investigated co-current upward and downward laminar Taylor flow in the large Bond number regime ($Bo = 248$). They adopted a front-tracking simulation approach, and focused on bubble profiles and velocity fields in the bubble and liquid film. Figueroa-Espinoza and Fabre (2011) also investigated upward and downward co-current 2D planar flow in the high Bond number regime ($Bo > 57$). This configuration is non-physical, but can provide insights into more

complex phenomena that cannot be captured in the commonly studied axisymmetric configuration. In particular, their study focused on the transition to faster rising non-symmetric bubble shapes, which were theorized to cause bubble coalescence in the 3D studies of Anglart and Podowski (2002).

Kang *et al.* (2010) investigated Taylor bubble profiles, rise velocities, film thicknesses, and wake lengths. They developed a front tracking method for interface modeling, and suggested that conventional VOF implementations may be too diffusive for many applications. Kang *et al.* (2010) investigated the effects of varying liquid-to-vapor density and dynamic viscosity ratios, and found negligible effects for values as low as 25 and 10, respectively. They also proposed a correlation for the peak value of wall shear stress that occurs near Taylor bubble tails.

Van Baten and Krishna investigated mass transfer in capillary scale Taylor flow from the gas to liquid (van Baten and Krishna, 2004) and from the wall to liquid (van Baten and Krishna, 2005). These studies only solved for the liquid-phase flow, and Taylor bubbles were assumed to be cylindrical with hemispherical caps. Results from these investigations were employed to formulate and validate mass transfer correlations. Asadolahi *et al.* (2011) employed the Fluent VOF solver (ANSYS Inc.) to study hydrodynamics and heat transfer in microchannel Taylor flow. They found good agreement for bubble shapes and velocities with established results. Additionally, they determined that cyclic single unit-cell and full-channel-length simulations led to comparable hydrodynamic results. Hassanvand and Hasemabadi (2012) employed a VOF approach to study mass transfer and hydrodynamics in capillary scale Taylor flow. Close agreement with established results was found for liquid film thickness and bubble

velocity. They assumed fully developed inlet velocity fields, but noted that this assumption is only valid for long unit-cell flows.

Recently, capillary scale Taylor flow has been proposed as a benchmark for evaluating two-phase flow solvers (Aland *et al.*, 2013). Marschall *et al.* (2014) performed rigorous X-ray tomography based experiments of capillary scale Taylor flow in square channels to establish this benchmark. Marschall *et al.* (2014) evaluated a number of contemporary two-phase flow solvers using this dataset, and found good agreement for bubble length, bubble velocity, and pressure drop. Considered solvers included: DROPS (Groß *et al.*, 2002) (level-set), FS3D (Boger *et al.*, 2010) and TURBIT-VOF (Ghidersa *et al.*, 2004) (VOF with interface reconstruction), and interTrackFoam (Tuković and Jasak, 2012) (interface tracking).

Overall, many simulation based studies have been performed to investigate Taylor flow phenomena. However, most have focused on bubble and liquid velocities, bubble shapes, and liquid film thicknesses. In many cases, these parameters can be predicted analytically or measured experimentally using photographic or particle image velocimetry techniques. In contrast, few studies consider local pressure changes in the liquid film, slug, and bubble-to-slug transition, which are difficult to measure experimentally due to the quasi-periodic nature of Taylor flow.

A variety of simulation approaches have been employed to study two-phase Taylor flows, including body-fitted mesh, front-tracking, and VOF techniques. Body-fitted techniques were employed in many early studies, but are not well suited to cases with large interface deformations or interface breakup. The present study of intermediate Bond

number flows spans a wide range of anticipated bubble profiles, from axially symmetric bubbles with rounded noses and tails (low Bo), to cases with highly prolate noses and flat tails (high Bo, high Re). Additionally, it is desirable to detect transitions from the Taylor flow regime to annular or churn regimes to ensure that results are physically meaningful. Thus, a more versatile VOF-based approach is adopted in this investigation.

Most simulation studies focus on flows in the high Bond number ($\mathrm{Bo} \gtrsim 40$) and capillary ($\mathrm{Bo} \lesssim 5$) regimes. Limited information is available for the intermediate Bond number range, which is of particular interest for bubble pumps and air-lift pumps. A number of studies have emphasized the importance of interface and surface-tension-force modeling in microchannel Taylor flows. These criteria are expected to be important for intermediate Bond number flows where capillary forces are significant. Thus, surface tension modeling approaches are given close attention in this study.

3.1.3 Present investigation

The present investigation develops a comprehensive hydrodynamic description of vertical upward Taylor flow in the intermediate Bond number regime. A computational approach is formulated to simulate single unit-cell Taylor flows over the range of conditions of interest: $6.6 < (L_b + L_s) / D < 15$, $0.540 < \beta < 0.650$, $5 < \mathrm{Bo} < 20$, $250 < \mathrm{N_f} < 1000$, and $20 < \mathrm{Re}_j < 1500$. Results are applied to inform and independently validate hydrodynamic sub-models for liquid slug frictional pressure drop, Taylor bubble region frictional pressure drop, and transition pressure losses. Full-channel-length simulations are also performed to evaluate hydrodynamic sub-models for more realistic conditions with interacting unit cells of different dimensions and characteristics. These sub-models are integrated with kinematic results from Chapter 2 to achieve closure. The overall

mechanistic flow model is evaluated with experimental results from Chapter 2, and is compared with representative Taylor flow models from the literature.

3.2 Single Unit-Cell Simulations for Hydrodynamic Sub-Model Development

3.2.1 Governing equations and numerical implementation

This section presents the simulation approach employed for the single unit-cell studies performed to inform and validate Taylor flow hydrodynamic sub-models. This formulation is based on the open source two-phase pseudo-VOF finite volume solver: *interFoam* (The OpenFOAM Foundation, 2014). An incompressible flow model is employed in this study because only relatively small changes in total pressure are anticipated ($\lesssim 5\%$). Compressibility effects may be significant in other Taylor flow cases with relatively large pressure drops or phase change (Eskin and Mostowfi, 2012). Fluid material properties are assumed uniform in each phase. This leads to the simple continuity constraint:

$$\frac{\partial u_{\mathrm{i}}}{\partial x_{\mathrm{i}}} = 0 \tag{3.8}$$

Here, u is the velocity field and x is the spatial coordinate. The continuity equation is not solved directly in the proposed formulation, but rather, is satisfied through iterative solution of the momentum and pressure equations.

The momentum equation is formulated neglecting compressibility effects. An effective cell face viscosity ($\mu_{\mathrm{eff,f}}$) is employed, which could incorporate an eddy viscosity component for turbulent flow simulations. Gravitational body forces are applied as ρg, where ρ is the local fluid density and g is the gravitational acceleration vector. Surface tension forces are applied in the momentum equation as a body force f_{s}.

$$\frac{\partial(\rho u_i)}{\partial t} + \rho u_j \frac{\partial u_i}{\partial x_j} = -\frac{\partial p}{\partial x_i} + \frac{\partial}{\partial x_j}\left(\mu_{\text{eff,f}} \frac{\partial u_i}{\partial x_j}\right) + \rho g_i + f_{s,i} \tag{3.9}$$

Here, p is the pressure field, and t is the time coordinate.

In the base interFoam solver, the surface tension force (f_s) is evaluated by applying differential operations to the phase-fraction scalar field α_1. Here, α_1 is 1 in liquid-filled cells, 0 in gas-filled cells, and ranges from 0 to 1 in the vicinity of interfaces. In the original continuum surface tension force (CSF) model (Brackbill *et al.*, 1992):

$$f_{s,i} = \sigma \left\{ \frac{\partial}{\partial x_j} \left[\frac{\partial \alpha_1}{\partial x_j} \Big/ \left(\frac{\partial \alpha_1}{\partial x_k} \frac{\partial \alpha_1}{\partial x_k} \right)^{1/2} \right] \right\} \frac{\partial \alpha_1}{\partial x_i} \tag{3.10}$$

Here, σ is the surface tension of the liquid-gas fluid pair, the middle term is a numerical approximation of interface curvature (κ), and $\partial\alpha_1/\partial x_i$ is a smoothed delta function centered on the interface. Integrating across the interface leads to the established result that the net surface tension force per unit area is $\sigma\kappa$. However, in practice, numerical errors in the evaluation of κ and $\partial\alpha_1/\partial x_i$ can lead to the development of spurious currents in the vicinity of the interface (Deshpande *et al.*, 2012). Accurate evaluation of surface tension forces is expected to be critical for simulation of Taylor flows in the intermediate Bond number regime. Thus, the *sharp surface tension force* (SSF) model of Raeini *et al.* (2012) is implemented in this study. This formulation was reported to be more accurate than the base CSF model, but adds significant computational cost. The SSF algorithm is outlined in Figure 3.3.

1. The phase fraction field (α_1) is smoothed to damp out numerical noise (α_{1s})
2. The interface curvature (κ) is evaluated
3. The interface curvature (κ) is smoothed in a weighted fashion, with greater weighting assigned to values near the interface center (i.e., the $\alpha_1 = 0.5$ isosurface)
4. A distributed delta function field is obtained from a sharpened version of the phase fraction field (α_1*): $\delta = \partial\alpha_1^*/\partial x_i$
5. Surface tension forces are evaluated on cell faces: $f_{s,f,i} = \sigma\kappa_f\delta_{f,i}$
6. Surface tension forces are filtered to remove components tangent to interfaces, yielding $f_{s,f,\perp,i}$
7. The surface tension body force ($f_{s,i}$) is obtained as the cell face area average of $f_{s,f,\perp,i}$
8. The capillary pressure field is evaluated as: $\partial^2 p_c/\partial x_i \partial x_i = \partial f_{s,f,\perp,i}/\partial x_i$

Figure 3.3 – Summary of the sharp surface tension force (SSF) model of Raeini *et al.* (2012)

The pressure-Poisson equation is formed by evaluating the divergence of the momentum equation. Following the approach of Weller *et al.* (1998), the transport coefficients of the pressure equation are obtained in a semi-discretized fashion from the diagonal entries of the momentum matrix equation ($1/A_D$). The pressure and momentum equations are iteratively corrected at each time step such that the incompressible continuity constraint is approached ($\partial u_i/\partial x_i \rightarrow 0$). Additionally, following the approach of Raeini *et al.* (2012), the pressure field is decomposed into capillary and dynamic components ($p = p_c + p_d$). The capillary component is obtained from the SSF algorithm (Figure 3.3), and is independent of the pressure-momentum coupling at each time step. Thus, it is evaluated explicitly to improve computational efficiency.

$$\frac{\partial}{\partial x_i}\left(\frac{1}{A_D}\frac{\partial p_d}{\partial x_i}\right) = \frac{\partial u_i}{\partial x_i} + \frac{\partial}{\partial x_i}\left[\frac{1}{A_D}\left(f_{s,i} - \frac{\partial p_c}{\partial x_i}\right)\right] \tag{3.11}$$

The phase fraction field is advected with the fluid velocity, and is governed by the hyperbolic transport equation:

$$\frac{\partial \alpha_1}{\partial t} + \frac{\partial \left(u_i^* \alpha_1 \right)}{\partial x_i} = 0 \tag{3.12}$$

Here, u^* is the compressive velocity field ($u^* = u + u_c$), which is corrected to counteract numerical diffusion of the interface. The compressive component, u_c, acts normal to the interface, and is evaluated as: $u_c = (1-\alpha_1)\min\left[c_\alpha |u|, \max_i(|u_i|)\right]\nabla\alpha_1 / \left(|\nabla\alpha_1| + \varepsilon\right)$ (in this study $c_\alpha = 2$ and $\varepsilon = 10^{-8}$ times the average cell edge length). The argument of the resulting compressive advection operation $\left(u_{c,i}\alpha_1\right)$ is proportional to $\alpha_1(1-\alpha_1)$, ensuring that the effect of u_c is negligible far from liquid-gas interfaces. Detailed discussions of this technique can be found in (Deshpande *et al.*, 2012; Marschall *et al.*, 2012; Rusche, 2002).

In this study, fluid-pair surface tension (σ) values are assumed constant. The fluid density in each mesh cell is evaluated as a phase-fraction weighted average.

$$\rho = \alpha_1 \rho_L + (1-\alpha_1)\rho_G \tag{3.13}$$

A similar approach is used for evaluating mixture viscosity in the base interFoam solver. This approach is valid with sufficient mesh resolution in the vicinity of the interface. However, to reduce computational costs, the formulation of Marschall *et al.* (2012) is adopted here. This approach weights the liquid- and gas-phase viscosities depending on the relative orientations of the interface ($\hat{n}_{int}$) and cell faces ($\hat{n}_f$), accounting for whether the individual phase values act in series or parallel.

1. **WHILE** $t < t_{end}$ **DO**
    1. Update Δt for stability
    2. Update fluid and turbulence properties
    3. Phase equation sub-cycle (α_1)
    4. Evaluate the SSF algorithm to obtain f_c and p_c
    5. **DO** PIMPLE
        1. Form momentum (u) equation
        2. **DO** PISO
            1. Form pressure equation
            2. Solve p_d-Poisson equation
            3. Correct u
    6. **LOOP**
2. **LOOP**

Figure 3.4 – Summary of the two-phase flow solver algorithm

$$\mu_{\text{eff,f}} = \left(\hat{n}_{\text{int,i}}\hat{n}_{\text{f,i}}\right)\left[\alpha_1\mu_{\text{L}} + \left(1-\alpha_1\right)\mu_{\text{G}}\right] + \left(1-\hat{n}_{\text{int,i}}\hat{n}_{\text{f,i}}\right)\left[\frac{\alpha_1}{\mu_{\text{L}}} + \frac{1-\alpha_1}{\mu_{\text{G}}}\right]^{-1} \tag{3.14}$$

A summary of the solution algorithm for each time step is presented in Figure 3.4. First, the phase fraction transport equation is evaluated. A special-purpose bounded hyperbolic system solver (MULES (The OpenFOAM Foundation, 2014)) is applied to maintain α_1 in [0, 1]. The phase fraction equation is updated in three sub-time steps per outer solver iteration, which permits larger global time steps. The SSF algorithm is then evaluated, yielding updated values of f_c and p_c.

Next the program enters the pressure–velocity loop, in which p_d and u are corrected in an alternating fashion (Rattner and Garimella, 2014). The process of correcting the pressure and velocity fields in sequence is known as pressure implicit with splitting of operators (PISO) (Issa, 1982). In the employed solver, PISO is repeated for multiple iterations at each time step. This process is referred to as merged PISO- semi-implicit

method for pressure-linked equations (SIMPLE), or the pressure-velocity loop (PIMPLE) process, where SIMPLE is an iterative pressure-velocity solution algorithm for steady flows (Patankar, 1980). In the present study, the PIMPLE process is iterated twice per time step, and the PISO loop is iterated three times per PIMPLE loop. The outer algorithm loop then continues at the next time step.

3.2.2 Simulation case setups

The simulation domain is a 2D axisymmetric region containing one unit cell (Taylor bubble and liquid slug) with radial and axial extents R and H, respectively (Figure 3.5). The domain moves in the frame of the bubble to simplify post-processing. The top and bottom edges of the domain are coupled with cyclic conditions for the velocity (u) and phase fraction (α_1) fields, representing flow in an infinite train of identical unit cells. A fixed jump condition (Δp) is applied for the dynamic pressure field (p_d) between the top and bottom edges of the domain. This approach leads to slower solution convergence than for specified velocity profiles at the top or bottom, as has been employed in some previous studies (Hassanvand and Hasemabadi, 2012). However, it is necessary to accurately describe flow in short slugs, which do not permit steady fully developed velocity profiles that can be specified apriori.

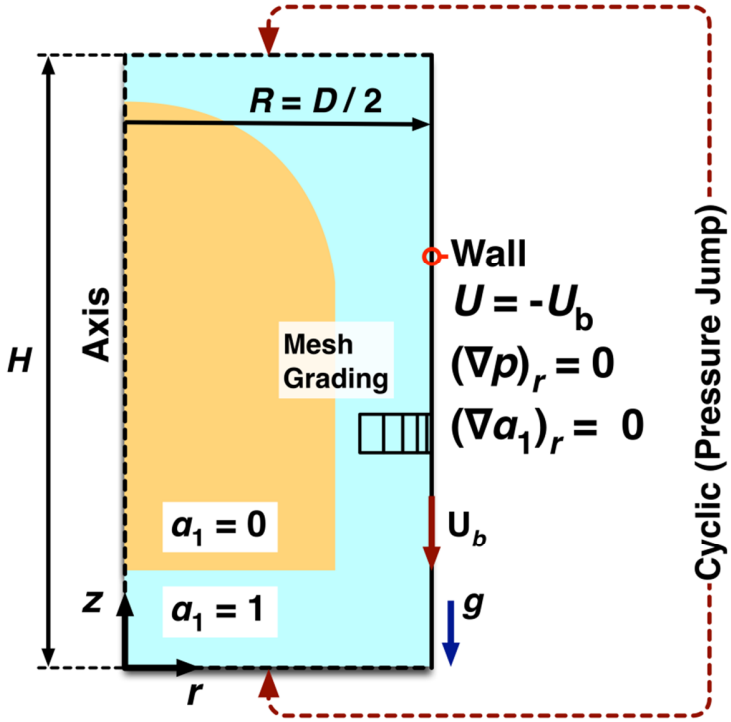

Figure 3.5 – Schematic of cyclic unit-cell simulation domain

The channel wall is modeled as a no-slip boundary for the velocity field, with dynamically varying velocity $u_{\text{wall}} = -U_b(t)\hat{z}$. The wall is specified as a zero-gradient boundary condition for the dynamic pressure (p_d) and phase fraction (α_1) fields. All domain boundaries are specified with zero-gradient conditions for the capillary pressure field (p_c), as the interface should not contact boundaries. The dynamic and capillary pressures are only specified to within a constant in this configuration due to the incompressible flow description. Thus additional constraints of zero pressure in the center of the domain are specified for both fields.

The domain is discretized with a rectilinear orthogonal mesh. The mesh is graded finer near the wall such that $\Delta r(r = 0) = 10 \times \Delta r(r = \text{D}/2)$. Computations are performed

for 2.0 simulation seconds for each case, and results are averaged from t = 1.5 - 2.0 s. This run time and averaging window is found to be sufficient to ensure well converged results for the conditions considered in this investigation.

For each case, the total superficial velocity (j) is evaluated as the average domain axial velocity over the sample time range. The bubble velocity (U_b) is similarly evaluated as the average gas-phase velocity over the sample time range. The Taylor bubble and liquid slug lengths are evaluated between the bounds of the uppermost and lowermost mesh rows satisfying average $\alpha_1 < 0.5$ – the bubble nose and tail positions, respectively. The hydrodynamically fully developed liquid film thickness is determined by averaging over the axial middle 50% of the bubble region. For the bubbles considered in this study, this excludes nose- and tail-region variations while ensuring sufficient sample data for well-converged measurements. Bubble region frictional pressure gradients ($\nabla p_{f,b}$) are evaluated as the radially averaged and time-averaged axial dynamic pressure gradients ($p_d = p - p_{hs}$) in the middle 50% of the bubble regions. Slug frictional pressure gradients ($\nabla p_{f,s}$) are similarly evaluated from the average wall shear stress in the middle 50% of liquid slugs ($\nabla p_{f,s} = 4\tau_w / D$). Finally, the transitional pressure change is evaluated as:

$$\Delta p_{trans} = \Delta p - \Delta p_{hs} - L_b \nabla p_{f,b} - L_s \nabla p_{f,s} \tag{3.15}$$

$$\Delta p_{hs} = gH\left[\alpha\rho_G + (1-\alpha)\rho_L\right] \tag{3.16}$$

Here alpha refers to the average gas volumetric fraction in the domain (void fraction), and p is the radially averaged pressure field. Representative total (p), hydrostatic (p_{hs}), and dynamic (p_d) radially averaged pressure traces are presented in Figure 3.6, illustrating this decomposition (Bo = 10, N_f = 500, Re_j = 465).

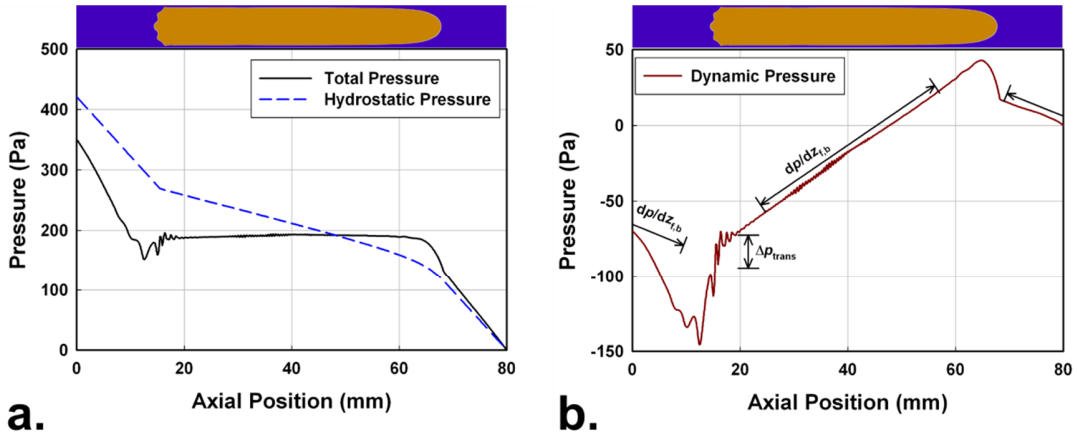

Figure 3.6 – (**a**) Total (p), hydrostatic (p_{hs}), and (**b**) dynamic pressure traces for the single unit cell study with: Bo = 10, N_f = 500, Re_j = 465

3.2.3 Simulation cases and analysis

The flow configuration described in the previous section (3.2.2) can be specified with the following non-dimensional groups.

- AR – unit-cell aspect ratio (H / D = (L_b + L_s) / D)
- β – relative Taylor bubble length (L_b / H)
- Bo – Bond number $\left(\left(\rho_L - \rho_G\right) gD^2/\sigma\right)$
- N_f – Effective viscosity parameter $\left(\rho_L^2 gD^3/\mu_L^2\right)^{1/2}$
- Re_j – Superficial velocity Reynolds number $\left(\rho_L jD/\mu_L\right)$
- P^* – Dimensionless dynamic pressure change $\left(\left(\Delta p - \Delta p_{hs}\right)/\Delta p_{hs}\right)$

Table 3.1 – Summary of simulation cases for single unit-cell studies

AR	Bo	N_f	β Range	Re_j Range
10	10	500	0.581 – 0.639	64 – 752
10	10	1000	0.561 – 0.598	22 – 1504
10	10	250	0.614 – 0.650	68 – 326
10	5	500	0.540 – 0.606	283 – 765
10	20	500	0.620 – 0.631	333 – 467
6.6	10	500	0.583 – 0.618	23 – 402
15	10	500	0.591 – 0.631	272 – 671

Simulations were conducted in the intermediate Bond number regime for: $6.6 < AR < 15$, $0.540 < \beta < 0.650$, $5 < Bo < 20$, $250 < N_f < 1000$, and $20 < Re_j < 1500$. Overall, 45 cases spanning these ranges of conditions were simulated. As discussed in Section 3.2.2, it was not possible to specify flow rate boundary conditions for the short unit cells considered in this study. Rather total pressure drops (P^*) were set, and time-averaged flow rates (j) evaluated from solution results. Similarly, relative Taylor bubble lengths (β) depend on bubble shape profiles, which were not known *a priori*. Thus, initial bubble volumes (α) were specified, and time-averaged β values obtained from the results. The non-dimensional and dimensional governing parameter ranges for these cases are summarized in Tables 3.1 and 3.2, respectively.

Table 3.2 – Summary of parameter ranges for simulation cases

D	8.0	mm
H	80	mm
ρ_L	1000	kg m^{-3}
ρ_G	10	kg m^{-3}
μ_L	$2.24 – 8.96 \cdot 10^{-3}$	kg m^{-1} s^{-1}
μ_G	$2.0 \cdot 10^{-4}$	kg m^{-1} s^{-1}
Δp	340 - 370	Pa

Table 3.3 – Summary of mesh independence study results

Grid	β	Re_j	P^*	δ_f / D	U_b (m s^{-1})	$\nabla p_{f,b}$ (Pa m^{-1})	$\nabla p_{f,s}$ (Pa m^{-1})	Δp_{trans} (Pa)
25 × 500	0.587	63	-0.180	0.0514	0.0805	-1850	80.5	8.91
38 × 760	0.581	53	-0.187	0.0536	0.0751	-1930	82.0	7.69
57 × 1140	0.581	64	-0.193	0.0539	0.0816	-1950	112.8	4.53
86 × 1720	0.580	60	-0.195	0.0545	0.0778	-1970	91.9	4.47

A grid independence study was conducted to determine appropriate mesh resolutions for these studies at the conditions: AR = 10, $\beta \sim 0.58$, Bo = 10, $N_f = 500$, $Re_j \sim 60$, $P^* \sim -0.19$. Considered grid sizes ($N_r \times N_z$) were: 25 × 500, 38 × 760, 57 × 1140, 86 × 1720. Representative bubble profiles and film-region grids for these studies are presented in Figure 3.7. All considered cases satisfied the mesh criterion of Gupta *et al.* (2009) with at least five cells spanning the liquid film thickness. Nearly identical bubble profiles are found in all four cases, with almost hemispherical noses and wavy film regions near bubble tails. Bubble tail curvature varies slightly between renderings in Figure 3.7. However, this is primarily an unsteady effect due to tail oscillations (see Mao and Dukler (1990)), and similar time-varying trends were found in all four cases.

In the intermediate Bond number regime, V_L is highly sensitive to total pressure drop (see Section 3.1.1). Thus, flow rates varied slightly between cases due to variations in initial void fraction and minor accumulated conservation errors in α_1 ($53 \leq Re_j \leq 64$). Results from these simulations are summarized in Table 3.3. Bubble velocities and pressure drops are reported in dimensional form, which is more intuitive for these cases.

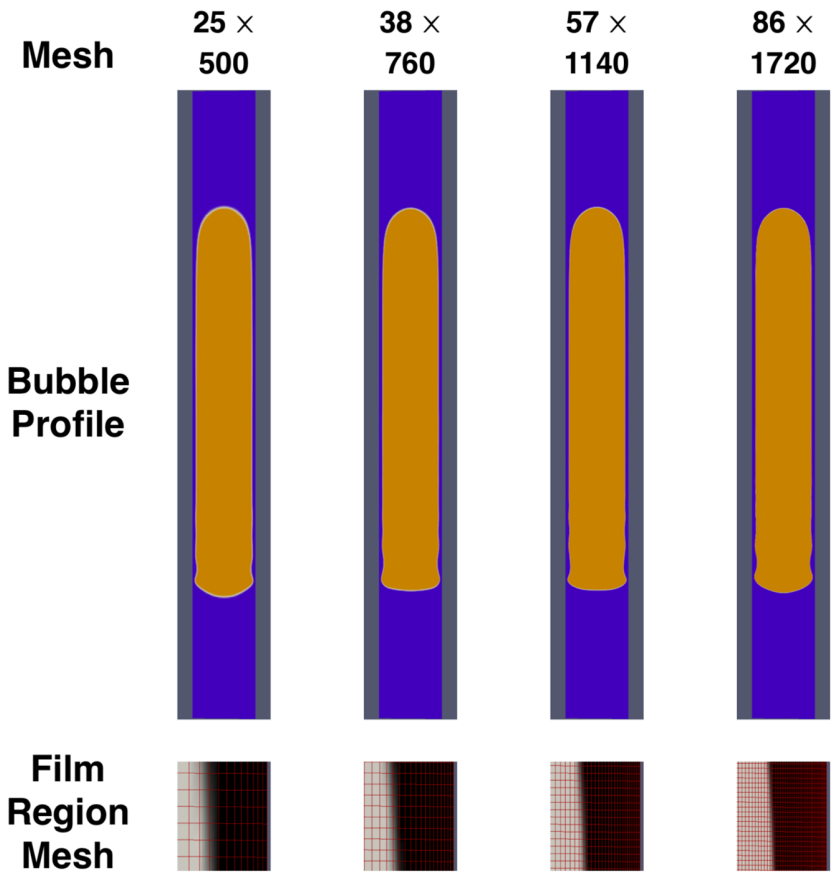

Figure 3.7 – Representative bubble shape profiles and film mesh resolutions from the grid independence study

Most measured quantities are relatively well converged over the span of considered mesh resolutions (Δr_{max} / Δr_{min} ~ 3.4). The values of β, P^*, δ_f / D, U_b, and $\nabla p_{f,b}$ vary by less than 8% of the finest mesh resolution case values. The superficial velocity (Re_j) varies more significantly, but this is mainly due to the difficulty in assigning appropriate pressure jump boundary conditions to specify j. The liquid slug frictional pressure drop varies more significantly, but seems to be converged to within ±15% for the two highest resolution cases. The transition pressure losses trend toward lower values with increasing

mesh resolution, but seem to be well-converged for the two highest resolution cases. Considering these results, the 57 × 1140 grid is selected for the main simulation studies as an acceptable compromise between computational cost and mesh independence.

The validity of simulation results can be assessed using independently formulated models for hydrodynamically fully developed liquid film thickness (δ_f) and Taylor bubble rise velocity (U_b) in the intermediate Bond number regime. In Chapter 2, it was demonstrated that the analytical result for laminar falling film on a vertical flat plate with negligible interfacial shear predicted measured film thicknesses well. However, experimental uncertainty was large for film thickness data (20 – 60%); therefore, detailed analysis was not feasible. Here, a more rigorous model for validation that accounts for channel-wall curvature and interfacial shear is employed. These corrections are necessary for reduced N_f cases (increased δ_f/D), and because of the numerically increased gas-phase viscosity (μ_G = 2.0 · 10^{-4} kg m^{-1} s^{-1}). The average film velocity is obtained by exact solution of the 1-D axisymmetric fully developed Navier-Stokes equation.

$$U_f = \frac{4}{\pi\left[D^2-\left(D-2\delta_f\right)^2\right]}\int_{D/2-\delta_f}^{D/2}(2\pi r)\left\{\begin{array}{l}\dfrac{g\left(\rho_L-\rho_G\right)}{4\mu_L}\left[\left(\dfrac{D}{2}\right)^2-r^2+2\left(\dfrac{D}{2}-\delta_f\right)^2\ln\left(\dfrac{2r}{D}\right)\right]\\ +\dfrac{\tau_{int}\left(D/2-\delta_f\right)}{\mu_L}\ln\left(\dfrac{2r}{D}\right)\end{array}\right\}dr \tag{3.17}$$

Interfacial shear is predicted using the laminar developing flow result of Shah and London (1978). The laminar bubble flow assumption is adopted here because Re_b < 300 for all simulation cases.

$$f_b = \frac{4}{Re_b}\left\{\frac{3.44}{\sqrt{L_b^*}}+\left[\frac{1.25}{4L_b^*}+16-\frac{3.44}{\sqrt{L_b^*}}\right]\Big/\left[1+0.00021\left(L_b^*\right)^{-2}\right]\right\} \tag{3.18}$$

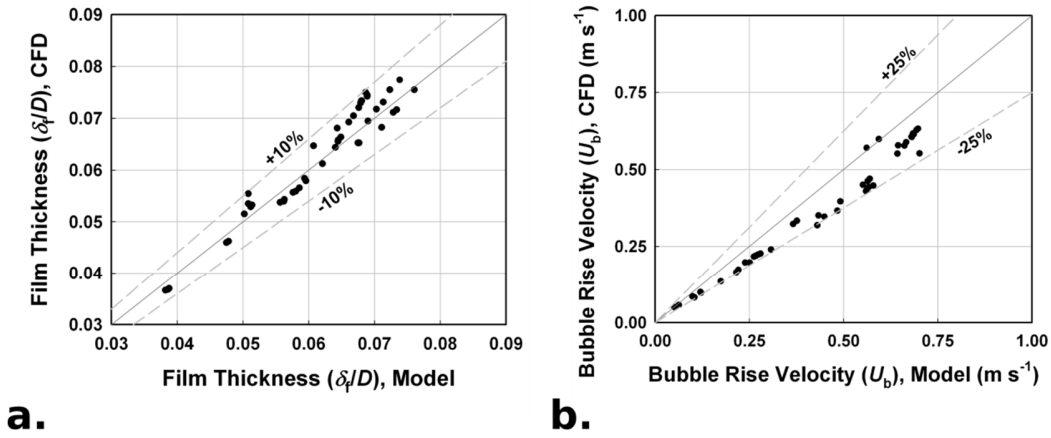

Figure 3.8 – Comparison of analytical model predictions and simulation results for (**a**) liquid film thickness, and (**b**) Taylor bubble rise velocity

$$\mathrm{Re}_\mathrm{b} = \frac{\rho_\mathrm{G}\left(U_\mathrm{b}+U_\mathrm{f}\right)D_\mathrm{b}}{\mu_\mathrm{G}} \qquad L_\mathrm{b}^{*} = \frac{L_\mathrm{b}}{\mathrm{Re}_\mathrm{b}\,D_\mathrm{b}} \tag{3.19}$$

$$\tau_\mathrm{int} = \frac{f_\mathrm{b}}{8}\rho_\mathrm{G}\left(U_\mathrm{b}+U_\mathrm{f}\right)^2 \tag{3.20}$$

Close agreement is found between simulation film thicknesses in the middle 50% of bubble regions and analytical model predictions (Figure 3.8a), with all cases agreeing to within 10%, and an average absolute deviation of 4.0% ($\mathrm{AAD} = 1/\mathrm{n}\sum\left|\delta_{\mathrm{f,mod}}-\delta_{\mathrm{f,sim}}\right|/\delta_{\mathrm{f,sim}}$, for n data points). Similar, but slightly poorer agreement is found if fully developed laminar bubble flow is assumed (AAD = 4.2% for $f_\mathrm{b} = 64 / \mathrm{Re}_\mathrm{b}$). This indicates that developing flow effects in Taylor bubbles may have a minor influence on liquid film thickness in the intermediate Bond number regime.

The bubble rise velocity model proposed in Chapter 2 is also employed for simulation validation, and is summarized as follows:

$$U_{\mathrm{b}} = C_0\left(\mathrm{Re}_j,\ \mathrm{Bo},\ \mathrm{Ca}\right) j + \Gamma\left(\mathrm{Bo},\ \mathrm{N_f}\right)\sqrt{gD} \tag{3.21}$$

$$C_0 = f_{\mathrm{LS}} C_{0,\mathrm{LS}} + \left(1 - f_{\mathrm{LS}}\right) C_{0,\mathrm{Ca}} \tag{3.22}$$

$$f_{\mathrm{LS}} = \left(\frac{1}{1 + 4840\,\mathrm{Re}_j^{-0.163}} \right)^{0.816/\mathrm{Bo}} \tag{3.23}$$

$$C_{0,\mathrm{LS}} = 1.20 + \frac{1.09}{1 + \left(\mathrm{Re}_j/805\right)^4} \tag{3.24}$$

$$C_{0,\mathrm{Ca}} = \frac{1}{1 - 0.61\mathrm{Ca}^{0.33}} \tag{3.25}$$

$$\Gamma = \begin{cases} 0.344\left[1 - \exp\left(\dfrac{-0.01\mathrm{N_f}}{0.345}\right)\right]\sqrt{1 + \dfrac{20}{\mathrm{Bo}} - \dfrac{93.7}{\mathrm{Bo}^2} - \dfrac{676.5}{\mathrm{Bo}^3} + \dfrac{2706}{\mathrm{Bo}^4}}\,\dfrac{1 - 0.96\exp\left(-0.0165\mathrm{Bo}\right)}{1 - 0.52\exp\left(-0.0165\mathrm{Bo}\right)} & \mathrm{Bo} > 4.55 \\ 0 & \mathrm{Bo} \le 4.55 \end{cases} \tag{3.26}$$

Analytical model predictions and simulation results for Taylor bubble rise velocity show good agreement (Figure 3.8b), with 64% of model predictions agreeing with simulation results to within 25% (AAD = 20.5%). Model results for U_{b} over-predict simulation results by 20% on average. This discrepancy may be due to the higher $\mathrm{N_f}$ (1520 – 3030) and Re_j (480 – 4460) conditions used to formulate the bubble rise velocity model in Chapter 2. Overall these results for δ_{f} and U_{b} indicate general validity of the single unit-cell simulations, and support the use of this simulation data set to formulate hydrodynamic models of Taylor flow in the intermediate Bond number regime.

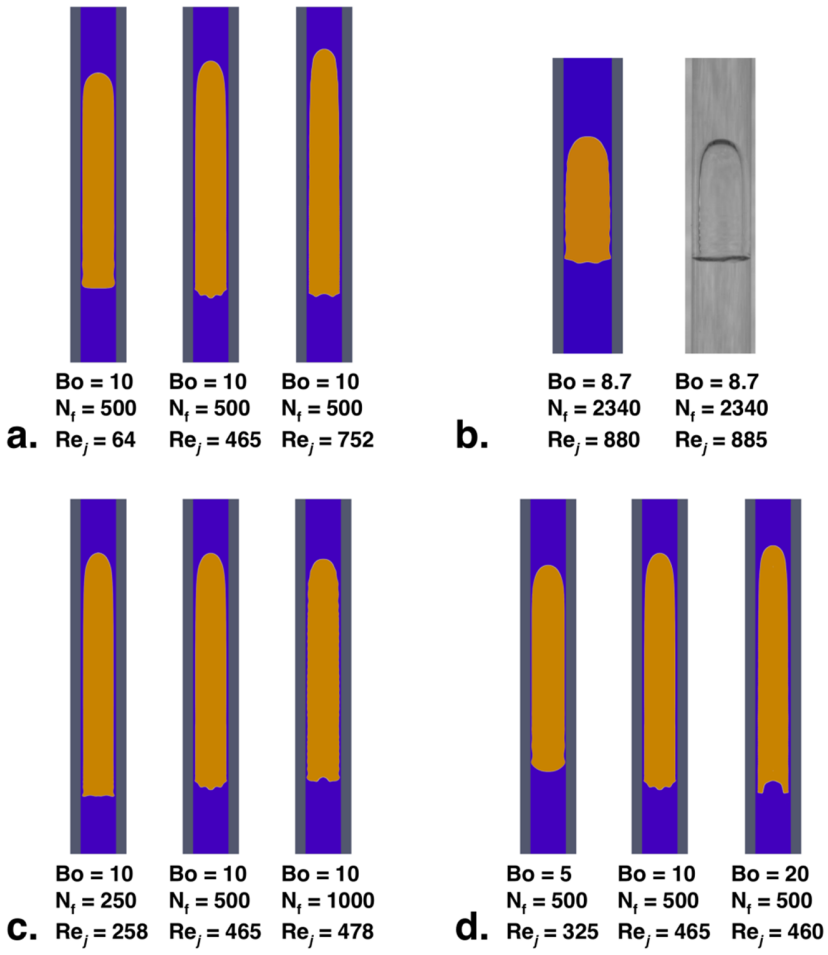

Figure 3.9 – Representative bubble shape profiles at: **a**. Varying Re_j, **b**. Near-experimental conditions, **c**. Varying viscosity number (N_f), **d**. Varying Bo

Representative bubble profiles from these studies are presented in Figure 3.9. For the baseline conditions (Bo = 10, N_f = 500), increasing the flow rate (Re_j) leads to greater film thickness (δ_f), reduced film waviness near the bubble tail, and increasingly prolate bubble noses (Figure 3.9a). For the three bubble cases presented in Figure 3.9a, the bubble-tip normalized interface curvatures (relative to a sphere with the channel radius: $\kappa^* = \kappa / (2/R)$) increase with Re_j as $\kappa^*(Re_j = 64) = 1.28$, $\kappa^*(Re_j = 465) = 4.20$, $\kappa^*(Re_j =$

752) = 5.28. An additional case was run at reduced effective viscosity (N_f = 2340) and increased Reynolds number (Re_j = 880), matching an experimental condition from Chapter 2 of air-water flow ($p = p_{amb}$, T = 22°C) in an 8.0 mm diameter tube (Figure 3.9b). The simulated and experimentally observed bubble profiles present close qualitative agreement, with relatively flat noses, capillary waves in the liquid film regions, and skirted bubble tails. At greater effective viscosity (N_f = 250) film thickness increases, and film capillary waves and bubble tail oscillations are dampened (Fig 3.9c). At reduced Bond numbers (Bo = 5), bubble tails become more rounded and film thickness is reduced, consistent with capillary-scale results (Figure 3.9d). Similarly, at Bo = 20, bubble tails can become concave and film thickness increases.

3.3 Hydrodynamic Model Formulation and Closure

As discussed in Section 3.1.1, the dynamic component of pressure drop in Taylor flow can be decomposed into bubble-region friction ($\nabla p_{f,b}$), slug-region friction ($\nabla p_{f,s}$), and flow-transition (Δp_{trans}) components. Hydrodynamic sub-models for these contributions are formulated and assessed in the following sections.

3.3.1 Bubble-region frictional pressure change gradient

The bubble-region frictional contribution is generally the dominant component of p_d in the intermediate Bond number regime due to relatively long bubbles ($\beta \gtrsim 0.5$) and thick laminar liquid films ($\delta_f / D \gtrsim 0.05$). The bubble-region frictional pressure change acts in the upward direction in vertical channels because the liquid film flows downward. This leads to greater liquid flow rates in air-lift and bubble pumps than would be predicted if hydrodynamic effects were neglected (i.e., assuming $\Delta p = \Delta p_{hs}$). For the

considered simulation cases, bubble-region frictional pressure changes ($L_b \nabla p_{f,b}$) range from -40 – -20% of total unit-cell pressure drops.

If interfacial shear is neglected, hydrodynamically fully developed bubble-region frictional pressure change can be evaluated as: $\nabla p_{f,b} = -(\rho_L - \rho_G) g (1-\alpha_b)$. This result is valid in the limits of $\mu_G/\mu_L \to 0$ and low bubble velocities. In this investigation, a more general result is proposed:

$$\tau_{int}(\pi D_b) - \tau_w(\pi D) = \frac{\pi}{4}\left(D^2 - D_b^2\right)(\rho_L - \rho_G) g \tag{3.27}$$

$$\nabla p_{f,b} = \frac{4\tau_w}{D} \tag{3.28}$$

Here, τ_w is the bubble-region wall shear stress and τ_{int} is the interfacial shear stress, evaluated assuming either fully developed laminar flow (f_b = 64/Re$_b$ and Equation 3.20) or developing laminar flow (Equations 3.18 – 3.20). Bubble-region frictional pressure gradient predictions from these models are compared with simulation results in Figure 3.10. All three models yield agreement to within 10% with simulation results for all considered cases. The negligible-interfacial-shear formulation yields an average absolute deviation of 4.5% ($\text{AAD} = 1/N \sum \left|\nabla p_{f,b,mod} - \nabla p_{f,b,sim}\right| / \nabla p_{f,b,sim}$, for N cases). The fully developed laminar flow model leads to improved agreement with simulation results (AAD = 2.7%). The model that accounts for developing Taylor bubble flow interfacial shear yields an AAD of 1.9%, and is thus recommended for use in the intermediate Bond number range. This result indicates that developing laminar flow effects in Taylor bubbles are minor, but not negligible in intermediate Bond number flows.

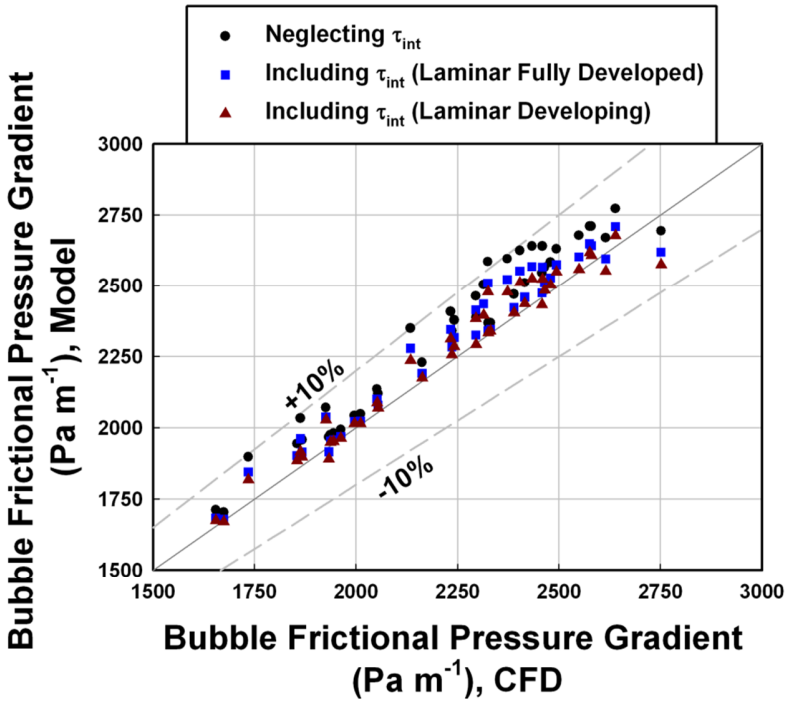

Figure 3.10 – Comparison of proposed models for bubble-region frictional pressure gradient with simulation results

3.3.2 Liquid-slug frictional pressure drop gradient

In the literature, liquid-slug region frictional pressure drop gradients have been modeled assuming either fully developed laminar (Delano, 1998; Liu *et al.*, 2005) or turbulent (de Cachard and Delhaye, 1996; Garimella *et al.*, 2002; Reinemann *et al.*, 1990; Sylvester, 1987) channel flows. In the laminar case, the friction factor result $f_{\mathrm{f,s,lam,FD}} = 64/\mathrm{Re}_j$ applies, where $\nabla p_{\mathrm{f,s}} = f_{\mathrm{f,s}} \rho j^2 / 2D$. For fully developed turbulent flows, the correlation of Petukhov *et al.* (1970) is employed.

$$f_{\mathrm{f,s,turb,FD}} = \left[0.790 \ln\left(\mathrm{Re}_j\right) - 1.64\right]^{-2} \tag{3.29}$$

Relatively short liquid slugs have been found in experimental investigations of Taylor flow in the intermediate Bond number regime ($L_s / D \sim 1 - 5$, Section 2.3.4). Thus, it may be important to consider developing flow effects on liquid-slug frictional pressure drops. Representative developing channel flow models for laminar (Shah and London, 1978) and turbulent (Nellis and Klein, 2009) flow are presented in Equations 3.30-31.

$$f_{f,s,lam,Dev} = \frac{4}{\mathrm{Re}_j}\left[\frac{3.44}{\sqrt{L^*}} + \frac{1.25/\left(4L^*\right)+16-3.44/\sqrt{L^*}}{1+0.00021/L^{*2}}\right] \qquad L^* = \frac{L_s}{D\,\mathrm{Re}_j} \tag{3.30}$$

$$f_{f,s,turb,Dev} = f_{f,s,turb,FD}\left[1+\left(\frac{D}{L_s}\right)^{0.7}\right] \tag{3.31}$$

Liquid slug frictional pressure drop gradient results for all four models are compared with simulation results in Figure 3.11. Results are also summarized for average absolute deviation (AAD) and fraction of predictions within 25% of simulation values (Table 3.4). Data from the highest N_f cases (N_f = 1000, lowest effective viscosity) are excluded from this comparison because large wake regions behind Taylor bubbles were observed for these conditions; therefore, slug frictional and transitional pressure drops could not be clearly distinguished. This effect can be observed qualitatively in the representative

Table 3.4 – Summary of model performances for predicting liquid slug frictional pressure drop

Friction Factor Model	**AAD**	**% Error < 25%**
Fully developed laminar	28%	63%
Developing laminar (Shah and London, 1978)	141%	8%
Fully developed turbulent (Petukhov *et al.*, 1970)	36%	37%
Developing turbulent (Nellis and Klein, 2009)	29%	39%

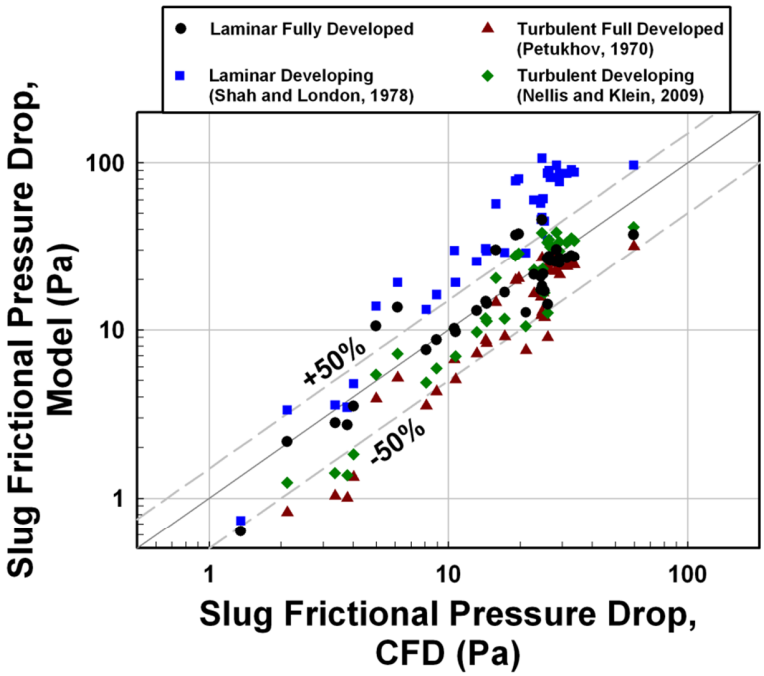

Figure 3.11 – Comparison of proposed models for liquid slug-region frictional pressure gradient with simulation results

bubble tail-to-slug region streamline profiles in Figure 3.12 (3.12a. Bo = 10, N_f = 500, Re_j = 465, 3.12b. Bo = 10, N_f = 1000, Re_j = 478).

Based on this study, the fully developed laminar friction factor result is most appropriate for predicting intermediate Bond number slug frictional pressure drops for the range of conditions considered ($60 < Re_j < 1340$, AAD = 28%, 63% of cases predicted to within 25% of CFD values). It may be surprising that the laminar developing flow result yields poor accuracy considering the short slug lengths in these studies ($2.6 < L_s / D < 6.1$). However, the developing flow model assumes a uniform inlet velocity profile. This is significantly different from the Taylor flow condition in which liquid

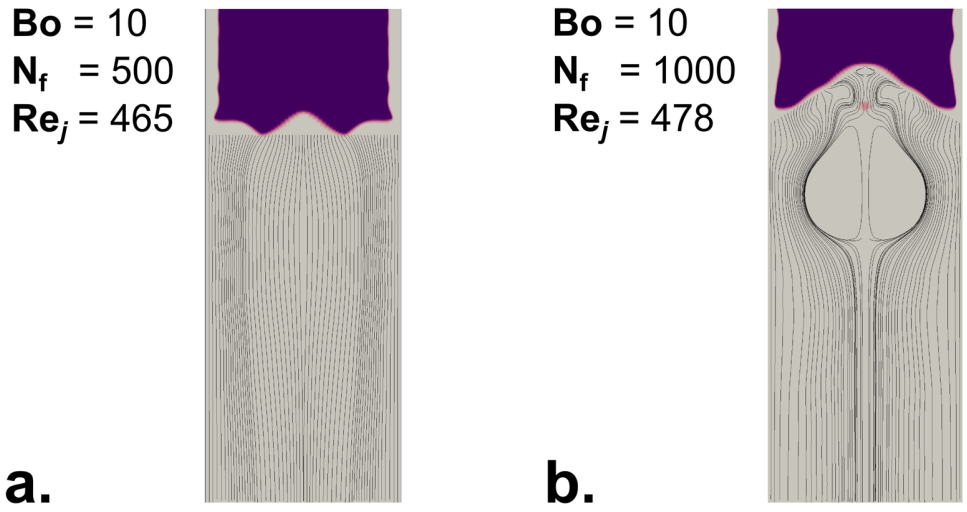

Figure 3.12 – Comparison of bubble tail-to-slug region streamlines with (**a**) greater ($N_f = 500$) and (**b**) reduced ($N_f = 1000$) effective viscosities

enters the slug through an annular jet (draining liquid film). Additionally, film-to-slug flow transition effects may disrupt conventional channel-flow development mechanisms.

The fully developed turbulent flow result also yields poor agreement (AAD = 36%, 37% of cases predicted within 25% error), as is expected for the considered laminar flow conditions $\left(\mathrm{Re}_j < 1500\right)$. The developing turbulent flow model achieves fair agreement with simulation results (AAD = 29%, 39% of cases predicted within 25% error). However, this agreement may be coincidental considering the relatively low values of Re_j and the fact that no turbulence model was employed in the simulations. For generality, the universal correlation of Churchill (1977) (for smooth channels) is recommended. This correlation converges to the fully developed laminar friction factor (within 1% for $Re_j <$ 2100) that was found to agree best with simulation data from this study. The model of

Churchill (1977) can also be reasonably expected to apply for higher Re_j turbulent Taylor flows.

$$f_{\mathrm{f,s,Uni}} = 8\left\{\left(\frac{8}{\mathrm{Re}_j}\right)^{12} + \left[\left(2.457\ln\left(\frac{1}{\left(7/\mathrm{Re}_j\right)^{0.9}}\right)\right)^{16} + \left(\frac{3750}{\mathrm{Re}_j}\right)^{16}\right]^{-1.5}\right\}^{1/12} \tag{3.32}$$

3.3.3 Flow transition pressure loss

Four Taylor flow transition pressure loss models have been proposed in the literature. The model of Bretherton (1961) accounts for the difference in capillary pressure between the rounded noses and relatively flat tails of Taylor bubbles.

$$\Delta p_{\mathrm{trans,Bretherton}} = 7.16\left(3\mathrm{Ca}\right)^{2/3}\left(\sigma/D\right) \tag{3.33}$$

Kreutzer *et al.* (2005) extended the low-Re_j capillary scale results of Bretherton (1961) to include hydrodynamic effects.

$$\Delta p_{\mathrm{trans,Kreutzer}} = \frac{1}{2}\rho_{\mathrm{L}} j^2\left(\frac{10.88}{\mathrm{Re}_j^{2/3}\,\mathrm{Ca}^{1/3}}\right) \tag{3.34}$$

Dukler and Hubbard (1975) modeled the transition pressure loss as the pressure difference required for flow reversal from the draining liquid film to rising liquid slug. Here, U_{f} is negative (downward flow).

$$\Delta p_{\mathrm{trans,Dukler}} = \rho_{\mathrm{L}}\left[1-\left(\frac{D_{\mathrm{b}}}{D}\right)^2\right]\frac{\left(U_{\mathrm{b}}-U_{\mathrm{f}}\right)\left(j-U_{\mathrm{f}}\right)}{2} \tag{3.35}$$

Finally, Fukano *et al.* (1989) modeled the transition pressure loss as the dynamic pressure difference between the liquid film and liquid slug.

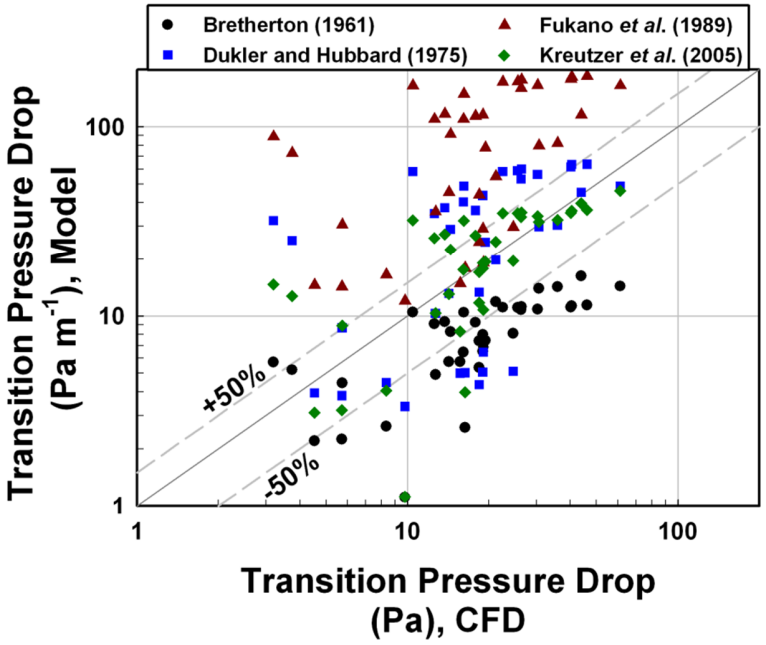

Figure 3.13 – Comparison of proposed models for transition pressure loss with simulation results

$$\Delta p_{\text{trans,Fukano}} = \frac{\rho_{\text{L}} \left(j - U_{\text{f}} \right)^2}{2} \tag{3.36}$$

All four models are compared with simulation results in Figure 3.13 and Table 3.5. Log-scale average absolute deviations $\left(\text{AAD}_{\text{log}} = 1/n \sum \left| \log_{10} \left(\Delta p_{\text{trans,mod}} / \Delta p_{\text{trans,exp}} \right) \right| \right)$ are

Table 3.5 – Summary of model performances for predicting flow transition pressure loss

Pressure Loss Model	AAD	AAD_{log}	% Error < 50%
Bretherton (1961)	57%	0.39	24%
Kreutzer *et al.* (2005)	53%	0.20	68%
Dukler and Hubbard (1975)	118%	0.34	34%
Fukano *et al.* (1989)	450%	0.59	16%

also reported. As in the liquid slug frictional pressure drop analysis (Section 3.3.2), the high N_f cases are excluded from these analyses.

In general, none of the considered models yield consistent agreement with simulation results. The model of Bretherton (1961) generally under-predicts transition pressure loss (Δp_{trans}). The model of Fukano *et al.* (1989) consistently over-predicts Δp_{trans}. The model of Dukler and Hubbard (1975) under-predicts Δp_{trans} for low Δp_{trans} but tends toward simulation results at greater Δp_{trans}. The model of Kreutzer *et al.* (2005) obtains the best agreement, with AAD = 53%, AAD_{log} = 0.20, and 68% of predictions within 50% of simulation values. While the model of Kreutzer *et al.* (2005) performs reasonably well for these conditions, it assumes a capillary number dependence for Δp_{trans}. At higher Reynolds numbers, the inertial-force based models of Dukler and Hubbard (1975) and Fukano *et al.* (1989) may be more appropriate.

As noted earlier, it is difficult to decouple $\nabla p_{f,s}$ and Δp_{trans} in some simulation cases. Thus, it is also informative to analyze combined slug pressure drops ($\Delta p_{s,c} = L_s \nabla p_{f,s} + \Delta p_{trans}$). Combined slug pressure drops are compared for all simulation cases, including those with N_f = 1000, in Figure 3.14. From this figure, it is clear that only accounting for fully developed laminar or turbulent channel flow frictional pressure drops leads to consistent under-prediction of overall pressure drop. The combined Churchill (1977) frictional and Kreutzer *et al.* (2005) transitional pressure drop model yields the best overall agreement: AAD = 0.23, with 89% of $\Delta p_{s,c}$ predictions within 50% of simulation values. The combined Churchill (1977) and Dukler and Hubbard (1975) model also performs reasonably well: AAD = 0.35, with 78% of $\Delta p_{s,c}$ predictions within 50% of simulation values.

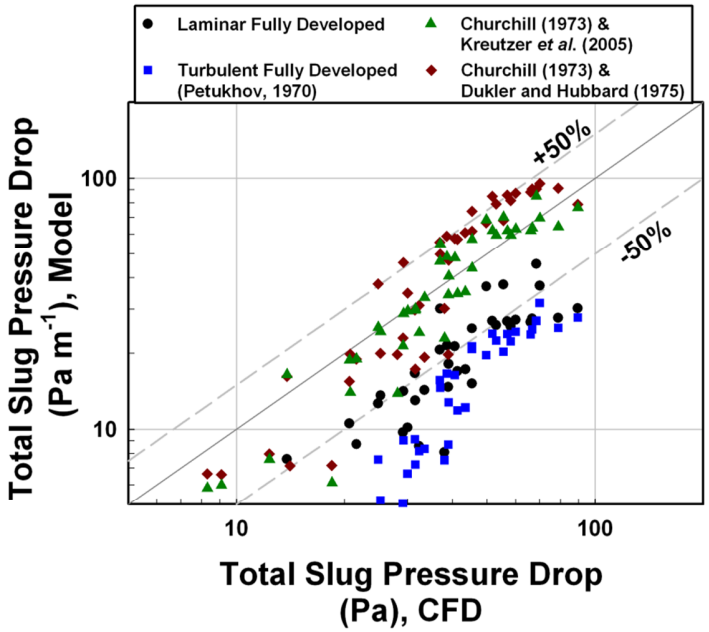

Figure 3.14 – Comparison of combined slug pressure drop models ($\Delta p_{s,c}$) with simulation results

Overall, excellent agreement is found between the proposed sub-model for $\nabla p_{f,b}$ and simulation results (AAD = 1.9%). This is possible because the liquid-film flow configuration is mechanistically simple, and can be modeled as a 1-D flow. Relatively good agreement is found for liquid-slug frictional pressure drop: AAD = 28% assuming a laminar fully developed friction factor. The universal correlation of Churchill (1977) is proposed, but transitional and turbulent performance could not be evaluated with available laminar simulation data. Additionally, it is as yet unclear if it is necessary to, or how to, account for developing flow effects in short liquid slugs. Conventional developing channel flow results do not apply. Only fair agreement is obtained for prediction of transitional pressure drops (AAD_{log} = 0.20 (Kreutzer *et al.*, 2005)). These large errors are not surprising considering that there is still disagreement over the specific

mechanisms of transition pressure loss in Taylor flow. Thus, future investigations to refine models for $\nabla p_{f,s}$ and Δp_{trans} are warranted.

3.4 Full-Channel-Length Taylor Flow Simulations

3.4.1 Solution approach

A series of full-channel-length ($89 < L/D < 140$) simulations were conducted to evaluate the proposed Taylor flow sub-models under more realistic conditions with unit-cells of varying lengths and characteristics. For these comparatively computationally expensive cases, the solution algorithm described in the previous section was infeasible. Rather, the base interFoam solver (The OpenFOAM Foundation, 2014) was employed with minor modifications. A detailed description and analysis of the interFoam solver can be found in Deshpande *et al.* (2012).

In the idealized repeating unit-cell model of Taylor flow, the channel wall is fully wetted by liquid (Gupta *et al.*, 2009). However, for the more complex cases of Taylor-flow start-up and developing Taylor flow considered here, local wall dry-out can occur, and a suitable wall contact angle model must be employed. The base OpenFOAM library (version 2.2.0, (The OpenFOAM Foundation, 2014)) provides two relevant wall-contact angle formulations: a constant angle model ($\theta = \theta_0$), and a dynamic angle model $\left(\theta = \theta_0 + \left(\theta_a - \theta_r\right)\tanh\left(u_{cl}/u_\theta\right)\right)$. Here, θ_0, θ_a, and θ_r are user-specified static, advancing, and receding contact angle values, respectively. u_{cl} is a numerical approximation of the contact line velocity, and u_θ is a user-specified contact-line-velocity to contact-angle slope. These approaches are both empirical, and may not lead to realistic wetting behavior.

In this investigation, the experimentally informed contact angle model proposed by Kistler (1993) is employed. The numerical implementation is based on that of Berberovic (2008), and is summarized as follows:

$$\theta = H\left[\mathrm{Ca}_{\mathrm{cl}} + H^{-1}\left(\theta_{\mathrm{a}} \,||\, \theta_{\mathrm{r}}\right)\right] \tag{3.37}$$

$$H\left(x\right) = \cos^{-1}\left\{1 - 2\tanh\left[5.16\left(\frac{x}{1+1.31x^{0.99}}\right)^{0.706}\right]\right\} \tag{3.38}$$

Here, H(x) is referred to as the Hoffman function, and H^{-1}(x) is the inverse function. $\mathrm{Ca}_{\mathrm{cl}}$ is the capillary number based on the contact line velocity $\mathrm{Ca}_{\mathrm{cl}} = \mu U_{\mathrm{cl}}/\sigma$, and θ_{a} and θ_{r} are user-specified maximum advancing and receding contact angles, respectively. The contact angle model selects between applying θ_{a} and θ_{r} in the inverse Hoffman function in Equation 3.37 depending on whether the contact line is advancing or receding, respectively. In this study, $\theta_{\mathrm{a}} = 90°$ and $\theta_{\mathrm{r}} = 10°$. These values were found to lead to wall re-wetting after dryout events, which is expected for intermediate Bond number Taylor flows.

For some of the full-channel-length simulation cases, the base interFoam implementation was found to yield strong interface oscillations. These may be the result of spurious currents from the CSF model or interface compression scheme in the phase-fraction transport model. A simplified numerically increased viscosity approach was thus implemented to dampen such oscillations.

$$\mu_{\mathrm{eff}} = \alpha_1\mu_{\mathrm{L}} + \left(1-\alpha_1\right)\mu_{\mathrm{G}} + 4M_{\mathrm{G}}\left(1-\alpha_1\right)\alpha_1\mu_{\mathrm{L}} \tag{3.39}$$

In this model, the standard linear viscosity blending approach is employed instead of Equation 3.14. M_G is a user specified gain for the interface oscillation damping scheme. This approach leads to increased viscosity at the interface centerline ($\alpha_1 = 0.5$), and negligible effects outside the vicinity of the interface. Additionally, dead-bands are applied ($\alpha_1 < 0.05$, $\alpha_1 > 0.95$) so that small variations in α_1 in the liquid and gas bulk regions do not affect the viscosity field. In these studies, M_G is set to 20. While this value may seem high, the net effects are primarily to reduce non-physical interface distortions, and possibly to dampen liquid film capillary waves. In Taylor flow, the liquid-gas interface is commonly modeled as a no-shear boundary $\left(\left(\partial u_i/\partial x_j\right)\hat{n}_{int,j} = 0\right)$; therefore, artificially increasing the interface viscosity does not significantly affect the bulk flow. This can be illustrated with the 1-D model problem of fully developed annular liquid-gas counter flow in a vertical tube, which is representative of flow in the bubble-region of a Taylor flow unit cell. In the finite-volume VOF discretization, the governing equation for an annular cell (j) is:

$$0 = -\frac{dp}{dz} A_j + \rho_j g A_j - \tau_j \mathrm{per}_j + \tau_{j+1} \mathrm{per}_{j+1} \tag{3.40}$$

Here, dp/dz is the axial pressure gradient, ρ_j is the average cell density (Equation 3.13), A_j is the cell cross-section area, and per_j and per_{j+1} are the inner and outer cell perimeters, respectively. The cell perimeter shear stresses are evaluated as:

$$\tau_j = \mu_{eff} \frac{u_j - u_{j-1}}{\Delta r} \tag{3.41}$$

Here, μ_{eff} is the cell-face effective viscosity (Equation 3.39), u_j is the cell centered velocity, and Δr is the cell spacing. A zero-gradient condition is applied at the center axis

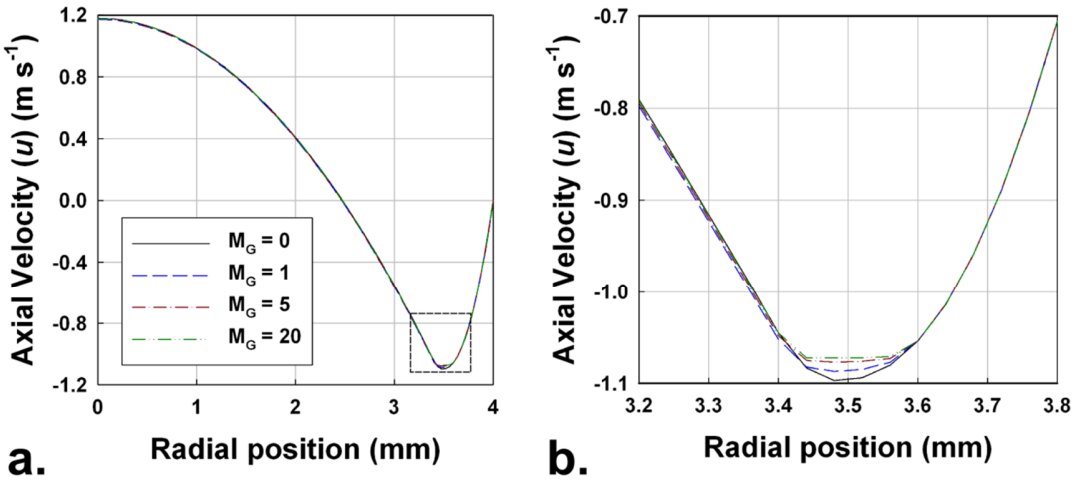

Figure 3.15 – (**a**) Predicted velocity profiles for 1-D annular counter-flow model problem, (**b**) zoomed-in view of interface region

(r = 0) and a no-slip condition is applied at the outer wall (u(r=D/2) = 0). This discretized problem is solved for a representative case of flow in a D = 8.0 mm tube. The axial pressure gradient is set to -175 Pa m^{-1}, ρ_L = 1000 kg m^{-3}, ρ_G = 10 kg m^{-3}, μ_L = 10^{-3} kg m^{-1} s^{-1}, and μ_G = 10^{-3} kg m^{-1} s^{-1}. A wall-wetting liquid film of thickness δ_f = 0.5 mm is specified, and the mesh resolution is set to Δr = 0.04 mm. The interface is modeled as being spread over four cells (δ_{int} = 0.16 mm), which is representative of VOF simulation results. The phase fraction field is thus:

$$\alpha_1(r) = \min\left\{1, \max\left[0, \frac{r-(D/2-\delta_f-\delta_{int}/2)}{\delta_{int}}\right]\right\} \tag{3.42}$$

Velocity profiles from these model problem studies are presented in Figure 3.15 for M_G = 0 (no modification), 1, 5, and 20. For these representative cases, the effect of the interface oscillation damping model is almost entirely confined to the thin interface

region (Figure 3.15b). The liquid downward flow rate only varies from 8.517×10^{-6} m^3 s^{-1} for $M_G = 0$ to 8.488×10^{-6} m^3 s^{-1} for $M_G = 20$ (-0.3%). The gas-phase velocities are slightly more affected, with the centerline velocity varying from 1.79 m s^{-1} for $M_G = 0$ to 1.78 m s^{-1} for $M_G = 20$. A maximum deviation of 0.6% is found for the $M_G = 1$ case ($u(r = 0) = 1.172$ m s^{-1}). Overall, this analysis indicates that the proposed interface oscillation damping scheme can be employed for the full channel length Taylor flow simulations with only minor errors introduced into overall flow behavior.

The overall solution algorithm for the full-channel-length cases is similar to that described in Section 3.2.1 (Figure 3.4). However, the standard CSF surface tension model (Brackbill *et al.*, 1992) is applied instead of the SSF model (Raeini *et al.*, 2012), eliminating one pressure equation solution per time step. Additionally, only one PIMPLE iteration is performed per time step, further reducing computational cost.

3.4.2 Simulation case setups

2D axisymmetric domains were employed for the full-channel-length simulations. The domain geometries were matched to the specific experimental conditions studied in Chapter 2, and include the following three cases: $D = 6.0$ mm and $L = 832$ mm, $D = 8.0$ mm and $L = 823$ mm, and $D = 9.5$ mm and $L = 846$ mm. As in the single unit-cell cases (Section 3.2.2), structured rectilinear meshes were employed with finer cell grading near the channel walls ($\Delta r(r = 0) \sim 10\ \Delta r(r = D/2)$). A schematic of the employed geometries is presented in Figure 3.16. Liquid-phase material properties were set to those of water at 22°C and atmospheric pressure (experimental conditions). The gas-phase density and viscosity were increased to improve numerical stability, following the approach discussed in Section 3.2.2. Material properties are summarized in Table 3.6.

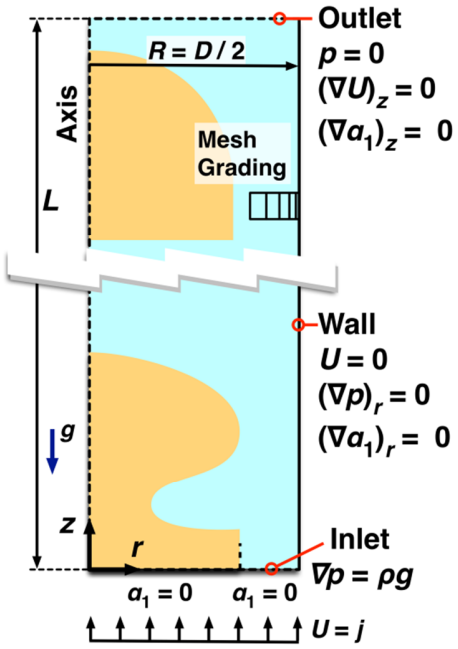

Figure 3.16 – Simulation geometries for full-channel-length simulations

In these studies, the channel inlets were modeled as uniform velocity boundaries ($u_{in} = j\hat{z}$). The inlets were specified to be in the annular flow pattern, with the interface position set such that liquid and gas flow rates match experimental values for the considered cases. The pressure inlet was modeled with a hydrostatic boundary condition ($\nabla p_{in} = \rho g$).

Table 3.6 – Summary of fluid material properties for full-channel-length simulations

ρ_L	998	kg m^{-3}
ρ_G	11.8	kg m^{-3}
μ_L	$9.59 \cdot 10^{-4}$	kg m^{-1} s^{-1}
μ_G	$1.8 \cdot 10^{-4}$	kg m^{-1} s^{-1}

These inlet conditions are different than those employed in the experimental studies. In experiments, liquid flowed into the main channel inlet, and gas was injected through a small port on the side of the tube. However, this configuration cannot be represented in axisymmetric simulations; therefore, axial co-flow was employed instead. Transition to Taylor flow was observed to occur relatively close to the gas inlet port in the experimental studies; therefore, the net effect of inlet flow configuration may be minor for the cases with $L/D \sim 100$. Additionally, in the experimental cases, inlet pressure and gas flow rate were specified (bubble-pump operation) rather than both gas and liquid flow rates. This simulation configuration was attempted, but was found to require very long run times to achieve converged results. Thus, liquid and gas flow rates were specified, and total pressure drop obtained from simulation results.

The channel wall was modeled as a no-slip boundary for the velocity field ($u_{wall} = 0$), and a zero-gradient boundary for the pressure field. The dynamic contact angle model described in Section 3.5.1 was employed as the wall boundary condition for the phase fraction field. The channel outlet was specified as a zero-normal-gradient condition for the velocity and phase fraction fields, and a fixed value boundary for the pressure field ($p_{out} = 0$ Pa (gage pressure)).

The full-channel-length simulation cases are summarized in Table 3.7. These cases were selected to be representative of the range of experimental conditions investigated in Chapter 2. All cases were initialized with representative internal fields from previous simulations, and computations were performed for 10 simulation seconds. Output values were obtained from averaged simulation data from $3 < t < 10$ s. This averaging window was found to be sufficient to obtain well converged results, and represents 2.2 – 4.5

Table 3.7 – Full-channel-length simulation cases

Case	D (mm)	L (mm)	V_G (ml min^{-1})	V_L (ml min^{-1})	∇p_{exp} (Pa m^{-1})
1	6.0	832	354	96	2950
2	6.0	832	543	174	3920
3	6.0	832	708	259	4900
4	8.0	823	614	83	2950
5	8.0	823	779	209	3920
6	8.0	823	708	308	4900
7	9.5	846	708	95	3920
8	9.5	846	850	267	4900

cycles of bubble flow through the channels (i.e., L / U_b = 1.6 – 3.2 s). Reported simulation results include:

- Total channel pressure drop gradient
- Void fraction in the domain regions corresponding to the high speed photography visualization windows in Chapter 2 (D = 6.0 mm: 495 < z < 566 mm, D = 8.0 mm: 495 < z < 583 mm, D = 9.5 mm: 546 < z < 629 mm)
- Taylor bubble rise velocity – measured as the volumetric average of $(1 - \alpha_1)u_z$ above the inlet region (z > 250 mm), averaged over simulation checkpoints collected every 1.0 simulation second (ss)
- Liquid film thickness – measured as the length-average of film thicknesses in the middle axial 50% of Taylor bubbles, averaged over simulation checkpoints.
- Taylor bubble and liquid slug lengths – average of discrete bubble and slug lengths measured in the middle axial 80% above the inlet regions at simulation checkpoints.

- Relative Taylor bubble lengths (β) – averaged over all measured bubble and slug lengths $\left(\beta = \sum L_b \Big/ \left(\sum L_b + \sum L_s\right)\right)$
- Bubble-region frictional pressure gradients – Measured as the bubble-length weighted average of average frictional pressure gradients in the middle axial 50% of bubble regions identified at the simulation checkpoints.
- Combined liquid slug frictional and transition pressure drops – Liquid slug frictional pressure gradients are measured in a manner similar to bubble-region frictional pressure gradients. Extrapolated transition pressure losses are determined using an approach similar to that used for the single unit-cell studies (Section 3.2.2). It is difficult to discriminate between these two pressure drop contributions; therefore, averages of combined pressure drops are reported ($\Delta p_{s,c} = L_s \nabla p_{f,s} + \Delta p_{trans}$).

Sampling uncertainties are reported as 95% confidence intervals around mean values for the Taylor bubble and liquid slug lengths, bubble region frictional pressure gradients, and combined liquid slug frictional and transition pressure drops.

3.4.3 Simulation results and analysis

A validation and grid independence study was first conducted to assess the sensitivity of the full-channel-length simulations to mesh resolution. This analysis focused on the case with: D = 8.0 mm, V_G = 614 ml min^{-1}, and V_L = 83 ml min^{-1} (case 4). Results are summarized in Table 3.8 for simulations with mesh resolutions ($n_r \times n_z$): 17 × 2743, 25 × 4115, 38 × 6331, and 57 × 9460. Experimental results (Chapter 2) and analytical model predictions are also included for comparison.

The proposed analytical Taylor flow model employed in this analysis is summarized as follows. The kinematic and dynamic constraints are first posed (Equations 3.1 – 3.7). Kinematic closure is obtained by incorporating models for Taylor bubble rise velocity (Equations 3.21 – 3.26), liquid film velocity (Equations 3.17 – 3.20), and bubble length (Equation 3.43).

$$\frac{L_b}{D} = 1.813\left\{\exp\left[1.815 - 0.866\left(\frac{U_b}{j}\right)^{2.176}\right]\left(\frac{\alpha}{1-\alpha}\right)^{1.637} + 1\right\} \tag{3.43}$$

Dynamic closure is obtained by incorporating sub-models for frictional pressure gradient in bubble regions (Equations 3.27 – 3.28), frictional pressure gradient in liquid slugs (Equation 3.32), and transition pressure losses using the model of Kreutzer *et al.* (2005) (Equation 3.34).

Representative renderings of bubble trains for the grid independence simulations are presented and compared with an experimental image in Figure 3.17. Similar bubble-profile characteristics are found between the experimental results and simulation cases, with relatively rounded bubble noses and nearly flat bubble tails. Overall, good agreement is found between the simulations, experiments, and analytical model for kinematic quantities (α, U_b, L_b, L_s, β, and δ_f) (Table 3.8). The analytical model predicts slightly reduced bubble length (L_b), and thus β, compared with experiments and simulation results. However, the submodel for L_b has been highlighted as having limited accuracy; therefore, simulation results may be more accurate for this quantity. Simulation results all agree with the experimentally measured δ_f within uncertainty (0.30 ± 0.09 mm), but tend toward the slightly lower analytical model value (0.277 mm) with

Table 3.8 – Grid independence study results for full-channel-length simulations (case 4, D = 8.0 mm, V_G = 614 ml min^{-1}, V_L = 83 ml min^{-1})

Case	∇p (Pa m^{-1})	α	U_b (m s^{-1})	δ_f (mm)	L_b (mm)	L_s (mm)	β	$\nabla p_{f,b}$ (Pa)	$\Delta p_{s,c}$ (Pa m^{-1})
Experiment	2950 ± 80	0.68 ± 0.03	0.29 ± 0.02	0.30 ± 0.09	84 ± 3	19 ± 6	0.893	-	-
Analytic model	2420	0.667	0.305	0.277	71	21	0.769	-1300	14.7
CFD (17 × 2743)	3330	0.626	0.328	0.391	66 ± 9	18 ± 3	0.800	1700 ± 300	20 ± 10
CFD (25 × 4115)	3260	0.619	0.321	0.344	74 ± 10	20 ± 4	0.811	1480 ± 270	40 ± 23
CFD (38 × 6331)	3000	0.642	0.311	0.317	83 ± 15	21 ± 3	0.823	1260 ± 290	34 ± 14
CFD (57 × 9460)	2760	0.677	0.298	0.281	98 ± 17	20 ± 2	0.849	1130 ± 250	28 ± 8

increasing mesh resolution. The liquid film is resolved with 5 – 20 mesh cells in these simulation cases (Figure 3.17). Thus, the incomplete convergence of δ_f indicates that the film mesh resolution criterion of Gupta *et al.* (2009) is insufficient for some cases of Taylor flow.

Simulation results for $\nabla p_{f,b}$ vary significantly with film thickness, but the three higher resolution cases agree with analytical model predictions (1300 Pa m^{-1}) within sampling uncertainty (1210 – 1380 Pa m^{-1}). Simulation sampling uncertainty for $\nabla p_{f,b}$ is relatively high (250 – 300 Pa m^{-1}), even with the large number of sampled bubbles (61 – 74 for each case) due to the wide range of unit-cell lengths. This uncertainty could be reduced with longer runtimes, but was not possible due to limited available computing resources. Similarly, the three highest mesh resolution cases agree for $\Delta p_{s,c}$ to within sampling uncertainty (20 – 36 Pa), but all three over-predict the analytical model value obtained using the Churchill (1977) frictional and Kreutzer *et al.* (2005) transitional pressure drop models (14.7 Pa). However, transitional pressure loss models have been found to only have limited accuracies (Section 3.3). Substantially different predictions are obtained for $\Delta p_{s,c}$ using the models of Dukler and Hubbard (1975) (20.2 Pa) and Fukano *et al.* (1989)

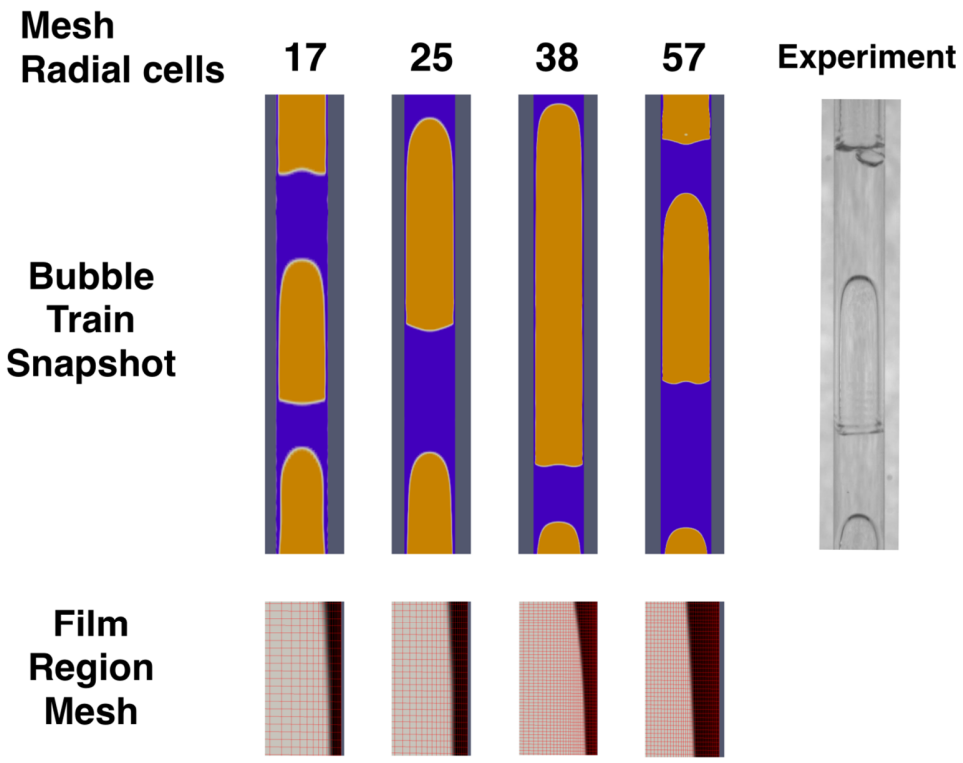

Figure 3.17 – Representative bubble trains from grid independence simulations (air-water flow, D = 8.0 mm, V_G = 614 ml min^{-1}, and V_L = 83 ml min^{-1})

(118 Pa). Similarly, analytical model predictions for overall pressure drop gradient (∇p) vary depending on which transition pressure loss correlation is employed: 2420 Pa m^{-1} (Kreutzer *et al.*, 2005), 2480 Pa m^{-1} (Dukler and Hubbard, 1975), and 3540 Pa m^{-1} (Fukano *et al.*, 1989).

Overall, asymptotic convergence of measured parameters with increasing mesh resolution was not found in this study, despite relatively high spatial resolutions. Such results are commonly encountered in two-phase flow simulations due to the difficulty of resolving the interface discontinuity on a finite mesh (cf. (Subramaniam and Garimella,

Table 3.9 – Comparison of bubble-region frictional pressure gradient between full-channel-length simulations and analytic model

Case	D (mm)	δ_f (mm)		$\Delta p_{f,b}$ (Pa)	
		CFD	Model	CFD	Model
1	6.0	0.273	0.172	805 ± 100	1080
2	6.0	0.320	0.179	1600 ± 230	1120
3	6.0	0.438	0.190	2090 ± 400	1180
4	8.0	0.344	0.277	1470 ± 270	1300
5	8.0	0.461	0.276	1830 ± 380	1290
6	8.0	0.461	0.277	1800 ± 330	1390
7	9.5	0.450	0.333	1590 ± 310	1310
8	9.5	0.529	0.331	1820 ± 320	1310

2009; Tuković and Jasak, 2012)). Still, over the 228% range of spatial resolution from the second (25 × 4115) to the finest mesh (57 × 9460), most measured parameters varied by less than 25%, indicating general convergence. While the finest mesh may yield more accurate results, a coarser mesh (n_r = 25, Δz = 0.2 mm) is employed for the remainder of this section due to limited computational resources.

The proposed bubble-region frictional pressure drop model is compared with full-channel length simulation results in Table 3.9. In general, simulation results yield much higher bubble region frictional pressure gradients than the analytical model. However, the analytical model demonstrated excellent agreement with simulation results in Section 3.3.1. The limited agreement found here is probably due to the meshes being under-resolved in liquid film regions. Thus, these simulations should be repeated with finer meshes in future studies to further evaluate models for $\nabla p_{f,b}$.

Table 3.10 – Comparison of slug-region combined frictional and transition pressure drop between full-channel-length simulations and analytic models

Case	D (mm)	Re_j	L_s (CFD) (mm)	$\Delta p_{s,c}$ (Pa)			
				CFD	Kreutzer *et al.* (2005)	Dukler and Hubbard (1975)	Fukano *et al.* (1989)
1	6.0	1670	5.3 ± 0.5	22 ± 2	23	14	71
2	6.0	2650	12.7 ± 1.8	32 ± 8	41	32	152
3	6.0	3580	10.4 ± 1.6	63 ± 16	63	59	261
4	8.0	1930	20.4 ± 3.7	40 ± 23	15	20	118
5	8.0	2740	15.2 ± 2.4	50 ± 21	24	32	172
6	8.0	2820	21.3 ± 3.1	40 ± 13	25	34	178
7	9.5	1870	22.2 ± 2.8	31 ± 11	10	25	152
8	9.5	2610	24.6 ± 2.9	50 ± 20	16	33	195
AAD				-	41%	25%	297%

Simulation results for total liquid-slug pressure drop ($\Delta p_{s,c}$) are compared with analytical model results in Table 3.10. Here, the slug frictional pressure gradient ($\nabla p_{f,s}$) is predicted using the model of Churchill (1977), and the transition pressure loss models of Kreutzer *et al.* (2005), Dukler and Hubbard (1975), and Fukano *et al.* (1989) are considered. The model of Kreutzer *et al.* (2005) performs relatively well for these cases, yielding an average absolute deviation (AAD) of 0.41. It performs best for the D = 6.0 mm cases (Bo = 4.9), but tends to under-predict pressure drop for the larger diameter cases (Bo = 8.6, 12.2). This behavior can be expected, because the model was developed using capillary-scale simulation data. The model of Fukano *et al.* (1989) leads to over-prediction of pressure drop (AAD = 2.97), as was found in the single unit-cell simulations (Section 3.3.3). The model of Dukler and Hubbard (1975) achieves the best performance (AAD = 0.25), predicting $\Delta p_{s,c}$ within sampling uncertainty for 7 of 8 cases.

3.5 Overall Taylor Flow Model Evaluation

The full proposed model for Taylor flow in the intermediate Bond number regime is evaluated in this section. The overall model formulation presented in Section 3.4.3 is employed here, except that two transitional pressure drop (Δp_{trans}) sub-models are considered. First, the model of Dukler and Hubbard (1975) is employed (Equation 3.35), as it yielded the best performance in the full-channel-length simulations (Section 3.4.3). The model of Kreutzer *et al.* (2005) has been validated for relatively low Reynolds number flows (Re_j < 1500). However, at higher mass fluxes, it predicts low values of Δp_{trans} compared to the inertial-force based models of Dukler and Hubbard (1975) and Fukano *et al.* (1989). Thus, an extended form of the Kreutzer *et al.* (2005) model is proposed that accounts for high mass flux effects.

$$\Delta p_{trans,Extended} = \frac{1}{2}\frac{\rho_L j^2}{Re_j^{2/3} Ca^{1/3}}\left(10.88 + \frac{60}{1+\left(Re_{j,L}/800\right)^{-2}}\right) \tag{3.44}$$

$$Re_{j,L} = \frac{\rho_L j_L D}{\mu_L} \tag{3.45}$$

At low liquid flow rates, the extended model converges to that of Kreutzer *et al.* (2005) (Equation 3.34). The extended model agrees relatively well with the single unit-cell data in Section 3.3.3 (AAD_{log} = 0.24). It yields slightly poorer agreement with simulation results than the original model of Kreutzer *et al.* (2005) (AAD_{log} = 0.20), but outperforms other considered models (AAD_{log}: 0.39 – 0.59). It should be noted that the transition model was fit to obtain agreement with measured liquid flow rates from the experimental study in Chapter 2. Thus, it should not be considered *independently*

validated. Sample calculations for comprehensive Taylor flow model are presented in Appendix Section A.1.

The proposed model formulations are assessed using experimental intermediate Bond number Taylor flow data (Chapter 2). Very unsteady, low-liquid flow rate data points (V_L < 30 ml min^{-1}) are excluded from this analysis. The resulting dataset includes 90 points of air-water flow at ambient temperature and pressure, and spans the ranges of: 4.9 < Bo < 12.2, 1520 < N_f < 3030, and 700 < Re_j < 4460. In dimensional form: 0.009 < j_L < 0.168 m s^{-1}, 0.048 < j_G < 0.542 m s^{-1}, 2950 < ∇p < 4900 Pa m^{-1}. The model is evaluated for the bubble-pump design problem, wherein j_L is predicted for specified j_G and ∇p. This problem has been identified as being significantly more challenging than predicting ∇p (j_L, j_G) (Section 3.1.1). Results from the proposed model formulations are compared to those obtained using representative models from the literature including:

- Sylvester (1987) – A mechanistic model formulated for large Bond number turbulent Taylor flows
- Liu *et al.* (2005) – A collection of sub-models models derived using experimental measurements of capillary-scale Taylor flow. Liu *et al.* (2005) did not propose a specific model for liquid film thickness, but referred to the analytical result of Thulasidas *et al.* (1995) for annular falling film with negligible interfacial shear. This result is thus incorporated here for closure.
- de Cachard and Delhaye (1996) – A mechanistic air-lift pump model for intermediate Bond number Taylor flows (1 < Bo < 14)

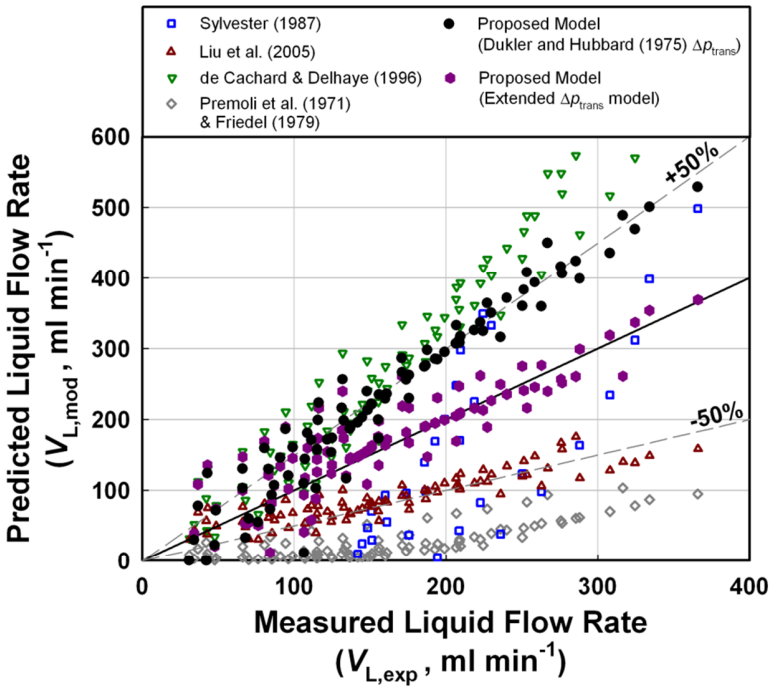

Figure 3.18 – Comparison of predicted liquid pumping rates from proposed Taylor flow model and other models in the literature with experimentally measured values.

- Generic two-phase flow approach – This model employs general purpose void fraction (Premoli *et al.*, 1971) and frictional pressure drop (Friedel, 1979) correlations for closure rather than flow-pattern-specific sub-models.

Predicted liquid flow rates from all considered models are compared with experimental values in Figure 3.18. Results are also summarized in terms of average absolute deviation ($\mathrm{AAD} = 1/n \sum \left| V_{\mathrm{L,mod}} - V_{\mathrm{L,exp}} \right| / V_{\mathrm{L,exp}}$), logarithmic scale (decade) error ($\mathrm{AAD}_{\log} = 1/n \sum \left| \log_{10} \left(V_{\mathrm{L,mod}} / V_{\mathrm{L,exp}} \right) \right|$), and percentages of liquid flow rate predictions within 25% and 50% of experimental values (Table 3.11).

Table 3.11 – Summary of model performances for predicting bubble-pump liquid flow rates

Model	AAD	AAD_{log}	%Error < 25%	%Error < 50%
Proposed model ($\Delta p_{trans,Dukler}$)	52%	0.18	11%	58%
Proposed model ($\Delta p_{trans,Extended}$)	29%	0.10	66%	82%
Sylvester (1987)*	143%	0.48	10%	18%
Liu *et al.* (2005)	44%	0.26	11%	66%
de Cachard and Delhaye (1996)	66%	0.21	13%	29%
Premoli *et al.* (1971) and Friedel (1979)	84%	0.92	0%	1%

*Only 44% of cases converged with the model of Sylvester (1987), AAD_{log} only includes converged cases

These results demonstrate that the proposed mechanistic model for intermediate Bond number Taylor flows with $\Delta p_{trans,Extended}$ yields more accurate liquid flow rate predictions (AAD = 29%) than other representative models from the literature. The formulation with $\Delta p_{trans,Dukler}$ tends to over-predict liquid flow rates, but still performs reasonably well compared with most models from the literature (AAD = 60%). Uncertainty in the model for L_b (Equation 3.43) may lead to incorrect prediction of the frequency of transition pressure drops, and thus the relatively poor performance of the Dukler and Hubbard (1975) model. The proposed hydrodynamic models for $\nabla p_{f,b}$ and $\nabla p_{f,s}$ were only independently validated for $Re_j < 1500$ in Section 3.3, and may also contribute to errors at higher Re_j conditions. Overall, further investigation into sub-models for L_b, $\nabla p_{f,s}$, and Δp_{trans} is warranted, particularly for transitional and turbulent flows in the intermediate Bond number regime.

The model of Sylvester (1987) achieves poor accuracy for liquid flow rate predictions (AAD = 143%), and only converges for 44% of the considered cases. For many of the cases that do converge, the relatively high predicted inter-phase slip resulting from the

large Bond number drift flux result ($U_b = C_0 j + \Gamma\sqrt{gD}$, with Γ = 0.35) leads to low predicted liquid pumping rates. For other cases, the assumed long liquid slugs (L_s/D = 24) lead to under-prediction of transition pressure drop frequency, and thus high liquid pumping rates. These results indicate that large Bond number turbulent flow results are not generally applicable in the intermediate Bond number regime.

The capillary scale model of Liu *et al.* (2005) leads to fair agreement with experimental results (AAD = 44%), but generally under-predicts liquid flow rates. This can be attributed in part to the proposed pressure drop correlation of Liu *et al.* (2005), which yields very high dynamic pressure drops. For the considered experimental cases, the model of Liu *et al.* (2005) yields P^* (∇p_d / ∇p_{hs}) values ranging from 0.51 – 2.00. In the proposed model with ($\Delta p_{trans,Extended}$), P^* ranges from –0.22 – 0.49. Furthermore, capillary scale models assume reduced distribution effects for the bubble rise velocity (low C_0) and negligible drift fluxes (Γ = 0). These assumptions lead to prediction of reduced inter-phase slip at intermediate and large Bond numbers, and thus, overprediction of liquid flow rates.

The air-lift pump model of de Cachard and Delhaye (1996) was intended for conditions similar to those considered in the present investigation, but still yields relatively high errors (AAD = 66%). In general, the model of de Cachard and Delhaye (1996) overpredicts liquid flow rates. This occurs, in part, because it assumes a low bubble rise velocity distribution parameter, representative of fully turbulent, large Bond number flows (C_0 = 1.20). This leads to reduced inter-phase slip than with the higher laminar-to-transitional result for C_0 (1.20 – 2.29) expected for many cases in this study.

Additionally, the employed turbulent liquid slug friction factor ($f_s = 0.316\,\mathrm{Re}_j^{-0.25}$) leads to low pressure drop predictions for low Re_j cases. Finally, the model of de Cachard and Delhaye (1996) does not account for transitional pressure drops, which contribute an average of 18% of total pressure drop in the proposed model (with $\Delta p_{\mathrm{trans,Extended}}$) in this study, and reach 44% in some cases.

The generic two-phase flow modeling approach leads to large error in predicted liquid flow rate (AAD = 84%), and generally under-predicts liquid flow rates. This occurs primarily because the two-phase frictional pressure drop model (Friedel, 1979) only yields positive ∇p_{d} values ($0.01 < P^* < 0.25$).

This analysis demonstrates that the proposed Taylor flow model with $\Delta p_{\mathrm{trans,Extended}}$ is accurate in the intermediate Bond number regime for laminar to turbulent flows ($700 < \mathrm{Re}_j < 4460$). The analysis of other models highlights the sensitivity of liquid flow rate predictions to selection of closure sub-models. It is critical to ensure that all relevant phenomena are modeled (e.g., transition pressure drops) and that employed sub-models are applicable for conditions of interest.

3.6 Discussion

In this investigation, Taylor flow simulations were performed over a wide range of conditions in the intermediate Bond number regime. Results were applied to inform and validate hydrodynamic sub-models for bubble-region frictional pressure drop gradient ($\nabla p_{f,b}$), slug frictional pressure drop gradient ($\nabla p_{f,s}$), and flow transition pressure loss ($\Delta p_{\mathrm{trans}}$). Close agreement with single unit-cell simulation results was obtained with a model for $\nabla p_{f,b}$ that accounts for channel curvature and liquid-to-gas interfacial shear

(AAD = 1.9%). However, only fair agreement was found with full-channel-length simulations at intermediate mesh resolutions ($n_r \times n_z = 25 \times \sim 4100$). A mesh sensitivity study was conducted, and results indicate that these meshes may have been under-resolved in film regions, contributing to this disagreement. Additionally, these results indicate that the film-region mesh criterion of Gupta *et al.* (2009) (5 spanning cells) may be insufficient in some cases. For the highest resolution case in the mesh sensitivity analysis ($n_r \times n_z = 57 \times 9460$ for case 4 in Table 3.7), close agreement with experimental results was obtained. Most evaluated quantities matched experimental values to within measurement and sampling uncertainty (α, δ_f, U_b, L_b, L_s, see Table 3.8), and small discrepancies were found for other quantities (6% for ∇p and 5% for β). Simulations for the other full-channel-length cases at this significantly higher mesh resolution would thus be valuable, and probably consistent with experimental results. However, such studies are computationally expensive, scaling approximately as $O(j\Delta r^{-3})$ for these 2D unsteady flows. Increasing radial mesh resolution from $n_r = 25$ to 57 incurs an approximately twelve-fold increase in computational cost.

Fully developed laminar channel flow frictional pressure drop results agreed relatively closely with single unit-cell simulation data (AAD = 28%). However, this result is somewhat counter-intuitive for the short liquid slugs considered in simulations ($2.5 < L_s / D < 6.1$). Future investigations to characterize and formulate modeling approaches for developing flow effects in short liquid slugs are thus warranted. The challenge here arises from the complex annular inlet pattern from liquid film to liquid slug regions, which is affected by Taylor bubble tail profiles (e.g., convex, flat, or skirted tails, see Figure 3.9) and wake region flow patterns (see Figure 3.11).

A number of mechanisms have been proposed for Taylor flow transition pressure loss, including capillary forces (Bretherton, 1961), combined capillary and inertial effects (Kreutzer *et al.*, 2005), liquid-film flow reversal (Dukler and Hubbard, 1975), and liquid-film flow stagnation (Fukano *et al.*, 1989). The model of Kreutzer *et al.* (2005) yielded the closest agreement with single unit-cell simulation data for $\mathrm{Re}_j < 1340$ (AAD = 53%). The model of Dukler and Hubbard (1975) performed best in the full-channel-length simulation studies for $1670 < \mathrm{Re}_j < 3580$ (AAD = 0.25). However, both models tend to under-predict pressure drop (over-predicting V_L) for the experimental data considered in Section 3.5. An empirical model was proposed to extend the applicability of the Kreutzer *et al.* (2005) model to high mass flux conditions (Equations 3.44 – 3.45). This model performed well for the considered experimental data set, but has not been independently validated.

A map of transition pressure drop models with axes of superficial Reynolds number (Re_j) and Bond number (Bo) is presented in Figure 3.19. Approximate bounding regions of successful model applications are reported, with representative references indicated in parentheses. These should not be considered to be strict regions of model validity, because transition $\Delta p_{\mathrm{trans}}$ predictions have not been independently validated in most studies. In some cases, different modeling studies have reported success at similar conditions with $\Delta p_{\mathrm{trans}}$ formulations that deviate substantially (e.g., for $500 \leq \mathrm{Re}_j \leq 5000$ and $1 \leq \mathrm{Bo} \leq 10$). The proposed extended formulation of Kreutzer *et al.* (2005) converges to the results of Kreutzer *et al.* (2005) and Bretherton (1961) at reduced Re_j and Bo, and it yields overall Taylor flow model success at higher Re_j (5,000 – 70,000) in Chapters 4, 6, and 7 of this thesis. However, it is unclear how to best reconcile this model with that of

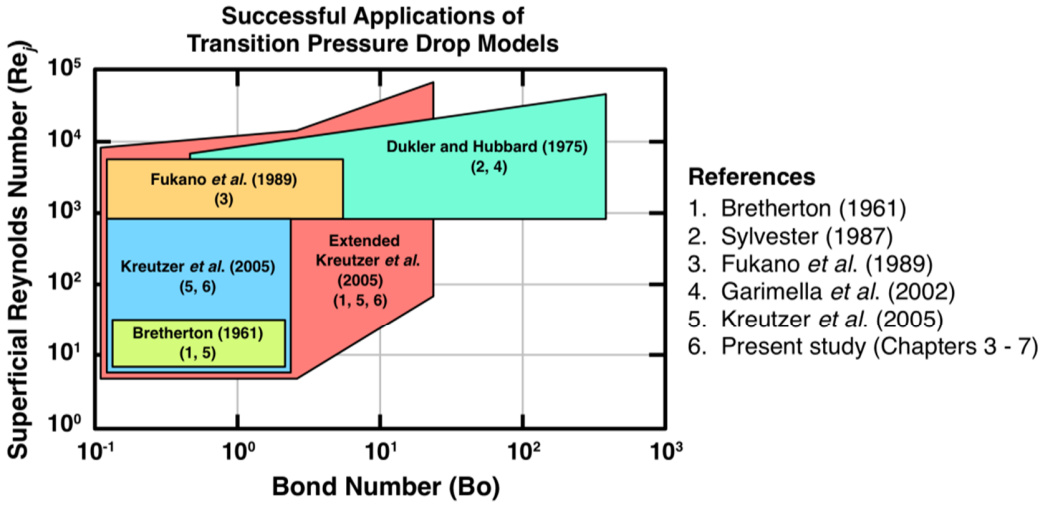

Figure 3.19 – Map of ranges of successful application of different Taylor flow transition pressure drop models. References for model applications are numbered in parentheses.

Dukler and Hubbard (1975) at high Bo. Appropriateness at low-Re high-Bo conditions is also unknown. Future investigations to clarify the mechanisms of transition pressure loss over widely varying flow conditions are thus needed to formulate a robust and universal approach for predicting Δp_{trans}.

Accurate prediction of L_b (or L_s) is a compounding factor in accounting for transition pressure losses, because the net effect in channel flow is $\nabla p_{trans} = \Delta p_{trans} / (L_b + L_s)$. Thus, even if accurate models can be formulated for Δp_{trans}, errors in unit cell length may lead to poor overall flow characterization. A model was proposed for L_b in the intermediate Bond number regime based on the experimental data of Chapter 2 (Equation 3.43, AAD = 22%). However, general validity of this model is unknown. Therefore, further studies to refine models for Taylor flow unit cell lengths are warranted.

Overall, good agreement was found between simulation and experimental and analytical results for key flow quantities such as liquid film thickness (Figure 3.8a), bubble region frictional pressure gradient (Figure 3.10), and many full channel-flow properties (e.g., α, β, U_b, Table 3.8). However, asymptotic convergence with increasing mesh resolution was not found in all cases, and oscillatory convergence was found for some parameters (see Tables 3.3 and 3.8). These challenges were discussed in Section 3.4.3, and can be attributed to the difficulty of resolving continuum mechanics phenomena with sharp discontinuities. One limitation of the employed VOF-based simulation approach is that, for a given flow, it will capture the liquid-gas interface with a similar number of cells (typically 3 – 5, depending on the interface compression strength c_α), regardless of the mesh resolution. Thus, mesh refinement can increase apparent interface sharpness, but cannot improve resolution of property transitions across the interface.

In future studies, it may be valuable to explore alternate simulation formulations. For example, a level-set based formulation could be adopted that assumes a finite interface thickness. Such an approach could be expected to have good convergence properties because the number of cells resolving the interface would increase if the mesh were refined. Alternatively, an interface-tracking moving-mesh approach could be employed (such as that of Tuković and Jasak (2012)), in which the liquid-vapor interface coincides with mesh cell boundaries, eliminating the need to resolve the interface over multiple cells.

The present investigation has employed laminar flow simulations. However, intermediate Bond number Taylor flows can occur over a range of laminar-to-turbulent

flow conditions. While mature eddy viscosity models have been developed for fully turbulent flows (e.g., k-ε, k-ω), the applicability for two-phase VOF simulations is unclear. However, these models have been employed in previous Taylor flow simulation studies (Taha and Cui, 2006). Additionally, for many Taylor flows in the intermediate Bond number regime, turbulent conditions may only arise in liquid slug regions. In the experimental cases considered in Section 3.5, the liquid slug Reynolds numbers (Re_j) approach 4460, however the bubble Reynolds numbers (Re_b) are less than 430, and the liquid film Reynolds numbers are less than 660 ($\mathrm{Re}_f = 4\rho_L U_f \delta_f / \mu_L$, $\mathrm{Re}_{f,crit}$ ~ 1600). Intermittency transport models have been proposed for single-phase flows with localized turbulence (Menter *et al.*, 2004), but formulations for two-phase flows are limited. It would be more appropriate to apply LES or DNS techniques for these conditions. Such approaches require 3D simulations, and would necessitate resolution of greater ranges of spatial and temporal scales. The bubble coalescence process in Taylor flow has been identified as inherently 3D for some flow conditions (Anglart and Podowski, 2002). Thus, it may be necessary to perform 3D simulations even for laminar full-channel-length studies.

The simulations and modeling approaches adopted here assume 2D axisymmetric Taylor flow. However, asymmetric wavy films (Figure 2.5a) and bubble tail profiles (Figure 2.7c) were observed in some cases in the accompanying experimental studies (Chapter 2). Asymmetric film profiles could result in increased inter-phase slip, permitting greater liquid drainage rates around rising Taylor bubbles, and reduced performance in gas-lift pump applications. Similarly, in practical applications, channels may be slightly inclined, resulting in 3D flow effects as bubbles distort and rise along the

upper surface (Taha and Cui, 2006). A recent investigation by Behafarid *et al.* (2015) demonstrated the potential for film dryout in inclined channels of non-wetting materials. Modeling of contact-line mechanics would be critical in these cases. Evaluation of such phenomena is beyond the scope of the present investigation, but this discussion highlights the breadth of open research questions in the fields of two-phase and Taylor flow.

3.7 Conclusions

This investigation focused on formulation of hydrodynamic closure models for Taylor flow in the intermediate Bond number regime. Simulation approaches were developed based on the interFoam algorithm to directly simulate two phase-flow at these conditions. Cyclic single unit-cell axisymmetric simulations were conducted over a wide range of flow conditions: $6.6 < (L_b + L_s) / D < 15$, $0.540 < \beta < 0.650$, $5 < Bo < 20$, $250 < N_f < 1000$, and $20 < Re_j < 1500$. Results from these 45 simulations were applied to independently evaluate models for: bubble-region frictional pressure gradient ($\nabla p_{f,b}$), liquid slug frictional pressure gradient ($\nabla p_{f,s}$), and transition pressure loss (Δp_{trans}). A simple model was proposed for $\nabla p_{f,b}$ that accounts for channel curvature and interfacial shear, and close agreement with simulation results was found (AAD = 1.9%). For the considered flow conditions ($Re_j < 1340$), fully developed laminar channel flow frictional pressure drop results were found to be relatively accurate for prediction of $\nabla p_{f,s}$ (AAD = 28%). A number of transition pressure loss models were also evaluated, and the formulation of Kreutzer *et al.* (2005) yielded the closest agreement with the single unit-cell simulation data (AAD = 53%).

Full channel-flow simulations were also conducted to evaluate the proposed hydrodynamic models under more realistic conditions with interacting unit-cells of

varying lengths and characteristics. Due to limited computational resources, simulation meshes were under-resolved in film regions. Thus, the proposed sub-model for $\nabla p_{f,b}$ could not be rigorously evaluated in these conditions. The proposed combined Churchill (1977) and Dukler and Hubbard (1975) model for slug-region dynamic pressure drop ($\Delta p_{s,c}$) was found to agree well with full channel-simulation results (AAD = 25%).

The complete set of proposed kinematic and hydrodynamic closure models for intermediate Bond number Taylor flow was evaluated using experimental data reported in Chapter 2. A formulation for Δp_{trans} was proposed to extend the applicability of the Kreutzer *et al.* (2005) model to high mass flux conditions. With this sub-model, predicted liquid flow rates agree relatively well with experimental results (AAD = 29%).

Overall, this investigation demonstrated independent validation of Taylor flow hydrodynamic sub-models over a large range of the intermediate Bond number regime. However, many open questions remain about Taylor flow mechanics. Critical challenges for future Taylor flow research include description of developing flow in liquid slugs, identification of flow-transition pressure loss mechanisms, and characterization of turbulence effects, particularly at transitional Reynolds numbers.

CHAPTER 4. COUPLING-FLUID HEATED BUBBLE PUMP GENERATORS: EXPERIMENTS AND MODEL DEVELOPMENT

4.1 Introduction

4.1.1 Overview

Conventional two-pressure absorption systems enable low-grade- or waste-heat activated cooling and heat pumping. However, the fundamental need for a solution pump limits implementation to settings with electrical infrastructure or available mechanical input. Additionally, the solution pump is often the primary point of failure. Single pressure absorption technology, such as the diffusion absorption refrigeration (DAR) (von Platen and Munters, 1928) and Einstein-Szilard (1930) cycles, address these limitations as fully thermally activated alternatives. These single-pressure systems are particularly attractive for applications such as medicine and vaccine refrigeration in developing countries and engine waste heat recovery in environments where even small electrical consumption for a solution pump in a conventional two-pressure absorption system is untenable.

While single-pressure absorption systems do not require complex hardware to pressurize the working fluid, mechanisms for circulating fluid are still needed for the operation of the heat and mass transfer components. The conventional approach for circulating absorbent solution has been to use a spot-heated bubble-pump generator (BPG) – a vertical tube in which intense localized heat from a flame or electrical heater near the base desorbs refrigerant vapor from solution, and the buoyancy of rising refrigerant bubbles lifts solution to an upper reservoir, which feeds the liquid flow through other system components.

This chapter is adapted from an accepted manuscript of an article published in Science and Technology for the Built Environment online (Rattner and Garimella, 2015a), available online: http://www.tandfonline.com/doi/full/10.1080/10789669.2015.1004978

In practice, BPG design for absorption systems has been a trial-and-error process, primarily due to the limited information that has historically been available for two-phase flows in the intermediate Bond number conditions typically employed ($5 \lesssim \mathrm{Bo} \lesssim 40$, $\mathrm{Bo} = \left(\rho_L - \rho_G\right) g D^2 / \sigma$). These flow conditions occur between the comparatively well characterized capillary/microchannel ($\mathrm{Bo} \lesssim 5$) and inertial/conventional ($\mathrm{Bo} \gtrsim 40$) scales (Reinemann *et al.*, 1990). Furthermore, while spot-heated BPGs offer a conceptually simple approach to refrigerant separation and fluid circulation, these devices necessitate a source of chemical fuel or high-grade energy to transfer sufficient heat over a small area. Thus, spot-heated BPGs cannot be employed in waste-heat recovery applications or many remote settings.

A schematic of a BPG connected to a liquid feed reservoir is presented in Figure 4.1. The main objective in bubble-pump design is to predict the liquid flow rate (V_L) given the tube diameter (D), the submergence ratio $S_r = H_{res} / H_{BP}$ (or the total pressure gradient $\Delta P_{net} / H_{BP}$), gas flow rate (or supplied generator heating $Q_{BPG} = \dot{m}_V i_{LV}$), and fluid properties.

BPGs are usually designed to operate in the Taylor flow regime, indicated schematically in Figure 4.1, in which elongated (Taylor) bubbles are separated by liquid slugs. Detailed discussions and reviews of prior work on Taylor flow can be found in Chapters 2 and 3. The Taylor flow pattern is desirable for bubble pump operation because liquid only flows downward in the thin films around the rising elongated bubbles, leading to low overall inter-phase slip. In general, raising the liquid reservoir level (H_{res} and S_r) increases the liquid flow rate, but reduces the available hydrostatic head driving flow

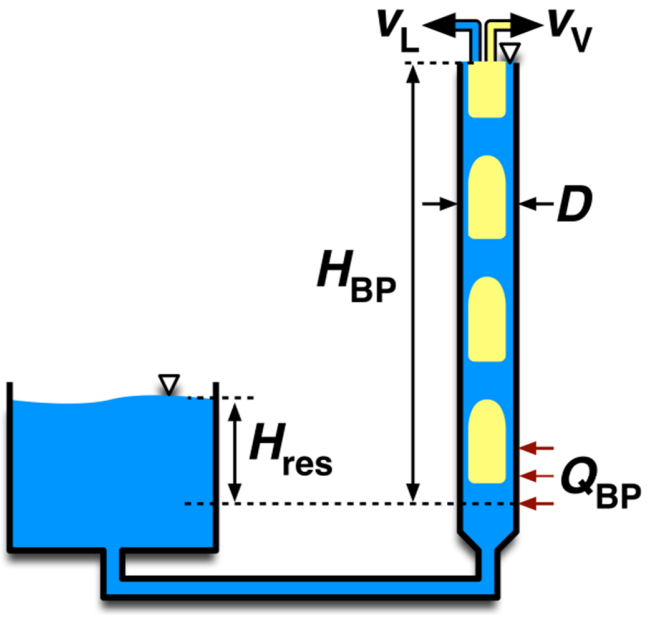

Figure 4.1 – Schematic of a bubble pump generator

through other system components. Liquid flow rates tend to increase with vapor flow rate (V_V or Q_{BPG}) up to a critical point, beyond which frictional resistance limits additional pumping. Finally, increasing the tube diameter lowers frictional resistance to flow, but may permit greater inter-phase slip, and thus has a complex effect on the liquid pumping rate.

4.1.2 Prior work

The earliest investigations directly applicable to BPG design focused on air-lift pumps, such as the modeling and experimental study by Stenning and Martin (1968) for 25 mm diameter tubes (Bo ~ 85). In these devices, gas is injected into the bottom of submerged tubes to entrain and lift liquid. Target applications include well dewatering and sediment removal (without risking damage to turbomachinery). While air-lift pumps superficially resemble BPGs, they have usually been considered with greater Bond

numbers and greater submergence ratios ($S_r \gtrsim 0.5$) than employed in absorption system BPGs ($S_r = 0.2 – 0.5$ (Almen, 2007)).

Reinemann *et al.* (1990) expanded on the air-lift pump studies of Stenning and Martin (1968), and investigated the effects of surface tension and reduced Reynolds numbers ($\mathrm{Re}_j = \rho_L jD/\mu_L < 8{,}000$) for intermediate Bond number flows (5 < Bo < 50). The authors reported good agreement between their experimental results and extended analytical model, except for submergence ratios below 0.7. The applicability to bubble pumps in absorption systems, which generally operate at lower submergence ratios, is thus unclear.

de Cachard and Delhaye (1996) also performed experimental investigation and modeling of air-lift pumps (1 < Bo < 14). Their proposed model was more robust than in earlier studies, accounting for surface tension and viscous effects on Taylor bubble rise velocity, the transition from laminar to turbulent falling liquid films, and the Taylor-to-churn flow transition. However, as in the study of Reinemann *et al.* (1990), this study focused on higher mass-flux flows than typically found in bubble pumps.

Delano (1998) adapted the model of Stenning and Martin (1968) to investigate the BPG in the Einstein-Szilard refrigeration cycle. For closure, his model incorporated an empirical slip ratio correlation (Griffith and Wallis, 1961), and assumed fully-developed laminar-flow frictional pressure drop in rising liquid slugs. Delano (1998) found that a relatively large frictional pressure drop correction had to be added to match experimental results for air-water flow in an 8.6 mm tube (Bo = 10).

Schaefer (2000) and White (2001) investigated five alternative closure formulations for the bubble pump model of Delano (1998), and were able to achieve improved agreement between model predictions and experimental data in some cases. Results from these investigations highlight the difficulty of modeling two-phase flow behavior in the intermediate Bond number conditions usually employed in BPGs, because the numerous closure formulations available in the literature lead to significantly different results. The high sensitivity of Taylor flow model predictions to the selection of individual closure sub-models was similarly demonstrated in Chapter 3.

van der Walt (2012) conducted a BPG modeling study, and incorporated flow-boiling heat transfer correlations to predict the developing flow in the short generator region. This model was compared to others reported in the literature, and substantial variations between predicted pressure drops were found. Belman-Flores *et al.* (2014) formulated a BPG model, and predicted the effects of varying configuration and operating parameters on the performance of a commercially available DAR system.

Pfaff *et al.* (1998) conducted an experimental investigation of spot-heated bubble pumps (10 – 14 mm diameter, Bo not available) with water-lithium bromide working fluid, an actual refrigerant-absorbent pair employed in absorption refrigeration systems. Pfaff *et al.* (1998) developed a simplified BPG model that did not account for frictional losses, and found experimental and predicted liquid flow rates to agree to within approximately 30%. Chan and McCulloch (2013) refined the model of Pfaff *et al.* (1998), and accounted for heat loss from the BPG. Their proposed model was validated with atmospheric pressure steam-water experimental data for high submergence-ratio conditions ($S_r = 0.5 – 0.8$, $6 < \text{Bo} < 23$).

Koyfman *et al.* (2003) performed experimental spot-heated bubble-pump investigations with R-22 at elevated pressures (250 kPa) using a 9 mm diameter bubble tube (Bo = 72). Heat was transferred from a coupling fluid through a small coiled copper tube around the base of the BPG. This approach represents an alternative to gas heating, but the relatively limited heat-transfer area still necessitated a high-temperature thermal source for operation.

Jakob *et al.* (2008) designed and fabricated a vertical shell-and-tube coupling-fluid-heated BPG for a residential-scale (2.5 kW cooling) DAR air-conditioning system. This approach employs the full outside area of the BPG tubes for heat transfer, enabling operation with relatively low-temperature- or waste-heat sources. Because vapor generation is distributed along the whole length of this BPG design, liquid pumping rates were lower than if all vapor generation occured at the base. Jakob *et al.* (2008) described five design iterations, attesting to the difficulty of designing a BPG to operate in this distributed heating mode. Detailed BPG models and performance results were not reported.

Dammak *et al.* (2010), conducted a modeling study of an inclined full-length heated BPG that could be integrated into a flat-plate solar collector. Their BPG model was based on the approach of White (2001), and accounted for the effects of component inclination. Such a design could enable passive solar-activated refrigeration, provided that sufficiently high generator temperatures can be achieved with a flat-plate collector. Analysis of such full-length heated BPGs introduces additional challenges, because the liquid and vapor flow rates and patterns evolve along the entire tube length, and are not established at the inlet as is usually assumed for spot-heat heated configurations.

Benhimidene *et al.* (2011) also conducted a modeling study of a full-length uniformly heated BPG. Void fraction results were compared to those obtained with other models in the literature, but liquid pumping predictions were not validated.

Garma *et al.* (2014) performed an Eulerian-Eulerian two-phase simulation of BPG flow. This study was conducted on a 2D axisymmetric mesh geometry, and well-established interfacial transport and wall boiling models were employed. Results were reported for uniform full-length heating and for spot-heating in the lower third of the domain. Jo *et al.* (2014) also performed Eulerian-Eulerian 2D axisymmetric simulations of full-length uniformly heated BPGs. Mesh independence was demonstrated, and results were compared with data from experimental studies and other flow-boiling simulations. Liquid pumping rate predictions were compared with those from the 1-D modeling study of Benhimidene *et al.* (2011), and significant variations were found. However, as discussed in Section 3.1.2.2, the two-fluid Eulerian-Eulerian simulation approach may not be appropriate for intermittent flow patterns, such as Taylor flow. A more comprehensive review of BPG technologies and investigations can be found in Benhimidene *et al.* (2010).

4.1.3 Present investigation

A number of investigations of spot-heated BPGs have been published. Jakob *et al.* (2008) performed one of the only experimental studies of BPGs that are heated along the entire component length. However, no flow models or detailed experimental measurements were reported for this configuration, which is crucial for harnessing low-temperature heat sources. Modeling and simulation studies of uniformly heated BPGs have been conducted, but experimental validation of pumping rate predictions has not yet

been achieved. More complicated BPG heating profiles, such as those that may occur with heat transfer from a coupling fluid, have not been explored.

Additionally, there are significant variations between bubble-pump models in accounting for surface tension effects, reduced Reynolds numbers, and frictional pressure drops. None of the models discussed here account for pressure drop due to flow transitions between the Taylor bubble and liquid slug sections, which can have a large effect on flow behavior if individual bubble-slug unit cells are relatively short (Chapter 3). Additionally, previously published bubble-pump models incorporate sub-models for Taylor bubble rise velocity (U_B), falling-film thickness (δ_F), and liquid slug length (L_s) that were developed for either large Bond number (Bo $\gtrsim$ 40) or capillary-scale flows (Bo $\lesssim$ 5). Closure sub-models validated for intermediate Bond number Taylor flow parameters have only recently been reported (Chapters 2 and 3).

In the present study, detailed experimental investigations are conducted for a full-length coupling-fluid-heated water-steam 7.8 mm tube inner diameter bubble pump (Bo = 9.7). The tube inner diameter and operating conditions are selected to be representative of bubble pumps studied in the literature (Almen (2007): D = 3 – 5 mm and Bo ~ 2 – 6, Delano (1998): D = 8.6 mm and Bo = 10, Pfaff *et al.* (1998): D = 10 – 14 mm (Bo not available)). A parametric study is conducted to determine the influence of heating rate, submergence ratio, and coupling-fluid inlet temperature on BPG operation. The effects of BPG working-fluid inlet subcooling are also studied.

A mechanistic coupled fluid-flow and heat-transfer model is developed for the BPG investigated here, and is validated with experimental results from this study. The model

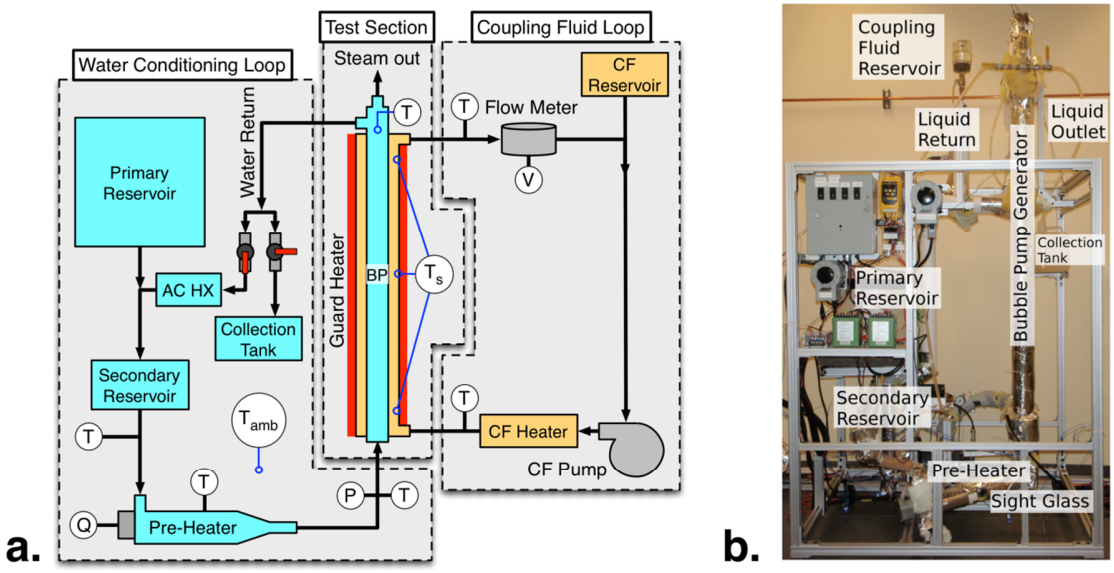

Figure 4.2 – Schematic (**a**) and labeled photo (**b**) of coupling-fluid heated bubble-pump facility

accounts for the effects of Taylor bubble diameter, liquid film and slug frictional resistances, flow-transition pressure drop, and acceleration pressure drop as steam is generated. Independently validated sub-models from Chapters 2 and 3 are adopted for closure. The heat-transfer model incorporates single-phase convective transport on the coupling-fluid side and subcooled and saturated flow boiling on the working-fluid side.

4.2 Experimental Facility and Procedure

An experimental facility was fabricated to study the full-length coupling-fluid heated BPG under investigation. The facility is divided into three main sections (Figure 4.2): the water conditioning loop, coupling fluid (CF) loop, and BPG test section.

4.2.1 Water conditioning loop

Distilled water is stored in a primary reservoir tank, which establishes the operating submergence ratio. A large diameter (0.38 m) reservoir is employed to reduce

fluctuations in the submergence ratio during experiments. The water flow from the primary reservoir is mixed with hot return water from the air-coupled heat exchanger, if available. This mixture flows to a small secondary reservoir (300 ml), which acts to reduce temperature fluctuations in the flow entering the pre-heater. The temperature of the cool outlet flow from the secondary reservoir is measured, and the flow continues through insulated hose to the water pre-heater. All temperature measurements are performed using calibrated T-type thermocouples (± 0.25 K uncertainty).

The water pre-heater is insulated, and contains a 1,000 W element, which is activated using an OMEGA® CNi3254 process PID controller. Sight glasses are installed in the pre-heater section, and were periodically checked to ensure that steam bubbles were not generated, which could have affected the BPG operation. In practice, the temperature controller cannot be set above 96°C without initiating bubble generation; therefore, the water entering the test section is subcooled. The test-section inlet temperature generally ranges from 89.2 – 95.2°C (4 – 10 K less than the saturation temperature), but is lower for the lowest flow-rate cases. This is representative of conditions in a full absorption system, where heat loss and imperfect heat recovery in a solution heat exchanger would lead to liquid subcooling at the BPG inlet. The heater power output is measured with an averaging watt transducer (Ohio Semitronics, Inc. model PC5-010EY25, ± 5 W uncertainty), which is used in conjunction with the temperature rise across the heater section and an estimated heat loss rate to infer the water flow rate at the test section inlet. No-flow tests were conducted, and a thermal resistance of approximately 2.2 K W^{-1} was measured between the pre-heater and ambient. This led to a typical heat loss rate of 20 W over the operating range of 60 – 700 W of input.

Temperature and pressure measurements are collected for the water flow 135 mm (± 5 mm) below the start of the heated BPG section to determine inlet conditions and effective submergence ratios. The pressure is measured with a differential pressure transducer (OMEGA® MMDWU2.5C1P4D0T2A3, 17.2 kPa range, ± 0.035 kPa uncertainty).

Outlet water from the BPG test section can be diverted to either a collection tank or the air-coupled heat exchanger. The collection tank can be weighed before and after experimental runs (digital scale, ± 1 g uncertainty) to determine an average liquid pumping rate with high accuracy (< 2 ml min^{-1} uncertainty). It is used for cases with lower water flow rates ($\lesssim$90 ml min^{-1}), when the pre-heater has sufficient power to bring relatively cool water from the primary reservoir close to T_{sat} (99.2°C for water at the local elevation of 320 m where p_{amb} = 98.6 kPa).

At higher flow rates, the pumped water is recirculated, and its flow rate is inferred from an energy balance over the pre-heater section. The air-coupled heat exchanger is used to slightly cool the recirculated pumped water, leading to a greater temperature rise through the pre-heater, and thus a reduced uncertainty in the inferred flow rate (± 2 – 6 ml min^{-1}). Conventional flow meters were not employed in the water conditioning loop due to the strict pressure drop limits in this passively driven system.

Ambient-air temperature is also measured during experiments, and is employed to estimate heat loss rates from the pre-heater.

4.2.2 Coupling fluid loop

The single-phase coupling fluid (CF) loop is fed from an ambient-pressure reservoir. The fluid is circulated with a variable-speed-drive gear pump, and is electrically heated to operating temperatures. Temperature measurements are collected at the CF inlet to and outlet from the BPG test section. The coupling-fluid flow rate is measured using a positive-displacement gear flow meter (AW Lake JVM-12KG, ± 0.3 ml min^{-1} uncertainty). These temperature and flow rate measurements are used in conjunction with estimated heat loss rates to infer the net heat transfer rate to the BPG test section.

In this investigation, Paratherm NF®, a mineral-oil based heat transfer fluid, is selected as the CF. Thermophysical fluid properties reported by the Paratherm Corporation (2013b) are employed.

4.2.3 Bubble-pump generator test section

The BPG test section is a co-flow upward tube-in-tube heat exchanger with boiling steam flow in the inner tube (ID = 7.8 mm), and coupling-fluid flow in the annulus ($D_{a,i}$ = 9.5 mm, $D_{a,o}$ = 10.9 mm). The inner steam tube extends 1.7 m above the start of the CF heated section. The lower 1.55 m of the steam tube is heated by the CF, and the remaining 0.15 m extend into a phase-separating settling vessel (Figure 4.3a). This tube length was selected to yield maximum heat-transfer area with the coupling-fluid channel (0.046 m^2) without significantly extending overall system dimensions for typical applications (e.g., a residential-scale refrigerator).

Conventional insertion-type thermocouples are installed in the liquid pool and at the steam outlet of the phase separator. To avoid disturbing the flow, fine thermocouple wire (40 AWG, 0.33 mm OD) is used to measure the outlet flow temperature from the steam

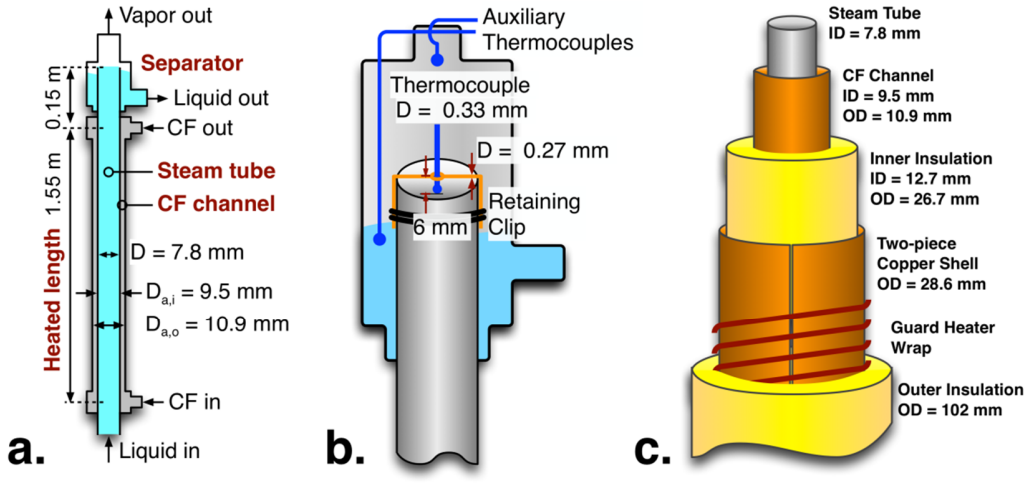

Figure 4.3 – **a**. Test section dimensions, **b**. Schematic and instrumentation of steam tube outlet and separator, **c**. Test section insulation and guard heater configuration

tube. This thermocouple wire is installed about 6 mm down the central axis from the top of the steam tube, and is held in place with a fine wire (30 AWG, 0.27 mm OD) (Figure 4.3b).

To minimize heat loss from the test section, an electrical guard heater configuration is employed. The coupling-fluid annulus outer tube (OD = 12.7 mm) is wrapped with 7 mm thick fiberglass insulation, which is covered with two half-pieces of axially cut copper tube (ID = 26.7 mm, OD = 28.6 mm). The two-piece copper shell provides structure around the insulation, and helps spread heat from the guard heater wire coiled around it. Three surface thermocouples are installed along the copper shell (near the bottom, at the middle, and near the top). The whole assembly is insulated with a 102 mm OD fiberglass jacket. Coupling-fluid only (no steam flow) tests were conducted, and a thermal resistance of approximately 1.1 K W^{-1} was measured between the coupling fluid and

copper shell, leading to estimated heat loss rates of 1 – 5 W for 25 – 200 W input. The guard heater and insulation configuration is shown schematically in Figure 4.3c.

4.2.4 Experimental procedure

Individual experimental runs were conducted for 10 – 20 minutes (longer for low-flow rate cases), and all measured values were logged every 30 s. The primary reservoir level, oil flow and heating rates, and guard heater power were adjusted throughout each run to maintain target operating conditions. Between runs, the facility was allowed to stabilize for 15 – 45 minutes to reach new steady-state operating conditions (about 90 minutes before the first run of the day).

Experiments were conducted at nominal submergence ratios of 0.2, 0.3, and 0.4 and nominal CF inlet temperatures of 110, 120, 130°C. For each submergence ratio and CF inlet temperature pair, tests were conducted over a range of nominal BPG heating rates in approximately 25 W increments. Due to CF pump limitations (maximum V_{CF} = 482 ml min^{-1}), the maximum measured BPG heating rates were greater for cases with higher CF inlet temperatures: 100 W at 110°C, 165 W at 120°C, 200 W at 130°C.

For all cases, the pre-heater controller was programmed to maintain a 95°C set-point. Average measured BPG inlet temperatures tended to increase with water flow rate ($T_{BP,in}$ = 79 – 95°C for $V_{L,in}$ = 15 – 235 ml min^{-1}), presumably because of reduced relative heat losses from the pre-heater outlet to the BPG inlet. The full test matrix of 57 nominal operating conditions is summarized in Table 4.1.

Table 4.1 – Summary of test matrix

Submergence Ratios	CF Inlet Temperature (°C)	Heating Rates (W)							
0.2	110	25	50	75	100				
0.3	120	25	50	75	100	125	150	165	
0.4	130	25	50	75	100	125	150	175	200

Ten of these conditions were re-tested to evaluate experimental repeatability. Variations in measured water pumping rates between original and repeated cases were less than 10%, and can be attributed to slight differences in operating conditions such as: water and CF BPG inlet temperatures, submergence ratios, and CF flow rates.

4.3 Data Reduction and Results

4.3.1 Data reduction

The measurements collected every 30 s during each experiment are averaged to obtain values for the data reduction procedure. The average operational submergence ratio is evaluated as:

$$S_r = \frac{p_{gauge} / (\rho_L g) - H_{prs}}{H_{BPG}} \tag{4.1}$$

Here, P_{gauge} is the measured gauge pressure, H_{prs} in the height difference between the pressure transducer and the start of the BPG heated section (135 mm), and H_{BPG} is the BPG height from the start of the heated section (1.7 m) (Figure 4.4a). An uncertainty of ± 5 mm is applied to H_{prs} because it is unclear where the pressure sensor is precisely located in the transducer. An uncertainty of ± 5 mm is also applied to H_{BPG} because it is difficult to specify where the BPG heated section should be considered to start and end in

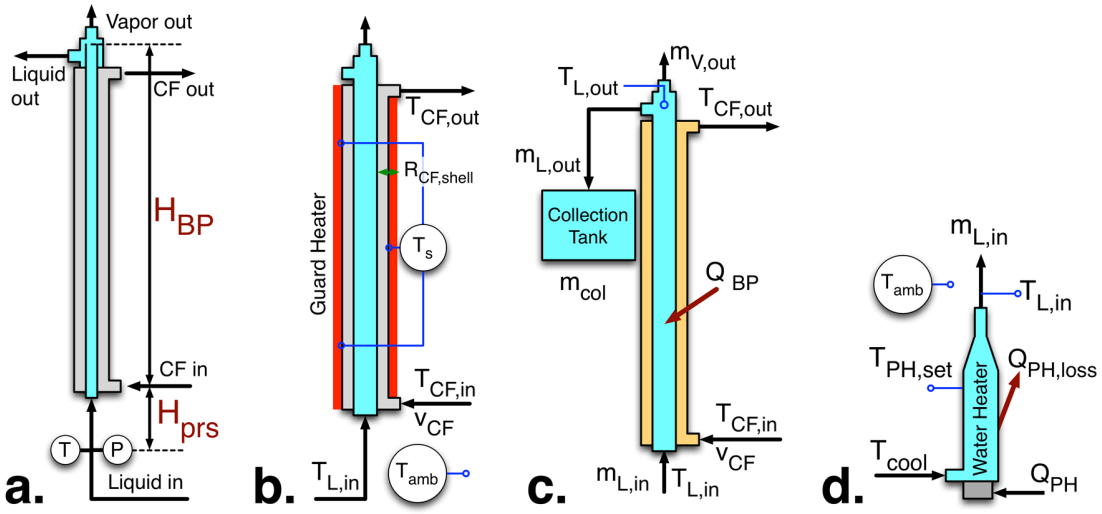

Figure 4.4 – Configurations employed in data reduction procedure for determining: **a**. Submergence ratio, **b**. Bubble-pump heating rate, **c**. Directly measured liquid flow rate, **d**. Inferred liquid flow rate

the CF inlet and outlet pipe unions. The resulting uncertainty in the reported average submergence ratios is ± 0.004.

The average net heat transfer rate to the BPG test section is evaluated as:

$$Q_{\mathrm{BPG}} = \frac{V_{\mathrm{CF}}}{\rho_{\mathrm{CF}}}\left[i_{\mathrm{CF}}\left(T_{\mathrm{CF,in}}\right) - i_{\mathrm{CF}}\left(T_{\mathrm{CF,out}}\right)\right] - \frac{\bar{T}_{\mathrm{CF}} - \bar{T}_{\mathrm{shell}}}{R_{\mathrm{CF,shell}}} \tag{4.2}$$

Here, V_{CF} is the measured CF flow rate, and $T_{\mathrm{CF,in}}$ and $T_{\mathrm{CF,out}}$ are the average inlet and outlet CF temperatures, respectively (Figure 4.4b). In all cases, the CF inlet-to-outlet temperature changes were greater than 6.8 K, which are measured with an uncertainty of < 5% (average uncertainty: 2%) using the calibrated thermocouples (±0.25 K). The second term on the right side of Equation 4.2 is an estimate of the heat loss rate from the CF to the guard heater shell, where $\bar{T}_{\mathrm{CF}} = \left(T_{\mathrm{CF,in}} - T_{\mathrm{CF,out}}\right)/2$, $\bar{T}_{\mathrm{shell}}$ is the arithmetic mean of the

three shell surface temperature measurements, and $R_{CF,shell}$ is the measured heat-transfer resistance between the coupling fluid and shell (1.1 K W^{-1}). The estimated heat-loss rate was evaluated to be within 1 – 5 W in these experiments. A conservative uncertainty estimate of 25% (± 0.03 K W^{-1}) is applied to this heat-loss rate. The resulting uncertainties in Q_{BPG} are below 5% (≤ 5 W in all cases).

At lower liquid flow rates ($\lesssim$90 ml min^{-1}) the pumped water is routed to the collection tank, which is weighed before and after an experimental run to determine the average flow rate. The steam flow exiting the phase separator entrains water droplets under some conditions; therefore, the flow is also directed to the collection tank (Figure 4.4c). Some fraction of the steam flow may condense inside the collection tank. Because the fraction of steam that condenses is unknown, a conservative correction factor of $\dot{m}_{V,out}/2$ is applied to the water flow rate with a full uncertainty of $\dot{m}_{V,out}/2$ (i.e. spanning the range of 0 to $\dot{m}_{V,out}$). This correction to the water flow rate is relatively small (< 2 ml min^{-1} water) for all cases using the collection method.

$$\dot{m}_{L,out} = \frac{m_{col,f} - m_{col,i}}{t_{run}} - \frac{\dot{m}_{V,out}}{2} \tag{4.3}$$

Here, $m_{col,i}$ and $m_{col,f}$ are the collection tank masses before and at the end of the run (± 1 g uncertainty), t_{run} is the runtime (600 – 1200 s, ± 5 s uncertainty), and $\dot{m}_{V,out}$ is the outlet steam flow rate (evaluated below). The relatively high uncertainty in the experimental runtime (5 s) is applied to account for some lag between when the valve to the collection tank is opened and closed, and when flow into the tank actually starts and

stops. The resulting uncertainty in the water pumping rate using the collection method is < 2 ml min^{-1} in all cases.

The steam flow rate is then obtained by performing mass and energy balances over the steam-tube control volume (Figure 4.4c):

$$\dot{m}_{\mathrm{L,in}} = \dot{m}_{\mathrm{L,out}} + \dot{m}_{\mathrm{V,out}} \tag{4.4}$$

$$Q_{\mathrm{BPG}} + \dot{m}_{\mathrm{L,in}} i_{\mathrm{L}}\left(T_{\mathrm{L,in}}\right) = \dot{m}_{\mathrm{L,out}} i_{\mathrm{L}}\left(T_{\mathrm{L,out}}\right) + \dot{m}_{\mathrm{V,out}} i_{\mathrm{V}}\left(T_{\mathrm{sat}}\right) \tag{4.5}$$

Here, the water outlet temperature is measured using the thermocouple wire at the top of the steam tube, and is found to be 99.2 C (T_{sat}) for nearly all cases. The outlet steam is assumed to be at T_{sat} in all cases. The steam flow rate varied from 300 – 8,200 ml min^{-1} for all cases, with typical uncertainties of 100 – 300 ml min^{-1}. At the lowest nominal heating rate (25 W) the steam flow uncertainty reached 26% in one case, but was found to be below 13% for all higher heating rate cases.

At higher pumping rates, the BPG outlet water is recirculated because the 1000 W pre-heater cannot generate sufficient heat to bring cool water from the primary reservoir up to the set-point temperature (95°C). In these cases, the water flow rate is inferred from an energy balance over the pre-heater instead of using the collection method (Figure 4.4d).

$$Q_{\mathrm{PH}} - \frac{\left(T_{\mathrm{L,cool}} + T_{\mathrm{PH,set}}\right)/2 - T_{\mathrm{amb}}}{R_{\mathrm{PH,amb}}} = \dot{m}_{\mathrm{L,in}}\left[i_{\mathrm{L}}\left(T_{\mathrm{L,in}}\right) - i_{\mathrm{L}}\left(T_{\mathrm{L,cool}}\right)\right] \tag{4.6}$$

Here, Q_{PH} is the continuously integrated average pre-heater power, $T_{\mathrm{L,cool}}$ is the water outlet temperature from the secondary reservoir, $T_{\mathrm{PH,set}}$ is the pre-heater set-point

temperature, T_{amb} is the measured ambient temperature, and $R_{PH,amb}$ is the measured thermal resistance from the pre-heater to the ambient (2.2 K W^{-1}). A 25% uncertainty is applied to the estimated heat loss term on the left side of Equation 4.6. The pre-heater energy balance is used in conjunction with the BPG mass and energy balances (Equations 4.4 – 4.5) to determine the BPG water and steam outlet flow rates. The inferred liquid pumping rates are less accurate (± 2 – 6 ml min^{-1}) than those obtained with the collection method (± < 2 ml min^{-1}). For cases where both methods can be employed reliably ($25 \le \dot{m}_{L,out} \le 90$ ml min^{-1}), the average absolute deviation between the two sets of pumping rate values is 4%.

4.3.2 Experimental results

Water pumping and BPG outlet steam flow rates are presented for all submergence ratio and CF inlet temperature combinations in Figure 4.5. As in spot-heated BPGs, pumping rates increase with submergence ratio, and generally increase with steam flow rate, but begin to plateau at higher values of V_V, presumably due to increased frictional resistance. Water pumping rates also increase with CF inlet temperature for equal steam flow rates. This occurs because a larger portion of the heat transfer and steam generation occurs near the bottom of the BPG with higher CF inlet temperatures (because $q \propto (T_{CF} - T_{sat})$), leading to reduced hydrostatic pressure drop.

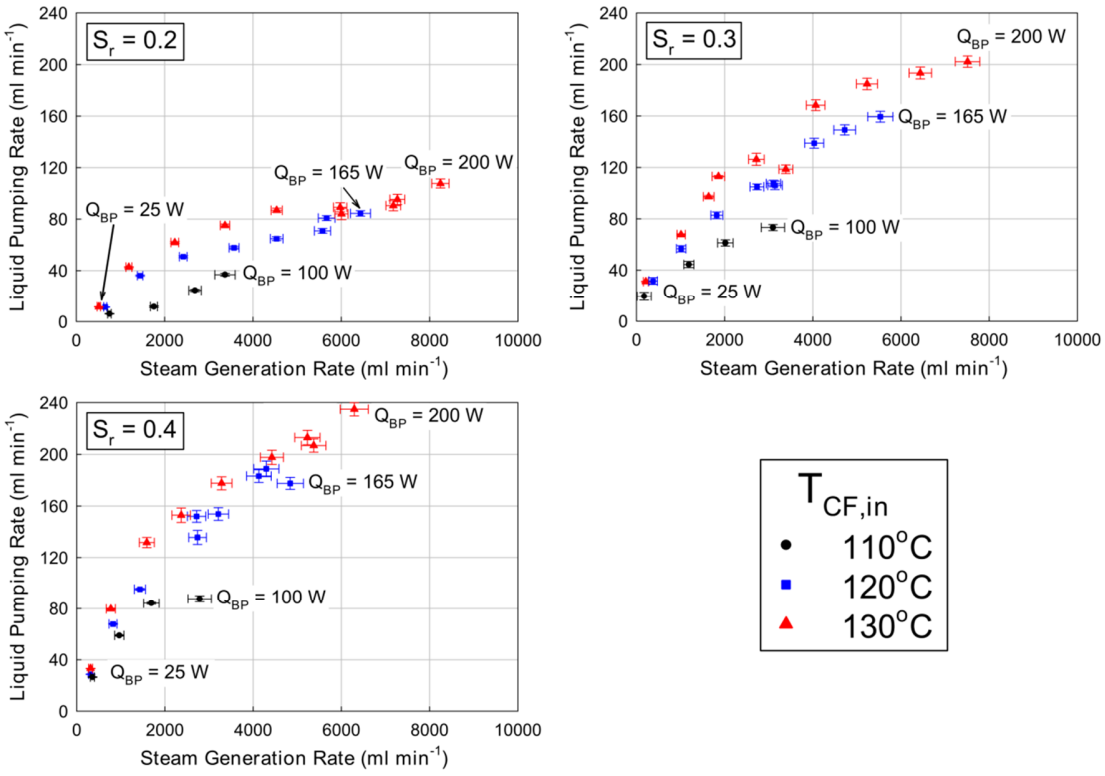

Figure 4.5 – Measured relative liquid pumping and steam generation rates for $S_r = 0.2 – 0.4$

4.4 Model Development and Results

4.4.1 Model overview

A steady segmented coupled fluid-flow and heat-transfer model is developed for the investigated coupling-fluid full-length heated BPG configuration. In this model, the steam-tube and CF channels are divided into 21 and 20 segments, respectively. The steam-tube wall is modeled as a thermal resistance between the steam-tube and CF channels. Mass, energy, and momentum balances are applied over each segment of the steam-tube channel. Energy balances are applied over each segment of the uniform-flow-rate CF channel. Flow properties (e.g. p, T, V_L) are stored at nodes representing inlet and outlet conditions for each segment. The domain is divided into subcooled and saturated

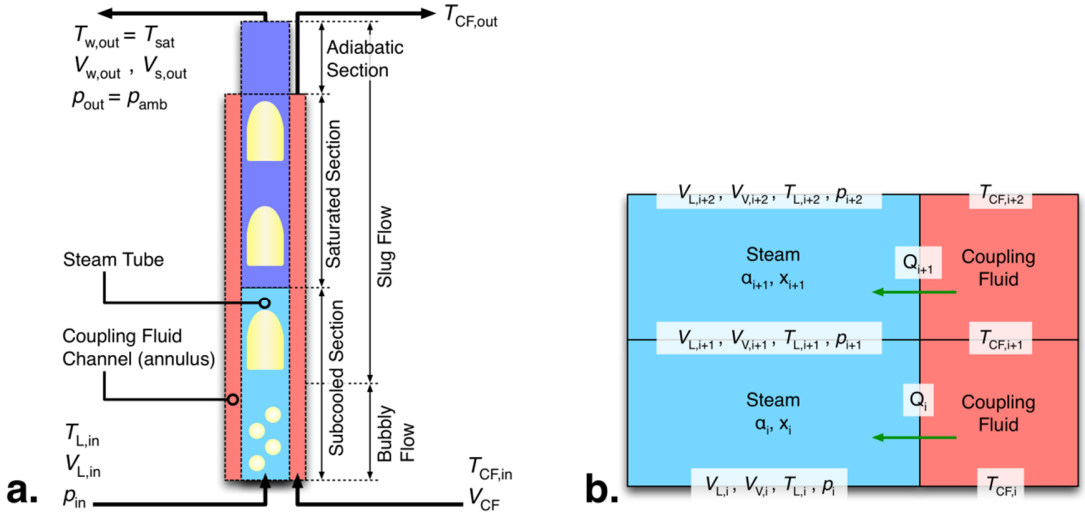

Figure 4.6 – Schematic (**a**) and discretization scheme (**b**) for BPG model

flow-boiling sections, with 10 equal length segments in each. The transition point between these two sections is solved dynamically as part of the model (i.e. $T_{L,11} = T_{sat}$). A final adiabatic segment is added to the end of the steam-tube channel to account for the unheated portion in the phase separator. The BPG water inlet temperature and gauge pressure ($p_{in} = \left[S_r \rho_L + (1 - S_r) \rho_{air} \right] g H_{BP}$) and CF flow rate and temperature are provided as input boundary conditions to the model. The BPG outlet gauge pressure is set to 0. The full model is implemented and solved using the Engineering Equation Solver (EES) software platform (Klein, 2014). A schematic of the model problem and discretization scheme is presented in Figure 4.6. Sample calculations for one subcooled segment in this model are presented in Appendix Section A.2.

Heat loss from the CF channel to the surroundings is neglected in this model, because it was only found to amount to 1 – 5 W in experiments. This simplification ensures that $T_{CF} \geq T_{sat}$ in all segments; therefore, steam condensation does not need to be modeled in

the final segments for low heating-rate cases. The model is described in detail in the following sections, with representative values reported for a case at intermediate operating conditions: $S_r = 0.299$, $T_{CF,in} = 120.5°C$, $V_{CF} = 231.2$ ml min^{-1} ($Q_{BPG} \sim 125$ W), and $T_{L,in} = 94.8°C$.

4.4.2 Steam-tube channel mass balance

A basic mass balance is performed over each segment of the steam-tube channel (i):

$$\dot{m}_{L,i} + \dot{m}_{V,i} = \dot{m}_{L,i+1} + \dot{m}_{V,i+1} \tag{4.7}$$

For the representative model case, the water flow rate decreases from 183.3 – 145.9 ml min^{-1} from the BPG inlet to outlet, and the steam flow rate reaches 4,076 ml min^{-1} at the outlet (with a peak quality of 0.016). The development of the steam and water flow rates is presented in Figure 4.7. The steep increase in vapor generation rate at axial position z = 360 mm coincides with the transition from subcooled to saturated boiling (where all input heat directly causes boiling). For this case, the predicted liquid outlet flow rate (145.9 ml min^{-1}) is 5% greater than the measured value of 138.8 ml min^{-1}, indicated on the left axis of Figure 4.7 in blue. The predicted steam generation rate of 4,076 ml min^{-1} is only 1.1% greater than the measured value of 4,032 ml min^{-1}, indicated on the right axis of Figure 4.7 in red.

4.4.3 Steam-tube channel energy balance

Energy balances are applied over each segment of the steam-tube channel. In the lower, subcooled portion of the domain, some fraction of the generated heat ($q_{L,i}$) leads to sensible heating of the bulk liquid flow, and the remainder ($q_{V,i}$) causes steam generation:

$$\dot{m}_{L,i+1} i_{i+1} - \dot{m}_{L,i} i_i = q_{L,i} A_i \tag{4.8}$$

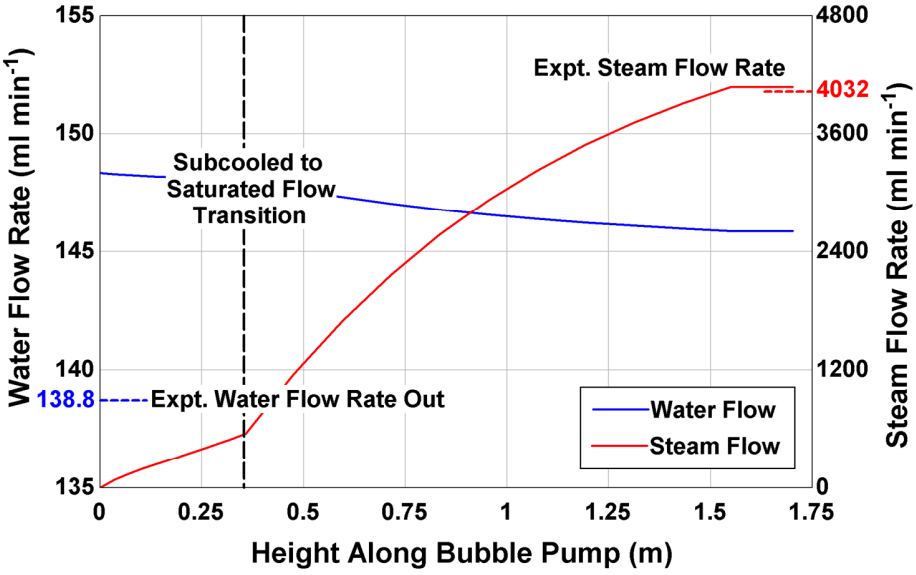

Figure 4.7 – Liquid and vapor flow rate development along the BPG length for the representative model case

$$\left(\dot{m}_{V,i+1} - \dot{m}_{V,i}\right) i_{LV} = q_{V,i} A_i \tag{4.9}$$

Here, A_i is the steam-tube channel segment inner area. Under certain conditions, some fraction of the generated steam may condense in the subcooled liquid bulk, but that effect is neglected in this model.

The Liu and Winterton (1991) flow boiling model is employed to predict heat transfer rates in this investigation because it was fit to both subcooled and saturated flow experimental data. This heat transfer model applies correction factors to single-phase liquid heat transfer ($h'_{L0} = a_{L0}\, h_{L0}$) and no-flow nucleate boiling ($h'_{NB} = a_{NB}\, h_{NB}$) convection coefficients to account for interactions between these two phenomena in flow boiling. For subcooled boiling, this correlation blends the two heat transfer mechanisms quadratically:

$$q_{\mathrm{LW,sub,i}} = \sqrt{\left[h'_{\mathrm{L0,i}}\left(T_{\mathrm{wall,i}} - T_{\mathrm{L,i}}\right)\right]^2 + \left[h'_{\mathrm{NB,i}}\left(T_{\mathrm{wall,i}} - T_{\mathrm{sat,i}}\right)\right]^2} \tag{4.10}$$

Here, T_{L} is the liquid bulk temperature and T_{wall} is the local steam-tube inner wall temperature, which is evaluated using a heat transfer balance with the CF channel (discussed in the following section). Following this formulation, it is unclear how to optimally decouple the sensible (q_{L}) and phase-change (q_{V}) components of $q_{\mathrm{LW,sub}}$. Here, we employ the same quadratic weighting used to obtain $q_{\mathrm{LW,sub}}$:

$$q_{\mathrm{L,i}} = q_{\mathrm{LW,sub,i}}\left[\frac{h'_{\mathrm{L0,i}}\left(T_{\mathrm{wall,i}} - T_{\mathrm{L,i}}\right)}{q_{\mathrm{LW,sub,i}}}\right]^2 \tag{4.11}$$

$$q_{\mathrm{V,i}} = q_{\mathrm{LW,sub,i}}\left[\frac{h'_{\mathrm{NB,i}}\left(T_{\mathrm{wall,i}} - T_{\mathrm{sat}}\right)}{q_{\mathrm{LW,sub,i}}}\right]^2 \tag{4.12}$$

In the representative model case, the resulting sensible and phase change heat fluxes range from 5,400 – 3,500 and 2,100 – 1,400 W m^{-2}, respectively, and generally decrease along the length of the subcooled section.

In the saturated portion of the domain, which begins at the point where $T_{\mathrm{L}} = T_{\mathrm{sat}}$ (z = 360 mm), the wall heat flux is evaluated as:

$$q_{\mathrm{i}} = \sqrt{h'^2_{\mathrm{L0,i}} + h'^2_{\mathrm{NB,i}}}\left(T_{\mathrm{wall,i}} - T_{\mathrm{sat}}\right) \tag{4.13}$$

In the representative case, this saturated-boiling heat flux ranges from 4,600 – 1,300 W m^{-2}, decreasing in the flow direction.

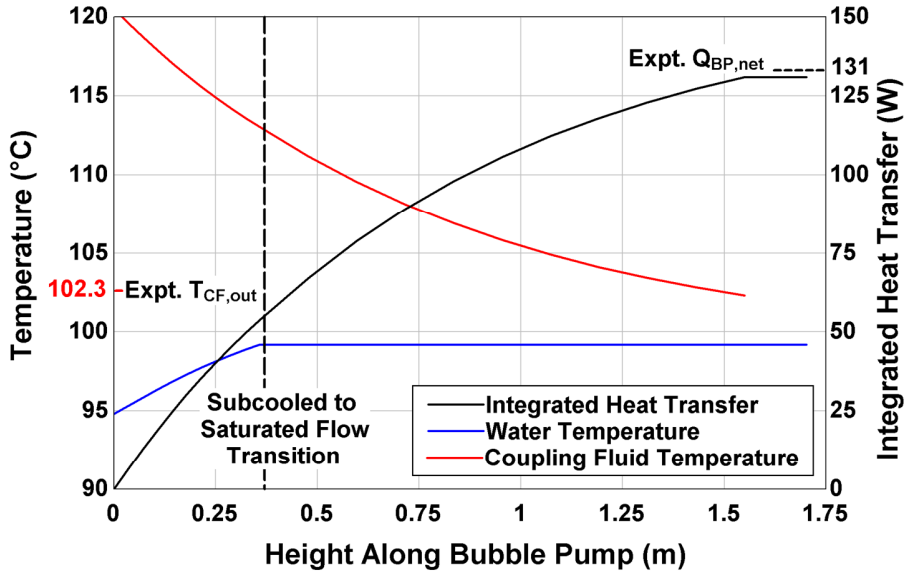

Figure 4.8 – Developing water-steam and CF temperature profiles, and heat transfer profile for the representative model case

The water-steam side saturated-flow energy balance is simply:

$$\left(\dot{m}_{V,i+1} - \dot{m}_{V,i}\right) i_{LV} = q_i A_i \tag{4.14}$$

The final segment representing the portion of the steam-tube channel in the unheated phase-separator is modeled assuming q = 0 (i.e. no phase change). The water and coupling fluid temperatures and integrated heat transfer (up to each z position along the BPG length) profiles are presented in Figure 4.8.

While the local heat flux decreases along the BPG length, spot heating in the first 100 mm with the same CF inlet temperature and thermal resistance would only lead to 18 W of heat transfer: 14% of the total (131 W). Thus, increased heat transfer area, as in the

proposed BPG configuration, is crucial for effectively harnessing low-grade thermal sources (here $T_{CF,in} - T_{sat} \sim 21$ K).

4.4.4 Steam-tube channel momentum balance

A momentum balance is applied to each segment of the steam-tube channel, accounting for pressure drop due to hydrostatic forces (fluid weight), fluid acceleration (as the flow rate of steam increases), and hydrodynamic effects (frictional flow resistance and flow-transition losses):

$$p_i - p_{i+1} = \Delta p_{hs,i} + \Delta p_{acc,i} + \Delta p_{d,i} \tag{4.15}$$

The hydrostatic pressure drop in a segment of height $H_{seg,i}$ is:

$$\Delta p_{hs,i} = \left[\left(1-\alpha_i\right) \rho_L + \alpha \rho_V \right] g H_{seg,i} \tag{4.16}$$

The hydrostatic pressure drop is the dominant component, accounting for 4,760 Pa. This is only slightly less than the total pressure change (4,790 Pa), because frictional flow resistance in the draining liquid films around Taylor bubbles (-1,390 Pa) effectively balances other hydrodynamic pressure drop contributions (1,410 Pa). The fluid-acceleration pressure-drop is evaluated assuming uniform phasic velocities at the inlet and outlet of each segment:

$$\Delta p_{acc,i} = \rho_L \left[U_{L,i+1}^2 \left(1-\alpha_{i+1}\right) - U_{L,i}^2 \left(1-\alpha_i\right) \right] + \rho_V \left[U_{V,i+1}^2 \alpha_{i+1} - U_{V,i}^2 \alpha_i \right] \tag{4.17}$$

The phasic velocities (U_L and U_V) are evaluated as:

$$U_{L,i} = \frac{\dot{m}_{L,i}}{\rho_L \left(1-\alpha_i\right) A_{st}} \tag{4.18}$$

$$U_{V,i} = \frac{\dot{m}_{V,i}}{\rho_V \alpha_i A_{st}} \tag{4.19}$$

Here, A_{st} is the cross sectional area of the 7.8 mm steam-tube channel. The net pressure drop due to fluid acceleration is relatively small in the representative case (11.9 Pa).

Accurate prediction of the void fraction (α) and hydrodynamic pressure drop gradient ($\nabla p_{d,i} = \Delta p_{d,i} / H_{seg,i}$) requires flow-regime specific modeling, and is described in the next section.

4.4.5 Two-phase flow model

Two-phase flow behavior depends strongly on flow regime. Therefore, the Taitel *et al*. (1980) bubbly-to-Taylor flow regime transition criterion is evaluated for each steam-tube-channel segment.

$$\text{IsBubbly}_i = \left\{ j_{L,i} - 2.34\, j_{V,i} + 1.07 \left[\frac{\sigma g (\rho_L - \rho_V)}{\rho_L^2} \right]^{1/4} > 0 \right\} \tag{4.20}$$

Here $j_{L,i}$ and $j_{V,i}$ are the local superficial water and steam velocities, respectively. Using this model, the first four subcooled segments (143 mm) in the representative case are predicted to contain bubbly flow, and the remainder have Taylor flow. In these bubbly flow segments, general purpose void fraction (Premoli *et al.*, 1971) and frictional pressure drop correlations (Friedel, 1979) are employed. At the end of the bubbly flow section in the representative case, the void fraction and frictional pressure gradient reach 0.315 and 72 Pa m^{-1}, respectively. In the remaining segments, a mechanistic Taylor flow model is employed.

The intermediate Bond number regime Taylor flow model proposed in Chapters 2 and 3 is adopted here, and is summarized as follows. The model idealizes Taylor flow assuming repeating identical *unit cells*, each comprised of a liquid slug and cylindrical Taylor bubble. Continuity in each unit cell requires equal volumetric fluxes through cross-sections of the bubble and liquid slug portions. Assuming uniform velocity profiles in the liquid slug (U_s), Taylor bubble (U_b), and liquid film (U_f):

$$U_s = j = \alpha_b U_b + (1-\alpha_b) U_f \tag{4.21}$$

Here α_b is the void fraction in the portion of the unit cell from the tail to nose of the Taylor bubble. At the steam-tube outlet in the representative case, α_b = 0.88, and the bubble diameter is 7.3 mm. At this same point, the model predicts: U_s = 1.49 m s^{-1}, U_b = 1.79 m s^{-1}, and U_f = -0.62 m s^{-1} (i.e. downward flow).

Additionally, continuity requires that the upward steam flow rate in the portion of the unit cell containing the Taylor bubble ($\beta = L_b/(L_s + L_b)$) equals the total steam flow rate.

$$j_V = \beta \alpha_b U_b \tag{4.22}$$

The total unit-cell void fraction is thus:

$$\alpha = \beta \alpha_b \tag{4.23}$$

In the representative model case, α and β increase along the steam tube and reach outlet values of 0.81 and 0.92, respectively.

The Taylor bubble rise velocity model formulated in Chapter 2 is adopted here. This model incorporates capillary-scale (Liu *et al.*, 2005) and large Bond number results (Bendiksen, 1985; White and Beardmore, 1962), and was validated for intermediate Bond number flows.

$$U_{\mathrm{b}} = C_0 j + \Gamma\sqrt{gD} \tag{4.24}$$

$$C_0 = f_{\mathrm{LS}} C_{0,\mathrm{LS}} + \left(1 - f_{\mathrm{LS}}\right) C_{0,\mathrm{Ca}} \tag{4.25}$$

$$f_{\mathrm{LS}} = \left(\frac{1}{1 + 4840\,\mathrm{Re}_j^{-0.163}} \right)^{0.816/\mathrm{Bo}} \tag{4.26}$$

$$C_{0,\mathrm{LS}} = 1.20 + \frac{1.09}{1 + \left(\mathrm{Re}_j / 805\right)^4} \tag{4.27}$$

$$C_{0,\mathrm{Ca}} = \frac{1}{1 - 0.61\mathrm{Ca}^{0.33}} \tag{4.28}$$

$$\Gamma = \begin{cases} 0.344\left[1 - \exp\left(\dfrac{-0.01\mathrm{N_f}}{0.345}\right)\right]\sqrt{1 + \dfrac{20}{\mathrm{Bo}} - \dfrac{93.7}{\mathrm{Bo}^2} - \dfrac{676.5}{\mathrm{Bo}^3} + \dfrac{2706}{\mathrm{Bo}^4}}\,\dfrac{1 - 0.96\exp\left(-0.0165\mathrm{Bo}\right)}{1 - 0.52\exp\left(-0.0165\mathrm{Bo}\right)} & \mathrm{Bo} > 4.55 \\ 0 & \mathrm{Bo} \le 4.55 \end{cases} \tag{4.29}$$

$$\mathrm{Re}_j = \frac{\rho_{\mathrm{L}} jD}{\mu_{\mathrm{L}}} \qquad \mathrm{Bo} = \frac{\left(\rho_{\mathrm{L}} - \rho_{\mathrm{V}}\right) gD^2}{\sigma}$$
$$\mathrm{Ca} = \frac{\mu_{\mathrm{L}} j}{\sigma} \qquad \mathrm{N_f} = \sqrt{\frac{\rho_{\mathrm{L}}\left(\rho_{\mathrm{L}} - \rho_{\mathrm{V}}\right) gD^3}{\mu_{\mathrm{L}}^2}} \tag{4.30}$$

Here Re_j is the liquid slug Reynolds number (39,300 at the outlet), Bo is the Bond number (9.6), Ca is the capillary number (0.007 at the outlet), and $\mathrm{N_f}$ is a measure of relative gravitational-to-viscous forces (7,270). For the representative case, the predicted

bubble rise velocity increases from 0.21 – 1.79 m s^{-1} over the length of the Taylor-flow portion of the BPG.

In most prior investigations of Taylor flow, liquid films have been modeled as free-falling flows with negligible interfacial stress (Sylvester, 1987; Thulasidas *et al.*, 1995). The film-flow model validated in Chapter 3 is adopted here, which accounts for the effects of interfacial shear. This correction is expected to be more important for the higher volumetric vapor fluxes considered in this study; j_V = 1.44 m s^{-1} in the representative steam-flow case, but $j_V \leq 0.54$ m s^{-1} for all air-water flow cases considered in Section 3.5.

$$U_f = \frac{4}{\pi\left[D^2 - \left(D - 2\delta_f\right)^2\right]} \int_{D/2-\delta_f}^{D/2} (2\pi r) \left\{ \begin{array}{l} \dfrac{g\left(\rho_L - \rho_G\right)}{4\mu_L}\left[\left(\dfrac{D}{2}\right)^2 - r^2 + 2\left(\dfrac{D}{2} - \delta_f\right)^2 \ln\left(\dfrac{2r}{D}\right)\right] \\ + \dfrac{\tau_{int}\left(D/2 - \delta_f\right)}{\mu_L} \ln\left(\dfrac{2r}{D}\right) \end{array} \right\} dr \tag{4.31}$$

$$f_b = \frac{4}{\mathrm{Re}_b}\left\{\frac{3.44}{\sqrt{L_b^*}} + \left[\frac{1.25}{4L_b^*} + 16 - \frac{3.44}{\sqrt{L_b^*}}\right] \Bigg/ \left[1 + 0.00021\left(L_b^*\right)^{-2}\right]\right\} \tag{4.32}$$

$$\mathrm{Re}_b = \frac{\rho_V\left(U_b - U_f\right)D_b}{\mu_G} \qquad L_b^* = \frac{L_b}{\mathrm{Re}_b\, D_b} \tag{4.33}$$

$$\tau_{int} = \frac{f_b}{8}\rho_V\left(U_b - U_f\right)^2 \tag{4.34}$$

A developing laminar flow model is employed to determine the bubble friction factor (Equations 4.32 – 4.34 (Shah and London, 1978)). The laminar flow assumption is applied because Re_b < 1420 for all considered cases. The liquid film is also modeled assuming laminar flow (Equation 4.31). In the representative steam-flow case $\mathrm{Re}_f \leq 2060$,

and $\mathrm{Re_f} \leq 2950$ for all considered cases ($\mathrm{Re_f} = 4\rho_L U_f \delta_f / \mu_L \leq 3000$ for applicability of laminar flow results (de Cachard and Delhaye, 1996)). The film thickness (δ_f) and bubble region void fraction ($\alpha_b = \left(D - 2\delta_f\right)^2 / D^2$) are determined by substitution of the film mean velocity (Equation 4.31) into the continuity constraint (Equation 4.21). For the representative case, liquid-film thickness increases from 0.19 – 0.25 mm (δ_f / D = 0.025 – 0.032) along the length of the Taylor flow section. The frictional pressure gradient due to film-to-wall shear around the Taylor bubbles is:

$$\tau_{int}\left(\pi D_b\right) - \tau_{wall}\left(\pi D\right) = \frac{\pi}{4}\left(D^2 - D_b^2\right)\left(\rho_L - \rho_V\right) g \tag{4.35}$$

$$\nabla p_{f,b} = \frac{4\tau_{wall}}{D} \tag{4.36}$$

This pressure gradient is negative because it acts in the bulk flow direction (upward), opposing the downward flowing film, and approaches -1,130 Pa m^{-1} at the steam-tube outlet.

Average Taylor bubble lengths in each segment are estimated using the correlation proposed in Chapter 2 for intermediate Bond number flow.

$$\frac{L_b}{D} = 1.813\left\{\exp\left[1.815 - 0.866\left(\frac{U_b}{j}\right)^{2.176}\right]\left(\frac{\alpha}{1-\alpha}\right)^{1.637} + 1\right\} \tag{4.37}$$

For the representative case, this predicts L_b = 260 mm (34 × D) at the steam tube outlet. At that point, $\beta = L_b / \left(L_b + L_s\right) = 0.918$; therefore, liquid slugs are predicted to only be L_s = 23 mm (3 × D).

The liquid slug is usually found to be turbulent in this investigation. In the representative case, $\mathrm{Re}_j = 39,300$ at the steam-tube outlet. Frictional resistance in the liquid slug is evaluated using the universal (laminar-to-turbulent) channel flow correlation of Churchill (1977). Liquid slugs are relatively short for most considered cases (L_s / D = 3 – 4 for the representative case). However, results from Section 3.3.2 indicate that developing channel flow friction factor corrections should not be applied for liquid slugs.

$$f_s = 8\left\{\left(\frac{8}{\mathrm{Re}_j}\right)^{12} + \left[\left(2.457\ln\left(\frac{1}{\left(7/\mathrm{Re}_j\right)^{0.9}}\right)\right)^{16} + \left(\frac{3750}{\mathrm{Re}_j}\right)^{16}\right]^{-1.5}\right\}^{1/12} \tag{4.38}$$

$$\nabla p_{\mathrm{f,s}} = f_s \frac{\rho_{\mathrm{L}} j^2}{2D} \tag{4.39}$$

In the representative case, the liquid-slug frictional pressure gradient approaches 3,030 Pa m^{-1} at the steam-tube outlet. However, the net effect of this flow resistance is small, because the liquid slugs only account for a minor portion of the tube length.

The precise mechanisms of pressure loss at Taylor-bubble to liquid-slug transitions are not yet fully characterized for the intermediate Bond number regime. At the capillary-flow limit, surface tension forces are the major component of transitional pressure drop ($\Delta p_{\mathrm{trans}}$) (Bretherton, 1961; Kreutzer *et al.*, 2005). For large Bond number flows, inertial effects dominate $\Delta p_{\mathrm{trans}}$ (Dukler and Hubbard, 1975; Fukano *et al.*, 1989). This model

employs the empirical extended capillary scale transition pressure drop model proposed in Section 3.5.

$$\Delta p_{\text{trans}} = \frac{1}{2}\frac{\rho_{\text{L}} j^2}{\text{Re}_j^{2/3}\,\text{Ca}^{1/3}}\left(10.88 + \frac{60}{1+\left(\text{Re}_{j,\text{L}}/800\right)^{-2}}\right) \tag{4.40}$$

$$\text{Re}_{j,\text{L}} = \frac{\rho_{\text{L}} j_{\text{L}} D}{\mu_{\text{L}}} \tag{4.41}$$

In the representative case, the predicted flow transition pressure drop increases from 27 – 270 Pa over the length of the Taylor flow portion of the BPG. For this case, the total pressure drop contribution of Δp_{trans} is 1160 Pa, which is much greater than the liquid slug frictional contribution (250 Pa), and is of similar order to the bubble region frictional resistance (-1390 Pa). Thus, accurate prediction of Δp_{trans} and the frequency of transitional pressure drops (i.e., $L_{\text{b}} + L_{\text{s}}$) are critical for modeling Taylor flow in the intermediate Bond number regime.

The liquid film, liquid slug, and transition pressure drops are combined to yield the hydrodynamic pressure drop in each segment:

$$\frac{\Delta p_{\text{d,i}}}{H_{\text{seg,i}}} = \beta \nabla p_{\text{f,b,i}} + (1-\beta)\nabla p_{\text{f,s,i}} + \frac{\beta}{L_{\text{b}}}\Delta p_{\text{trans}} \tag{4.42}$$

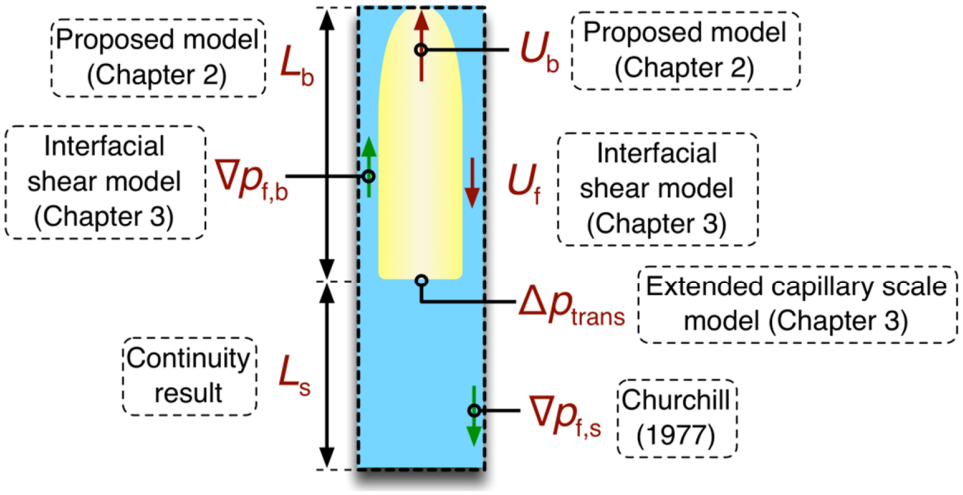

Figure 4.9 – Schematic summary of mechanistic Taylor-flow model

In the representative case, the hydrodynamic pressure drop gradient reaches a minimum of -140 Pa m^{-1} at z = 596 mm, and increases to the outlet value of 150 Pa m^{-1} as the flow accelerates (increasing $\nabla p_{f,s}$ and Δp_{trans}). A schematic summary of the developed Taylor flow model is presented in Figure 4.9. The development of the pressure and void fraction along the steam-tube channel is presented in Figure 4.10. The void fraction profile displays jumps at the transitions from bubbly to Taylor flow and from subcooled to saturated flow.

4.4.6 Coupling-fluid side model

The CF flow is modeled as single-phase fluid flow with constant thermophysical properties evaluated at T_{sat} = 99.2°C (Table 4.2). The assumption of constant CF properties does not significantly affect the model results because the relevant properties: k_{CF} and $c_{p,CF}$ only vary by 1.5% and 7%, respectively, over the considered operating conditions (99.2 – 130°C). For all experimental cases, the coupling-fluid flow was found

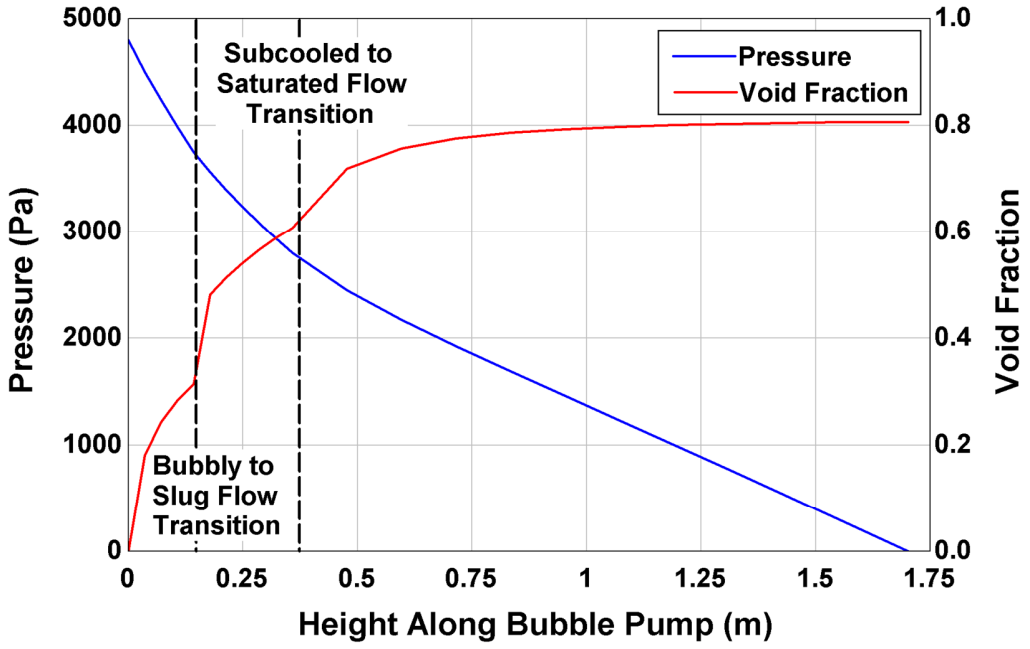

Figure 4.10 – Pressure and void fraction profiles along the steam-tube channel for the representative model case

to be laminar ($\mathrm{Re}_{CF} = \rho_{CF} U_{CF} D_{H,CF} / \mu_{CF} \leq 115$, where $D_{H,CF} = D_{a,o} - D_{a,i}$ = 1.4 mm). The annular-flow fully developed heat-transfer coefficient (h_{CF} = 360 W m^{-2} K^{-1}) was evaluated using a built-in Engineering Equation Solver function (Klein, 2014), which performs a curve-fit to values reported by (Shah and London, 1978). The heat transfer rate and inside tube-wall temperature ($T_{wall,i}$) in each segment are evaluated using a thermal resistance-network model:

$$q_i(\pi D) = \frac{T_{CF,i+1} - T_{wall,i}}{\dfrac{1}{h_{CF}(\pi D_{a,i})} + \dfrac{\ln(D_{a,o}/D_{a,i})}{2\pi k_t}} = \frac{T_{CF,i+1} - T_{wall,i}}{R'_{CF} + R'_t} \tag{4.43}$$

Table 4.2 – Thermophysical properties for coupling fluid (Paratherm NF® at 99.2°C)

Density ($kg\ m^{-3}$)	Specific Heat ($kJ\ kg^{-1}\ K^{-1}$)	Thermal Conductivity ($W\ m^{-1}\ K^{-1}$)	Dynamic Viscosity ($kg\ m^{-1}\ s^{-1}$)
831	2.25	0.10	$3.6 \cdot 10^{-3}$

Here the CF convection resistance ($R'_{CF} = 0.094$ m K W^{-1}) dominates the conduction resistance through the stainless-steel tube wall ($k_t = 14$ W m^{-1} K^{-1}, $R'_t = 0.002$ m K W^{-1}). A down-winding scheme ($T_{CF,i+1} - T_{wall,i}$) is employed to avoid oscillations in the CF temperature distribution.

The energy balance for each segment of the coupling fluid channel is:

$$\left(T_{CF,i} - T_{CF,i+1}\right)\left(\dot{m}_{CF} c_{p,CF}\right) = H_{seg,i} \frac{T_{CF,i+1} - T_{wall,i}}{R'_{CF} + R'_t} \tag{4.45}$$

In the representative case, the coupling fluid temperature varies from 120.5°C at the channel inlet, to 102.3°C at the end of the heated section. In the corresponding experiment, the CF outlet temperature was slightly lower (102.1 °C), in part due to heat loss to the surroundings. Heat loss from the CF channel was not included in this model because of the additional complexity that would be required to predict condensation rates in the last segments of the steam-tube in cases where $T_{CF,out} < T_{sat}$.

4.4.7 Comparison of model predictions and experimental results

In the representative model case ($S_r = 0.299$, $T_{CF,in} = 120.5$°C, $V_{CF} = 231.2$ ml min^{-1}, $T_{L,in} = 94.8$°C), predicted and experimental BPG heating rates agree closely: 130.9 and 131.4 W, respectively. This parameter is not a strong discriminating metric for model

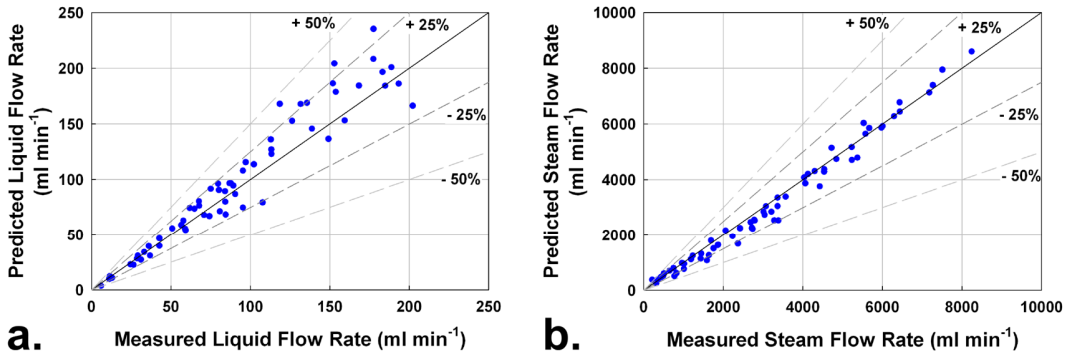

Figure 4.11 – Comparison of measured and predicted liquid (**a**) and vapor (**b**) outlet flow rates

performance, however, because in most cases $Q_{\mathrm{BPG}} \sim \dot{m}_{\mathrm{CF}} c_{\mathrm{p,CF}} \left(T_{\mathrm{CF,in}} - T_{\mathrm{sat}}\right)$. The liquid pumping rate ($V_{\mathrm{L,out}}$) however, is very sensitive to model formulation, and its prediction is the primary objective of bubble pump modeling. In the representative case, the predicted liquid pumping rate (145.9 ml min^{-1}) is 5% higher than the measured value of 138.8 ml min^{-1}. This is reasonably accurate considering the indirect nature of the modeling problem. The predicted (4,076 ml min^{-1}) and experimental (4,032 ml min^{-1}) steam flow rates are very close for this case (1.1% error). This model predicts liquid pumping rates within 25% of experimental values for 90% of the 67 tested points (100% within 50% of experimental values). Steam outlet flow rates are predicted within 25% of experimental values for 91% of the cases. The relative predicted and measured outlet flow rates are presented in Figure 4.11. This close agreement between measured and predicted flow rates indicates that this model can be reliably employed for BPG design under similar operating conditions.

The proposed model is generally stable, but did not completely converge for two cases. Those two cases could only be solved to within ± 0.003 S_{r}. This instability can be

attributed to a discontinuity in the two-phase flow model, which only assigns one flow-pattern to each model segment (bubbly or Taylor flow). In some cases, the predicted transition point may oscillate and fail to converge.

4.5 Discussion

This investigation demonstrates that single-pressure absorption systems can potentially operate with very low source temperatures using coupling-fluid full-length heated BPGs ($T_{CF,in} - T_{sat} \sim 11$ K). Previous investigations have shown that DAR systems with water refrigerant can operate with generator temperatures as low as 70 – 83°C (Pfaff *et al.*, 1998). With the proposed BPG design, such a system could operate with 81 – 94°C heat input, which could be delivered from combustion-engine coolant or a solar-thermosyphon, among other low-grade heat sources. In such applications, the need for a coupling-fluid pump could be eliminated, enabling solely thermally driven refrigeration. Additionally, the BPG investigated here demonstrated stable operation with submergence ratios as low as 0.2. This indicates that similar designs could enable relatively compact single-pressure absorption systems, because the hydrostatic difference between the primary reservoir level and BPG outlet ($\Delta p_{net} = S_r \rho_L g H_{BPG}$) limits the pressure drop through all other systems components.

Liquid pumping rates were generally found to increase with submergence ratio, CF inlet temperature, and heat input (CF flow rate). This result suggests a BPG optimization problem where increased pumping rate must be balanced with the available heat source temperature and system height. In some previous investigations (Delano, 1998), the BPG was assumed to operate at the maximum liquid pumping rate point, beyond which hydrodynamic resistance prevented additional flow. However, identification of optimal

Table 4.3 – Predicted effect of changing submergence ratio with fixed inlet subcooling ($T_{L,in}$ = 94.8°C, $T_{CF,in}$ = 120.5°C, V_{CF} = 231.2 ml min^{-1}), Q_{BPG} = 131 W for all cases

Submergence Ratio	$V_{L,out}$ (ml min^{-1})	$V_{V,out}$ (ml min^{-1})	Sensible Heating Fraction
0.279	132.3	4,260	0.299
0.299	145.9	4,080	0.329
0.319	157.3	3,920	0.354

system performance requires a more complex, fully coupled analysis. For example, increased solution flow rate through a falling-film absorber could lead to greater mass-transfer resistance (thicker films) and smaller driving concentration gradients.

Additionally, increased liquid flow rate in a BPG with fixed inlet subcooling (or for saturated azeotropic solutions) would cause a greater fraction of input heat to be used for sensible heating, and less for refrigerant generation. Only some portion of this *parasitic* sensible liquid heating can be recovered in a solution heat exchanger. For the representative model case, increasing the liquid pumping rate (by increasing S_r from 0.299 to 0.319) without changing $T_{L,in}$ (94.8°C) leads to greater predicted sensible heating (33% to 35% of input) and reduced steam generation (4,080 to 3,920 ml min^{-1}) (Table 4.3). Thus, BPG design and optimization should only be performed on a full-system level. The experimental and model results reported in this study can be integrated with other system- and component-level models to perform some of this optimization *a priori*, and streamline the iterative design process.

One particular coupled component- and system-level effect identified in this study is the sensitivity of the BPG to the liquid inlet subcooling. Previous investigations have

Table 4.4 – Predicted effect of changing subcooled liquid inlet temperature (T_{sat} = 99.2°C) with other parameters fixed (S_r = 0.299, $T_{CF,in}$ = 120.5°C, V_{CF} = 231.2 ml min^{-1}), Q_{BPG} = 131 W in these cases

$T_{L,in}$ (°C)	$V_{L,out}$ (ml min^{-1})	$V_{V,out}$ (ml min^{-1})
93.8	133.1	3,820
94.8	145.9	4,080
95.8	160.1	4,400

generally assumed that saturated liquid flows into the BPG (or azeotropic solution at the bubble point). However, for the low flow rates encountered in these passively driven absorption systems, even a small amount of heat loss upstream of the BPG inlet could cause significant subcooling. Changing the water-inlet temperature by 1 K in the representative case leads to a 10% change in the predicted liquid pumping rate, which could significantly affect absorption system performance (Table 4.4).

This investigation focused on boiling water bubble pumps at ambient pressure (ρ_V = 0.58 kg m^{-3}). Operating pressures, and thus vapor-phase densities, are generally higher in actual absorption systems. Vapor volumetric flow rates would thus be lower for a similar BPG integrated into an absorption system, and the resulting pumping rates could be significantly lower. Artificially increasing the vapor phase density by a factor of 5 (to 2.9 kg m^{-3}) for the representative case leads to a reduced predicted liquid pumping rate of 53.8 ml min^{-1} (from 145.9 ml min^{-1}) (Table 4.5). Further investigation is thus warranted to determine how well the experimentally observed trends and model predictions apply under pressurized absorption system operating conditions, in which the vapor density is expected to be higher than that of steam at the conditions considered here. In actual

Table 4.5 – Predicted effect of increased vapor-phase density (S_r = 0.299, $T_{L,in}$ = 94.8°C, $T_{CF,in}$ = 120.5°C, V_{CF} = 231.2 ml min^{-1}), Q_{BPG} = 129.1 – 130.9 W in these cases

Vapor Density Multiplier	ρ_V (kg m^{-3})	$V_{L,out}$ (ml min^{-1})	$V_{V,out}$ (ml min^{-1})
1	0.58	145.9	4,080
3	1.75	87.1	1,610
5	2.91	53.8	1,050

absorption systems, it may be desirable to employ smaller diameter BPG tubes, which can deliver similar pumping rates at reduced vapor volumetric flow rates under certain conditions (Reinemann *et al.*, 1990). Increased pumping rates could also be achieved with greater BPG heating rates, which were generally limited by the coupling-fluid flow rates in this investigation.

4.6 Conclusions

A full-length coupling-fluid heated bubble-pump generator design was investigated. This configuration can enable operation of single-pressure refrigeration systems using very low temperature thermal sources – as low as ~11°C above T_{sat} in this study. Detailed experimental studies were conducted over a range of submergence ratios, coupling-fluid inlet temperatures, and heating rates.

A detailed mechanistic coupled fluid-flow and heat-transfer model was developed for this bubble-pump generator design. The model demonstrated good agreement with data, predicting liquid pumping rates within 25% of measured values for 90% of the 67 tested cases. This model was employed to investigate the effects of key operating parameters, including submergence ratio, liquid inlet subcooling, and vapor-phase density.

This investigation has highlighted certain phenomena for which further investigation is needed before coupling-fluid heated bubble pump generators can be reliably designed, *a priori*, for use in absorption systems. In particular, the vertical upward Taylor flow pattern is still not completely characterized for intermediate Bond number conditions. Tools for prediction of liquid slug length and transition pressure drops are of particular interest. Additionally, the predicted effects of increased vapor-phase density at the operating pressures typically employed in absorption systems should be validated. With such results, the ability to harness low-temperature thermal resources using absorption systems can be greatly advanced.

CHAPTER 5. SIMULATION OF FLOW BOILING AND DISTRIBUTED HEATED BUBBLE-PUMP GENERATOR MODEL ASSESSMENT

5.1 Introduction

5.1.1 Overview

Diffusion absorption refrigeration (DAR) is a fully passive thermally activated cooling technology. It is thus well suited to off-grid cooling needs. However, conventional systems require high input temperatures (150 – 200°C (Jakob *et al.*, 2008; Srikhirin *et al.*, 2001)), usually delivered with electrical resistance heaters or chemical fuel (e.g., propane). If the required source temperatures can be reduced, many new applications can be realized using solar-thermal or waste-heat sources.

One key reason for the high source temperatures required in existing DAR systems is the conventional bubble-pump generator (BPG) component design. In this component, input heat causes desorption (evaporation) of refrigerant from the liquid solution stream. The buoyancy of refrigerant vapor bubbles rising through the vertical BPG tube lifts solution, providing the hydrostatic head to drive flows through other system components. Thus, this one component establishes the solution and refrigerant flow rates through the DAR system, and, therefore, significantly affects overall device performance. In conventional *spot-heated* BPG designs, all heat is transferred through a small region near the base of the component. Such a configuration is relatively simple to design and analyze because adiabatic two-phase flow results can be applied over a major portion of the component length. However, high source temperatures are required to transfer all input heat over a small area ($Q = h\,A\,(T_{source} - T_{BPG})$).

This chapter uses, as a starting point, the published journal paper: Rattner, A.S., Garimella, S., 2014. Simple mechanistically consistent formulation for volume-of-fluid based computations of condensing flows. Journal of Heat Transfer, 136(7).

Recently, alternate *distributed-heated* BPG configurations have been proposed (Benhimidene *et al.*, 2011; Dammak *et al.*, 2010; Jakob *et al.*, 2008) (Chapter 4). In these implementations, vapor generation occurs along most of the component length, increasing heat transfer area and reducing required source temperatures. In Chapter 4, an experimental investigation was performed for a full-length coupling-fluid (CF) heated tube-in-tube BPG. A detailed segmented component model was formulated, and overall experimental validation was demonstrated (e.g., for liquid pumping rates (V_L), vapor generation rates (V_V), and total heat transfer rates (Q_{BPG})). This represented the first experimentally validated model of a distributed-heated BPG.

While global agreement was found between the proposed model and experimental results, validation of local quantities is more challenging. Visual access was not available in the experimental system due to the metal tube walls, guard heaters, and fiberglass insulation wrap. Even if transparent materials were employed, it would be difficult to quantitatively analyze visualization data, as in Chapter 2, due to optical distortion through both coaxial tubes and the CF channel. Additionally, the developing flow pattern would necessitate data collection at multiple positions along the component length. As a result, the applicability of selected sub-models and potential sources of error are difficult to assess experimentally.

In the present investigation, two-phase flow phase-change simulations of the flow-boiling process in the BPG generator configuration proposed in Chapter 4 are performed. By directly solving the governing continuity (pressure), momentum, and thermal energy equations, detailed local flow data are obtained. These results are applied to assess the underlying assumptions and sub-models employed in the segmented BPG model (Chapter

4). There are multiple relatively mature approaches to simulating adiabatic two-phase flows, including Volume-of-Fluid (VOF) (Hirt and Nichols, 1981), Level-Set (Sussman *et al.*, 1994), and interface tracking (Unverdi and Tryggvason, 1992). However, the field of simulating two-phase flows with phase change is still in its infancy. Therefore, it is necessary to formulate and validate a suitable phase-change modeling approach as part of this investigation.

This study focuses on techniques suitable for "one-fluid" based simulations, which solve a single set of governing conservation equations, consistent with the underlying physics. "Two-fluid" approaches (e.g., Eulerian-Eulerian) describe interactions between phases in a spatially averaged manner with subgrid-scale models. Representative two-fluid flow boiling simulation studies have been reported by Krepper *et al.* (2007), Koncar and Krepper (2008), and Talebi *et al.* (2009). BPG-specific flow-boiling two-fluid simulations have been performed by Garma *et al.* (2014) and Jo *et al.* (2014). However, such approaches may not be suitable for the Taylor flow pattern expected in the majority the considered BPG length, for which flow structures (bubbles and liquid slugs) are large relative to the mesh resolution (see Section 3.1.2.2). In the following section, reviews of prior work on phase-change simulation techniques for two-phase flows with an emphasis on flow-boiling studies are presented.

5.1.2 Prior work

Mature commercially (ANSYS Fluent, ANSYS CFX, COMSOL Multiphysics) and freely available (OpenFOAM) software tools have been developed for simulating two-phase liquid-gas flows without phase change. Most of these programs track the development of the fluid phases with a phase-fraction field, α_1, which ideally varies from

zero in the vapor phase to one in the liquid phase. In the Volume-of-Fluid (VOF) formulation (Hirt and Nichols, 1981), the local material properties are weighted by α_1, yielding a single set of governing equations valid for an entire simulation domain. Such VOF simulation frameworks can be extended to account for phase change by incorporating source and sink terms in the phase, momentum, continuity/pressure, and energy equations. Multiple approaches have been proposed for evaluating these source terms, including: (a) rate parameters, (b) adaptation of analytical models and experimentally developed heat transfer correlations, and (c) direct evaluation of interfacial transport rates.

5.1.2.1 Rate parameter based models

Yang *et al.* (2008) performed simulations and experimental investigations of flow boiling of R141b in a horizontal tube. Their formulation employed compressible momentum and continuity equations, and coupled phase-change source terms were added to the phase and thermal energy transport equations. Geometric interface reconstruction was performed using the piecewise-linear approach implemented in ANSYS Fluent. The rate of phase change (S, kg m^{-3} s^{-1}) at the interface was controlled with an empirical parameter r (s^{-1}), and was set proportional to the relative temperature difference from the saturated condition ($(T - T_{sat}) / T_{sat}$):

$$S = \begin{cases} r\alpha_1\rho_L \dfrac{T - T_{sat}}{T_{sat}} & T \geq T_{sat} \\ r(1-\alpha_1)\rho_V \dfrac{T - T_{sat}}{T_{sat}} & T < T_{sat} \end{cases} \tag{5.1}$$

Yang *et al.* (2008) found that a value of $r = 100\ s^{-1}$ was sufficient to maintain the interface within 1 K of the saturation temperature without introducing large numerical oscillations. However, r acts as a surrogate for the characteristic thermal time scale of mesh cells ($\tau_{cell} = \rho c_p \Delta x^2/k$), and should therefore depend on the simulation mesh resolution and fluid properties. Qualitative agreement was demonstrated with experimental results (e.g., for axial void fraction profile), however the simulation mesh may have been under-resolved. Liquid film thickness was only 1 – 2 cells in annular flow, compared with the 5+ cells advised by Gupta *et al.* (2009).

Fang *et al.* (2010) simulated boiling flows in a vapor venting microchannel, in which a semipermeable membrane permitted vapor removal to improve heat transfer performance and reduce frictional losses. In their investigation, coupled terms were introduced to the phase and energy equations to account for phase change, but no modifications were made to the momentum or continuity equations to account for volume generation from boiling. Fang *et al.* (2010) adopted the phase-change rate parameter model of Yang *et al.* (2008), but selected the same value for r ($100\ s^{-1}$), even though they used a much finer mesh resolution and a different working fluid (water).

Kunkelman and Stephan (2009) performed 2D VOF-based simulations of nucleate boiling. Their implementation employed the microscale thermal resistance model proposed by Hardt and Wondra (2008) to determine phase-change rates in interface-containing cells. They noted that continuum-scale transport resistance may have been dominant at the considered mesh resolution, but this approach ensured that interface-cells were maintained close to saturation temperatures. They implemented a subgrid-scale

model to account for contact-line evaporation at the wall. Validation studies were performed for cases of growth and detachment of single evaporating bubbles.

Thiele (2010) employed an empirical rate-parameter-based approach for modeling horizontal film condensation, and applied a limiting condition to ensure that the amount of vapor condensed per time step did not exceed the amount present in the cells. It was shown that the rate parameter approach with fixed r did not yield convergent results with increasing mesh resolution. Again, this can be attributed to the fact that the characteristic thermal time scale of a mesh cell (τ_{cell}) depends on its size.

5.1.2.2 Analytical solution and correlation based models

Jeon *et al.* (2009) simulated the condensation of a rising vapor bubble in a liquid medium using the VOF approach. Phase-change source terms were introduced to the phase fraction and energy equations, but the momentum and continuity equations were not modified to account for the volumetric reduction due to condensation. The condensation rate was modeled by applying the convection coefficient from the correlation of Kim and Park (2008) at the interface. This approach has the advantage of incorporating experimentally validated data into the model description, but limits applicability to simulations with similar phase-change conditions. Additionally, the use of an average heat transfer coefficient over the entire bubble surface limits the accuracy of a CFD simulation, in which local interface temperature gradients may vary significantly.

Thiele (2010) adapted the Nusselt (1916) flat-plate falling-film condensation solution into a form applicable to individual mesh cells. Thiele (2010) implemented his model in the OpenFOAM interFoam framework (Weller, 2002). No interface reconstruction is performed in interFoam, reducing computational cost and simplifying support of

unstructured meshes. Rather, a compressive velocity field is superimposed in the vicinity of the interface to reduce numerical diffusion (based on (Rusche, 2002; Weller, 2002)). Because interfacial geometry data were not available, Thiele (2010) developed a simplified model in which the assumed interface area in each cell scales with α_1, approaching 0 at α_1 = 0,1 and a maximal value at α_1 = 0.5. This approach was shown to achieve grid independence for a horizontal condensing film simulation. However, the applicability of this approach to general condensation configurations is unclear.

5.1.2.3 Interfacial transport based models

Bothe and Warnecke (2005) developed a computational model to study mass transfer from rising gas bubbles in a liquid medium. While technically an adiabatic absorption process, this problem is closely related to condensation. In this investigation, mass transfer across the interface was modeled by applying an equilibrium concentration to interface cells, and solving the species transport equation throughout the domain. The interface itself was reconstructed using the piecewise linear interface calculation (PLIC) method (Rider and Kothe, 1998).

Subramaniam and Garimella (2009) performed 2D and 3D simulations of falling lithium bromide-water films over cooled horizontal tubes in a water vapor atmosphere, as would be employed in the absorber component of an absorption chiller. As in the study by Bothe and Warnecke (2005), the interface was reconstructed using the PLIC method, and phase-change mass transfer rates were determined by solving the species transport equation directly. They also employed a thermal energy equation to account for coupled heat and mass transfer effects. Both these studies neglected volumetric and velocity changes due to phase change.

Marschall *et al.* (2012) also investigated the problem of mass transfer across liquid-gas interfaces, and implemented their models in the OpenFOAM interFoam framework. Because geometric interface data were not available, Marschall *et al.* (2012) implemented a continuum species transport (CST) model applied to interface cells, analogous to the widely used continuum surface-tension force (CSF) model (Brackbill *et al.*, 1992).

Juric and Tryggvason (1998) implemented a model in which the effects of the interface (surface tension, phase change heating and volumetric fluxes, etc.) are applied to the discretized equations as smoothed delta functions. The actual interface is modeled as connected points overlaid on the main simulation mesh that are advected at each time step in a combined Lagrangian/Eulerian formulation. This approach increases program complexity, but avoids any numerical diffusion of the interface and allows direct evaluation of interfacial transport quantities. They validated this model for 1-D evaporation, and grid-independence was demonstrated. Two-dimensional film-boiling simulations were also performed. In a follow-on study, Esmaeeli and Tryggvason (2004a, b) extended this model to support 3D simulations on structured rectilinear grids. Validation studies were performed for falling liquid films, the Rayleigh-Taylor instability with heat and mass transfer, evaporation of a superheated liquid film, and film boiling. These simulations were shown to achieve grid independence, and close agreement with experimental and analytical results was obtained.

Mukherjee and Kandlikar (2005) formulated a level-set based approach to simulate growth of a single vapor bubble in a microchannel with flowing water. The evaporation rate was determined from the temperature gradient at the interface, and the interface

signed-distance function was updated explicitly based on this value. Qualitative agreement was found with experiments for bubble shape and wall-dryout.

Son and Dhir (2008) formulated a similar level-set implementation to study nucleate boiling. A microlayer evaporation model was incorporated into the wall boundary conditions to account for subgrid-scale effects. Wall heat-flux agreement to within ± 25% was achieved for 3D studies when nucleation site density and waiting times were specified explicitly.

Tao *et al.* (2009) investigated bubble growth in liquid films, motivated by the application of water spray cooling. Their model accounted for volumetric generation during boiling and the associated momentum source. The phase change rate was determined based on the difference of normal heat fluxes across the interface; therefore, geometric reconstruction was presumably performed. However, no phase-change term was applied to the phase transport equation. Results were reported for the growth and detachment of a 2D bubble and associated surface heat transfer.

Zhang *et al.* (2011) investigated film boiling using an approach based on that developed by Esmaeeli and Tryggvason (2004a, b), in which the interface is reconstructed using the PLIC algorithm and directly advected. The phase change rate is determined by evaluating the normal conduction heat transfer rates on both sides of the liquid-vapor interface. The actual interface velocity is calculated from a mass balance across the interface (ρ_L ($U_{n,L} - U_{int}$) = ρ_V ($U_{n,V} - U_{int}$)). A full 3D simulation was performed for the growth, necking, and break-off of a single vapor bubble. A number of simplifications were employed in this study, including assuming a linear temperature

profile from the wall to the interface (at T_{sat}). Material properties and operating conditions were selected to model a non-physical fluid with relatively small differences between the liquid and vapor phases and weak dynamic effects ($\rho_V/\rho_L = 0.1$, $\mu_V/\mu_L = 0.1$, Re = 1, Ja = 0.1).

5.1.3 Present investigation

A variety of phase-change modeling approaches have been proposed for two-phase flow simulations. Rate parameter and analytical solution/correlation based phase-change models have been adopted in many studies because of the relative ease of implementation as volumetric source terms in the governing equations. However, general applicability of more empirical formulations has been limited. Interfacial transport based approaches resolve the governing mechanisms of phase change, and rigorous validation has been demonstrated for some. However, such models have relied on geometric interface reconstruction or direct tracking and advection of the interface, which are both computationally expensive and difficult to perform on unstructured meshes. Such studies have primarily focused on relatively small domains with single or few bubbles/droplets.

An alternative phase-change modeling formulation is proposed in the present study in which cells containing the interface are identified using a relatively simple and fast graph traversal algorithm. Phase change source terms are then applied to such interface cells without the need for geometric reconstruction. Interface cells are forced to the equilibrium state instantaneously, similar to rate parameter methods (Fang *et al.*, 2010; Thiele, 2010; Yang *et al.*, 2008), but in a dynamic fashion that yields mesh independence. This formulation is first evaluated for condensation phase-change configurations, which are numerically more stable than corresponding evaporation problems. Validation is then

demonstrated for horizontal film condensation (Stefan problem) and for smooth and wavy falling-film condensation.

This simulation approach is then adapted to support evaporative phase change, and validated for horizontal film evaporation. This formulation is then applied to a representative distributed CF-heated BPG flow with the tube-in-tube geometry investigated in Chapter 4. This analysis focuses on the saturated-flow portion of the component, including both the inner- (working fluid) and CF-channels. To improve numerical stability, this analysis is performed with relaxed transport properties compared with the steam-water working fluid investigated in Chapter 4 (increased μ_L, increased ρ_V/ρ_L). Simulation data are applied to assess heat transfer, two-phase flow kinematic, and hydrodynamic sub-model predictions from the segmented model. Potential approaches to enable simulation of target working fluids and operating conditions are discussed.

5.2 Simulation Formulation

5.2.1 Governing equations

Simulation of phase-change problems in the VOF approach requires solution of the governing mass, momentum, energy, and phase equations. In this model, the incompressible continuity equation is modified with a source term ($\dot{v}_{pc}$) representing the volumetric change per unit volume due to phase change. In reality, phase-change flows are compressible. However, the full compressible form of the continuity equation is not necessary because the densities of the liquid and vapor phases are assumed constant. Rather, a *volume transport equation* is employed:

$$\frac{\partial u_i}{\partial x_i} = \dot{v}_{pc} \tag{5.2}$$

The momentum equation is formulated neglecting compressibility effects. An effective viscosity (μ_{eff}) is employed, which could incorporate an eddy viscosity for turbulent flow simulations. Surface tension and net gravitational forces are incorporated into a term f (Equation 5.3), following the interFoam formulation (Weller, 2002). Surface tension forces are obtained without geometric reconstruction by estimating local curvature and interface orientation using differential operations on the phase field α_1 (Kissling *et al.*, 2010).

$$f_{\text{i}} = -\left(\frac{\partial \rho}{\partial x_{\text{i}}}\right) g_{\text{j}} x_{\text{j}} + \sigma \left\{ \frac{\partial}{\partial x_{\text{j}}} \left[\frac{\partial \alpha_{\text{l}}}{\partial x_{\text{j}}} \Big/ \left(\frac{\partial \alpha_{\text{l}}}{\partial x_{\text{k}}} \frac{\partial \alpha_{\text{l}}}{\partial x_{\text{k}}} \right)^{1/2} \right] \right\} \frac{\partial \alpha_{\text{l}}}{\partial x_{\text{i}}} \tag{5.3}$$

Here, g is the gravitational acceleration vector, and σ is the fluid surface tension.

The complete momentum equation is formulated using $p_{\rho\text{gh}}$ – the pressure field without the hydrostatic component:

$$\rho \frac{\partial u_{\text{i}}}{\partial t} + \rho u_{\text{j}} \frac{\partial u_{\text{i}}}{\partial x_{\text{j}}} - \mu_{\text{eff}} \frac{\partial u_i}{\partial x_{\text{j}} \partial x_{\text{j}}} = -\frac{\partial p_{\rho\text{gh}}}{\partial x_{\text{i}}} + f_{\text{i}} \tag{5.4}$$

A simplified thermal energy transport equation is employed to solve for the enthalpy (i), in which viscous dissipation and pressure transport terms are assumed negligible compared to the large convective and conduction heat fluxes typically encountered during phase change (Equation 5.5). As in the momentum equation, an effective conductivity ($(k/\rho)_{\text{eff}}$) is employed to permit incorporation of eddy diffusivity for turbulent flow simulations. A volumetric heat source term ($\dot{q}_{\text{pc}}$) is included to account for the latent heat of phase-change.

$$\frac{\partial i}{\partial t} + \frac{\partial}{\partial x_\mathrm{i}}\left(u_\mathrm{i} i\right) = \frac{\partial}{\partial x_\mathrm{i}}\left[\left(\frac{k}{\rho}\right)_\mathrm{eff} \frac{\partial T}{\partial x_\mathrm{i}}\right] - \dot{q}_\mathrm{pc} \tag{5.5}$$

Finally, the hyperbolic phase transport equation (Equation 5.6) is modified with a generation term to account for the change in liquid volume fraction due to phase change ($\dot{\alpha}_{1,\mathrm{pc}}$). The modified velocity field (u^*) includes corrections based on the gradient of the phase field to compress the interface and counteract numerical diffusion (Weller, 2002).

$$\frac{\partial \alpha_1}{\partial t} + \frac{\partial}{\partial x_\mathrm{i}}\left(u_\mathrm{i}^* \alpha_1\right) = \dot{\alpha}_{1,\mathrm{pc}} \tag{5.6}$$

These governing equations are discretized with the OpenFOAM library following the finite volume approach, and are evaluated using the solution procedure described in Section 5.2.4.

5.2.2 Material properties

Thermophysical material properties are evaluated for each mesh cell. Surface tension (σ) and the phase change enthalpy (i_{LV}) are assumed uniform. The fluid density (ρ), viscosity (μ), and thermal conductivity (k) are defined to be the volume-fraction weighted average of the liquid and vapor phase values:

$$\theta = \alpha_1 \theta_\mathrm{L} + \left(1 - \alpha_1\right)\theta_\mathrm{V} \qquad \theta \in \left[\rho, \mu, k\right] \tag{5.7}$$

A more precise model would evaluate the effective viscosity and thermal conductivity depending on the gradient of the phase field (i.e., whether the transport resistances of the two phases act in series or in parallel, see Marschall *et al.* (2012) and Section 3.2.1). However, such corrections are not significant provided the simulation mesh is sufficiently

fine in the neighborhood of the interface, which is required for other reasons in the proposed phase change model (described in the following sections).

The specific heat of the fluid (c_p) is evaluated using a mass-weighted average for each mesh cell:

$$c_p = \frac{\alpha_1 \rho_L c_{p,L} + (1-\alpha_1)\rho_V c_{p,V}}{\rho} \tag{5.8}$$

The liquid and vapor specific heats are assumed constant in the present investigation; therefore, the fluid enthalpy can be related to temperature as:

$$i = (T - T_{sat})c_p \tag{5.9}$$

The enthalpy of phase change is not included in the above expression because it is accounted for in $\dot{q}_{pc}$.

5.2.3 Phase-change model

The phase change model developed here operates only on mesh connectivity (i.e., on which cells share faces) and volumetric field data (e.g. values of T, i, α_1 … specified for each mesh cell), which are readily available in the OpenFOAM environment. Thus, it does not require geometric interface reconstruction as in other formulations that infer how the interface surface intersects individual mesh cells.

At the beginning of the simulation, a graph of the mesh is formed where nodes and edges correspond to mesh cells and cell faces, respectively. During each time step, a scan is performed over the graph edges. Any *cell pairs* with phase fraction (α_1) values

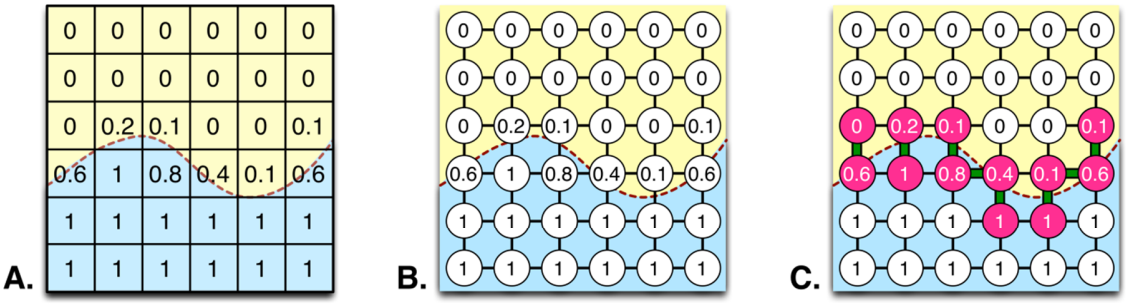

Figure 5.1 – Interface cell identification process: The phase fraction field on mesh cells (A) yields a graph (B) from which cell pairs straddling $\alpha_{1,int}$ = 0.5 form the interface (C)

straddling an interface threshold value (e.g, $\alpha_{1,int} = 0.5$) are added to an interface cell set. This interface cell identification process is summarized graphically in Figure 5.1.

The phase-change phenomena considered in this investigation (condensation and evaporation) are physically localized processes, acting on nearly infinitesimally thin interfaces. However, without geometric reconstruction, it is not possible to identify precisely which cells are intersected by the interface, but only which *cell pairs* straddle the interface. Additionally, this approach supports common initial conditions where adjacent cells have phase values of $\alpha_1 = 0$ and $\alpha_1 = 1$ (i.e., for adjacent vapor and liquid regions), causing the interface to be coplanar with a cell face.

Defining *cell pairs* to contain the interface is consistent with the notion of an infinitesimally thin interface because as the mesh is refined, the total volume of the interface cells approaches 0. Thus, this phase-change model requires a sufficiently fine mesh in the neighborhood of the interface. Cells with a *wall* boundary condition on a face are also added to the interface set, enabling direct condensation on walls.

Next, an initial non-limited volumetric phase change heating rate is evaluated for interface cells:

$$\dot{q}_{\mathrm{pc},0} = \frac{\rho c_{\mathrm{p}} \left(T - T_{\mathrm{sat}} \right)}{\Delta t} \tag{5.10}$$

Here, Δt is the simulation time-step value.

This approach resembles the empirical rate parameter model employed by Yang *et al.* (2008), Fang *et al.* (2010), and Thiele (2010). However, here, the phase change heating rate is defined to force the interface to the saturation temperature at *every* time step, recovering the physical equilibrium condition. In Yang *et al.* (2008), Fang *et al.* (2010), and Thiele (2010), the rate parameter was fixed and was independent of the simulation time step size, permitting the interface temperature to diverge from the saturation temperature. Conceptually, the present model assumes that the interface cells reach the equilibrium condition instantaneously, and thus have negligible internal heat transfer resistance and characteristic thermal time scales of $\tau_{\mathrm{cell}} = 0$. Again, this approach is valid, provided that the mesh is sufficiently fine in the neighborhood of the interface, so that the interface cells contribute a minor portion to the total condensation heat transfer resistance. For example, for a case of evaporation of a liquid film resolved with 50 uniform mesh cells, this approach would under-predict the overall thermal resistance by at most ~2% (corresponding to the cell with the major portion of phase-change in the two-cell thick interface region). If the mesh is refined in the vicinity of the interface, then this error can be further reduced.

Limiting must be applied to the obtained phase change heating rate (Equation 5.10). To ensure physical results, the mass of fluid condensed in a mesh cell during a time step must not exceed the mass of vapor present in that cell (Thiele, 2010). This limiting condition would be necessary, for example, if a small amount of vapor flowed into a highly subcooled liquid cell. If the unlimited phase-change rate result were applied (Equation 5.10), then the cell temperature would be forced to T_{sat}, even if the equilibrium state should still be that of subcooled liquid. Similar results apply for evaporation of liquid.

$$\dot{q}_{\text{lim,mass,cond}} = -\frac{(1-\alpha_1)\rho_V i_{LV}}{\Delta t} \tag{5.11}$$

$$\dot{q}_{\text{lim,mass,evap}} = \frac{\alpha_1 \rho_L i_{LV}}{\Delta t} \tag{5.12}$$

Here, $(1 - \alpha_1)\rho_V$ and $\alpha_1\rho_L$ are the vapor and liquid masses per volume in mesh cells, respectively. $i_{LV}/\Delta t$ is the per-mass heating rate for complete phase-change of fluid in one time step.

For numerical stability in an advection simulation, the CFL condition requires that the local velocity does not transport fields beyond one grid cell per time step ($u_x < \Delta x/\Delta t$). Similarly, the phase-change process in a mesh cell should not sink or source more volume than that of the cell per time step. This condition is ensured by limiting the local volumetric rate of volume change to $1/\Delta t$ so that the local velocity in a cell containing the interface does not exceed the CFL limit:

$$\dot{q}_{\text{lim,CFL,cond}} = -\frac{i_{LV}}{\Delta t}\left(\frac{1}{\rho_V} - \frac{1}{\rho_L}\right)^{-1} \tag{5.13}$$

$$\dot{q}_{\text{lim,CFL,evap}} = \frac{h_{\text{LV}}}{\Delta t}\left(\frac{1}{\rho_{\text{V}}} - \frac{1}{\rho_{\text{L}}}\right)^{-1} \tag{5.14}$$

Here, $(1/\rho_{\text{V}} - 1/\rho_{\text{L}})$ is the change of specific volume due to phase change, and $-i_{\text{LV}}/\Delta t$ is the per-mass heating rate for complete phase change in one time step. In an alternate approach, the simulation time step size could be adjusted dynamically to satisfy this CFL condition. However, this might lead to unnecessarily small time steps due to sharp temperature profiles from initial conditions or few relatively insignificant cells at the intersection of domain boundaries.

Thus, the limiting operations for condensation ($\dot{q}_{\text{pc}} < 0$) and evaporation phase change ($\dot{q}_{\text{pc}} > 0$) are defined as:

$$\dot{q}_{\text{pc}} = \begin{cases} \max\left(\dot{q}_{\text{pc,0}}\ ,\ \dot{q}_{\text{lim,mass,cond}}\ ,\ \dot{q}_{\text{lim,CFL,cond}}\right) & \dot{q}_{\text{pc,0}} < 0 \\ \min\left(\dot{q}_{\text{pc,0}}\ ,\ \dot{q}_{\text{lim,mass,evap}}\ ,\ \dot{q}_{\text{lim,CFL,evap}}\right) & \dot{q}_{\text{pc,0}} > 0 \end{cases} \tag{5.15}$$

Once $\dot{q}_{\text{pc}}$ is obtained for interface cells, the volumetric generation ($\dot{v}_{\text{pc}}$) and phase fraction generation ($\dot{\alpha}_{1,\text{pc}}$) terms can be evaluated:

$$\dot{v}_{\text{pc}} = \frac{\dot{q}_{\text{pc}}}{i_{\text{LV}}}\left(\frac{1}{\rho_{\text{V}}} - \frac{1}{\rho_{\text{L}}}\right) \tag{5.16}$$

$$\dot{\alpha}_{1,\text{pc}} = -\frac{\dot{q}_{\text{pc}}}{\rho i_{\text{LV}}} \tag{5.17}$$

5.2.4 Algorithm implementation

The phase-change modeling approach is implemented using the OpenFOAM finite volume library (2014), and is based on the packaged interFoam VOF solver (Weller,

2002). OpenFOAM provides implementations of many key components needed for continuum mechanics simulation including: mesh reading, differencing and upwinding schemes, linear system solvers, and algorithm parallelization, and enables intuitive definition of field operations and PDEs (Weller *et al.*, 1998). The interFoam solver supports adiabatic incompressible two-phase fluid-fluid flows without phase change. No geometric interface reconstruction or tracking is performed in interFoam; rather, a compressive velocity field is superimposed in the vicinity of the interface to counteract numerical diffusion. The condensation flow solver developed here adds a thermal energy transport equation, modifies the base equations with phase change terms, and provides support for generic phase-change models. Thus, phase-change models can be selected by the user during runtime, and new models can be easily incorporated.

At startup, the solver loads the mesh, reads in fields and boundary conditions, and initializes sub-models for two-phase fluid properties, turbulence (if selected), and the phase-change model. During this initialization stage, the phase-change model constructs the graph of mesh-cell connectivity used to identify interface cells.

The main solver loop is then initiated. First, the time step is dynamically modified to ensure numerical stability. In the base interFoam solver, the time step is only adjusted to satisfy the CFL condition. Here, it is also corrected to ensure that the thermal diffusion stability condition is satisfied for all cells *i*:

$$\Delta t \leq l \min\left[\Delta^2 \Big/ \left(\frac{k}{\rho c_\mathrm{p}} \right)_\mathrm{eff} \right]_\mathrm{i} \tag{5.18}$$

Here, l is a user-defined constraint (typically 1/4 or 1/6 in 2D or 3D simulations, respectively) and Δ is the minimum cell-edge length. This condition in not typically considered in fluid flow simulations, but is necessary for phase-change simulations where thermal conduction plays a significant role and the mesh is finely graded near the interface.

Next, the two-phase fluid mixture properties and turbulence quantities are updated. The phase-change model is then evaluated, and the $\dot{q}_{\mathrm{pc}}$, $\dot{v}_{\mathrm{pc}}$, and $\dot{\alpha}_{1,\mathrm{pc}}$ fields are obtained.

The discretized phase fraction equation (Equation 5.6) is then solved for a user-defined number of sub-time steps (typically 2 – 3) using the multidimensional universal limiter with explicit solution (MULES) solver. This solver is included in the OpenFOAM library, and performs conservative solution of hyperbolic convective transport equations with defined bounds (0 and 1 for α_1).

Once the updated phase field is obtained, the program enters the pressure-velocity loop, in which p and u are corrected in alternating fashion. The process of sequentially correcting the pressure and velocity fields is commonly referred to as: Pressure Implicit with Splitting of Operators (PISO) (Issa, 1982). In the OpenFOAM environment, PISO is repeated for multiple iterations at each time step. This process is referred to as merged PISO-SIMPLE or the PIMPLE process, where the Semi-Implicit Method for Pressure-Linked Equations (SIMPLE) is an iterative pressure-velocity solution algorithm for steady flows (Patankar, 1980).

First the matrix equation for the momentum equation is formed. Then the inner pressure-velocity correction process (PISO) is initiated. In PISO, an intermediate velocity field is first obtained, and the cell-face volume fluxes ($\nabla\cdot\phi$) are evaluated and corrected for gravitational forces, the continuum surface tension force, and boundary conditions. The pressure-Poisson equation is then formed and solved. Following the approach of Weller *et al.* (1998), the coefficients of the pressure equation are obtained from the diagonal entries of the momentum matrix equation ($1/A_D$). For *incompressible* flows, the pressure equation would be:

$$\frac{\partial}{\partial x_i}\left(\frac{1}{A_D}\frac{\partial p_{\rho gh}}{\partial x_i}\right)=\nabla\cdot\phi \tag{5.19}$$

Here, $\nabla\cdot\phi$ is the numerical equivalent of the divergence of the velocity field ($\partial u_i/\partial x_i$) for a cell. As the pressure-velocity loop (PIMPLE) is iterated, $\nabla\cdot\phi$ approaches zero, recovering the incompressible continuity condition. However, for the phase-change flows investigated here, $\partial u_i/\partial x_i=\dot{v}_{pc}$. Thus, the pressure equation becomes:

$$\frac{\partial}{\partial x_i}\cdot\left(\frac{1}{A_D}\frac{\partial p_{\rho gh}}{\partial x_i}\right)=\nabla\cdot\phi-\dot{v}_{pc} \tag{5.20}$$

After the pressure equation is solved, the velocity field is corrected with the resulting pressure field, and boundary conditions are updated. The pressure-velocity loop (PIMPLE) continues for a user specified number of iterations.

Finally, the thermal energy transport subsection is entered. First, the enthalpy field is reevaluated from the temperature field (Equation 5.9). Then, for a user-defined number of

steps (typically 2 – 3), alternating correction of the energy equation (Equation 5.5) and update of the temperature field ($T(i)$) are performed. This process is employed because temperature and enthalpy are coupled, but are not directly proportional for many fluids, and thus cannot be solved together in a single system of linear equations. Alternating correction of the i and T fields leads to convergence for both fields in a similar fashion to the PIMPLE algorithm (OpenFOAM Foundation, 2014) for u and $p_{\rho gh}$. The actual evaluated thermal energy equation (Equation 5.21) incorporates an artificial enthalpy diffusion term. This is added to avoid solution "checker-boarding," an effect that occurs when neighboring cells are decoupled in a first order differential equation, leading to alternating field values.

$$\left\{\frac{\partial}{\partial t}(\ )+\frac{\partial}{\partial x_\mathrm{i}}(u_\mathrm{i}\,\cdot)-\frac{\partial}{\partial x_\mathrm{i}}\left[\left(\frac{k}{\rho c_\mathrm{p}}\right)_\mathrm{eff}\frac{\partial}{\partial x_\mathrm{i}}(\ )\right]\right\} i=\frac{\partial}{\partial x_\mathrm{i}}\left[\left(\frac{k}{\rho}\right)_\mathrm{eff}\frac{\partial T}{\partial x_\mathrm{i}}-\left(\frac{k}{\rho c_\mathrm{p}}\right)_\mathrm{eff}\frac{\partial i}{\partial x_\mathrm{i}}\right]-\dot{q}_\mathrm{pc} \quad (5.21)$$

In Equation 5.21, terms on the left side of the matrix equation are solved implicitly (indicated by the operator notation), and terms on the right side are applied explicitly.

The main solver loop iterates until program termination. A summary of the simulation algorithm is presented in Figure 5.2. This simulation approach is first evaluated for canonical condensation phase change phenomena (Section 5.3), and then refined to improve performance for evaporative phase change in the distributed-heated BPG design (Section 5.4).

5.3 Validation for Condensation Phase Change

5.3.1 Horizontal film condensation

The phase-change model and solver developed here are first tested for grid independence and accuracy for horizontal film condensation on an infinite plane – a

1. Initialize simulation data and phase change model
2. **WHILE** $t < t_{end}$ **DO**
    1. Update Δt for stability
    2. Update fluid properties
    3. Update phase change model ($\dot{q}_{pc}$, $\dot{v}_{pc}$, $\dot{\alpha}_{pc}$)
    4. Phase equation sub-cycle
    5. **DO** PIMPLE
        1. Form u equation
        2. PISO
            1. Obtain and correct face fluxes (ϕ)
            2. Solve p-Poisson equation
            3. Correct u
    6. **LOOP**
    7. Update $i(T)$
    8. **DO** Energy Loop
        1. Solve i equation
        2. Update $T(i)$
    9. **LOOP**
3. **LOOP**

Figure 5.2 – Summary of phase-change flow solver algorithm

configuration with relatively weak dynamic effects. In this case, vapor condenses to form a liquid film on the top surface of an isothermal plate (at T_w) in a pure atmosphere. This is similar to the horizontal film validation studies conducted by Juric and Tryggvason (1998) and Thiele (2010).

By assuming a linear temperature profile from T_{wall} at the lower wall to T_{sat} at the interface, a control volume analysis leads to an analytical solution for the film thickness $\delta_{mod}(t)$:

$$\delta_{mod}(t) = \left[2t \left(\frac{k}{\rho c_p} \right)_L \left(\frac{1}{2} + \frac{i_{LV}}{c_{p,L} \Delta T} \right)^{-1} \right]^{1/2} \tag{5.22}$$

Table 5.1 – Properties of saturated isobutane at 25°C

Property	Liquid	Vapor
ρ (kg m^{-3})	550.6	9.12
μ (kg m^{-1} s^{-1})	$1.51 \cdot 10^{-4}$	$7.73 \cdot 10^{-6}$
k (w m^{-1} K^{-1})	0.089	0.017
c_p (kJ kg^{-1} K^{-1})	2.45	1.82
σ (kg s^{-2})	0.0099	
i_{LV} (kJ kg^{-1})	329.4	

Here, the initial condition of $\delta(t = 0) = 0$ is assumed.

Isobutane at $p_{sat}(25°C)$ is selected as the modeled fluid due to its moderate values of liquid-to-vapor property ratios and phase change enthalpy ($\rho_L/\rho_V = 60.4$, Ja = 0.037 for $\Delta T = 5$ K). Simulation of fluids with greater liquid-to-vapor property ratios and phase change enthalpies requires finer meshes and smaller time steps to adequately resolve the increased range of scales and heat and mass flux magnitudes. Relevant thermophysical properties for saturated isobutane at 25°C are summarized in Table 5.1.

A 2D rectangular domain is employed with horizontal and vertical dimensions of 5.0 mm and 1.0 mm, respectively ($0 \le x \le 5$ mm, $0 \le y \le 1$ mm). The mesh is defined with four uniform cells per horizontal row, and grading in the vertical direction with cells in the bottom row being half the height of the uppermost row. Zero-normal-gradient boundary conditions are applied to the vertical sides of the domain (i.e., $\nabla\theta \cdot \hat{n} = 0$, or equivalently, $\partial\theta/\partial x = 0$ for all solved fields θ). Thus, the domain represents a section of an infinitely wide condensing film. The bottom wall is set to T_w = 20°C, and the top "freestream" boundary is set to the saturation temperature: T_{sat} = 25°C. All fluid entering

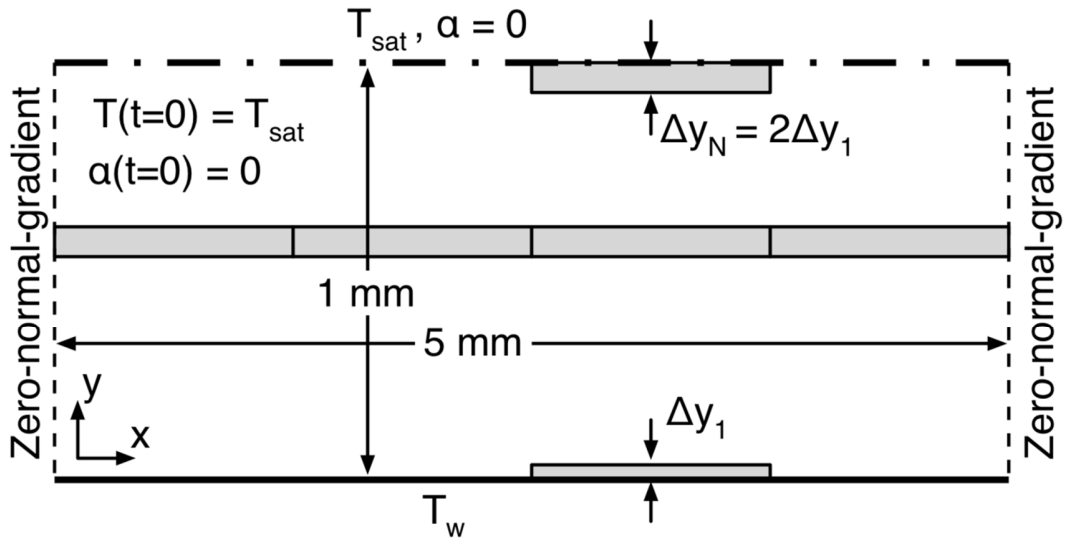

Figure 5.3 – Geometry for horizontal film condensation studies

through the freestream boundary is vapor ($\alpha_1 = 0$). The domain is initialized with uniform conditions $T = 25°C$ (T_{sat}) and $\alpha_1 = 0$ (all vapor). A schematic of the simulation domain is presented in Figure 5.3.

The grid independence study is conducted for cases of n = 84, 112, 150, 200, and 267 rows in the y-direction. The simulation time step is modified dynamically following the method described in the algorithm implementation section. Results are recorded at every 0.02 simulation seconds (ss) for 5 ss.

The development of the liquid film thicknesses and relative errors are presented for representative cases in Figure 5.4. Here, the film thickness is evaluated as the total liquid volume divided by the base area. While the analytical solution (δ_{mod}) is independent of x, numerical solution leads to slight variations in the x direction.

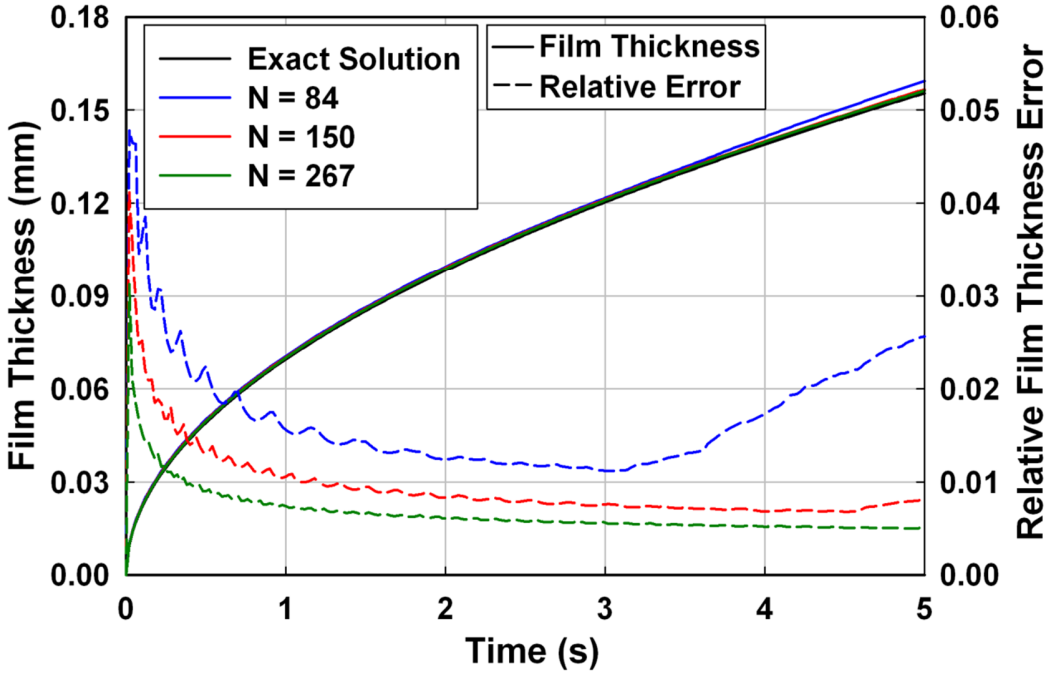

Figure 5.4 – Development of horizontal condensing film thickness for varying mesh resolutions

Relative errors in predicted film thickness are greater during the beginning of simulations (0.03 – 0.05) because the liquid films are initially under-resolved on the fixed meshes. After about 1 s of simulation, these relative errors decrease to 0.005 – 0.015, but eventually begin to grow on the coarser meshes (N = 84, 112, 150). Integrated simulation error can be estimated as the film thickness error ($|\delta_{sim} - \delta_{mod}|$) summed over time steps i, weighted by Δt (0.02 s) (Table 5.2):

$$E = \sum_i \left|\delta_{sim} - \delta_{mod}\right| \Delta t \tag{5.23}$$

A power-law curve fit to these results data indicates that the total error for the condensation study scales with the mesh resolution as $E \propto \Delta y^{0.84}$ ($R^2 = 0.93$).

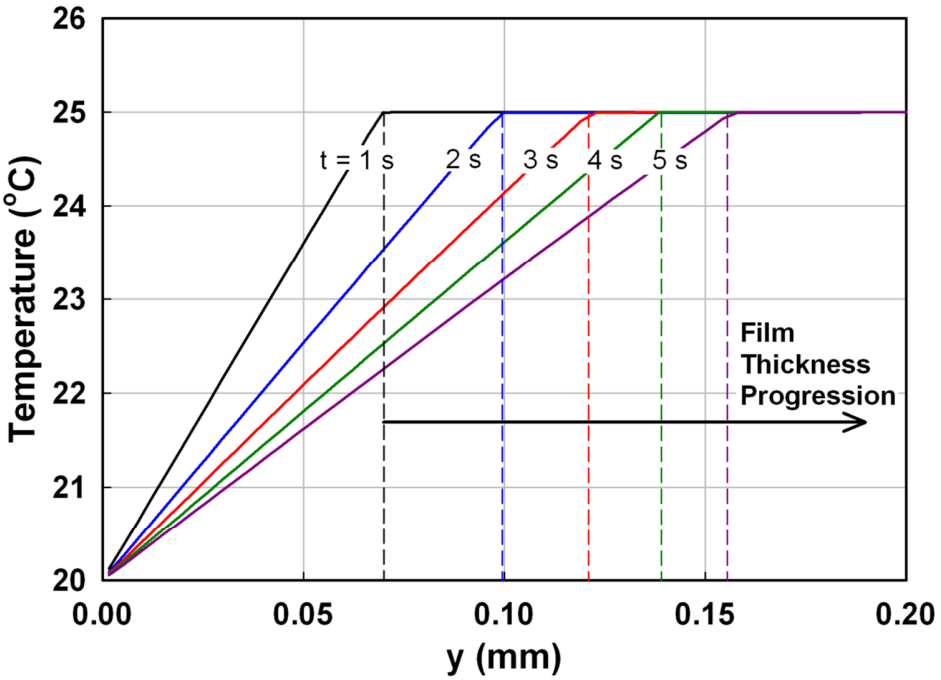

Figure 5.5 – Horizontal condensing film temperature profiles

Representative vertical centerline temperature plots for the n = 200 case are presented in Figure 5.5. These results indicate that linear temperature profiles from T_{wall} to T_{sat} are obtained in the liquid film, in agreement with the analytical solution.

Table 5.2 – Horizontal film condensation simulation convergence

	Simulation (n)					
	84	**112**	**150**	**200**	**267**	**Exact**
$\delta(t = 5)$ (mm)	0.1594	0.1569	0.1566	0.1563	0.1562	0.1554
E (μm s)	8.51	5.25	4.32	3.61	3.11	

5.3.2 Smooth falling-film condensation

Smooth laminar falling-film condensation on a vertical isothermal wall represents a phase-change configuration with more complex dynamics, but for which analytical solutions can still be obtained. Following the Nusselt analysis (Nusselt, 1916), the temperature varies linearly from T_{wall} at the wall to T_{sat} at the interface, and the film thickness and velocity profiles are:

$$\delta_{mod} = \left[\frac{3\Gamma\mu_L}{\rho_L(\rho_L - \rho_V)g} \right]^{1/3} \tag{5.24}$$

$$u_{mod}(x) = \frac{3\Gamma}{\rho_L \delta}\left[\frac{x}{\delta} - \frac{1}{2}\left(\frac{x}{\delta}\right)^2 \right] \tag{5.25}$$

Here, Γ is the film mass flow per unit width of the vertical plate (kg m^{-1} s^{-1}).

The condensation simulations are conducted in a 2D rectangular simulation domain (~2.5 mm wide × ~25 mm tall). A thin guide vane (50 μm wide by 0.25 mm tall) is positioned so that the inlet film thickness corresponds to the value obtained from Equation 5.24. The guide vane is employed to avoid numerical instabilities that can arise if the liquid-phase fixed-velocity and vapor-phase zero-normal-velocity-gradient boundary conditions are specified on adjacent mesh faces. In particular, inlet liquid can sometimes be drawn out of the domain through the vapor boundary section if these conditions are applied side-by-side. The wall temperature is set to T_{wall} (20°C), and the vapor boundaries (top and freestream) are set to T_{sat} (25°C). The guide vane and outlet sections are modeled as zero-normal-temperature-gradient (adiabatic) surfaces. The

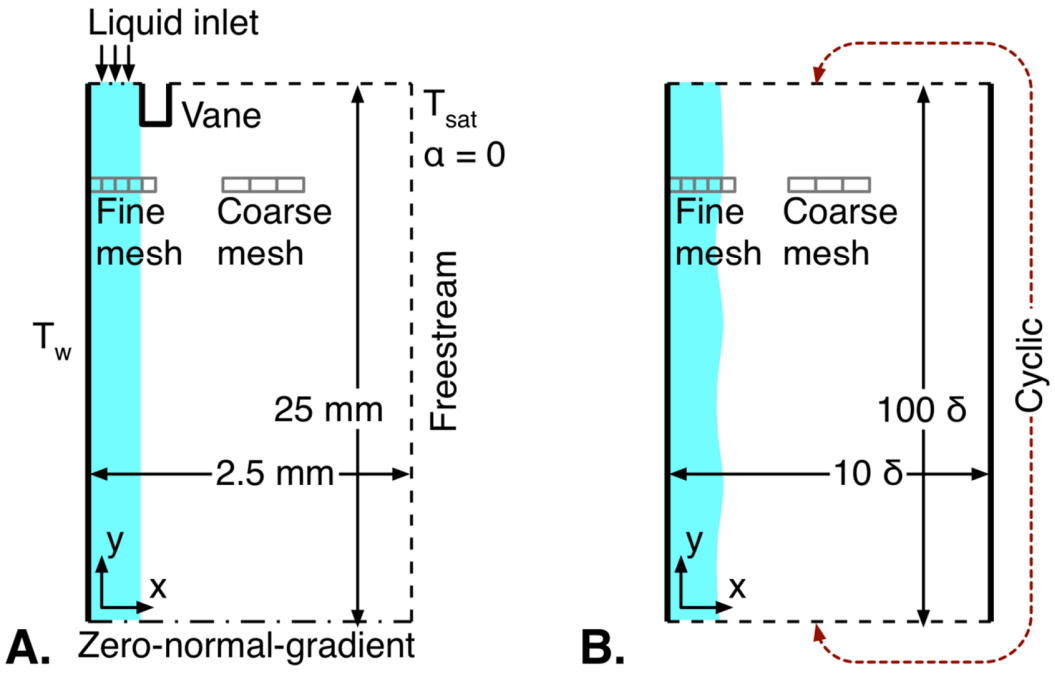

Figure 5.6 – (**a**) Smooth and (**b**) wavy falling-film simulation domains

liquid inlet flow is specified using the analytical temperature (linear) and velocity (Equation 5.25) profiles. The vapor boundaries are set with zero-normal-gradient velocity and inlet $\alpha_1 = 0$ (vapor) conditions. The bottom outlet is set with zero-normal-gradient α_1 and u conditions. A rectilinear mesh is employed with fine cells in the region of the film and guide vane (Δx = 3 μm, Δy = 11 μm for min(δ_{mod}) = 66.4 μm). In the vapor bulk region, cells are graded in the x-direction, becoming coarser towards the freestream. A schematic of the falling-film condensation domain and initial conditions is presented in Figure 5.6a.

As before, fluid properties correspond to saturated isobutane at 25°C. A range of inlet liquid flow rates and film thicknesses is selected corresponding to Re_f = 50, 100, 200, 400, 800, 1600 ($Re_f = 4\,\Gamma/\mu_L$). Assuming negligible interfacial shear, the wall shear stress

Table 5.3 – Smooth falling-film condensation heat fluxes

	Film Reynolds Number					
Heat Flux	**50**	**100**	**200**	**400**	**800**	**1600**
Simulated (W m^{-2})	6608	5305	4234	3364	2654	2107
Analytical (W m^{-2})	6471	5254	4211	3356	2668	2119
Relative Error	0.021	0.010	0.005	0.003	0.005	0.006

can be evaluated as: $\tau_{\text{wall}} = \delta \rho_{\text{L}} g$, and dimensionless wall distance as: $y^+ = \rho_{\text{L}} \sqrt{\delta g} \,/ \mu_{\text{L}}$. Using this metric, the wall-cell center points range from $y^+ = 0.31$ for the $\text{Re}_\text{f} = 50$ case to $y^+ = 0.55$ for the $\text{Re}_\text{f} = 1600$ case. These low values ($y^+ \lesssim 5$) indicate that near-wall fluid-flow and heat-transfer physics are well resolved. The falling-film condensation simulations are conducted for 0.5 seconds with values recorded at 0.025 s intervals.

For the six cases considered, the average wall heat fluxes agree with those obtained from the Nusselt analytical solution (Nusselt, 1916) to within a relative error of 0.021. Results for average wall heat fluxes are summarized in Table 5.3.

5.3.3 Wavy falling-film condensation

More detailed analyses indicate that smooth falling films on vertical plates are inherently unstable (Benjamin, 1957), and wavy behavior is initiated at non-zero Reynolds numbers. Waves tend to generate thin film regions with reduced heat transfer resistance, yielding increased condensation rates (Jayanti and Hewitt, 1996).

Analytical solutions for wavy film profiles are not readily available. Thus, a set of adiabatic falling-film simulations was performed to obtain "fully developed" wavy conditions to provide inlet conditions for the condensation studies. For these studies, 2D

rectilinear meshes were employed with wall conditions on the vertical boundaries. These studies were initialized with uniform stagnant films on the left wall with thicknesses (δ) corresponding to Re_f = 50, 100, 200, 400, and 800 (based on Equations 5.24 – 5.25). The right vertical wall was introduced to provide shear stress to the film interface, ensuring the development of waves. The top and bottom surfaces were mapped with *cyclic* boundary conditions for all fields, enabling the falling film to repeatedly flow through the domain so that slight interface disturbances can grow into fully developed waves. These initiating disturbances are deterministic and numerical in nature, resulting from floating point rounding error or iterative solution of the discretized equations to finite tolerances. However, the stable steady-state waves should be similar to those initiated by physical mechanisms (e.g., fluid velocity fluctuations, imperfect initial conditions). The mesh was graded finely near the left wall ($\Delta x = \delta/15$ for $x < 2.5\delta$) and more coarsely in the vapor bulk region with uniform $\Delta x = \delta/10$. The domain extents were scaled with δ as: $0 \le x \le 10\delta$ and $0 \le y \le 100\delta$. As before, fluid properties were selected to match saturated isobutane at 25°C. A schematic of the domain is presented in Figure 5.6b.

A modified version of the interFoam (Weller, 2002) solver was employed for these simulations in which the hydrostatic term was removed from the velocity correction, and applied instead as an explicit source term in the momentum equation ($\vec{f}_B = (\rho_L - \rho)\vec{g}$, see Section 3.2.1). This approach allows pressure continuity across the cyclic top and bottom boundaries despite the hydrostatic difference.

The five wavy film cases were simulated for 1 ss. Final wavy film profiles for t = 1.0 ss are presented in Figure 5.7.

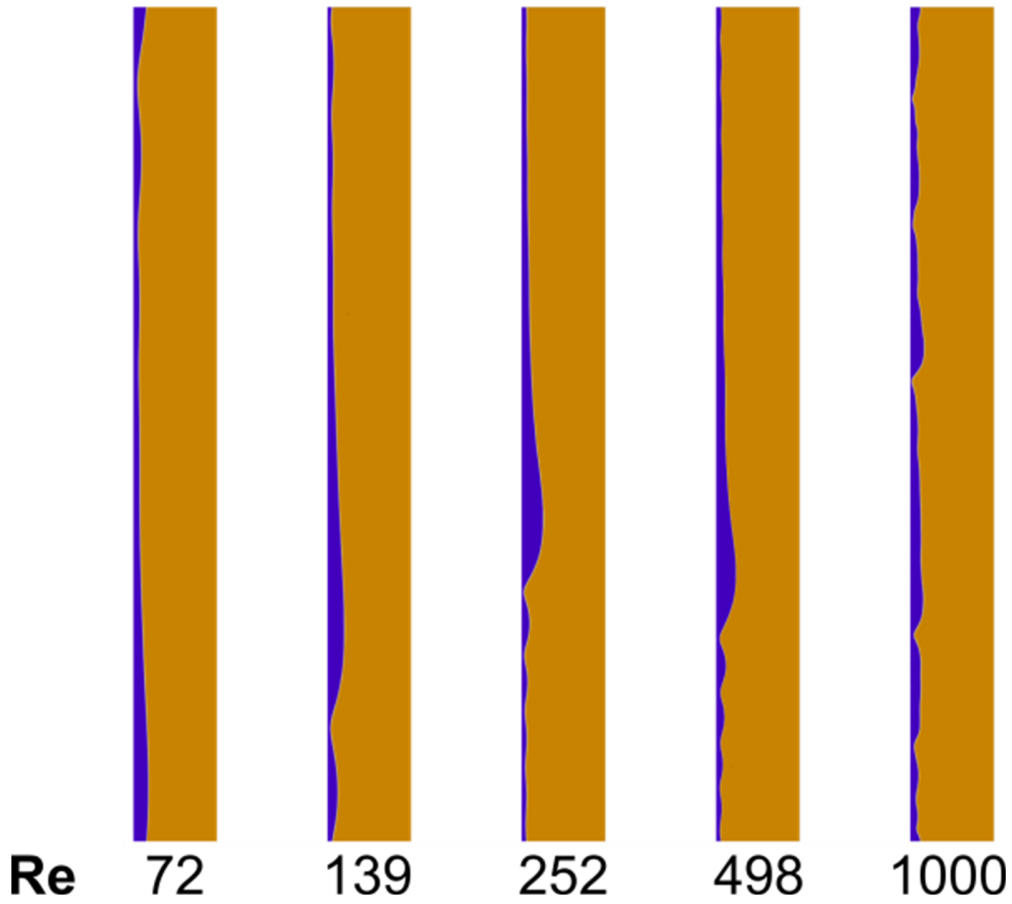

Figure 5.7 – Fully developed wavy falling-film profiles

Averaged Re_f values from $0.5 \le t \le 1$ ss based on liquid mass fluxes through the bottom surface at 0.0025 ss checkpoints are summarized in Table 5.4. For given $\overline{Re_f}$, the wavy film simulations predict lower $\overline{\delta}$ than the Nusselt model, consistent with the observations of Jayanti and Hewitt (1996).

Following the approach presented in the previous section, average wall-cell center point dimensionless wall distances range from $y^+ = 0.41$ for $Re_{f,an} = 50$ to $y^+ = 1.64$ for $Re_{f,an} = 800$. Maximum values, based on local film thickness, were found to range from

Table 5.4 – Wavy falling-film Reynolds numbers

Film thickness $\overline{\delta}$ (μm)	66	84	105	133	167
Nusselt $\mathrm{Re}_f\left(\overline{\delta}\right)$	50	100	200	400	800
Simulation $\overline{\mathrm{Re}_f}$	72	139	252	498	1000

$y^+ = 0.55$ for $\mathrm{Re}_{f,an} = 50$ to $y^+ = 2.15$ for $\mathrm{Re}_{f,an} = 800$. As before, these relatively low values of y^+ indicate that near-wall transport phenomena are well resolved.

Condensation studies are performed on the same meshes employed for the adiabatic wavy film simulations. The left wall is assigned a uniform surface temperature (T_{wall} = 20°C). The right vertical boundary is modeled with a freestream condition at T_{sat}, to allow inflow of "makeup" vapor for the condensed fluid. Outflow (zero-normal-velocity-gradient) conditions are applied to the bottom boundary. The inlet conditions (for α_1 and u) to the top boundary are adopted from the outlet conditions of the adiabatic wavy simulation. A linear temperature profile from T_{wall} to T_{sat} is applied to the top boundary to match the inlet film thickness. Initial conditions are mapped from t = 0.5 ss later from the adiabatic studies, allowing waves to develop. The condensation simulations are performed for 0.5 ss.

While exact solutions for wavy falling-film condensation heat transfer are not readily available, experimentally based correlations are available in the literature. Average heat fluxes obtained from the present simulations are compared with results from widely employed heat transfer correlations by Chen *et al.* (1987), Butterworth (1983), and Fujita

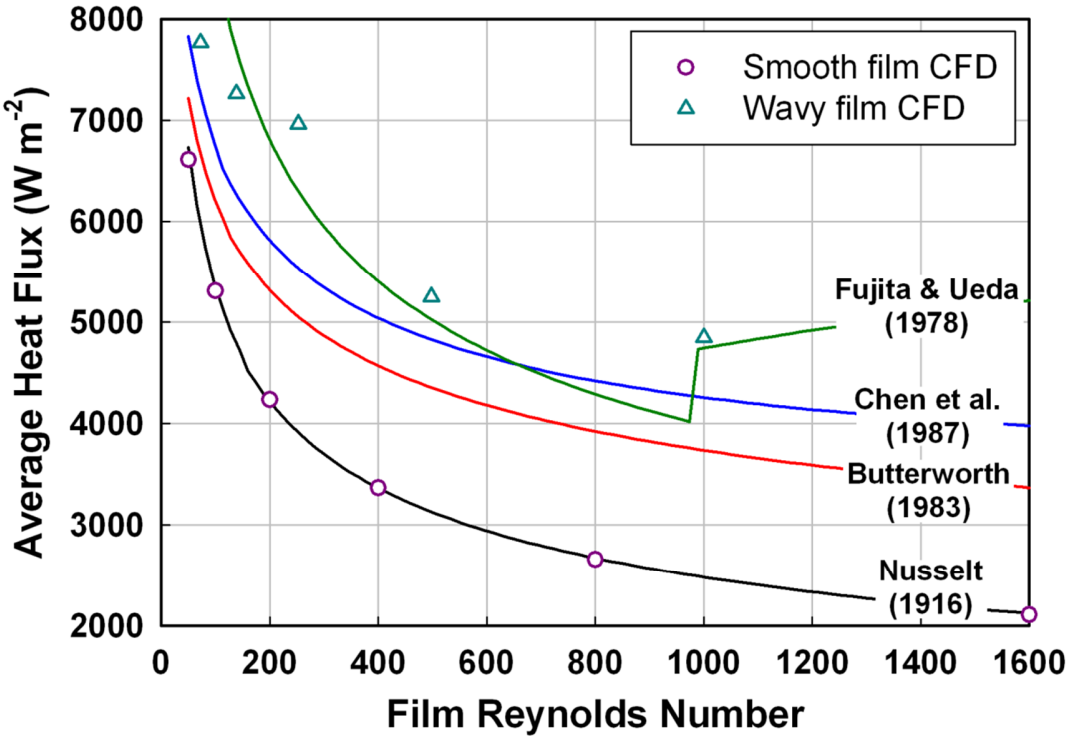

Figure 5.8 – Comparison of simulation and correlation heat flux predictions

and Ueda (1978) (no phase change heat transfer) (Figure 5.8). The heat transfer rates predicted using the Nusselt (1916) solution are also reported for reference.

The simulated wavy film condensation heat flux values are generally higher than predictions from correlations. Overall trends of steeply decreasing $q(\mathrm{Re_f})$ at lower $\mathrm{Re_f}$ (72 – 498) and more gradual reduction at higher $\mathrm{Re_f}$ (498 – 1000) agree with results from (Butterworth, 1983; Chen *et al.*, 1987; Nusselt, 1916). Additionally, all simulation heat fluxes lie within 11% of the locus of results from these models. More rigorous comparison is difficult due to the wide range of experimental conditions employed to develop these correlations. Causes of discrepancies with correlations could include:

1. 3D effects – studies conducted on 2D meshes cannot account for 3D wave structures and dynamics.
2. Long wavelength effects – simulation domains were 100δ in length, and thus suppress longer waveforms.
3. Fully developed waves – simulated waves were allowed to grow to "fully developed" forms, and may differ from developing waves observed in condensation experiments.
4. Assumed temperature profile – the assumed linear inlet temperature distributions in the films may differ from physical behavior.
5. Spurious currents – the employed standard continuum surface tension force model has been shown to generate spurious currents (Deshpande *et al.*, 2012), which may increase wave amplitude and thus wall heat flux. Alternate surface tension formulations (e.g., that of Raeini *et al.* (2012)) may reduce this effect.

5.3.4 Discussion of validation study results

Results from the horizontal film condensation studies indicate that the phase-change model developed here achieves grid independence at a nearly linear rate ($E \propto \Delta y^{0.84}$). While the approach of forcing interface cells to the equilibrium condition resembles that employed in earlier empirical rate parameter models (Fang *et al.*, 2010; Thiele, 2010; Yang *et al.*, 2008), grid independence is obtained here by dynamically matching the condensation rate to the time step size. Close agreement with analytical results was achieved for the more complex case of smooth falling-film condensation, with a maximum relative wall heat flux error of 2%. Reasonable agreement with experimentally developed heat transfer correlations was obtained for wavy falling-film condensation, but further investigation into this topic is warranted. These results demonstrate the applicability of the proposed model and solver to problems of engineering interest.

One limitation of the present phase-change model is the assumption of negligible internal heat transfer resistance and thermal time scales of interface cells (i.e. $T = T_{sat}$, always, for interface cells). Thus, relatively fine meshes are required in the neighborhood of the interface for accurate phase change predictions. However, even adiabatic interface-capturing multiphase flow solvers (e.g. interFoam (Weller, 2002)) require fine meshes near interfaces to resolve effects such as surface tension and interfacial shear. Therefore, the net computational cost of applying this condensation model to a sufficiently resolved adiabatic simulation may be relatively small.

5.4 Distributed-Heated Bubble-Pump Generator Flow-Boiling Simulations

5.4.1 Simulation of evaporation phase change

The formulated governing equations and analytical phase-change source terms are equally valid for the cases of condensation and evaporation (Sections 5.2.1 – 5.2.3). However, the nature of evaporation phase change necessitates different implementation and numerical techniques for multiple reasons:

1. From a thermodynamic perspective, the fluid phases in film condensation are in equilibrium states (subcooled liquid and saturated vapor). However, the liquid in film evaporation is superheated. In practice, film evaporation transitions to boiling under certain conditions. Thus an evaporation model must incorporate logic to suppress or model boiling.
2. Condensation is a numerically beneficial process in VOF simulations because it effects a volumetric sink on the interface. This yields compressive velocity currents that counteract numerical diffusion of the interface. In contrast, the volumetric source generated during evaporation acts to spread the interface, and places an additional

burden on interface compression schemes. Additionally, this volumetric source can cause false liquid or vapor production.

3. Film condensation is a stable process. For example, over-condensation in one time step will yield an overly-thick liquid film with increased heat transfer resistance, reducing the condensation rate in future time steps. In contrast, over-evaporation of a liquid film initiates a compounding process in which the film thickness and heat transfer resistance successively decrease, leading to "runaway" evaporation and dryout.

The phase-change model proposed in Section 5.2.3 is modified to address these challenges of evaporation phenomena. First, the phase-change heating term is forced to 0 for super-heated non-interface-containing wall-cells. This suppresses evaporation at the liquid-wall interface. Evaporation can still occur at the liquid-vapor interfaces of bubbles attached to heated walls, which is the physical mode of nucleate boiling. However, this approach does not permit the spontaneous formation of vapor bubbles on a completely wetted surface.

The second challenge (interface-spreading) is addressed with two modifications to the phase-change model. First, different interface identification threshold values ($\alpha_{1,\text{int}}$) are employed for condensation and evaporation. Here $\alpha_{1,\text{int}} = 0.9$ is employed for condensation ($T < T_{\text{sat}}$) and $\alpha_{1,\text{int}} = 0.1$ for evaporation ($T > T_{\text{sat}}$). This approach applies the evaporation source terms ($\dot{v}_{\text{pc}}$) on the "vapor side" of the interface. Thus, the volumetric source from evaporation will transport less and generate less liquid because the advective phase-fraction flux on vapor-side cell faces, $(u\alpha_1)_{\text{f}}$, will be small.

Second, a phase-change volume source splitting operation is applied, similar to the approach of Hardt and Wondra (2008). In this process, the vapor-phase portion of $\dot{v}_{\mathrm{pc}}$ $\left(\dot{q}_{\mathrm{pc}}/\left(i_{\mathrm{LV}}\rho_{\mathrm{V}}\right)\right)$ is shifted away from interface cells interface to the vapor region (down the gradient of α_{l}). Similarly, the liquid-phase portion of $\dot{v}_{\mathrm{pc}}$ $\left(-\dot{q}_{\mathrm{pc}}/\left(i_{\mathrm{LV}}\rho_{\mathrm{L}}\right)\right)$ is shifted into the liquid region. $\dot{v}_{\mathrm{pc}}$ is transferred from each interface cell to neighboring cells with distribution weighted by the relative dot product of the gradient of the phase-fraction field and cell-face area normal vectors $\left(\left(\partial\alpha_{\mathrm{l}}/\partial x_{\mathrm{i}}\right)A_{\mathrm{f,i}}\right)$. This process is applied in multiple passes (4) to ensure that potential $\dot{v}_{\mathrm{pc}}$ transfer between neighboring interface cells is almost entirely shifted to the vapor and liquid bulk regions. This algorithm is illustrated schematically in Figure 5.9. These two modifications to the phase-change model lead to slightly increased effective interface thickness. However, the overall algorithm still recovers the governing continuum scale phenomena, provided that the mesh is sufficiently resolved in the vicinity of the interface.

The third challenge of "runaway" evaporation is more fundamental. The physical counterpart (film dryout) to the numerical problem is a major safety concern in many thermal energy systems. This issue can only be addressed by reducing numerical discretization error. In the present investigation, fine meshes and small integration time steps are employed to limit error accumulation. Higher order discretization and integration schemes could also be employed in future studies. In the following section, the modified phase-change model is assessed for the problem of horizontal film evaporation (Stefan problem).

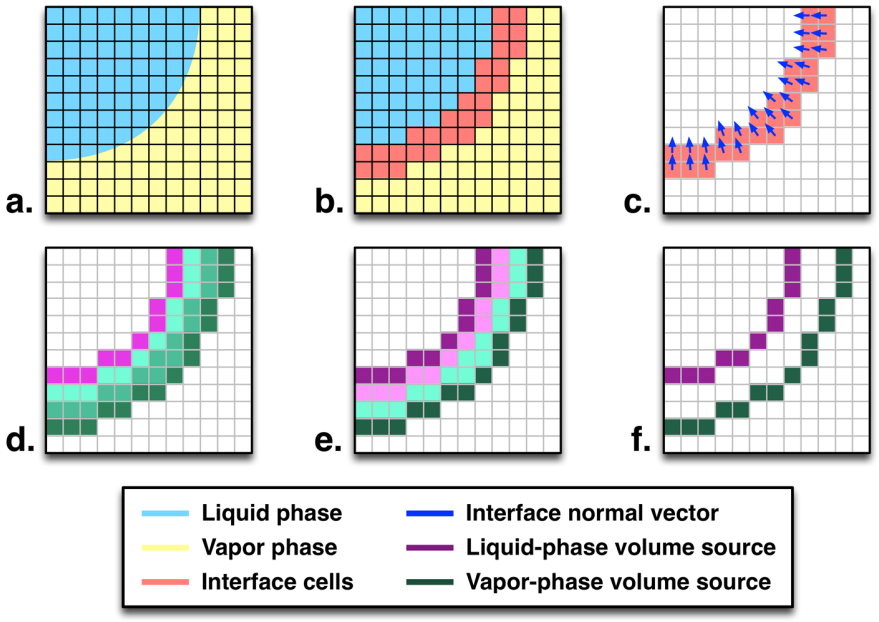

Figure 5.9 – Schematic of dilatation rate source ($\dot{v}_{pc}$) splitting and shifting process. **a**. Liquid-vapor interface profile, **b**. Interface-cell identification, **c**. Interface normal vector field, **d-f**. Progressive shifting of liquid and vapor phase-change volume sources away from interface.

5.4.2 Evaporative phase-change model assessment

The proposed evaporative phase-change model is applied to horizontal liquid film evaporation on a heated surface. The working fluid (isobutane at T_{sat} = 25°C), problem geometry, and top and side wall boundary conditions are the same as for the horizontal condensation studies (Section 5.3.1, Figure 5.3). The lower wall is set to 30°C, and 200 cells are employed in the vertical direction. The liquid film is set to an initial thickness of δ_i = 0.201 mm with a linear temperature profile from T_{wall} to T_{sat} in the film. The exact solution for developing film thickness is:

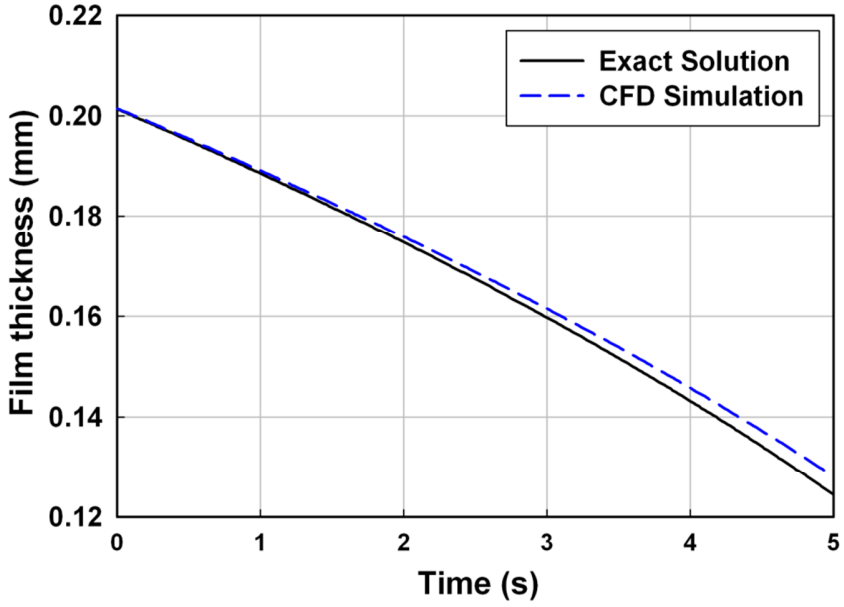

Figure 5.10 – Development of simulated evaporating horizontal film thickness

$$\delta_{\text{mod}}(t) = \left[\delta_{\text{i}}^2 + 2t \left(\frac{k}{\rho c_{\text{p}}} \right)_{\text{L}} \left(\frac{1}{2} - \frac{i_{\text{LV}}}{c_{\text{p,L}} \Delta T} \right)^{-1} \right]^{1/2} \tag{5.26}$$

Analytical model and simulation results for the evaporating film thickness are presented in Figure 5.10. Relative errors in evaporated film thickness ($|\delta_{\text{sim}} - \delta_{\text{mod}}| / (\delta_{\text{i}} - \delta_{\text{mod}})$) reach 4.8% after 5 simulation seconds. This error is relatively small, but is still significantly greater than was found for the corresponding condensation case with the same mesh resolution (0.6% error).

Representative interface-region phase-fraction (α_1) profiles for the horizontal film condensation and evaporation cases are presented in Table 5.5. Due to the compressive nature of condensation phase change ($\dot{v}_{\text{pc}} < 0$), the interface is only three cells thick. In contrast, evaporation causes interface dispersion, requiring a thickness of five cells for

Table 5.5 – Representative phase-fraction fields (α_1) in the vicinity of the interface for condensation and evaporation simulations

Condensation	Evaporation
1	0.9999980
1	0.9993100
1	0.9470470
0.971934	0.4134600
0	0.0103317
0	0.0001184
0	0.0000155

the transition from $\alpha_1 < 0.001$ to $\alpha_1 > 0.999$. Overall, this analysis demonstrates that the proposed modifications to the phase-change model are acceptable for evaporation simulations. However, care must be taken to limit discretization error and ensure sufficiently resolved interface regions.

5.4.3 Distributed-heated flow-boiling bubble-pump generator simulation

A simulation study is performed for the bubble-pump generator (BPG) configuration discussed in Chapter 4. As in previous sections, both the flow equations (for u, p, α_1) and thermal energy transport equation (for i and T) are solved simultaneously, and are coupled through the phase-change model (Section 5.4.1). The BPG is a co-flow upward tube-in-tube heat exchanger with evaporating working fluid flow in the inner tube (ID_i = 7.8 mm), and coupling-fluid (CF) flow in the annulus (OD_i = 9.5 mm, ID_o = 10.9 mm) (Figure 5.11a). In this study, the working fluid transport properties are relaxed compared with the ambient-pressure steam-water flows investigated in Chapter 4 (increased μ_L, increased ρ_V/ρ_L). This improves numerical stability and reduces the required mesh resolution while still allowing assessment of the segmented model approach proposed in Chapter 4. CF properties are representative of the mineral-oil based heat transfer fluid

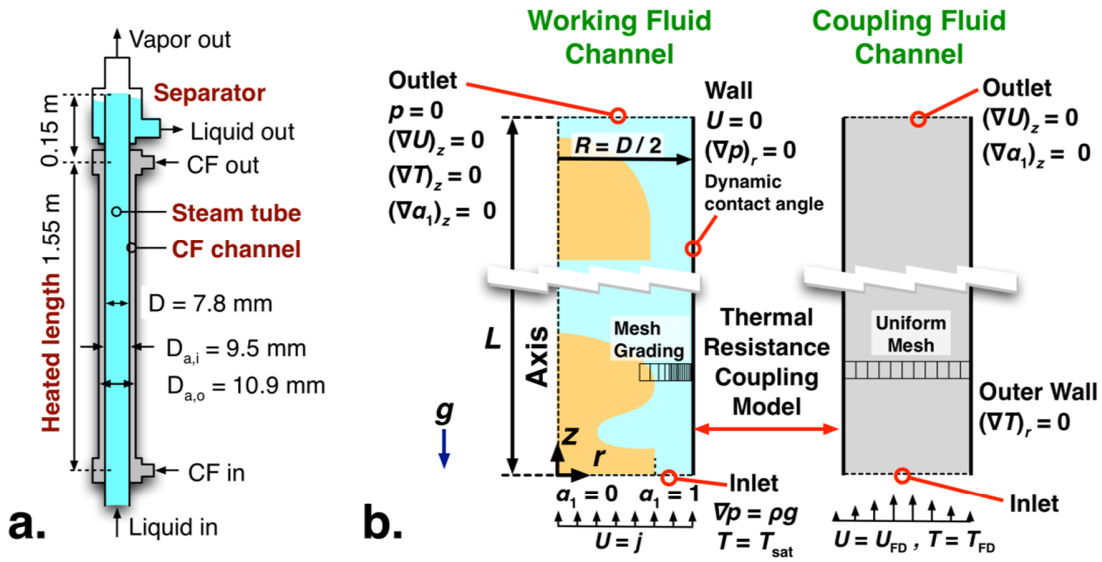

Figure 5.11 – **a**. Coupling-fluid heated bubble-pump generator geometry, **b**. Schematic of 2D axisymmetric simulation domain (coaxial working-fluid and coupling-fluid subdomains)

employed in experiments (Paratherm® NF). Fluid properties are summarized in Table 5.6. Properties of ambient-pressure steam-water (as employed in Chapter 4) are also reported for reference.

The studied case focuses on an L = 0.30 m long section of the saturated flow portion of the BPG. In the simulation results, this domain contains 8.2 Taylor bubble-liquid slug unit cells on average (average unit cell length 36.6 mm). Liquid and vapor inlet flow rates into this portion of the domain are $V_{L,in}$ = 100 ml min^{-1} and $V_{V,in}$ = 400 ml min^{-1}. The CF flow enters the domain at V_{CF} = 200 ml min^{-1} and $T_{CF,in} - T_{sat}$ = 10 K. For these conditions, the segmented model predicts a liquid outlet flow rate of $V_{L,out}$ = 95 ml min^{-1}, vapor outlet flow rate of $V_{V,out}$ = 635 ml min^{-1}, and total heat transfer rate of Q = 15.7 W.

Table 5.6 – Working fluid and coupling fluid properties for the distributed heated flow evaporation simulations. Properties for ambient pressure steam-water included for reference (as employed in Chapter 4).

	Simulation Working Fluid		Ambient Pressure Steam-Water	
Property	**Liquid Phase**	**Vapor Phase**	**Liquid Phase**	**Vapor Phase**
Density (kg m^{-3})	1000	20	958.9	0.6
Dynamic viscosity (kg m^{-1} s^{-1})	3.0×10^{-3}	3.0×10^{-4}	2.8×10^{-4}	1.2×10^{-5}
Specific heat (kJ kg^{-1} K^{-1})	2.0	1.5	4.2	2.1
Thermal conductivity (W m^{-1} K^{-1})	0.50	0.05	0.68	0.03
Surface tension (kg s^{-2})	0.040		0.059	
Enthalpy of phase change (kJ kg^{-1})	200		2259	
	Coupling Fluid			
Density (kg m^{-3})	800			
Dynamic viscosity (kg m^{-1} s^{-1})	5×10^{-3}			
Specific heat (kJ kg^{-1} K^{-1})	2000			
Thermal conductivity (W m^{-1} K^{-1})	0.1			

Segmented model predicted inlet and outlet conditions for this section of the saturated flow boiling section are summarized in Table 5.7.

The simulation domain is presented schematically in Figure 5.11b, and includes coupled 2D axisymmetric sub-domains for the working fluid and CF channels. The working fluid mesh is refined near the wall (Δr = 0.031 mm for $2.88 \leq r \leq 3.88$ mm, 32 cells thick). This fine mesh region (1.0 mm thick) resolves the anticipated thin films around Taylor bubbles (δ_f ~ 0.6 mm) with about 19 cells, exceeding the criterion of 5 cells suggested by Gupta *et al.* (2009). An additional 45 cells extend from r = 0 – 2.88 mm, and are graded such that the ratio of neighboring cell widths is 1.03 (i.e., matching

Table 5.7 – Inlet conditions and segmented model predicted outlet conditions for simulation saturated flow boiling domain

Parameter		Inlet Value	Outlet Value (Predicted)	
Liquid flow rate	V_L	100.0	95.3	ml min^{-1}
Vapor flow rate	V_V	400.0	635.1	ml min^{-1}
Coupling fluid temperature	$T_{CF} - T_{sat}$	10.0	7.1	K
Coupling fluid flow rate	V_{CF}	200.0	200.0	ml min^{-1}

the film-region mesh resolution at r = 2.88 mm). In Chapter 3, ~50 radial-cell meshes were found to be sufficient to yield converged adiabatic Taylor flow simulations at similar conditions. The mesh contains 4296 equal-height cells in the axial direction (Δz = 0.10 mm). The CF channel is meshed with 28 uniform-width cells in the radial direction (Δr = 0.025 mm), and 4296 cells in the axial direction (matching the working fluid channel). The inner stainless-steel tube wall is not resolved in detail, but rather is modeled as a thermal resistance between the two sub-domains ($R''_{wall} = 6.9 \times 10^{-5}$ m^2 K W^{-1} based on the outer surface area). Two coarser mesh simulations are also performed to assess simulation convergence (see Section 5.4.4).

The inner channel is simulated following the overall formulation presented in Section 5.2.4 with the evaporative phase change model described in Section 5.4.1. This approach does not account for nucleate boiling on the wall; therefore, all phase change proceeds as convective flow evaporation. This assumption is reasonable because nucleate boiling heat flux is expected to be minimal at predicted wall temperatures ($T_{wall} - T_{sat}$ = 2.7 – 4.1 K) with the simulation working fluid properties. Using the correlation of Rohsenow (1952)

with parameters tabulated in Ghiaasiaan (2008), predicted nucleate boiling heat transfer coefficients are only 2.7 – 6.4 W m^{-2} K^{-1}. In comparison, flow evaporation coefficients of ~650 W m^{-2} K^{-1} are obtained using the model of Liu and Winterton (1991).

The fluid inlet at the bottom of the working fluid domain is alternated between annular flow (vapor core, liquid annulus, R_{int} = 3.75 mm, 85% of the time, period 0.077 s) and all liquid flow (15% of the time) at u_z = 0.177 m s^{-1} and $T = T_{sat}$. This inlet condition produces bubbles of length ~1.5D, which is representative of the Taylor flow pattern that is expected to enter this portion of the BPG.

The inlet pressure is specified with a hydrostatic boundary condition ($\partial p/\partial z = \rho g$). The top of the domain (outlet) is modeled as an outflow boundary, with zero normal-gradient conditions for α_1, u, and T. The outlet pressure is specified to be 0 (ambient pressure). The wall is modeled as a no-slip surface for the velocity field (u = 0), and a zero-normal-gradient boundary for pressure. The wall contact-angle boundary condition is specified using the model of Kistler (1993) as implemented by Berberovic (2008), and is described in Section 3.4.1. The wall temperature is modeled with an explicit coupling condition between the two domains. At the end of each simulation time step, the following conditions are applied for each working-fluid and CF wall cell-face-pair i.

$$\left(\frac{\partial T_{CF,wall}}{\partial r}\right)_i \leftarrow (1-s)\left(\frac{\partial T_{CF,wall}}{\partial r}\right)_i + s\frac{T_{CF,wall,i} - T_{wall,i}}{R''_{wall}\, k_{CF}} \tag{5.27}$$

$$\left(\frac{\partial T_{wall}}{\partial r}\right)_i \leftarrow -\left(\frac{\partial T_{CF,wall}}{\partial r}\right)_i \frac{k_{CF}}{k_{wall,i}} \frac{OD_i}{ID_i} \tag{5.28}$$

Here, s is an under-relaxation factor employed to ensure simulation stability ($s = 0.1$). $T_{CF,wall}$ and T_{wall} are the wall surface temperatures in the CF and working fluid domains, respectively. k_{wall} is the working fluid thermal conductivity at the wall (generally $k_{wall} = k_L$).

The velocity profile in the CF sub-domain is specified to be that of fully-developed laminar annular flow ($Re_{CF} = 33$). The governing thermal energy transport equation for the sub-domain is:

$$\frac{\partial T_{CF}}{\partial t} + u_i \frac{\partial T_{CF}}{\partial x_i} = \frac{\partial}{\partial x_i}\left[\left(\frac{k}{\rho c_p}\right)_{CF} \frac{\partial T_{CF}}{\partial x_i}\right] \tag{5.29}$$

Equation 5.29 is solved during each simulation time step after stage 2.9 in the solver algorithm (Figure 5.2), and before updating the wall heat-transfer coupling condition (Equations 5.27 – 5.28). The temperature inlet to the domain is specified as that of laminar hydrodynamically and thermally fully developed annular flow with an insulated outer wall, an assumed wall resistance ($R''_{wall} = 6.9 \times 10^{-5}$ m^2 K W^{-1}), and flow-boiling convection coefficient of $h_{evap} = 1000$ W m^{-2} K^{-1}. The sub-domain top surface (outlet) is modeled as a zero-normal-gradient temperature boundary. The outer wall is assumed adiabatic ($\partial T / \partial r = 0$), and the inner wall temperature boundary condition is coupled to that of the working fluid, as described above.

The simulation is initialized for 2 ss. Simulation output data are then collected for 4 ss ($U_b\, t / L \sim 5$), with checkpoint logging every 0.2 ss.

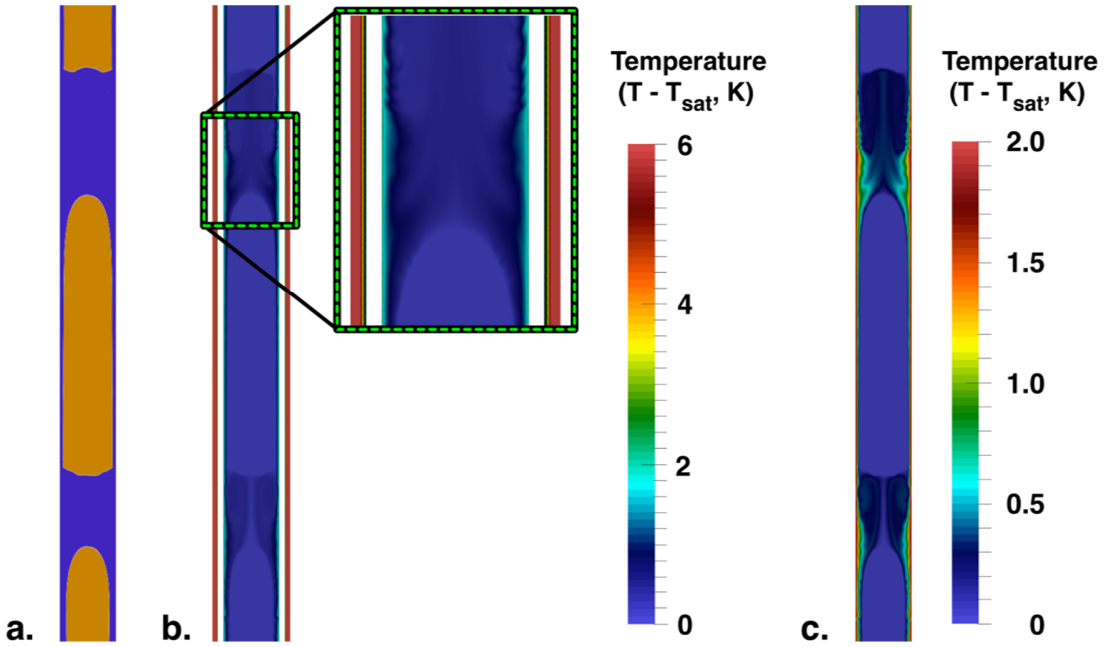

Figure 5.12 – Representative flow-boiling simulation two-phase flow pattern. **a**. Working fluid phase distribution, **b**. Working fluid and coupling fluid temperature profiles with zoom-in of bubble-nose region, **c**. Detail view of working fluid temperature distribution.

5.4.4 Overall simulation assessment

The simulation progressed in a stable fashion. The evaporating phase-change model refinements (Section 5.4.1) ensured that liquid-vapor interface sharpness was maintained. The working-fluid channel flow was generally in the Taylor flow regime (Figure 5.12a), although bubble interface profiles were occasionally distorted. Representative temperature profiles in the working fluid and coupling fluid channels are presented in Figure 5.12b-c. Vapor-bulk temperatures were generally found to be within 0.02 K of T_{sat}. Average wall y^+ values were 0.25 (peak 3.2), indicating that the mesh is well resolved in the near-wall region.

Time-averaged volume and energy balances were performed over the working-fluid domain to assess conservation during the simulation. Average liquid and vapor flow rates were measured to be $V_{L,in}$ = 99.5 ml min^{-1} and $V_{V,in}$ = 399.8 ml min^{-1}, respectively. Phase change heating resulted in 261.7 ml min^{-1} of volume generation. Averaged outlet flow rates were evaluated to be $V_{L,out}$ = 99.8 ml min^{-1} and $V_{V,out}$ = 661.2 ml min^{-1}. Net volume conservation was thus achieved to within 0.008 ml min^{-1}. However, a small amount of numerical liquid production occurred (5.6 ml min^{-1}) due to the implementation of the phase-change volume production source term ($\dot{v}_{pc}$), as discussed in Section 5.4.1.

Of the 18.26 W of heat transferred to the working fluid through the channel wall, 17.78 W resulted in evaporative phase change, and 0.43 W was removed via the superheated liquid outlet flow. This sensible heating can occur, even for the saturated inlet conditions, because the liquid film and liquid slug domains are slightly superheated (up to ~2 K in this study). The remaining 0.05 W resulted in sensible thermal storage in the domain from the assumed initial condition ($T(t = 0) = T_{sat}$), and decays to 0 W as the simulation time increases.

A mesh sensitivity study was performed with the baseline grid (working fluid channel: $n_r \times n_z$ = 77 × 4296, CF channel: $n_r \times n_z$ = 28 × 4296) and two coarser grids (working fluid channel: $n_r \times n_z$ = 55 × 3072 and 40 × 2160, CF channel: $n_r \times n_z$ = 20 × 3072 and 15 × 2160). Time- and volume averaged simulation results are summarized in Table 5.8. Most directly measured quantities (Q_{BPG}, $V_{V,out}$, α) deviate by less than 4% between all three cases. The coarser mesh simulation yielded somewhat distorted bubble profiles, which resulted in relatively high bubble rise velocities and reduced

Table 5.8 – Key parameter values from mesh sensitivity study. Relative deviations from baseline mesh results indicated in parentheses.

Parameter	Coarser Mesh (40 × 2160, 15 × 2160)	Coarse Mesh (55 × 3072, 20 × 3072)	Baseline Mesh (77 × 4296, 28 × 4296)
Heat transfer (Q_{BPG}, W)	18.96 (+3.8%)	18.57 (+1.7%)	18.26
Outlet vapor flow rate ($V_{V,out}$, ml min^{-1})	685.5 (+3.7%)	684.1 (+3.5%)	661.2
Vapor phase rise velocity (U_b, m s^{-1})	0.446 (+13.2%)	0.383 (-2.8%)	0.394
Void fraction (α)	0.489 (-2.4%)	0.510 (+1.8%)	0.501
Dynamic axial pressure gradient ($\nabla p_{d,z}$, Pa m^{-1})	-778 (-24.8%)	-1015 (-1.9%)	-1035
Total axial pressure gradient (∇p_z, Pa m^{-1})	4331 (+9.4%)	3892 (-1.7%)	3959

hydrodynamic pressure recovery. These quantities agree to within 3% between the coarse and baseline mesh. Similarly, the total axial pressure gradient ($\nabla p_z = (\alpha\rho_G + (1 - \alpha)\rho_L)g + \nabla p_d$) agrees to within 2% for these higher resolution cases. Overall, this analysis indicates that mesh independent results are obtained with the baseline mesh.

5.4.5 Heat transfer analysis

CF and smoothed inner wall temperatures are compared between time-averaged simulation results and segmented model predictions in Figure 5.13a. The CF temperature decreases by 18.1% more over the length of the domain in the simulation case ($T_{CF,sim}$ = 10.0 → 6.5 K, Q_{BPG} = 18.3 W) than in the segmented model (T_{CF} = 10.0 → 7.1 K, Q_{BPG} = 15.7 W). This discrepancy is primarily due to the greater evaporative heat transfer

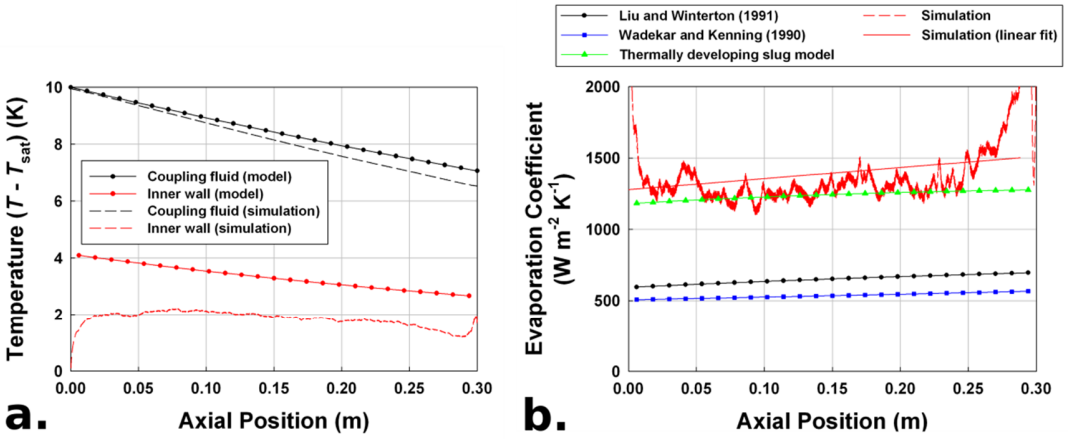

Figure 5.13 – Comparison of model and simulation profiles of (**a**) coupling fluid and inner-channel inner-wall temperatures and (**b**) convective flow evaporation heat transfer coefficient

coefficient predicted in the simulation ($h_{evap,avg}$ = 1390 W m^{-2} K^{-1}) than obtained with the flow evaporation model of Liu and Winterton (1991) ($h_{evap,avg}$ = 650 W m^{-2} K^{-1}). This increased heat transfer coefficient can be inferred from the lower simulation wall temperature in Figure 5.13a ($T_{wall,avg,sim}$ = 1.84 K, $T_{wall,avg,mod}$ = 3.32 K), and is presented directly in Figure 5.13b. CF channel convection heat transfer coefficients agree closely between simulation ($h_{CF,sim}$ = 332 W m^{-2} K^{-1}) and segmented model ($h_{CF,mod}$ = 352 W m^{-2} K^{-1}) results. As a result of the increased CF-to-working fluid heat transfer rates, average vapor outlet flow rates are slightly higher in the simulation (+4.1%, 661.2 ml min^{-1}) than predicted with the segmented model (635.1 ml min^{-1}) (Figure 5.14). If the average simulation evaporative heat transfer coefficient is specified as an input to the segmented model, overall heat transfer rates agree to within 4% ($Q_{BPG,sim}$ = 18.26 W, $Q_{BPG,mod}$ = 18.97 W). Outlet flow rate agreement also improves slightly for this case ($V_{L,out,sim}$ = 99.8

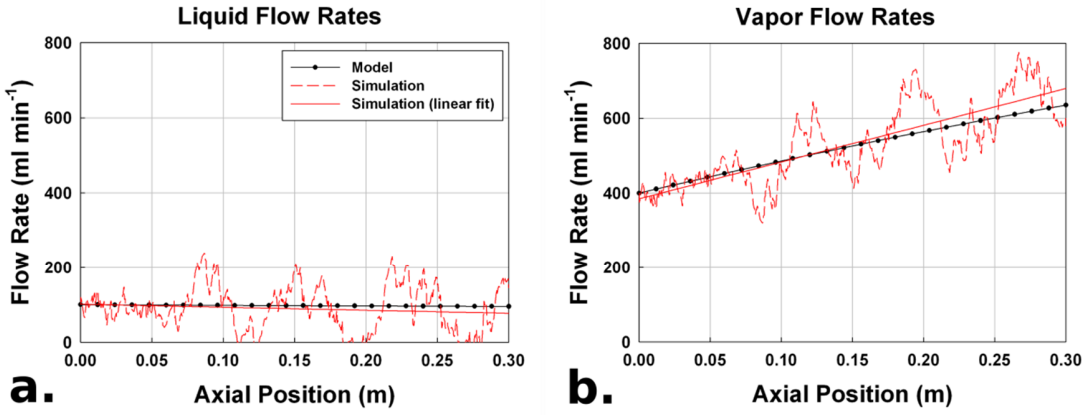

Figure 5.14 – Comparison of model and simulation profiles of (**a**) liquid and (**b**) vapor axial flow rates

ml min^{-1} and $V_{V,out,sim}$ = 661.2 ml min^{-1}; $V_{L,out,mod}$ = 94.3 ml min^{-1} and $V_{V,out,mod}$ = 684.6 ml min^{-1}).

Results from this simulation indicate significantly higher convective flow evaporation heat transfer coefficients ($h_{evap,sim,avg}$ =1390 W m^{-2} K^{-1}) than predicted with the model of Liu and Winterton (1991) ($h_{evap,mod,avg}$ = 650 W m^{-2} K^{-1}):

$$h_{evap,LW} = \left[1 + x\,\mathrm{Pr}_L\left(\frac{\rho_L}{\rho_V} - 1\right)\right]^{0.35}\left(0.023\frac{k_L}{D}\mathrm{Re}_{L0}^{0.8}\,\mathrm{Pr}_L^{0.4}\right) \tag{5.30}$$

Here, the segmented model predicted quality (x) ranges from 0.074 – 0.118, the liquid Prandtl number is Pr_L = 12, the liquid-to-vapor density ratio is 50, and the liquid-only Reynolds number is $\mathrm{Re}_{L0} = GD/\mu_L$ = 99. The resulting predicted evaporative heat transfer coefficient increases with quality from 600 – 700 W m^{-2} K^{-1} along the domain. This correlation was formulated semi-empirically using experimental flow boiling data to modify turbulent single-phase channel flow results. It is therefore possible that this

formulation is not valid for the low (laminar) Reynolds number and mass flux (G = 38 kg m^{-2} s^{-1}) conditions considered in this study.

An alternate, flow-regime-specific, mechanistic evaporative heat transfer modeling approach was proposed by Wadekar and Kenning (1990) for large Bond number turbulent flows. Their model applies fully developed heat transfer results for the liquid-film in bubble regions and channel flow in slug regions. For the laminar conditions considered in the present investigation, radial conduction heat transfer would be dominant in liquid films, and the slug region channel flow Nusselt number would be Nu ~ 3.7. The overall predicted heat transfer coefficient is:

$$h_{\text{evap,WK}} = \frac{2\beta k_{\text{L}}}{D \ln\left[D/\left(D-2\delta_{\text{f}}\right)\right]} + \frac{3.7\left(1-\beta\right)k_{\text{L}}}{D} \tag{5.31}$$

Here, β is the relative Taylor bubble length ($\beta = L_{\text{b}} / (L_{\text{b}} + L_{\text{s}})$) predicted using the Taylor flow model formulated in Chapter 3 (β = 0.53 – 0.65). δ_{f} is the predicted liquid film thickness (0.62 mm). The resulting heat transfer coefficient increases from 510 – 570 W m^{-2} K^{-1} along the length of the domain (Figure 5.13b).

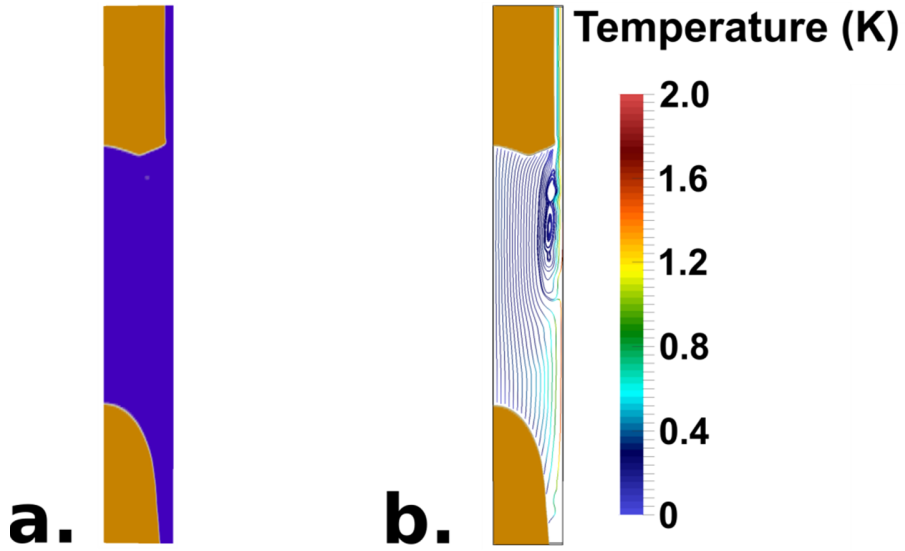

Figure 5.15 – **a**. Representative liquid-slug region from evaporating flow simulation, **b**. Streamlines in bubble-wake region (colored by $T - T_{sat}$)

These results indicate that the mechanisms of evaporative heat transfer in the intermediate Bond number regime at these laminar flow conditions (Re_j = 440 – 690) may be significantly different than assumed in these two models. In particular, intense circulation in the wake regions trailing Taylor bubbles may transport more heat from the wall than would be predicted for fully developed channel flow (Figure 5.15). As discussed in Chapter 2, liquid slugs are significantly shorter in the intermediate Bond number regime (L_s / D ~ 1 – 6) than for high Bond number turbulent flows (L_s / D ~ 16, (Taitel *et al.*, 1980)), as considered by Wadekar and Kenning (1990). Therefore, the relative importance of bubble-wake heat transfer enhancement may be much more significant for intermediate Bo. This result is consistent with the findings of Chapter 3, which indicated that bubble-to-slug flow-transition pressure losses dominate slug channel-flow pressure drops. Additionally, expected thermal developing flow lengths

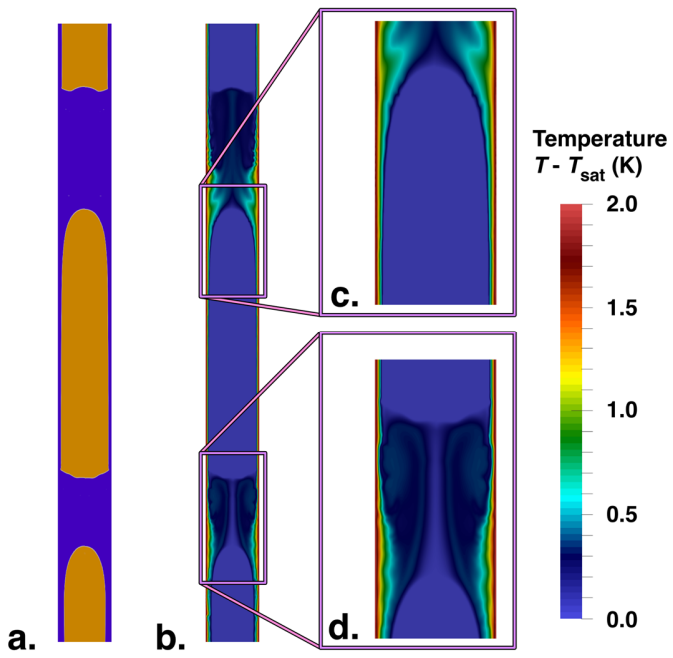

Figure 5.16 – **a**. Representative phase distribution from simulation results, **b**. Temperature field in region, **c**. Detail view of temperature field near the bubble nose (note that the near-wall temperature profile is relatively unchanged over the slug-to-film transition), **d**. Detail view of temperature field neat the bubble tail (note that the thermal boundary layer thins in the wake region before it starts to thicken further into the slug)

($0.06\ \mathrm{Re}_j\ \mathrm{Pr}_L\ D$) vary from 2.5 – 3.7 m along the length of the channel, about 200 – 400 times the predicted slug lengths. Similarly, the falling liquid film flows may not reach thermally fully developed states for the relatively short average bubble lengths found in these studies ($L_{b,avg} / D = 3.3$, $L_{b,avg} / \delta_{f,avg} = 41.7$). In comparison, for these conditions, the models of Mitrović (1988) and Lel *et al.* (2009) predict falling-film thermal development lengths of $47\delta_f$ and $35\delta_f$, respectively.

A representative simulation snapshot is presented in Figure 5.16 to permit evaluation of these potential heat transfer enhancement mechanisms. As can be observed in the

detail view of the liquid slug region (Figure 5.16d), the bubble wake causes the wall thermal boundary layer to thin in the near-tail-region before it gradually thickens in the thermally developing liquid slug bulk. Therefore, the heat transfer effect of the wake can be conceptualized and modeled as a reset of the thermal boundary layer (initiating a new developing channel flow region in each liquid slug). In contrast, the near-wall thermal boundary layer appears to continue unperturbed from the liquid slug bulk to the bubble-film region (Figure 5.16c). This may occur because the rounded bubble nose permits a gradual transition between the two regions without wake effects. Therefore, developing film-flow effects are not significant. Based on these results, a modification to the mechanistic flow evaporation heat transfer coefficient model (Equation 5.31) is proposed, which accounts for each slug as a new developing channel flow region (using the results of Hornbeck (1965) correlated by Shah and London (1978)).

$$\mathrm{Nu}_{\mathrm{DevSlug}} = 3.66 + \frac{\left(0.049 + 0.020/\mathrm{Pr}_{\mathrm{L}}\right)\mathrm{Gz}_{\mathrm{s}}^{1.12}}{1 + 0.065\mathrm{Gz}_{\mathrm{s}}^{0.7}} \tag{5.32}$$

$$\mathrm{Gz}_{\mathrm{s}} = \frac{D\,\mathrm{Re}_{j}\,\mathrm{Pr}_{\mathrm{L}}}{L_{\mathrm{s}}} \tag{5.33}$$

$$h_{\mathrm{evap,DevSlug}} = \frac{2\beta k_{\mathrm{L}}}{D\ln\left[D/\left(D-2\delta_{\mathrm{f}}\right)\right]} + \frac{\left(1-\beta\right)k_{\mathrm{L}}}{D}\mathrm{Nu}_{\mathrm{DevSlug}} \tag{5.34}$$

Here, $\mathrm{Gz_s}$ is the slug Graetz number, and increases along the length of the channel in the segmented model case from 3310 – 7130, corresponding to increasing Re_j (460 – 670) and decreasing liquid slug length (L_s = 12.8 – 8.7 mm). The resulting average slug-region heat transfer coefficient increases from 1670 to 2260 W m^{-2} K^{-1} along the channel length, and is 2 – 3 times that of the fully developed liquid film (~750 W m^{-2} K^{-1}). The overall

flow-evaporation coefficient (Equation 5.34) increases from 1180 to 1280 W m^{-2} K^{-1} along the length of the channel, and agrees with the linear fit to the simulation heat transfer coefficient to within 15% (Figure 5.13b). The linear fit to the simulation heat transfer coefficient is skewed slightly high due to entrance and exit effects in the domain. The proposed developing slug flow model matches more closely with the linear fit to simulation data between z = 0.05 to 0.25 m (3.5% average absolute deviation).

While good agreement with simulation results was obtained using the developing slug flow convective coefficient model (Equations 5.32 – 5.34) in this case, further investigation into intermediate Bond number Taylor flow evaporation is needed. The proposed model is specific to laminar flow, and other formulations may be more appropriate for turbulent conditions (as in Chapter 4). Additionally, this simulation study does not account for nucleate boiling effects, which could also modify liquid slug and film flow patterns and convection characteristics.

Even with potentially large discrepancies in h_{evap}, overall heat transfer predictions using the model of Chapter 4 agreed closely with experimental values (averaged absolute deviation for Q_{BPG} = 3.7%). This occurred because BPG operating conditions were almost always limited by the CF thermal capacity rather than CF-to-working fluid thermal resistance (i.e., $T_{CF,out}$ ~ T_{sat}). Additionally, single-phase CF-to-tube thermal resistance was generally predicted to be dominant due to the low thermal conductivity of the CF (~0.1 W m^{-1} K^{-1}) and laminar CF flow conditions. As such, large variations in working-fluid side convection resistance would not significantly affect predicted BPG behavior. However, under different operating conditions, accurate prediction of flow boiling heat transfer coefficients may be critical.

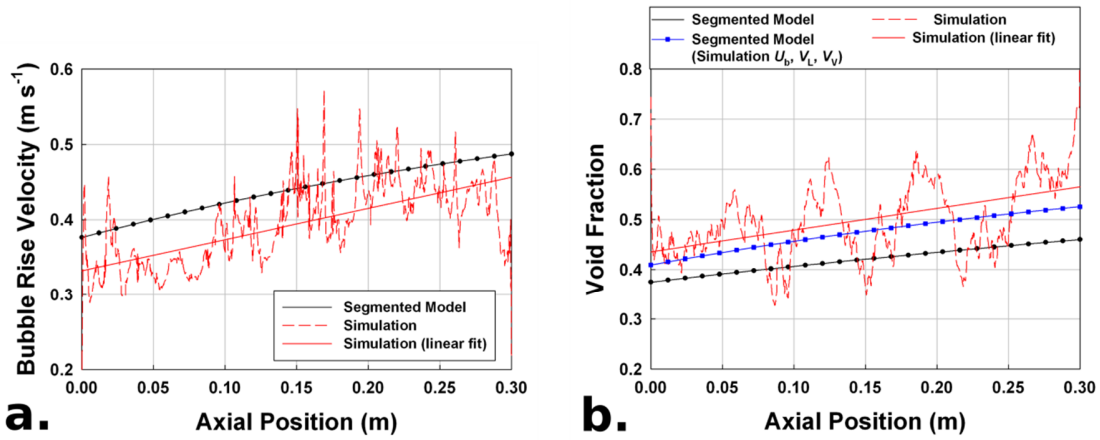

Figure 5.17 – Comparison of model and simulation profiles of (**a**) bubble rise velocity and (**b**) void fraction

This simulation also predicted slight bulk liquid superheating (~2.4% of input heat for the domain, $T_{L,out} - T_{sat} = 0.13$ K). This effect could be incorporated into the segmented model proposed in Chapter 4 as an adjustment to the subcooled-to-saturated flow boiling transition point (e.g., transition at $T_L = T_{sat} + \Delta T$). This fraction of sensible heating would be much smaller when averaged over the full heated BPG length (~1.55 m vs. 0.3 m here), and may be further reduced for the turbulent flow conditions expected for actual BPG operation. Thus, the slight improvement in segmented model fidelity may not outweigh the cost of increased complexity and the challenge of predicting the degree of liquid superheating.

5.4.6 Taylor flow kinematics and hydrodynamics

Gas-phase (Taylor bubble) velocity profiles are presented in Figure 5.17a from the segmented model and time-averaged simulation data. A best fit linear trend line is also presented for the simulation data because results are not fully converged to a smooth

curve after 4 ss. The segmented model velocities are slightly higher than simulation results, locally deviating from the simulation trend line by 7 – 13%. One possible explanation is that Taylor bubbles may have finite acceleration rates for this evaporating flow configuration, and locally do not reach adiabatic fully developed rise velocities. Another possible explanation is that the Taylor bubble rise velocity model formulated in Chapter 2 based on air-water flow data (viscous number $N_f = \left(\rho_L^2 g D^3 / \mu_L^2\right)^{1/2} = 1500 - 3000$) may over-predict velocities for high liquid-phase viscosities (reduced N_f). This result is consistent with findings for higher effective viscosity flows ($N_f = 250 - 1000$, here $N_f = 712$) in Chapter 3 (see Figure 3.8b).

Axial void fraction profiles are presented in Figure 5.17b for the segmented model and time-averaged simulation cases. On average, the baseline segmented model under-predicts simulation results (14 – 19%). This is primarily due to the lower bubble rise velocities in the simulation (7 – 13%). The slightly higher predicted vapor flow rates in the simulation also contribute to the discrepancy ($V_{V,sim} = 400 \rightarrow 661$ ml min^{-1}, $V_{V,mod} = 400 \rightarrow 635$ ml min^{-1}). If simulation linear trend line values are specified for U_b, V_V, and V_L, then the average void fraction discrepancy decreases to 5.4% (Figure 5.17b). For all intermediate Bond number Taylor flows investigated in Chapters 3 and 4, hydrostatic pressure drop was the dominant component of flow resistance. Thus, accurate prediction of void fraction is critical for BPG model validity. Here, local void fraction agreement to within 20% indicates reasonable performance of the segmented model. If the discrepancy in U_b can be resolved, then it may be possible to substantially improve accuracy of void fraction predictions.

Other Taylor flow kinematic quantities (δ_f, L_b, L_s, β) cannot be assessed locally without very long simulation times. Therefore, these quantities are compared based on full simulation domain averages, following the approaches employed in Section 3.4.2. The segmented model predicts that liquid film thickness varies over $\delta_f = 0.614 - 0.621$ mm along the length of the domain. This agrees closely with the time- and axially averaged simulation result of $\delta_f = 0.613$ mm. In the segmented model, the predicted Taylor bubble length increases from $L_b = 14.5 - 16.2$ mm from the inlet to outlet. The liquid slug length decreases, correspondingly, from $L_s = 12.8 - 8.7$ mm. The simulation yields average bubble and slug lengths of $L_b = 25.5 \pm 3.8$ mm and $L_s = 11.0 \pm 1.5$ mm. Here, uncertainties are reported as 95% confidence intervals for 141 bubble and 128 slug instances. The simulation average slug length falls in the segmented model range. The baseline segmented model (Equation 2.30) predicts shorter bubble lengths than found in simulation results. However, if simulation trend lines are specified as model inputs for j, U_b, and α, then the resulting range (15.9 – 23.4 mm) approaches the simulation value of 25.5 mm. These results show reasonable agreement considering the difficulty of accurately predicting bubble and slug lengths (see Sections 2.4.4 and 3.6). Similarly, if the simulation trend lines are specified for U_b, V_V, and V_L, then the segmented model relative Taylor bubble lengths ($\beta = L_b/(L_b + L_s) = 0.560 - 0.717$) approaches the simulation value (0.718). Overall, this analysis indicates general validity of the intermediate Bond number kinematic Taylor flow model (Chapter 2), provided that U_b can be predicted accurately.

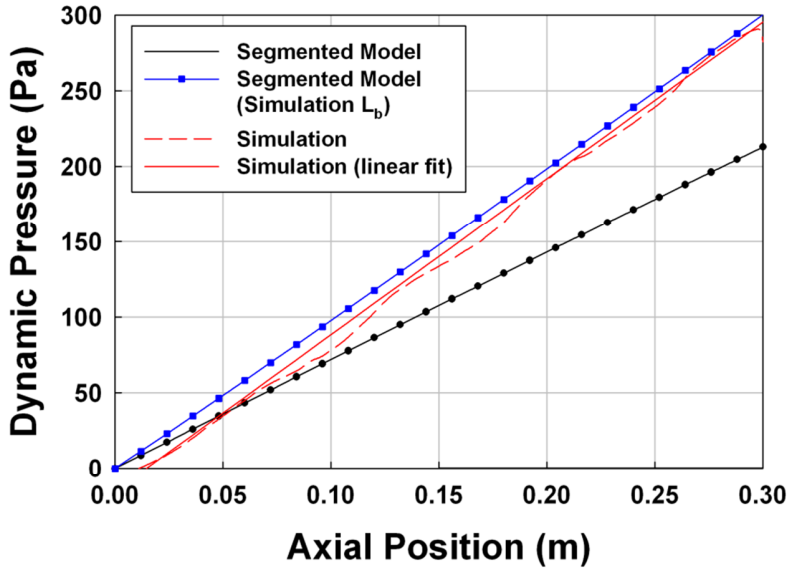

Figure 5.18 – Comparison of segmented model and simulation axial hydrodynamic pressure profiles

Time-averaged hydrodynamic pressure gradients are presented in Figure 5.18 for simulation results based on wall shear stress values ($\nabla p_d = -4\ \tau_w / D$). These results agree reasonably well with baseline segmented model results for ∇p_d ($\nabla p_{d,sim}$ = 1035 Pa m^{-1}, $\nabla p_{d,mod}$ = 710 Pa m^{-1}, 31.4% deviation). However, the baseline model assumes shorter Taylor bubbles ($L_{b,sim}$ = 25.5 mm, $L_{b,mod}$ = 14.5 – 16.2 mm), and thus, a higher frequency of flow-transition pressure losses. If the average simulation bubble length is specified as an input to the segmented model, then $\nabla p_{d,mod}$ = 982 pa m^{-1} (5.1% deviation). This comparison provides validation for the hydrodynamic Taylor flow modeling approach employed in Chapter 4. However, results are sensitive to both the unit cell length and flow transition pressure loss formulation, as demonstrated in Section 3.6.

5.4.7 Discussion

In this investigation, direct simulations were performed for the Taylor flow evaporation process in the proposed distributed CF-heated BPG design. Results from this simulation indicate general validity of the segmented model formulated in Chapter 4. Reasonable agreement was found between simulation and segmented model results for heat transfer and phase change rates (Q_{BPG}, 14% discrepancy), bubble rise velocity (U_b, 7 – 13%), and liquid film thickness (δ_f, 0.7%). If simulation flow rates and bubble rise velocities are specified as inputs to the segmented model, void fraction profiles (α) agree to within 5.4% on average. With these adjustments to the segmented model, predictions for Taylor bubble length (L_b), liquid slug length (L_s), and relative bubble length (β) lie approach simulation results. Similarly, if simulation bubble lengths and flow rates are specified as segmented model inputs, average hydrodynamic pressure gradients (∇p_d) agree to within 5.1%.

The higher heat transfer rates found in simulation cases resulted from the flow evaporation convection coefficient (~1390 W m^{-2} K^{-1}), which significantly exceeded values predicted with established models (~650 W m^{-2} K^{-1} (Liu and Winterton, 1991), ~540 W m^{-2} K^{-1} (Wadekar and Kenning, 1990)). A simple mechanistic heat transfer model that accounts for the effect of wake at the bubble-tail to slug transitions as a "reset" of the thermal boundary layer was proposed. The resulting heat transfer coefficient agrees with averaged simulation results to within 15%. However, additional research is needed to evaluate and extend this approach for other conditions, especially for turbulent flows and when nucleate boiling heat transfer is significant.

Moderate deviations in U_b (7 – 13%) between the simulation results and segmented model resulted in relatively large discrepancies for α, L_b, L_s, β, and ∇p_d. Thus, accurate prediction of U_b is critical for overall segmented model validity. The discrepancy may be due to a limited range of validity for the Taylor bubble rise velocity model proposed in Chapter 2. A potential physical explanation was also identified for this effect. As evaporation proceeds along the length of the channel, the superficial velocity (j) continuously increases. However, the gas phase velocity may lag behind the fully developed adiabatic value ($U_b = C_0 j + \Gamma(g\,D)^{1/2}$). This effect may be more significant for the relatively high liquid-phase viscosity (μ_L) and vapor-phase density (ρ_V) considered here than with target working fluids (e.g., steam-water, NH_3-NaSCN).

Simulations were initiated for representative ambient-pressure steam-water experimental conditions studied in Chapter 4. However, the lower steam-water liquid-phase viscosity ($\mu_{L,water} = 2.84 \times 10^{-4}$ kg m^{-1} s^{-1} compared to $\mu_L = 3.0 \times 10^{-3}$ kg m^{-1} s^{-1}) and vapor-phase density ($\rho_{steam} = 0.58$ kg m^{-3} compared to $\rho_V = 20$ kg m^{-3}) necessitated finer spatial (mesh resolution) and temporal discretization. Additionally, the higher superficial Reynolds numbers ($Re = \rho_L j D/\mu_L$) necessitated turbulence modeling. Due to the fine near-wall grid resolution required to resolve thin liquid films (low y^+), standard eddy viscosity models (e.g., k-ε or k-ω) could not be employed. Some success was found with the low-Reynolds number cubic model of Lien *et al.* (1996). This model predicted negligible eddy viscosity (ν_t) in the laminar liquid films, and reasonable values of ν_t in turbulent liquid slugs. However, this turbulence model has somewhat limited stability characteristics, and occasionally caused solver crashes. Therefore, direct simulation of

distributed heated BPG flows with target working fluids and flow conditions may be feasible with additional computational resources and fine tuning of turbulence models.

One limitation of this simulation approach is that it can only resolve convective evaporation phase change, and not nucleate boiling. Nucleate boiling is expected to be an important mode of heat transfer for many BPG flows, especially in the subcooled near-inlet region. The proposed phase change simulation approach can be applied to resolve growth and detachment of individual bubbles. However, the 3D nature of nucleate boiling and wide range of scales between individual bubbles and full-channel flows make direct simulation extremely computationally expensive. Alternatively, a combined one-/two-fluid simulation formulation could be employed in which small nucleating bubbles are modeled with a spatially averaged subgrid-scale approach (Lahey Jr. and Drew, 2001; Žun *et al.*, 1993) until coalescence to grid-scale bubbles occurs. Such an approach could also be valuable for many flows with both small dispersed flow structures (e.g., small bubbles and mist) and channel-scale structures (e.g., Taylor bubbles and liquid slugs).

5.5 Conclusions

In this investigation, a thermally driven phase-change model and solver was developed for liquid-vapor flow VOF simulations. This phase-change model operates on cell values, and thus does not require geometric interface reconstruction. The model was employed to study horizontal film condensation, and results were found to converge to analytical solutions nearly linearly with mesh resolution. Simulations of smooth and wavy laminar falling-film condensation on vertical plates were performed. Wall heat flux values for the smooth film cases were found to agree with analytical solutions to within 2%. Validation studies for wavy film condensation were less conclusive due to the wide

range of heat transfer rates predicted by established correlations. Heat transfer rates obtained from the present study were found to lie within 11% of the locus of values obtained from commonly employed correlations, indicating general agreement.

This phase-change model was then extended to support evaporation phenomena while maintaining interface sharpness and accurate volumetric phase generation rates. The refined formulation was validated for a case of horizontal film evaporation. Axisymmetric simulations of distributed CF-heated BPG flow were performed. Results from this study provided confirmation of the segmented CF-heated BPG model formulated in Chapter 4. If discrepancies in evaporative heat transfer coefficients and Taylor bubble rise velocities are accounted for, close agreement was found between segmented model and simulation predictions for heat transfer rates (Q_{BPG}), axial phase flow rate profiles (V_L, V_V), void fraction (α), liquid film thickness (δ_f), Taylor bubble and liquid slug lengths (L_b, L_s, β), and hydrodynamic pressure gradient (∇p_d). Taylor bubble wake and thermally developing flow effects were identified as causes for the high convective evaporation coefficient values found in the simulation case. A simple mechanistic model that accounted for these effects was proposed, and good agreement with simulation results was obtained. Acceleration effects could explain the relatively low Taylor bubble rise velocities found for the simulation case. However, ranges of validity of the analytic Taylor bubble rise velocity model should also be assessed.

Potential approaches were discussed to enable simulation of distributed-heated BPG flows with target working fluids (e.g., steam-water, NH_3-NaSCN). Such studies will necessitate greater computational resources to resolve the increased ranges of scales. Additionally, turbulence modeling for such conditions represents an open challenge (see

Section 3.6). By developing a combined one-/two-fluid simulation formulation, it may be possible to simulate subcooled flow boiling phenomena. With such advances, it is expected that reconstruction-free simulations can be performed for many liquid-vapor phase change processes of interest.

CHAPTER 6. LOW-SOURCE-TEMPERATURE DIFFUSION ABSORPTION REFRIGERATION: MODELING AND CYCLE ANALYSIS

6.1 Introduction

6.1.1 Background

The diffusion absorption refrigeration (DAR) cycle (von Platen and Munters, 1928) has the potential to be implemented as a fully passive refrigeration technology. The technology can deliver cooling using solely thermal input, requiring no electrical input for pumps, compressors, or external fans. Historically, DAR systems have been employed in niche applications such as hotel room refrigerators, for which quiet operation is desirable. In this configuration, electrical resistance heating is employed to drive the cycle. DAR devices have also been commercialized for use in camping/recreational vehicles, wherein heat can be supplied from chemical fuel (e.g., propane). However, both of these applications do not exploit the main advantage of the DAR cycle as one that can be driven by potentially low-exergy sources.

Recently, the DAR cycle has received renewed attention for critical off-grid applications (Acuña *et al.*, 2013; Rodríguez-Muñoz and Belman-Flores, 2014). For example, such systems could be used for medicine and vaccine refrigeration ($T_{cool} \lesssim$ 5°C) in developing countries where electricity or chemical fuel supplies are unavailable or unreliable. In such applications, heat could be supplied with a passive solar thermosyphon or direct solar heating (Dammak *et al.*, 2010) (Figure 6.1a). Similarly, this technology could be employed for stationary generator waste-heat activated refrigeration or air-conditioning in military forward operating bases (Figure 6.1b) where electricity use must be carefully budgeted.

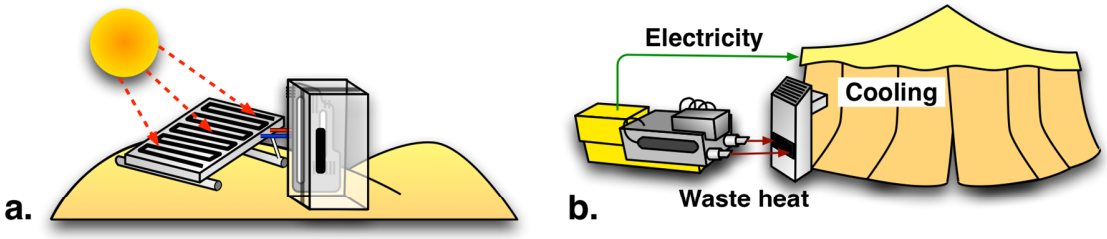

Figure 6.1 – Potential applications for diffusion absorption refrigeration systems for (**a**) off-grid solar activated refrigeration or (**b**) stationary generator waste heat recovery

6.1.2 DAR cycle description

A schematic of the basic DAR cycle is presented in Figure 6.2. Because the DAR cycle is intended for operation in a fully passive, thermally activated fashion, mechanical means of circulating working fluid between components (e.g., electrically driven compressors or pumps) should not be employed. Rather, fluid is transported through passive mechanisms. In the bubble-pump generator (BPG), liquid solution is lifted by the buoyancy of rising desorbed refrigerant-vapor bubbles. This process establishes the hydrostatic head that drives liquid flow through other components in the system (e.g., absorber and solution heat exchanger (SHX)).

DAR systems are pressurized with an inert low-density non-condensable, non-absorbable gas, usually helium or hydrogen. Net gas circulation is effected by the density difference between warm refrigerant-poor gas mixture rising out of the absorber and cool refrigerant-rich gas flowing downward from the evaporator. Thus, the cycle can be idealized as two passively circulating fluid loops (liquid and gas) that interact in the absorber.

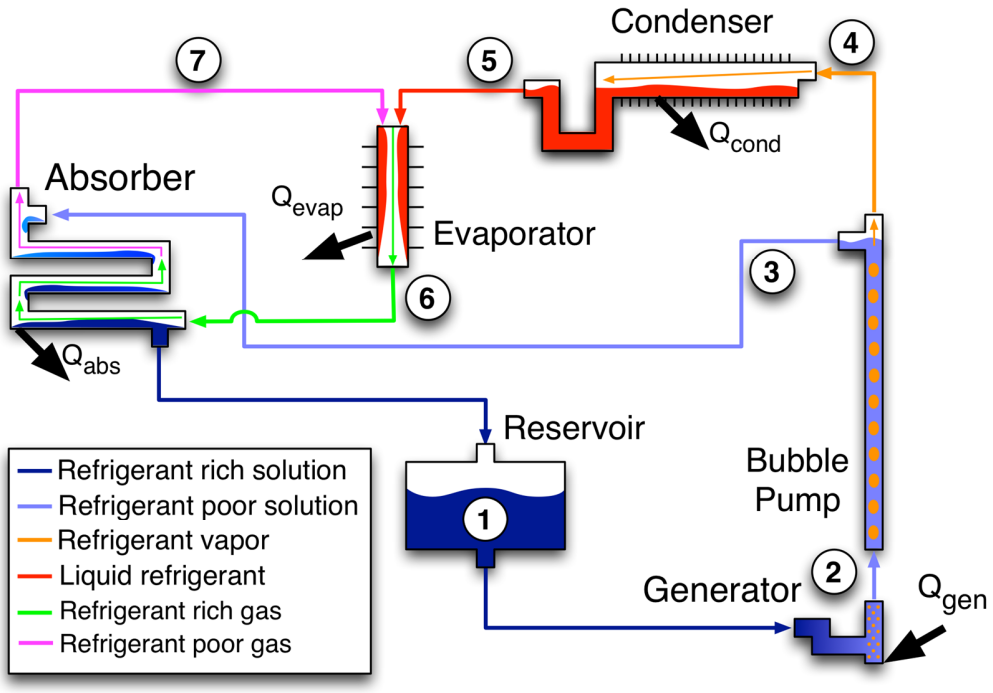

Figure 6.2 – Schematic of basic DAR cycle configuration

The DAR cycle operates at nearly a single total pressure, with only slight (~1%) variations due to hydrostatic effects. Thus, the conventional throttling mechanism for refrigerant expansion and cooling employed in vapor-compression and two-pressure absorption systems cannot be utilized. Rather, the liquid refrigerant stream flowing out of the condenser is contacted with refrigerant-poor (low vapor pressure) auxiliary gas flowing from the absorber. The vapor pressure difference between these two streams causes refrigerant evaporation and the cooling effect. DAR systems have conventionally operated with ammonia refrigerant, water absorbent, and helium or hydrogen auxiliary gas (Zohar *et al.*, 2005).

In the basic DAR cycle implementation (Figure 6.2), absorbent-dilute (refrigerant-rich) solution (DS) flows from the reservoir to the generator (1), where it is heated to

desorb refrigerant vapor. The refrigerant vapor and solution flow up through the bubble-pump generator (BPG) (2), and are lifted by the buoyancy of the vapor bubbles. Refrigerant vapor separates from the solution flow at the BPG outlet, and continues to the condenser (4). The refrigerant rejects heat to the surroundings as it flows through the condenser and exits as subcooled liquid (5). The liquid refrigerant partially flashes in the presence of the refrigerant-poor auxiliary gas mixture at the evaporator inlet. The two-phase mixture continues to evaporate and cools the conditioned space as it flows through the evaporator towards the absorber vapor inlet (6). Absorbent-concentrated (refrigerant-poor) solution (CS) from the BPG (3) flows into the absorber solution inlet, and contacts the gas stream from the evaporator in a counter-flow fashion (3 → 1). Refrigerant is absorbed from the gas mixture into the solution, rejecting heat to the surroundings and regenerating both the DS (1) and auxiliary gas streams (7). The DS returns to the reservoir, and the refrigerant-poor gas rises to the evaporator inlet, completing the cycle.

Additional components are incorporated in practical systems to improve efficiency (Zohar *et al.*, 2007). A solution heat exchanger (SHX) is employed to recover heat from the high-temperature solution flow exiting the BPG, preheating the cool solution flowing out of the reservoir. A gas heat exchanger (GHX) is similarly incorporated for recuperation between the cool evaporator and warm absorber gas outlet streams. A refrigerant pre-cooler (RPC) can also be employed to precool liquid refrigerant entering the evaporator. A rectifier component may also be necessary if a relatively volatile absorbent, such as water, is employed. This component cools the vapor stream flowing out of the bubble-pump generator (BPG), condensing and separating the absorbent, and increasing the refrigerant purity. This process can lower the minimum evaporator

temperature, but also reduces the cooling capacity because some refrigerant will be condensed and removed with the rectifier reflux.

Commercial DAR systems can operate at refrigeration cooling coefficients of performance (COP = Q_{evap} / Q_{BPG}) of 0.2 – 0.3 (Jakob *et al.*, 2008). This value is significantly lower than vapor compression (COP ~ 2.0 – 3.0) or two-pressure absorption systems (0.5 – 1.0), but can be achieved with only thermal input.

6.1.3 Motivation and objectives

Conventional DAR systems require high source temperatures of 150 – 200°C (Jakob *et al.*, 2008; Srikhirin *et al.*, 2001) to deliver cooling at temperatures suitable for refrigeration. If this required input temperature can be reduced ($\lesssim$ 130°C), then DAR systems can operate with abundant low-grade thermal sources, such as solar heat or engine waste heat. A number of investigations have been performed to reduce source temperatures through the adoption of alternate refrigerant-absorbent pairs (other than NH_3-H_2O). These include R134a-He (Wang *et al.*, 2011), R22-DMAC (Zohar *et al.*, 2009), NH_3-$LiNO_3$ (Wang, 2012), and NH_3-NaSCN (Acuña *et al.*, 2013). H_2O-LiBr has also been considered (Pfaff *et al.*, 1998), but may not be suitable for refrigeration-grade cooling due to the relatively high freezing point of water (0°C).

In conventional BPG designs, heat is transferred to the working fluid through a small region near the base of the component. This *spot-heated* configuration limits heat transfer area, necessitating high source temperatures for given heating rates (i.e., $T_{source} - T_{BPG} \propto Q_{BPG}/A$). Alternate *distributed-heated* BPG designs have been proposed in recent investigations (Dammak *et al.*, 2010; Jakob *et al.*, 2008) and in Chapter 4 of this

thesis, which provide larger heat transfer area, permitting operation with reduced source temperatures. However, this distributed-heated configuration is significantly more challenging to design and analyze.

Existing DAR device designs may not be suitable for operation with alternate working fluids at significantly reduced source temperatures. In previous experimental investigations, system performance has been ensured with high-flux liquid condenser and absorber cooling (Jakob *et al.*, 2008; Srikhirin and Aphornratana, 2002) or forced internal fluid circulation (Wang, 2012). While these approaches have enabled proof-of-concept demonstrations, fully passive, low-source-temperature operation is necessary for target applications. Therefore, detailed component- and system-level models must be formulated to guide DAR development efforts under more constrained operating conditions. Such models will also be valuable for refinement of conventional DAR equipment. In the following section, reviews of prior work on low-source temperature DAR design and DAR modeling are presented.

6.1.4 Prior work

6.1.4.1 Low-source-temperature DAR systems

A number of detailed investigations have been performed on commercially available DAR implementations with NH_3-H_2O-H_2/He working fluids (Chen *et al.*, 1996; Srikhirin and Aphornratana, 2002; Zohar *et al.*, 2005). Such systems can operate fully passively with high BPG temperatures, and deliver a wide range of cooling COPs (T_{source} = 140 – 200°C and COP = 0.05 – 0.20 (Srikhirin *et al.*, 2001); T_{source} = 160 – 230°C and COP = 0.20 – 0.30 (Jakob *et al.*, 2008)). Low-source-temperature DAR systems have also been experimentally demonstrated in recent years. Jakob *et al.* (2008) developed a DAR system with high efficiency (up to COP = 0.48), high capacity (Q_{evap} = 2.5 kW cooling),

and relatively low source temperature (T_{source} = 130°C) with NH_3-H_2O-He working fluid. However, this system was only designed for chiller and A/C applications (T_{evap} = 6°C), and employed forced liquid cooling for the evaporator and condenser. Ben Ezzine *et al.* (2010b) demonstrated a fully passive (air-cooled) experimental DAR system with source temperatures of 125 – 150°C. They employed a new hydrocarbon working fluid mixture (C_4H_{10}-C_9H_{20}-He), which permitted use of low-cost copper heat and mass exchangers. Evaporator temperatures of -10°C were reported, but cooling performance was only rated for delivery temperatures of 9°C, with COPs of 0.10 – 0.14.

Wang (2012) demonstrated a low-source temperature (T_{source} = 93°C) DAR-based cooling system with NH_3-$LiNO_3$-He as the working fluid. Evaporator temperatures of -13°C were reported (COP = 0.16). However, the system employed both forced liquid external condenser and absorber cooling and mechanical internal fluid circulation. While these experimental systems represent significant advances in the field, fully passive, low-source-temperature ($\lesssim$130°C) cooling at refrigeration temperatures ($T_{cool} \lesssim$ 5°C) has not yet been achieved. The current range of demonstrated DAR operating conditions is summarized in Figure 6.3.

A number of cycle-level modeling studies have also been performed focusing on low-source-temperature DAR systems. Zohar *et al.* (2009) investigated a number of organic refrigerant-DMAC absorbent pairs. Operation at source temperatures of 135 – 150°C was predicted for R22-DMAC and R32-DMAC. Ben Ezzine *et al.* (2010a) modeled a DAR system with the R124-DMAC refrigerant-absorbent pair. They applied representative state point temperatures for both air and water cooled condenser and absorber components. Evaporator temperatures of -20 – 0°C were predicted for T_{BPG} = 120°C in

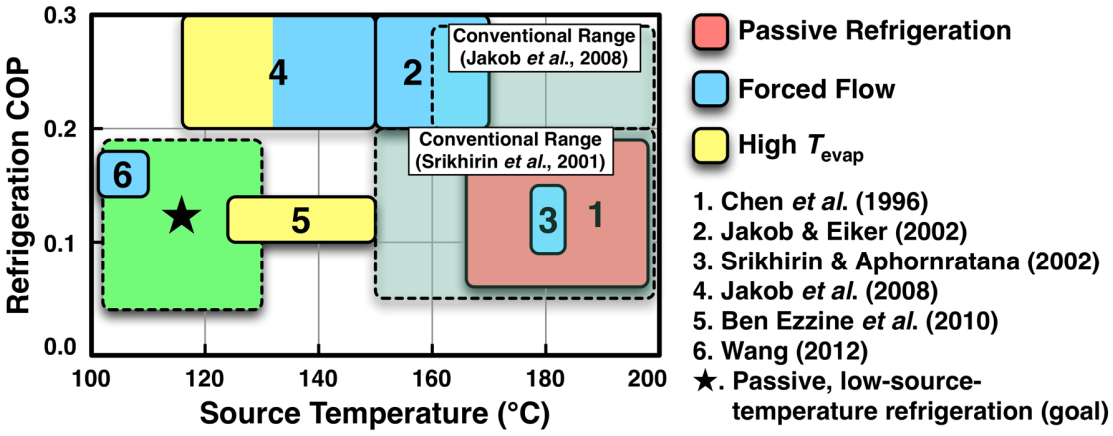

Figure 6.3 – Map of demonstrated DAR operating condition windows

the air-cooled implementation. Wang *et al.* (2011) proposed an implementation with a binary organic refrigerant (R23/R134a) and DMF absorbent. Very low cooling temperatures (T_{cool} = -40°C) were predicted with heat source temperatures of 110 – 160°C.

Acuña *et al.* (2013) compared DAR system operation with NH_3-H_2O, NH_3-$LiNO_3$, and NH_3-NaSCN refrigerant-absorbent pairs. Operating parameters for the cycle model were based on experimental results from the study of Jakob *et al.* (2008). The NH_3-$LiNO_3$ and NH_3-NaSCN pairs were predicted to significantly outperform NH_3-H_2O at low source temperatures (120°C). A number of other DAR cycle modeling efforts were reviewed by Rodríguez-Muñoz and Belman-Flores (2014).

Overall, these investigations highlight a number of promising cycle configurations and alternate working fluids that could enable fully passive low-source-temperature refrigeration. However, almost all have employed somewhat simplified closure relations

(e.g., assumed state points, approach temperatures, and flow rates). Therefore, detailed component-level design models are needed before the proposed systems can be realized.

6.1.4.2 DAR modeling and design studies

A number of experimental and cycle level modeling studies have been performed for DAR systems. However, few detailed, experimentally validated component- and system-level design models have been reported.

Srikhirin and Aphornratana (2002) developed a partial DAR cycle model that incorporated selected state values from an experimental facility. This approach enabled rating of individual components, but not prediction of overall system performance. BPG flow rates were predicted using a curve fit to experimental (air-water) component measurements. Zohar *et al*. (2005, 2007, 2008) published a series of complete thermodynamic system level DAR models that assumed certain state point values and temperature changes, effectively setting the fluid flow rates. Chaouachi and Gabsi (2007) developed a DAR system model that incorporated a bubble pump model to determine the refrigerant and solution flow rates, but employed a number of simplifying assumptions such as perfect rectification, complete vapor absorption, and isothermal cooling. Rattner and Garimella (2011a) developed a cycle level model that incorporated mechanistic BPG and gas loop passive circulation descriptions. Component heat-transfer rates were predicted using assumed overall conductance (UA) values rather than specified approach temperatures. This permitted more realistic analysis of a specific physical system at varying operating conditions. These cycle-level modeling efforts provide starting points toward practical system design. However, all DAR components operate passively, with many incorporating complex two-phase heat and mass transfer

phenomena. Detailed component-level models are therefore needed to realize target UA values and heat transfer rates.

The BPG component has received the most attention in the literature. A number of investigations have been performed focusing on the spot-heated configuration (adiabatic bulk flow) with air-water flow (de Cachard and Delhaye, 1996; Delano, 1998; Reinemann *et al.*, 1990; Schaefer, 2000; White, 2001). Pfaff *et al.* (1998) conducted an experimental investigation of spot-heated bubble pumps with water-lithium bromide working fluid. Koyfman *et al.* (2003) performed an experimental study of spot-heated R22 bubble-pumps. van der Walt (2012) performed a BPG modeling study, and incorporated flow-boiling heat transfer correlations to predict the developing flow in the short generator region.

A number of recent BPG investigations have focused on the distributed-heated configuration, which could enable operation at lower source temperatures. Jakob *et al.* (2008) designed and fabricated a vertical shell-and-tube coupling-fluid-heated BPG for a residential-scale DAR air-conditioning system. However, no component models were reported. Dammak *et al.* (2010) performed a modeling study of an inclined full-length heated BPG that could be integrated into a flat-plate solar collector. Benhimidene *et al.* (2011) also modeled a full-length uniformly heated BPG. Rattner and Garimella (2015a) formulated a model for a full-length coupling-fluid heated BPG, and experimentally validated it with an ambient pressure steam-water based system. Garma *et al.* (2014) performed an Eulerian-Eulerian two-phase simulation of BPG flow. Jo *et al.* (2014) also performed simulations of full-length uniformly heated BPGs. While a number of

distributed-heated BPG studies have been performed, experimental validation of models at realistic DAR system operating conditions has not yet been reported.

No detailed heat and mass transfer models have been reported for the condenser, evaporator, gas heat exchanger (GHX), solution heat exchanger (SHX), solution subcooler, and passively circulating gas loop. Only one model has been proposed for the DAR absorber (Rattner and Garimella, 2012). While some experimental studies provide implementation details (Ben Ezzine *et al.*, 2010b; Jakob *et al.*, 2008; Srikhirin and Aphornratana, 2002; Wang, 2012), limited resources are available for actual device design. Additionally, all flows in DAR systems are passively activated. Thus, component performances are tightly coupled, and system design must be performed in an integrated fashion.

6.1.5 Present investigation

Results from previous investigations of DAR technology indicate that low-source-temperature ($T_{source} \lesssim 130°C$), fully passive, and refrigeration-grade cooling ($T_{evap} \lesssim 5°C$) can be achieved. Such performance goals necessitate the use of alternate working fluids (other than NH_3-H_2O-H_2/He), improved and accurate distributed-heated BPG designs, and significant reconfiguration of other cycle components.

In this investigation, analyses are performed to develop a small capacity (10 – 30 W cooling), fully passive DAR refrigerator with NH_3-NaSCN-He as the working fluid mixture. This system is designed to operate in an environment with a low ambient air velocity (U_{amb} = 0.12 m s^{-1} assumed here), such as an indoor setting with background ventilation or outdoors with a breeze. Detailed, first-principles-based, coupled fluid and heat and mass transfer models are formulated to guide design of the more complex

system components: the BPG, condenser, evaporator, absorber, and passive circulation gas loop. The simpler single-phase heat exchangers (GHX, SHX, and solution subcooler) are not considered here for brevity. Results from these detailed analyses inform simplified models (e.g., UA-LMTD descriptions), which are incorporated into a complete cycle model. This cycle model is employed to predict system-level performance over varying operating conditions. In Chapter 7, these models are applied to develop a complete experimental DAR system. Experimental results are used to assess model accuracy and identify future research needs and paths to DAR technology refinement.

6.2 Component-Level Modeling and Results

6.2.1 Fluid properties

Thermodynamic and transport properties for the ammonia-sodium thiocyanate (NH_3-NaSCN) mixture are determined using correlations from Infante Ferreira (1984). That study proposed correlations for the crystallization curve (ψ_{cryst}), vapor-pressure (p_v), liquid-phase enthalpy (i_L), liquid density (ρ_L), liquid viscosity (μ_L), and thermal conductivity (k_L). The correlation for liquid viscosity was fit to data for -10°C < T < 60°C. At higher temperatures (as in the BPG), the viscosity correlation predicts negative values. Thus a limiting condition was applied so that μ_L is not less than the pure ammonia value (Fenghour *et al.*, 1995). No surface tension data are available for the NH_3-NaSCN mixture. Thus, values for the similar mixture NH_3-$LiNO_3$ are employed as an approximation (Zacarias *et al.*, 2013). Similarly, no binary diffusion data are available for the mixture ($D_{ab,L}$); therefore, the generalized Stokes-Einstein approach is employed for predicting this property.

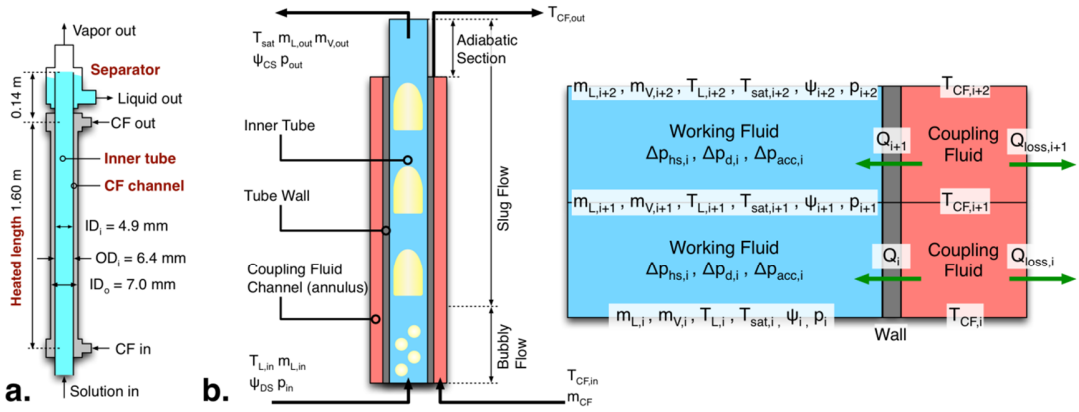

Figure 6.4 – **a**. Schematic of bubble-pump generator design, **b**. Segmented model configurations and discretization approach

Pure ammonia fluid properties (as in the BPG vapor phase or condenser) are evaluated using the model of Tillner-Roth *et al.* (1993) and transport property correlations included in the Engineering Equation Solver software (Klein, 2014). NH_3-He mixture gas phase thermodynamic and transport properties (i_G, ρ_G, k_G, μ_G, $D_{ab,G}$) are evaluated by applying ideal gas mixing rules.

6.2.2 Bubble-pump generator

The bubble-pump generator (BPG) design considered here (Figure 6.4a) is similar to the configuration proposed in Chapter 4. Two-phase working fluid flows upward in a narrow vertical tube as vapor is desorbed. Heat is supplied by co-flow coupling fluid in an outer annular channel. The inner tube terminates in a settling tank to separate the liquid solution and vapor refrigerant streams. This configuration was shown to achieve stable liquid pumping at low coupling-fluid inlet temperatures ($T_{CF,in} - T_{sat} \sim 10$ K for ambient pressure steam-water flow in Chapter 4), enabling DAR system operation with low-grade thermal sources. Additionally, low submergence ratio (the ratio of solution reservoir level to BPG height, $S_r = H_{res} / H_{BPG}$) operation was demonstrated ($S_r = 0.2$ –

0.4), enabling compact system configurations. A model is developed here, accounting for the coupled two-phase flow, flow boiling heat transfer, and mixture effects in the BPG. This is an expanded formulation based on the pure-fluid BPG model proposed in Chapter 4.

Representative model results are reported for a configuration with inner tube dimensions of ID_i = 4.9 mm and OD_i = 6.4 mm, and outer tube dimensions of ID_o = 7.0 mm and OD_o = 9.5 mm (Figure 6.4a). The full BPG length is 1.74 m, with heat transfer between the working fluid and coupling fluid occurring in the lower 1.60 m. In this case, subcooled dilute solution flows into the BPG inlet at $T_{L,in}$ = 64.0°C and a NaSCN mass fraction of $\psi_{in} = \psi_{DS}$ = 0.538. The inner tube absolute pressure is p_{sys} = 1.15 MPa, yielding an inlet saturation temperature of $T_{sat,in}$ = 73.0°C. The heating coupling fluid enters the annular channel at $T_{CF,in}$ = 120.2°C and a flow rate of V_{CF} = 175 ml min^{-1}. Heat loss from the coupling fluid to the surroundings is evaluated assuming an overall thermal resistance of R_{loss} = 2.0 K W^{-1}. The driving pressure difference corresponds to a submergence ratio of S_r = 0.275 (i.e., $p_{in} - p_{out} = \rho_L g H_{BPG} S_r = 4590$ Pa). The relatively minor variations in hydrostatic pressure along the component are neglected in the evaluation of fluid properties. An ambient temperature of T_{amb} = 24°C is assumed. This value is lower than that employed in some residential refrigerator rating protocols (T_{amb} = 32°C (United States Department of Energy, 2012)), but is representative of anticipated operating conditions (i.e., room temperature). The effect of varying ambient conditions on overall DAR system performance is analyzed in Section 6.3.

The model is axially segmented, with 20 main diabatic BPG segments (1.60 m total), and a single adiabatic segment (0.14 m) corresponding to the portion of the inner tube in

the settling vessel. Consecutive segment lengths increase at a constant ratio (+8.8%, $\Delta z_{20}/\Delta z_1 = 5$) to better resolve sharp variations near the BPG inlet. Flow properties are determined at the end points of each segment, and mass, species, energy, and momentum balances are applied over each segment (Figure 6.4b).

Mass balances are applied over each segment of the BPG inner tube.

$$m_{L,i} + m_{V,i} = m_{L,i+1} + m_{V,i+1} \tag{6.1}$$

Liquid and vapor flow rates are predicted to vary from the BPG inlet to outlet from 54.1 – 49.4 g min^{-1} and 0 – 4.7 g min^{-1}, respectively (55.4 – 50.6 ml/min and 0 – 676 ml min^{-1}). The predicted vapor flow rate peaks at z = 1.16 m (4.77 g min^{-1}), and decreases slightly toward the outlet value of 4.70 g min^{-1} due to heat loss to the surroundings. Liquid and vapor flow rate profiles are presented for the representative case in Figure 6.5.

NaSCN species balances are applied over each segment of the inner tube.

$$m_{L,i}\psi_i = m_{L,i+1}\psi_{i+1} \tag{6.2}$$

The predicted solution concentration varies from the dilute solution value of ψ_{DS} = 0.538 at the BPG inlet to the concentrated solution value of ψ_{CS} = 0.589 at the outlet. This corresponds to an increase in saturation temperature at p_{sys} = 1.15 MPa from 73.1 – 87.4°C along the length of the BPG.

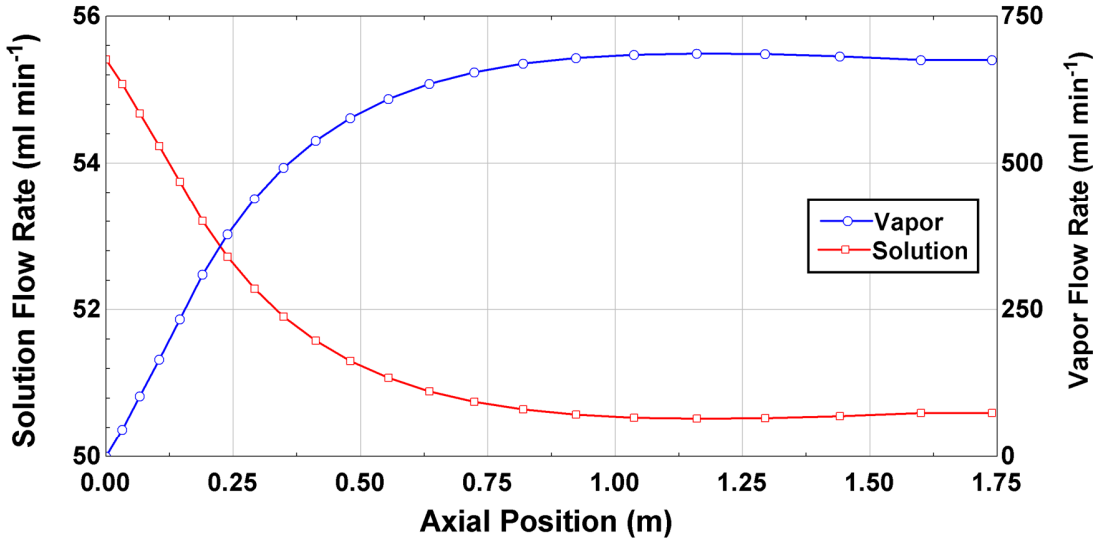

Figure 6.5 – Developing liquid and vapor flow rate profiles in the bubble-pump generator

Heat transfer from the coupling fluid (CF) annulus is modeled using a correlation for fully developed laminar flow (Re_{CF} = 50, h_{CF} = 720 W m^{-2} K^{-1} (Shah and London, 1978). Radial conduction resistance through the stainless steel inner tube (k_{wall} = 14 W m^{-1} K^{-1}) is minor (R_{tube}/R_{CF} = 0.04). Heat loss from the coupling fluid channel to the surroundings is evaluated assuming equal thermal resistance along the component length ($R_{loss,i} = R_{loss} \times H_{BPG}/\Delta z_i$). Segmental CF energy balances and inner wall temperatures are evaluated as follows:

$$m_{CF} c_{p,CF} \left(T_{CF,i+1} - T_{CF,i} \right) = -Q_i - Q_{loss,i} \tag{6.3}$$

$$Q_i = \frac{T_{CF,i} - T_{wall,i}}{R_{CF,i} + R_{cond,i}} \tag{6.4}$$

$$Q_{\text{loss,i}} = \frac{T_{\text{CF,i}} - T_{\text{amb}}}{R_{\text{loss,i}}} \tag{6.5}$$

Here, m_{CF} is the coupling fluid flow rate (147 g min^{-1}), $c_{\text{p,cf}}$ is the specific heat (2.18 kJ kg^{-1} K^{-1}), $T_{\text{wall,i}}$ is the inner-tube inner-wall temperature, and T_{amb} is the ambient temperature (24°C). Over the length of the BPG, the CF flow temperature decreases from 120.2°C to 86.7°C. A heat duty of 144.6 W is transferred to the working fluid, while 34.4 W is lost to the surroundings.

The heat transfer and energy balance models for the NH_3-NaSCN mixture must account for the variation of saturation temperature with solution concentration. Additionally, heat loss to the surroundings can cause condensation near the outlet of the BPG. Heat transfer to the working fluid is partitioned between liquid sensible heating ($Q_{\text{L,i}}$), vapor generation and sensible heating of the vapor ($Q_{\text{V,i}} = Q_{\text{i}} - Q_{\text{L,i}}$) as follows.

$$m_{\text{L,i+1}} i_{\text{L,i+1}} - m_{\text{L,i}} i_{\text{L,i}} = Q_{\text{L,i}} \tag{6.6}$$

$$m_{\text{V,i+1}} i_{\text{V,i+1}} - m_{\text{V,i}} i_{\text{V,i}} = Q_{\text{i}} - Q_{\text{L,i}} \tag{6.7}$$

The heat transfer from the inner tube wall to the liquid and vapor phases is evaluated based on the model of Liu and Winterton (1991), which was validated for subcooled flow boiling. This model applies correction factors to single-phase liquid heat transfer ($h'_{\text{L0}} = a_{\text{L0}} \times h_{\text{L0}}$) and no-flow nucleate boiling ($h'_{\text{NB}} = a_{\text{NB}} \times h_{\text{NB}}$) convection coefficients to account for interactions between these two phenomena. For subcooled boiling, this correlation blends the two heat transfer mechanisms quadratically:

$$Q_{\text{i}} = \left\{ \left[h'_{\text{L0,i}} \left(T_{\text{tube,i}} - T_{\text{L,i}} \right) \right]^2 + \left[h'_{\text{NB,i}} \left(T_{\text{wall,i}} - T_{\text{sat,i}} \right) \right]^2 \right\}^{1/2} \tag{6.8}$$

Here, T_L is the liquid bulk temperature. The same quadratic weighting employed in the original correlation is used to partition Q into sensible (Q_L) and phase-change (Q_V) contributions (Equation 6.9). A limiting factor is applied so that the liquid temperature cannot exceed the saturation temperature. Nucleate boiling is predicted to be a significant mode of heat transfer in the lower portion of the BPG; h'_{NB} = 5780 → 820 W m^{-2} K^{-1} from z = 0 → 0.72 m, corresponding to 45% → 6% of local wall heat flux. For segments with negative heat transfer (condensation, z > 1.16 m in this case), the nucleate boiling contribution to Q_i is set to 0 and heat transfer is partitioned between phases as in saturated flow condensation (i.e. $T_L = T_{sat}$). The h'_{L0} portion of the Liu and Winterton (1991) model was employed in segments with condensation for consistency and because the mechanisms of convective flow evaporation and convective flow condensation are similar. Furthermore, the in-tube contribution to heat transfer resistance is minor (h'_{L0} ranges from 2710 – 3350 W m^{-2} K^{-1}, h_{CF} = 720 W m^{-2} K^{-1}). Therefore, relatively large uncertainties in phase-change heat transfer coefficients in the upper portion of the BPG with relatively small temperature differences ($T_{CF} - T_{sat}$) would only have minor effects on overall predictions.

$$Q_{L,i} = \begin{cases} \min\left\{ \dfrac{\left[h'_{L0,i}\left(T_{wall,i} - T_{L,i}\right)\right]^2}{Q_i^2}, m_{L,i+1} i_{L,i+1} - m_{L,i} i_{L,i} \right\} & Q_i \geq 0 \\ m_{L,i+1} i_L\left(T_{sat,i+1}, \psi_{i+1}\right) - m_{L,i} i_{L,i} & Q_i < 0 \end{cases} \tag{6.9}$$

Predicted coupling fluid, liquid, and saturation temperature profiles are presented for the representative case in Figure 6.6. Near the BPG inlet, the bulk solution temperature (T_L) is significantly below the local saturation temperature $T_{sat} = T_V$ (i.e., subcooled flow boiling). The NH_3-NaSCN mixture transitions to saturated flow at z = 0.15 m.

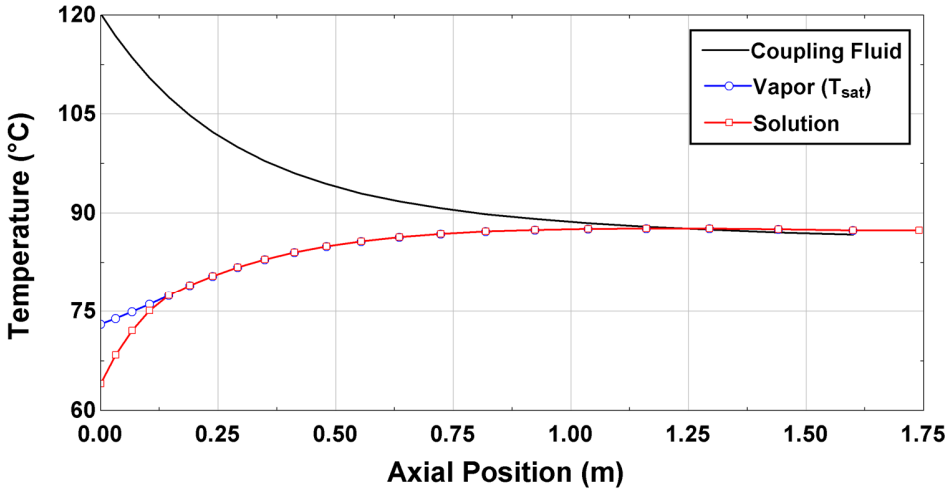

Figure 6.6 – Developing solution, vapor, and coupling fluid temperature profiles along the length of the bubble-pump generator

Condensation is predicted to occur from z = 1.16 – 1.6 m (the separator portion is assumed adiabatic). The CF temperature approaches that of the working fluid flow around the transition to flow condensation.

A momentum balance is applied over each segment of the NH_3-NaSCN channel, accounting for hydrostatic pressure drop, fluid acceleration, and dynamic (including frictional) pressure changes.

$$p_{\mathrm{i}} - p_{\mathrm{i+1}} = \Delta p_{\mathrm{hs,i}} + \Delta p_{\mathrm{d,i}} + \Delta p_{\mathrm{acc,i}} \tag{6.10}$$

The hydrostatic contributions (Δp_{hs}) are evaluated based on the average void fraction in each segment.

$$\Delta p_{\mathrm{hs,i}} = \left[\alpha_{\mathrm{i}} \rho_{\mathrm{V}} + \left(1 - \alpha_{\mathrm{i}}\right) \rho_{\mathrm{L}} \right] g \Delta z_{\mathrm{i}} \tag{6.11}$$

The hydrostatic contributions to pressure drop are found to be dominant in this study accounting for 4540 Pa (Δp_{net} = 4590 Pa).

Fluid acceleration pressure changes are evaluated based on the local void fraction and phasic velocities ($U_L = j_L/(1-\alpha)$, $U_L = j_V/\alpha$), as in Chapter 4. The net contribution of fluid acceleration to total pressure drop is relatively minor for this case (41 Pa).

A detailed two-phase flow sub-model is employed to determine local void fraction and dynamic pressure changes for local flow rates, channel geometry, and fluid properties. The model accounts for the transition from bubbly to Taylor flow and for the relatively complex flow phenomena that occur in the intermediate Bond number regime ($5 < Bo < 40$, $Bo = 10$ for the representative case). This model is based on the formulation developed in Chapter 4.

For the representative case, the transition from bubbly to Taylor flow is predicted to occur at z = 0.07 m. For this particular case, net frictional flow resistance is quite small (13 Pa). At the outlet of the BPG, the Taylor-bubble region frictional pressure gradient is ∇p_b = -875 Pa m^{-1}, the liquid slug frictional pressure gradient is ∇p_s = 861 Pa m^{-1}, and the bubble-to-slug flow transition pressure gradient is ∇p_{trans} = 618 Pa m^{-1} (84 Pa per flow transition, 0.14 m long unit cells). At the outlet, the relative bubble length is $\beta = L_b / (L_b + L_s) = 0.853$. Thus the outlet dynamic pressure change gradient is:

$$\nabla p_d(z = 1.60\text{ m}) = \beta \nabla p_b + (1-\beta)\nabla p_s + \frac{\Delta p_{trans}}{L_b + L_s} =$$
$$0.853\left(-875\text{ Pa m}^{-1}\right) + (1-0.853)\left(861\text{ Pa m}^{-1}\right) + \frac{84\text{ Pa}}{0.116\text{ m} + 0.020\text{ m}} = -1.7\text{ Pa m}^{-1} \quad (6.12)$$

Based on the large magnitudes of each term in Equation 6.12, the low overall dynamic frictional pressure change magnitude is specific to this particular case. For other flow conditions, ∇p_d may constitute a significant portion of the overall pressure drop.

For the representative case, a driving pressure difference of 4590 Pa is predicted to yield liquid and refrigerant flow rates of 49 g min^{-1} (50.6 ml min^{-1}) and 4.7 g min^{-1} (676 ml min^{-1}), respectively. Assuming a reservoir solution temperature of 35°C and dilute solution concentration of 0.538 ($\rho_{L,res}$ = 960.9 kg m^{-3}), this corresponds to a submergence ratio of S_r = 0.275. This provides sufficient excess height between the reservoir liquid level and top of the BPG (1.26 m) for the condenser, evaporator, gas heat exchanger, and absorber. By varying the submergence ratio between 0.241 and 0.311, the liquid flow rate can be adjusted from 25 to 70 ml min^{-1}. Thus, the design considered here is expected to provide sufficient control of liquid flow rates for proper absorber operation. Predicted BPG solution flow rates at varying source temperatures (110 – 130°C) and heating rates are presented in Figure 6.7. Optimal heating rates for maximum liquid pumping can be seen in this figure, as has also been reported in previous studies of conventional spot-heated BPGs (Delano, 1998). At higher heating rates, greater frictional resistance due to increased vapor volumetric flow limits solution pumping. Based on these results, the proposed design can provide sufficient liquid pumping rates for a wide range of DAR system operating conditions.

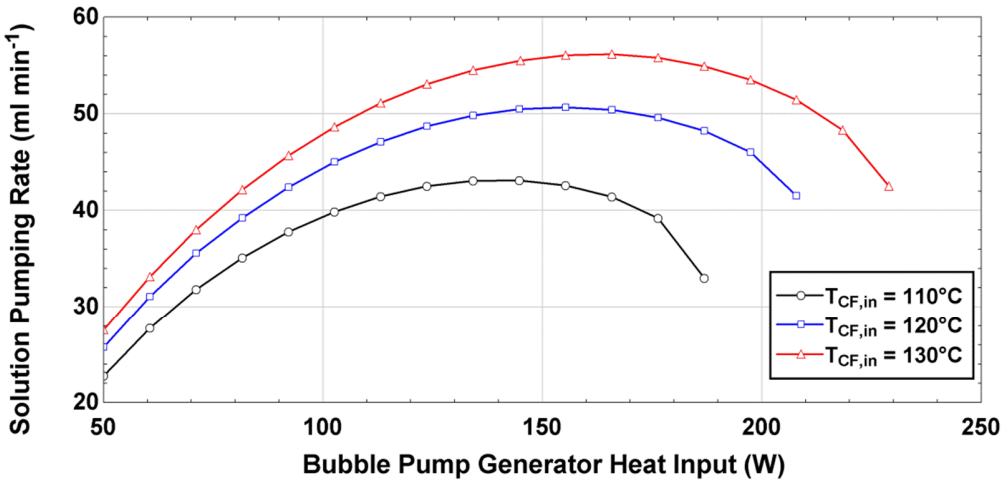

Figure 6.7 – Predicted bubble-pump generator solution flow rates at varying operating conditions (for $S_r = 0.275$, $T_{L,in} = 64.0°C$, $p_{sys} = 1.15$ MPa, $\psi_{DS} = 0.538$, $T_{amb} = 24.0°C$)

6.2.3 Condenser

The main challenge in designing a DAR condenser is achieving sufficient heat rejection to the surroundings ($Q_{cond} \sim i_{LV,NH3} \times m_{ref}$) with only passive transport mechanisms: natural convection (air flow driven by the elevated condenser temperature), ambient air circulation convection (low velocity "background" air flow in the environment), and radiation. In conventional DAR systems, a serpentine finned tube condenser is employed (Chen *et al.*, 1996). A large condenser is required in the proposed system design because the operating pressure is relatively low ($p_{sys} \sim 1.15$ MPa) to accommodate low source temperatures ($T_{BPG,CF,in} = 110 - 130°C$). This results in a low driving temperature difference for condenser cooling ($T_{sat,NH3}(p_{sys}) = 29.5°C$, $T_{amb} = 24°C$).

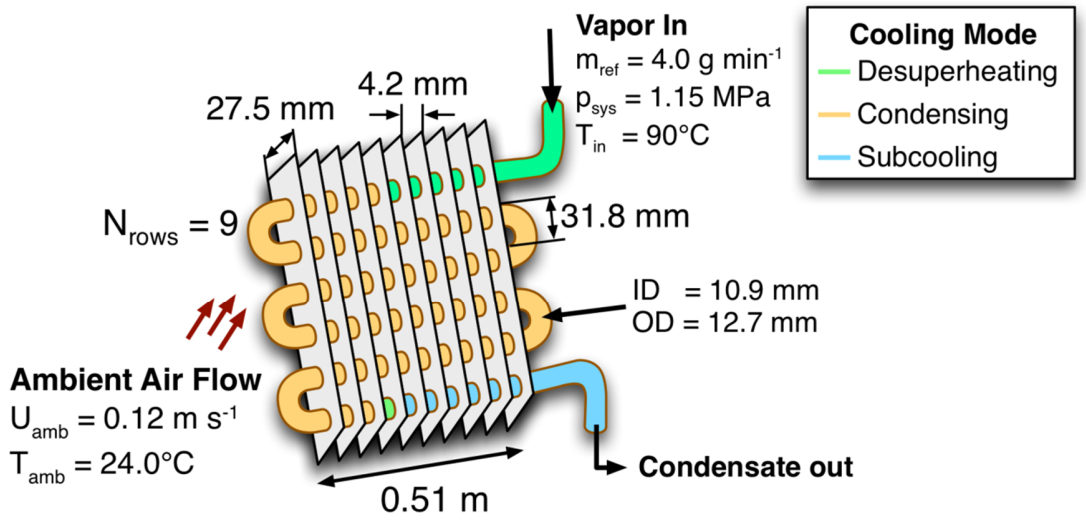

Figure 6.8 – Schematic and operating conditions for proposed condenser design

The proposed serpentine finned tube condenser design is presented in Figure 6.8. The design has 9 rows of stainless steel tubes (ID = 10.9 mm, OD = 12.7 mm, L_{row} = 0.51 m, L_{tot} = 4.57 m). Tube rows are spaced by p_{row} = 31.8 mm. The tubes are enhanced with press-fit smooth rectangular fins with thickness 0.19 mm and height 27.5 mm. A relatively wide fin pitch is selected (4.2 mm, 236 fins m^{-1}). This limits heat transfer area (total external heat transfer area: 1.79 m^2), but is necessary to prevent excessive flow resistance, which can reduce overall cooling performance. The spacing is less than the optimal value predicted with the model of Bar-Cohen and Rohsenow (1984) (7.4 mm at fin temperature T_f = 29.5 C). However, the proposed design is intended to take advantage of ambient air circulation in the enclosing ventilation hood, which augments natural-circulation-driven flow through the fin channels. The condenser is inclined slightly downward (towards the refrigerant outlet) so that condensate drains into the evaporator and acts a gas trap to prevent non-condensable helium ingress.

The condenser is modeled with three segments corresponding to the desuperheating, condensing, and subcooling portions of the component. For each section, a thermal resistance network is formed from the ammonia flow to the ambient. Segmental heat transfer is determined using the effectiveness-number of transfer units approach (ε-NTU) for cross-flow heat exchangers. Representative results are reported for operation with a system pressure of p_{sys} = 1.15 MPa, refrigerant flow rate of m_{ref} = 4.0 g min^{-1}, vapor inlet temperature of T_1 = 90°C, ambient air temperature of 24°C, and an ambient airflow velocity across the fins of U_{amb} = 0.12 m s^{-1}. This ambient air-flow is representative of background ventilation in an indoor operating environment or very low wind-speeds in an outdoor application.

In the first section, the vapor stream flow is laminar (Re_1 = 690). This results in an internal heat transfer coefficient of $h_{int,1}$ = 23 W m^{-2} K^{-1}. Conduction through the circular tube wall results in a minimal heat transfer resistance of 0.0016 m K W^{-1}. Ambient circulation through the fin channels (assumed U_{amb} = 0.12 m s^{-1}) results in a laminar channel flow heat transfer coefficient of $h_{ext,forced}$ = 22 W m^{-2} K^{-1} (Re_{ext} = 55). At the average fin temperature of $T_{f,1}$ = 27.5°C, natural convection through the fin channels results in a heat transfer coefficient of $h_{ext,nat,1}$ = 0.90 W m^{-2} K^{-1}. This value is predicted using the correlation of Elenbaas (1942), which determines the heat transfer rate relative to the ambient temperature, rather than the mean channel flow temperature. However, at the low thermal capacity rate ratio ($C_r = m_{ref}c_{p,NH3}/m_{air}c_{p,air}$ = 0.21), these values are very close: T_{inf} = 24.0°C, ($T_{air,in,1}$ + $T_{air,out,1}$) / 2 = 24.1°C. The forced and natural convection coefficients are blended using a standard power-law approach to arrive at a total external heat transfer coefficient:

$$h_{\text{ext,conv,1}} = \left(h_{\text{ext,forced}}^3 + h_{\text{ext,nat}}^3 \right)^{1/3} = 21.8 \text{ W m}^{-2} \text{ K}^{-1} \tag{6.13}$$

This result ($h_{\text{ext,conv,1}} \sim h_{\text{ext,forced}}$) indicates that, even at very low ambient air-flow rates (0.12 m s^{-1}), ambient air circulation convection is the dominant mode of heat rejection at the low driving temperature difference ($T_{\text{sat,NH3}}(p_{\text{sys}}) - T_{\text{amb}} = 5.5$ K).

Radiation heat transfer is modeled assuming that the rectangular fin array acts as a black body. The total heat transfer rate from the desuperheating section is evaluated from the bounding surface at the average fin temperature ($T_{\text{f,1}}$).

$$Q_{\text{rad,1}} = \sigma \left(2 L_1 p_{\text{row}} \right) \left(T_{\text{f,1}}^4 - T_{\text{amb}}^4 \right) = 0.26 \text{ W} \tag{6.14}$$

The effective radiation heat transfer coefficient ($h_{\text{eff,rad,1}}$) is determined by averaging over the total external finned surface area ($A_{\text{tot,1}} = 0.073$ m^2).

$$h_{\text{eff,rad,1}} = \frac{Q_{\text{rad,1}}}{A_{\text{tot,1}} \left(T_{\text{f,1}} - T_{\text{amb}} \right)} = 1.0 \text{ W m}^{-2} \text{ K}^{-1} \tag{6.15}$$

Finally, the combined convection and radiation external heat transfer coefficient is obtained as: $h_{\text{ext,1}} = h_{\text{ext,conv,1}} + h_{\text{eff,rad,1}} = 22.7$ W m^{-2} K^{-1}. Assuming a uniform value of $h_{\text{ext,1}}$, the total finned surface efficiency is determined to be $\eta_{\text{o,1}} = 0.95$. The net lengthwise thermal resistance from the refrigerant to ambient is $R'_{\text{net,1}} = 1.41$ m K W^{-1}. Finally, the desuperheating section length, heat transfer, and average fin temperature are solved implicitly as follows:

$$Q_1 = m_{\text{ref}} c_{\text{p,NH}_3} \varepsilon_1 \left(T_1 - T_{\text{amb}} \right) \tag{6.16}$$

$$\varepsilon_1 = f\left(NTU, \frac{m_{ref} c_{\mathrm{p,NH_3}}}{m_{air} c_{\mathrm{p,air}}} \right) \tag{6.17}$$

$$\mathrm{NTU}_1 = \frac{L_1 / R'_{\mathrm{net},1}}{m_{\mathrm{ref}} c_{\mathrm{p,NH_3}}} \tag{6.18}$$

$$Q_1 = m_{\mathrm{ref}} c_{\mathrm{p,NH_3}} \left[T_1 - T_{\mathrm{sat,NH_3}} \left(p_{\mathrm{sys}} \right) \right] \tag{6.19}$$

$$Q_1 = A_{\mathrm{tot},1} h_{\mathrm{ext},1} \left(T_{\mathrm{f},1} - T_{\mathrm{amb}} \right) \tag{6.20}$$

Here, the effectiveness (ε_1) is evaluated using results for cross-flow heat transfer. For the desuperheating heat transfer of 5.9 W, the required heat exchanger length is L_1 = 0.19 m.

Similar approaches are employed to model heat transfer in the condensing and subcooling segments of the condenser. In the condensing section, the internal heat transfer coefficient is evaluated using the correlation of Akers *et al.* (1958) for flow in horizontal tubes at an average quality of 0.5 ($h_{\mathrm{int},2}$ = 770 W m^{-2} K^{-1}). The condensing section accounts for the major portion of the component length (4.1 m) and heat transfer (Q_2 = 76.4 W). Internal convective heat transfer in the final subcooling segment (L_3 = 0.26 m) is modeled assuming laminar liquid flow ($h_{\mathrm{int},3}$ = 160 W m^{-2} K^{-1}). The ammonia stream is predicted to nearly approach the ambient temperature (T_{out} = 24.1°C, T_{amb} = 24.0°C, Q_3 = 1.7 W). The overall condenser heat transfer is 84.1 W.

Condenser outlet temperatures for varying refrigerant flow rates and ambient air velocities are presented in Figure 6.9 for $T_{\mathrm{cond,in}}$ = 90°C and p_{sys} = 1.15 MPa. For the anticipated ranges of refrigerant flow rates (3 – 5 g min^{-1}), ambient air velocities of only

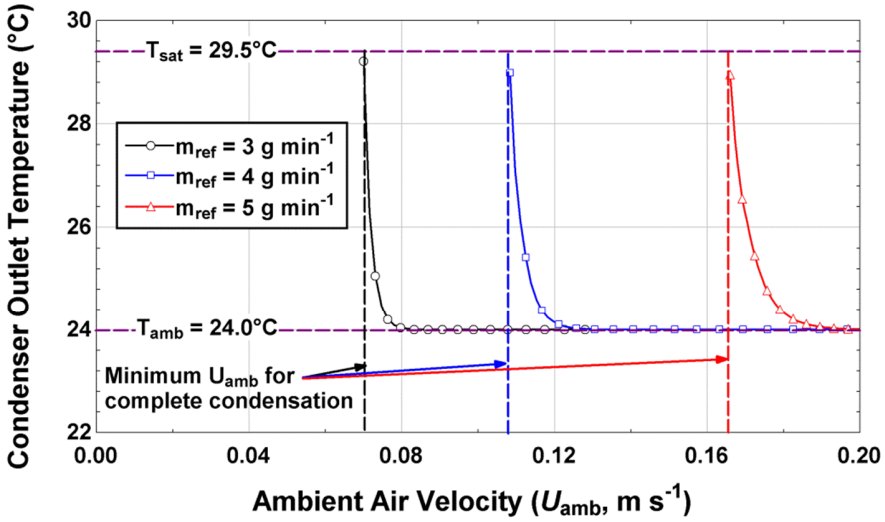

Figure 6.9 – Predicted condenser outlet temperatures for varying refrigerant flow rates and ambient air velocities ($T_{cond,in}$ = 90°C, p_{sys} = 1.15 MPa)

~0.1 – 0.2 m s^{-1} are sufficient for complete condensation. Refrigerant outlet temperatures approach T_{amb} at higher ambient air velocities (liquid subcooling). This indicates that the proposed DAR system design can function at low operating pressures (p_{sys} = 1.15 MPa) provided that some minimal ambient circulation is present.

If no ambient circulation is present (U_{amb} = 0) then the system pressure must be increased to 1.58 MPa to fully condense the refrigerant through natural convection and radiation heat transfer ($T_{sat,NH3}$(1.58 MPa) = 40.6°C, T_{amb} = 24.0°C). Under such stagnant air-side conditions, DAR system operation may also cause an ambient air temperature increase near the condenser, resulting in even greater required system pressures. For the baseline system operating conditions (ψ_{DS} = 0.538), this would necessitate a ~13 K increase in the BPG source temperature for equivalent operation ($T_{sat,NH3\text{-}NaSCN}$(p = 1.15 MPa, ψ = 0.538) = 73.0°C, $T_{sat,NH3\text{-}NaSCN}$(p = 1.58 MPa, ψ = 0.538) = 86.4°C).

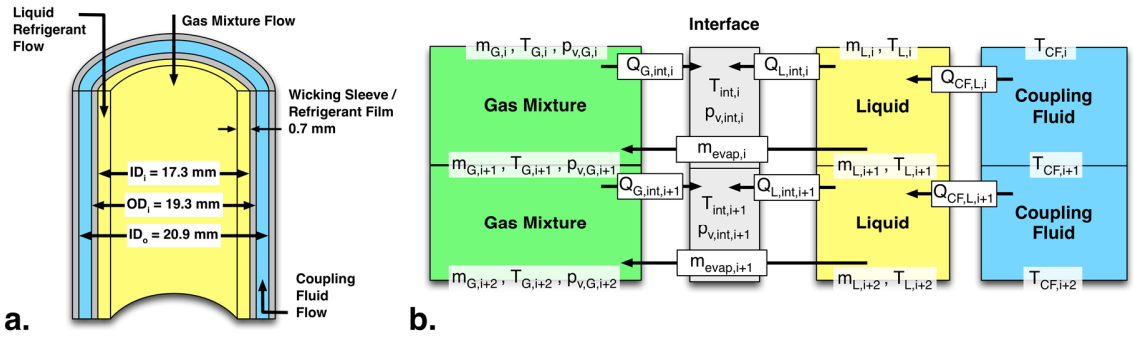

Figure 6.10 – **a**. Schematic of evaporator design, **b**. Segmented model discretization scheme

6.2.4 Evaporator

The evaporator component in the DAR cycle delivers cooling to the conditioned space through evaporative mass transfer of liquid refrigerant to a low-vapor-pressure auxiliary gas stream. This mode of operation differs significantly from conventional vapor-compression and two-pressure absorption system evaporators, in which refrigerant flashes to a two-phase state across a high-pressure-drop expansion device and continues to evaporate at the saturation temperature along the length of the component. Thus, DAR evaporator performance may be limited by both heat transfer resistance and interface-to-gas mass transfer resistance. Effective component design must account for both of these factors.

A tube-in-tube evaporator design is considered in this investigation (Figure 6.10a). Refrigerant (NH_3) and auxiliary gas (NH_3-He mixture) flow vertically downwards in an inner tube (ID_i = 17.3 mm, OD_i = 19.1 mm, L = 0.30 m). The liquid refrigerant is assumed to flow as a falling film on the tube wall. Coupling fluid (CF) water flows vertically upward (counter-flow) in a narrow outer annulus (ID_o = 20.9 mm). In actual

Table 6.1 – Representative evaporator operating conditions

System pressure	p_{sys}	1.15	MPa
Refrigerant inlet flow rate	$m_{L,in}$	4.0	g min^{-1}
Refrigerant inlet temperature	$T_{L,in}$	25.0	°C
Auxiliary gas inlet flow rate	$m_{G,in}$	20.0	g min^{-1}
Auxiliary gas inlet flow temperature	$T_{G,in}$	21.0	°C
Auxiliary gas inlet helium mass fraction	ξ_G	0.30	-
Coupling fluid flow rate	m_{CF}	80.0	g min^{-1}
Coupling fluid inlet temperature	$T_{CF,in}$	5.0	°C

applications, the evaporator would be directly air coupled (i.e., installed inside the conditioned space). Forced liquid coupling is employed here to enable more accurate experimental component performance measurement (see Part II). Results are reported for a representative case for which operating and inlet conditions are summarized in Table 6.1.

At the representative operating conditions, the refrigerant flow rate may be too low to ensure complete liquid film wetting of the inner tube. Similar considerations were highlighted in the design study of Jakob *et al.* (2008). Based on the model of El-Genk and Saber (2001), a minimum refrigerant flow rate of 26.9 g/min (~7 × $m_{L,in}$) is required to transition from the rivulet to continuous film flow mode (assuming a contact angle of 30°). Thus, a wicking cloth sleeve (representative thickness 0.7 mm) would be installed inside the evaporator to improve film distribution on the tube wall. It is assumed that this sleeve enforces an effective film thickness of δ_f = 0.7 mm, rather than the much thinner value that would be predicted with Nusselt film theory (δ_f = 0.05 mm at the inlet).

An axially segmented model (N_{seg} = 25, Δz = 12 mm) is employed to describe the varying properties and transport along the length of the evaporator component. Flow

properties are stored at the inlet and outlet nodes of each segment for the gas mixture, liquid refrigerant, and CF flows (Figure 6.10b). Liquid-to-gas interface properties are evaluated at the center of each segment. Mass, species, and energy balances are applied over each segment as appropriate.

The mass balances for each segment of the refrigerant and gas streams are defined as follows:

$$m_{L,i+1} = m_{L,i} - m_{evap,i} \tag{6.21}$$

$$m_{G,i+1} = m_{G,i} + m_{evap,i} \tag{6.22}$$

Here, m_{evap} is the rate of evaporation in each of the 25 segments, which ranges between 0.04 and 0.20 g min^{-1}. The refrigerant liquid flow rate is predicted to decrease from 4.0 to 2.7 g min^{-1} along the length of the component (32% evaporation).

Species balances are applied over each segment of the gas stream.

$$\xi_i m_{G,i} = \xi_{i+1} m_{G,i+1} \tag{6.23}$$

With the increasing vapor-phase ammonia concentration along the length of the component, the gas helium mass fraction decreases from 0.30 to 0.28 (helium mole fraction ξ* decreases from 0.65 to 0.63).

Thermal resistance from the liquid-bulk to the interface is modeled assuming conduction transport through half the film thickness (similar to the Nusselt assumption): $h_{L,int} = k_L/(\delta_f/2)$ = 1510 W m^{-2} K^{-1}. The same convection coefficient value is assumed for transport from the film bulk to the tube inner wall ($h_{L,tube}$ = 1510 W m^{-2} K^{-1}). The

effective conductivity of the liquid film may be slightly altered in practice because of the presence of the wicking material in the film. Thermal resistance from the gas phase to the interface is predicted assuming laminar-to-transitional flow (Re_G ~ 2100), resulting in a convective transport coefficient of: $h_{G,int}$ = 37 W m^{-2} K^{-1}. Thermal conduction resistance through the stainless steel tube wall is minimal: $R''_{tube} = 6.3 \times 10^{-5}$ m^2 K W^{-1}. Convection heat transfer in the coupling fluid (CF) channel is modeled assuming laminar annular flow (Re_{CF} = 40): h_{CF} = 1970 W m^{-2} K^{-1}. The net CF-to-liquid refrigerant resistance is:

$$R'_{CF,L} = \frac{1}{WF}\left\{\frac{1}{\pi ID_i h_{L,tube}} + \frac{\ln\left(OD_i/ID_o\right)}{2\pi k_{tube}} + \frac{1}{\pi OD_i h_{CF}}\right\} = 0.022 \text{ m W K}^{-1} \qquad (6.24)$$

Here, *WF* is the wetting factor, which represents the portion of the tube perimeter effectively wetted by refrigerant film in each segment. A value of *WF* = 1 is employed in the baseline case, but this parameter can be varied to simulate the effect of incomplete liquid distribution.

Gas phase thermal resistance is greater than that of the refrigerant liquid film or CF. However, this does not directly limit evaporator performance because the cooling heat-transfer path is from the CF to the liquid-gas interface. In cases where incomplete film wetting occurs, direct heat transfer could occur between the gas and CF (through the dry portion of the wall). This secondary transport path is not considered in this model.

The interface energy balance for each segment is defined as:

$$m_{evap,i} i_{LV,NH_3}\left(T_{int,i}\right) = \left[\pi\left(ID_i - 2\delta_f\right)\Delta z WF\right]\left[h_{L,int}\left(T_{L,i+1} - T_{int,i}\right) + h_{G,int}\left(T_{G,i+1} - T_{int,i}\right)\right] \qquad (6.25)$$

Driving temperature differences for heat transfer in each segment *i* are evaluated using downwind nodal values (i.e., $T_{L,i+1} - T_{int,i}$, $T_{G,i+1} - T_{int,i}$) for improved numerical stability. Evaporative mass transfer is modeled assuming that liquid flows from the film to interface, and vapor flows from the interface to the gas bulk. Corresponding energy balances are applied for the liquid, gas, and coupling fluid streams.

$$m_{L,i} i_{L,i} - m_{L,i+1} i_{L,i+1} - m_{evap,i} i_{L,int,i} = WF \left\{ \begin{array}{l} \left[\pi \left(ID_i - 2\delta_f \right) \Delta z \right] \left[h_{L,int} \left(T_{L,i+1} - T_{int,i} \right) \right] \\ + \dfrac{T_{L,i+1} - \left(T_{CF,i} + T_{CF,i+1} \right)/2}{R'_{CF,L}/\Delta z} \end{array} \right\} \tag{6.26}$$

$$m_{G,i} i_{G,i} - m_{G,i+1} i_{G,i+1} + m_{evap,i} i_{V,int,i} = WF \left\{ \left[\pi \left(ID_i - 2\delta_f \right) \Delta z \right] \left[h_{G,int} \left(T_{L,i+1} - T_{int,i} \right) \right] \right\} \tag{6.27}$$

$$m_{CF} c_{p,CF} \left(T_{CF,i+1} - T_{CF,i} \right) = WF \left\{ \frac{\left(T_{CF,i} + T_{CF,i+1} \right)/2 - T_{L,i+1}}{R'_{CF,L}/\Delta z} \right\} \tag{6.28}$$

The CF is counter-flow to the refrigerant and gas mix, thus the inlet to CF segment *i* is node *i*+1. In the discretized energy balance above, no working fluid-to-CF heat transfer is considered in the top segment (i = 1). This assumption is made to account for premixing of refrigerant and gas at the evaporator working fluid inlet. As indicated above, this evaporator design model does not account for heat transfer directly from the CF to gas stream (bypassing the refrigerant film) if $WF < 1$. This is expected to only lead to minor changes in evaporator operation because $R''_{G,int}$ (0.027 m^2 K W^{-1}) is large compared to $R''_{int,tube}$ (0.001 m^2 K W^{-1}).

At the developing laminar-to-transitional gas-phase conditions (Re_G = 2100, Sc_G = 0.92), the Sherwood number is predicted to be Sh_G = 8.4. For the NH_3-He gas mixture, this corresponds to a convective mass transfer coefficient of $h^*_{G,int}$ = 0.0048 kg m^{-2} s^{-1} Pa^{-}

[1] (units of mass flux/vapor pressure difference). The segmental evaporative mass transfer rate is:

$$m_{\text{evap,i}} = WFh^*_{\text{G,int}} \left(\frac{\text{MW}_{\text{NH}_3}}{R^* T_{\text{int,i}}} \right) \left[\pi \left(\text{ID}_\text{i} - 2\delta_\text{f} \right) \Delta z \right] \left(p_{\text{v,int,i}} - p_{\text{v,G,i+1}} \right) \tag{6.29}$$

Here, MW_{NH3} is the molar mass of ammonia (17.0 kg kmol^{-1}), R^* is the universal gas constant (8.314 kJ kmol^{-1} K^{-1}), and $p_{\text{v,int}}$ and $p_{\text{v,G}}$ are the NH_3 vapor pressures at the interface and in the gas bulk, respectively. The interface vapor pressure is $p_{\text{v,int}} = p_{\text{sat,NH3}}(T_{\text{int}})$, and varies from 573 – 445 kPa over the length of the component. The gas-phase vapor pressure is determined assuming ideal gas mixing ($p_{\text{v,g}} = (1 - \xi^*)p_{\text{sys}}$), and varies from 407 – 431 kPa along the length of the component. Thus, for this operating condition, the gas phase has the capacity to absorb additional refrigerant vapor and permit additional evaporative cooling if the component length is increased.

The evaporator mass transfer performance can be rated with an overall conductance: $\text{UA}^*_{\text{evap}} = m_{\text{evap}}/\text{LMPD}_{\text{evap}}$. Here, LMPD is the log-mean vapor pressure difference between the liquid refrigerant and gas streams, analogous to the more familiar log-mean temperature difference (LMTD). For the baseline operating conditions $\text{LMPD}_{\text{evap}}$ = 227 kPa, resulting in a conductance of $\text{UA}^*_{\text{evap}} = 9.4 \times 10^{-11}$ kg Pa^{-1} s^{-1}.

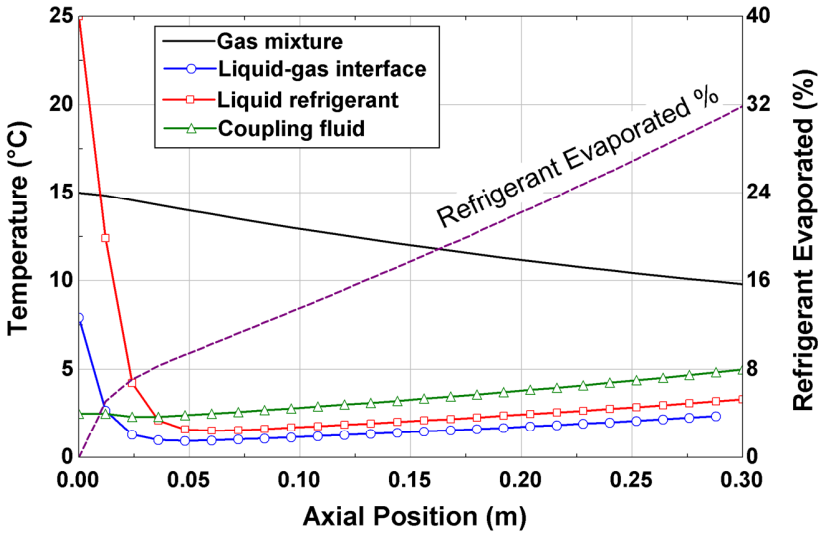

Figure 6.11 – Developing temperature profiles and evaporated refrigerant fraction in the evaporator for the representative case

The segmental mass transfer equation (6.29) and energy equations (6.25 – 6.28) are solved simultaneously to determine the component performance. The resulting temperature profiles for the gas, interface, refrigerant, and CF are presented in Figure 6.11 for the representative case. For this case, the refrigerant evaporation proceeds rapidly near the inlet of the component, yielding a minimum liquid temperature of 1.5°C 60 mm from the inlet. The interface temperature tracks that of the liquid refrigerant, reaching a minimum value of 0.9°C 48 mm from the inlet. The liquid refrigerant and interface temperatures increase slightly toward the working-fluid outlet (z = 0.30 m), where the heating counter-flow CF stream is warmer. The CF temperature approaches the minimum refrigerant temperature relatively closely ($T_{CF,out}$ = 2.5°C) due to the low interface-to-CF thermal resistance. In the representative case, 14.1 W of cooling is delivered to the CF stream. Due to relatively poor gas-phase heat transfer, the gas bulk

temperature only decreases from 15.0 – 9.8°C along the length of the component. Thus, even the relatively high gas flow rate ($m_{G,in}$ / $m_{L,in}$ = 5) only effects a minor parasitic cooling load ($m_{G,out} \times c_{p,G} \times (T_{G,in} - T_{G,out})$ = 6.1 W). In contrast, if the component were configured such that $T_{G,out} = T_{int,out}$, the gas cooling load would be 14.9 W. As such, DAR evaporators should be designed so that interface-to-CF (or conditioned space) heat transfer resistance is significantly less than interface-to-gas resistance.

A sensitivity study was conducted to identify the key factors that affect DAR evaporator performance. For these cases, the CF flow rate was adjusted to maintain the same temperature change along the length of the component (5 → 2.5°C). In this analysis, unless noted otherwise, all parameters are kept at the representative case conditions. Cooling capacity is particularly sensitive to the assumed wetting factor (*WF*). Varying *WF* from 1.00 – 0.53 results in decreasing cooling capacity, from 14.1 – 4.2 W (about 1 W loss per 0.05 reduction in *WF*). Furthermore, in actual implementations, film dryout may permit heat transfer from the warm gas to the tube, resulting in local CF heating.

Increasing the evaporator length from 0.15 – 1.0 m increases the evaporator cooling capacity from 5.8 – 37.2 W. For the longest case (L = 1.0 m), 64% of the refrigerant is evaporated, yielding significantly improved performance compared to the baseline case (32% evaporation). Based on this result, the proposed evaporator design may be undersized. However, in practice, the evaporator length must be balanced with that of the gas heat exchanger (GHX), which fits between the bottom of the evaporator and top of the absorber. It is also important to consider gas-loop frictional pressure drop changes due to modifications to the evaporator and GHX geometries. Furthermore, high

evaporation rates may lead to film dryout and heating of the CF by the gas stream, as previously discussed.

Increasing the gas flow rate from $m_{G,in}$ = 6 to 100 g min^{-1} increases cooling capacity from 5.8 to 22.0 W. However, only minor performance gains are predicted for $m_{G,in}$ > 50 g min^{-1}. Beyond this point, the evaporation process is not mass transfer limited and parasitic gas-phase cooling accounts for a greater portion of the evaporator capacity. The gas circulation is effected passively through natural convection. Therefore, greater flow rates may not be possible without excessive component and plumbing diameters to reduce frictional resistance. Additionally, the required GHX size may be impractical at high flow rates.

The evaporator performance is particularly sensitive to the gas phase inlet concentration ($\xi_{G,in}$). Increasing the inlet concentration from 0.285 to 0.400 (p_v = 427 → 300 kPa) increases the cooling capacity from 8.2 to 42.3 W. The highest concentration corresponds to a refrigerant evaporation fraction of 70%. This result suggests that the proposed evaporator design may, in fact, be adequately sized if the absorber is sufficiently effective. At 35°C and the baseline BPG CS concentration (ψ_{CS} = 0.589, Section 6.2.2), the solution vapor pressure is 269 kPa. Thus, if the absorber can achieve a gas-to-solution closest approach vapor pressure of $CAVP_{abs}$ ~ 30 kPa, then high evaporator performance (70% evaporation) can be achieved with the relatively small (L = 0.3 m) proposed design.

6.2.5 Absorber

The function of the DAR absorber is to absorb vapor refrigerant from the passively circulating gas stream. This regenerates the refrigerant capacity of the auxiliary gas,

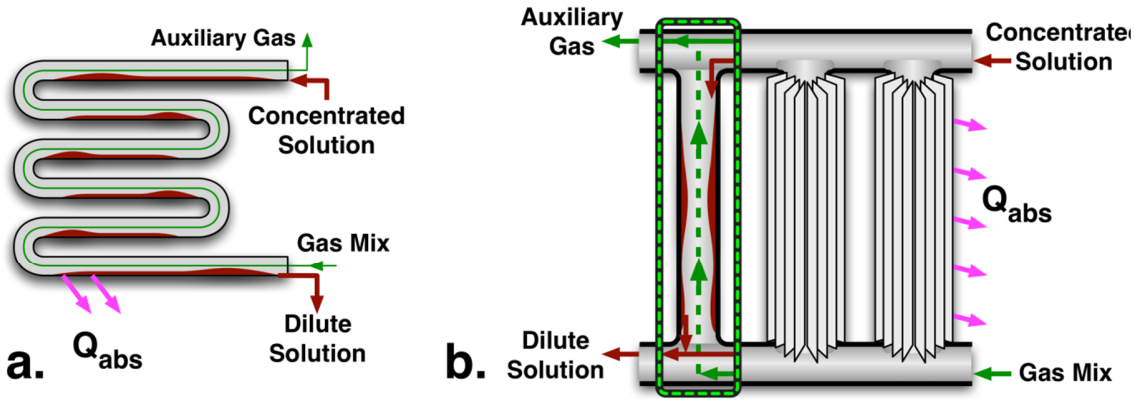

Figure 6.12 – **a**. Conventional serpentine-tube DAR absorber configuration, **b**. Proposed enhanced absorber design

enabling evaporative cooling in the evaporator. While numerous investigations have been performed focused on the absorber component in two-pressure sorption cycles, limited information is available for the single-pressure (DAR) configuration. The DAR absorber introduces a number of modeling and design challenges not encountered in two-pressure systems, including:

- Significant gas-phase mass transfer resistance due to the high inert gas (He) concentration
- Limited external cooling (natural convection and radiation) for passive cycle operation
- The need for two outlet streams (auxiliary gas and DS)

All passively cooled DAR systems (i.e., excluding experimental systems with forced liquid or air cooling) reported in the literature have employed the same single serpentine tube absorber configuration (Figure 6.12a). In this design, liquid and vapor contact in a counter-flow fashion through a long coiled tube. This approach ensures effective liquid-

vapor distribution as there is only a single fluid flow path, but presents a number of limitations, including:

- Limited interfacial area – Liquid generally flows in the rivulet or stratified pattern, only wetting the bottom of the absorber tube and yielding limited interfacial area for mass transfer.
- High pressure drop – The single long flow path can result in excessive gas-side pressure drop, especially for low-source temperature DAR systems with reduced driving temperature differences for passive auxiliary gas circulation.
- Poor scalability – While the single serpentine-tube design may be sufficient for small-scale DAR systems, absorption capacity can only be increased with a longer component, which in turn will increase pressure drop.
- Limited external heat transfer – Existing DAR systems have employed unenhanced (bare) absorber tubes, resulting in high external heat transfer resistances.

In this investigation, an alternate absorber design is proposed to address these limitations (Figure 6.12b). In this configuration, rising gas and downward flowing liquid contact in a counter-flow fashion in multiple parallel absorber tubes. This enables greater interface area – potentially up to the entire internal tube areas if film wetting is uniform. The multiple parallel short flow paths lead to reduced gas-phase pressure drop. Additionally, the number of absorber tubes can be increased for larger capacity implementations. Solution and gas maldistribution can limit performance of a multi-tube absorber, and is analyzed later in this section. Individual tubes are longitudinally finned in the same fashion as the solution subcooler, improving external heat transfer.

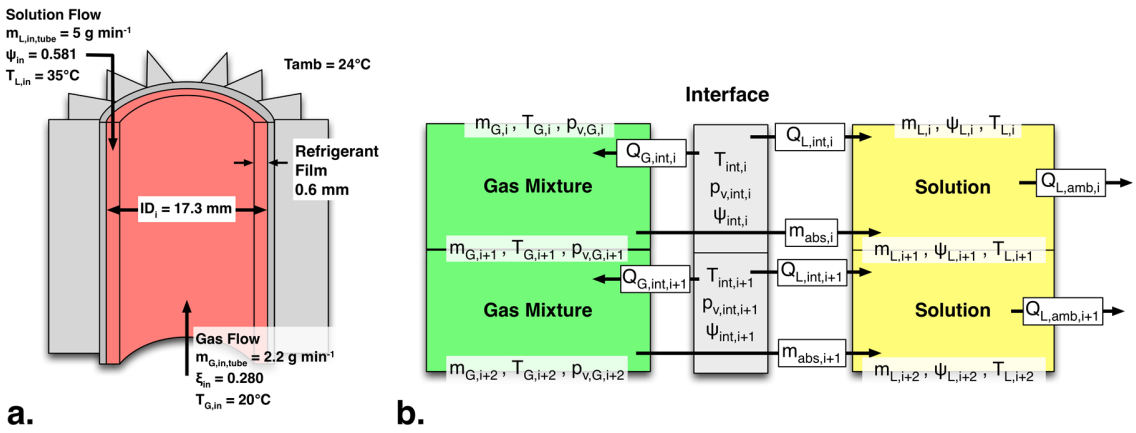

Figure 6.13 – Absorber model schematic and inlet conditions

A representative design is considered here with ten parallel vertical absorber tubes (ID = 17.3 mm, OD = 19.1 mm, L = 0.35 m). Each tube is wrapped with 12 H_{fin} = 25 mm tall, δ_{fin} = 0.35 mm thick, smooth corrugated aluminum fins (total external heat transfer area: 2.33 m^2). To improve internal film wetting, a helical wire insert would be installed in the tubes. This would enforce a film thickness similar to the wire diameter (δ_f = 0.6 mm assumed here). Results are reported for a representative case with p_{sys} = 1.15 MPa, T_{amb} = 25°C, solution inlet conditions of: $m_{L,in}$ = 50 g min^{-1}, $\psi_{L,in}$ = 0.581, $T_{L,in}$ = 35°C, and gas inlet conditions of: $m_{G,in}$ = 22 g min^{-1}, $\xi_{G,in}$ = 0.28, $T_{G,in}$ = 20°C. The model is formulated in a segmented fashion (N_{seg} = 25, equal length segments), with liquid- and gas-phase state points specified at the ends of each segment (i = 1 to N_{segs}+1) and interface conditions specified at the center of each segment (i = 1 to N_{segs}) (Figure 6.13).

Mass balances are applied over each segment of the liquid and gas subdomains.

$$m_{L,i+1} - m_{L,i} = m_{abs,i} \tag{6.30}$$

$$m_{G,i+1} - m_{G,i} = m_{abs,i} \tag{6.31}$$

For the representative case, the per-tube liquid flow rate increases from 5.00 – 5.19 g min^{-1} along the length of the absorber. This corresponds to a per-tube gas phase flow reduction from 2.20 – 2.01 g min^{-1}.

Species balances are also applied for the solution NaSCN and gas-phase helium contents.

$$m_{L,i}\psi_i = m_{L,i+1}\psi_{i+1} \tag{6.32}$$

$$m_{G,i}\xi_i = m_{G,i+1}\xi_{i+1} \tag{6.33}$$

The resulting solution concentration decreases from the CS value (ψ_{in} = 0.581) to the DS value (ψ_{out} = 0.559). The gas stream helium mass concentration increases from 0.280 – 0.307. This corresponds to an ammonia vapor pressure reduction from 433 – 398 kPa. Profiles of solution concentration and gas vapor pressure at bulk and interface values are presented for this representative case in Figure 6.14.

Sensible heat transfer from the liquid and gas streams to the interface is predicted assuming annular falling film flow. The gas-phase flow is laminar (Re_G ~ 190), resulting in a gas-to-interface convection coefficient of 19 W m^{-2} K^{-1}. Heat transfer from the liquid bulk to the interface is modeled as conduction through the liquid film ($h_{L,int}$ = 6870 W m^{-2} K^{-1}). This value is also assumed for convection from the liquid bulk to the inner tube wall. As in the evaporator analysis, a wetting factor (*WF*) correction is implemented to permit modeling of incomplete film coverage of the tube inner surfaces. For the representative case, *WF* = 1 is assumed.

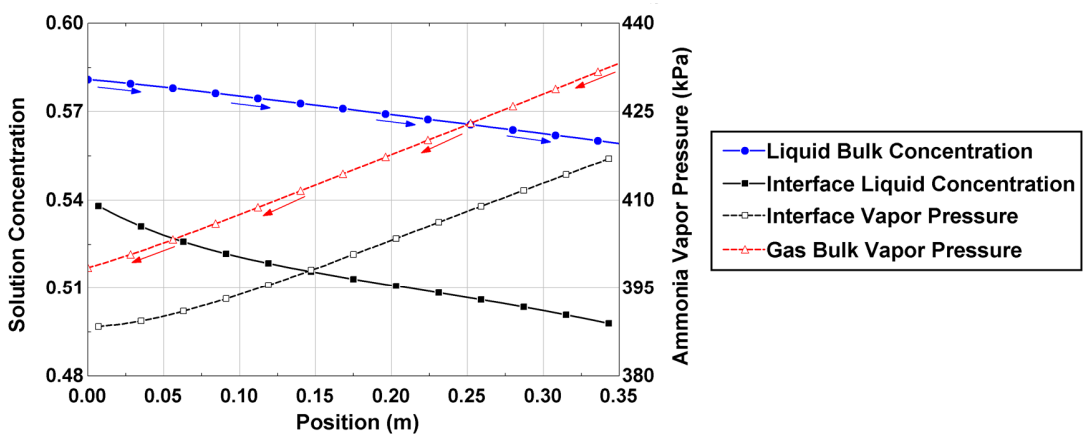

Figure 6.14 – Profiles of liquid-phase NaSCN concentration and gas-phase NH_3 vapor pressure

Conduction resistance through the tube wall is minimal; $R'_{wall} = 1.0 \times 10^{-3}$ m K W^{-1} for each tube.

Natural convection and radiation transport from the fins is evaluated at an average fin surface temperature ($T_{f,avg}$ = 31.8°C). The corrugated longitudinal fin configuration does not resemble canonical, well-characterized, heat transfer configurations; therefore, $h_{ext,out}$ is estimated by weighting the bounding vertical cylinder natural convection coefficient by the total external surface area ($A_{ext,out}$):

$$h_{ext,conv} = h_{cylinder}\left(D = OD + 2H_{fin}\right)\frac{\pi\left(OD + 2H_{fin}\right)L}{A_{ext}} = 1.0 \text{ W m}^{-2}\text{ K}^{-1} \qquad (6.34)$$

If the convection were modeled assuming free convection channel flow at the average fin-channel gap of 6.7 mm, the resulting convection coefficient would be h_{ext} = 0.6 W m^{-2} K^{-1}. External radiation fin heat transfer is modeled as in the condenser analysis, assuming that the tall fins can be approximated as a black surface at the bounding cylinder:

$$h_{\text{ext,rad}} = \sigma \frac{T_{\text{f,avg,2}}^4 - T_{\text{amb}}^4}{T_{\text{f,avg,2}} - T_{\text{amb}}} \frac{\pi\left(\text{OD} + 2H_{\text{fin}}\right)L}{A_{\text{ext}}} = 2.1 \text{ W m}^{-2} \text{ K}^{-1} \tag{6.35}$$

The net external transport coefficient (weighted by the exterior area) is thus 3.1 W m^{-2} K^{-1}, resulting in an exterior surface efficiency of 0.98. The resulting conduction resistance from the liquid bulk to the ambient is $R'_{\text{L,amb}}$ = 0.51 m K W^{-1}. Segmental energy balances for the liquid, interface, and gas are defined as follows.

$$m_{\text{L,i}} i_{\text{L,i}} - m_{\text{L,i+1}} i_{\text{L,i+1}} + m_{\text{abs,i}} h_{\text{NH}_3\text{,L}}\left(T_{\text{int,i}}\right) = WF\left[\frac{T_{\text{L,i+1}} - T_{\text{int,i}}}{R'_{\text{L,int}}/\Delta z_{\text{seg}}} - \frac{\left(T_{\text{L,i}} + T_{\text{L,i+1}}\right)/2 - T_{\text{amb}}}{R'_{\text{L,amb}}/\Delta z_{\text{seg}}}\right] \tag{6.36}$$

$$m_{\text{abs,i}} h_{\text{NH}_3\text{,LV}}\left(T_{\text{int,i}}\right) = WF\left[\frac{T_{\text{int,i}} - T_{\text{L,i+1}}}{R'_{\text{L,int}}/\Delta z_{\text{seg}}} - \frac{T_{\text{int,i}} - \left(T_{\text{G,i}} + T_{\text{G,i+1}}\right)/2}{R'_{\text{G,int}}/\Delta z_{\text{seg}}}\right] \tag{6.37}$$

$$m_{\text{G,i+1}} i_{\text{G,i+1}} - m_{\text{G,i}} i_{\text{G,i}} - m_{\text{abs,i}} h_{\text{NH}_3\text{,V}}\left(T_{\text{int,i}}\right) = WF\frac{\left(T_{\text{G,i}} + T_{\text{G,i+1}}\right)/2 - T_{\text{int,i}}}{R'_{\text{G,int}}/\Delta z_{\text{seg}}} \tag{6.38}$$

This analysis assumes that vapor ammonia (Quality = 1) flows from the gas stream to the interface, and into the solution stream as liquid ammonia (Quality = 0). Sensible heat transfer from the gas-to-interface and liquid-to-ambient are evaluated at average segment temperatures. Downwinding is employed to improve stability for liquid-to-interface heat transfer calculations. The resulting temperature profiles for the liquid, interface, and gas are presented in Figure 6.15. The liquid bulk temperature effectively matches that of the interface along the absorber length. The liquid-to-ambient driving temperature difference for heat rejection varies from 3.8 – 11 K along the length of the component. The gas temperature approaches that of the interface near the top of the absorber (min ($T_{\text{int}} - T_{\text{G}}$) =

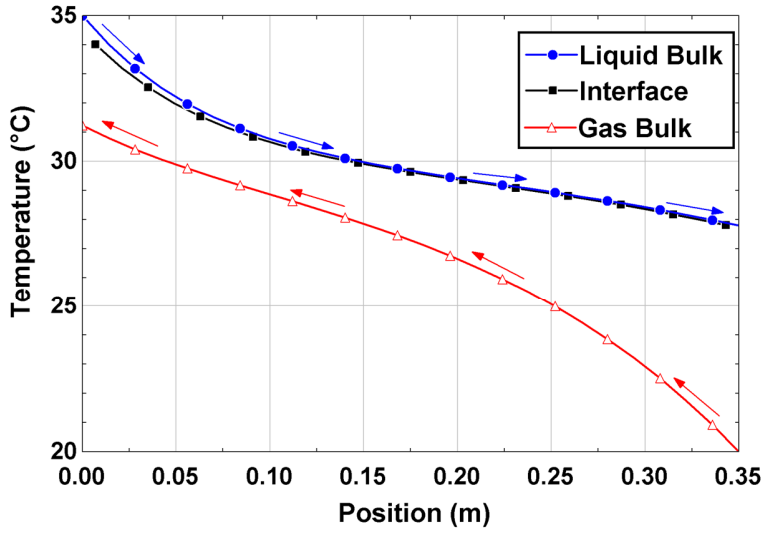

Figure 6.15 – Temperature profiles of solution, interface, and gas in the absorber

1.7 K). Liquid and gas streams exit the component slightly above the ambient temperature (24°C) at 27.8°C and 31.2°C, respectively.

Finally, a mass transfer analysis is performed for overall model closure. Mass transfer calculations are evaluated in two parts for the gas-to-interface and interface-to-liquid transport. Gas-to-interface mass transfer is evaluated assuming laminar convection ($Sh_{int,G}$ = 4.3, $R^{*\prime}_{G,int}$ = 1.5 × 10^{9} s^{-1}, units of mass flux/vapor pressure difference). Interface-to-liquid mass transfer is evaluated assuming diffusion through half the film thickness ($R^{*\prime}_{int,L}$ = 3.54 × 10^{5} kmol s kg^{-1} m^{-3}, units of mass flux/molar density difference). The segmental absorption mass transfer rates are evaluated through implicit solution of the following equations:

$$p_{v,int,i} = p_{v,NH_3\text{-}NaSCN}\left(T_{int,i}, \psi_{int,i}\right) \tag{6.39}$$

$$m_{\text{abs,i}} = \frac{\left(p_{\text{v,G,i}} + p_{\text{v,G,i+1}}\right)/2 - p_{\text{v,int,i}}}{R^{*'}_{\text{int,G}}/\Delta z_{\text{seg}}} \tag{6.40}$$

$$m_{\text{abs,i}} = \frac{\rho^{*}_{\text{NH3,int,i+1}} - \left(\rho^{*}_{\text{NH3,L,i}} + \rho^{*}_{\text{NH3,L,i+1}}\right)/2}{R^{*'}_{\text{int,L}}/\Delta z_{\text{seg}}} \tag{6.41}$$

The resulting gas, interface, and solution vapor pressure/concentration profiles are presented in Figure 6.14. Overall, nearly constant driving potentials for mass transfer persist along the length of the component. The absorber closest approach vapor pressure (CAVP = $p_{\text{v,G,out}} - p_{\text{v,NH3NaSCN}}(T_{\text{L,in}}, \psi_{\text{L,in}})$) is 111 kPa. In an ideal absorber, this value would approach 0 kPa. This CAVP can also be interpreted as a solution subcooling requirement for the absorber. With perfect liquid-to-vapor mass transport (CAVP = 0 kPa), the same absorber mass transfer performance could be realized with 14.5 K higher solution/ambient temperatures (i.e., $p_{\text{v,NH3NaSCN}}(T_{\text{L,in}}, \psi_{\text{L,in}}) = p_{\text{v,NH3NaSCN}}(T_{\text{L,in}} - 14.5\text{ K}, \psi_{\text{L,in}}) + 111$ kPa). Thus, the proposed absorber can be considered species-transport-limited. Gas-phase mass transfer resistance is relatively insignificant; if the gas-phase diffusivity is doubled, the total absorption rate only increases from 1.94 – 2.00 g min^{-1} (+3%). Liquid phase resistance is much more significant. Doubling the liquid-phase diffusivity increases the absorption rate from 1.94 – 2.83 g min^{-1} (+46%). The absorber performance can be characterized with an overall mass transfer conductance: $UA^{*}_{\text{abs}} = m_{\text{abs}} / \text{LMPD}_{\text{abs}}$. Here, LMPD is the log-mean vapor pressure difference between the solution and gas streams in the component. For the baseline operating conditions, $\text{LMPD}_{\text{abs}} = 135$ kPa, resulting in a conductance of $UA^{*}_{\text{abs}} = 2.4 \times 10^{-10}$ kg Pa^{-1} s^{-1}.

The absorber model predicts a per-tube refrigerant absorption rate of 0.19 g min^{-1} (1.9 g min^{-1} total). This corresponds to a full absorber heat-rejection rate of 42 W. At this

absorption rate, a maximum steady-state evaporator cooling capacity of $h_{LV,NH3} \times m_{abs}$ = 41 W can be achieved (not accounting for parasitic cooling). Absorber and evaporator performance are tightly coupled, and it is difficult to independently identify which is the more significant limitation on cycle performance. In Section 6.3, a parametric study is performed to quantify the effects of evaporator and absorber performance on overall cycle operation.

A sensitivity analysis was conducted to identify key factors affecting the performance of the proposed absorber design. Reducing the wetting factor (*WF* – effective fraction of tube area wetted by the liquid film) from 1.0 to 0.2 leads to a nearly linear reduction in absorption capacity from 1.9 to 0.5 g min^{-1}. Thus, implementation of wetting enhancement techniques, such as the proposed helical coil inserts, may be critical to achieving adequate component performance.

Varying the per-tube solution inlet flow rate has minimal effects for $m_{L,in,tube}$ = 2.5 – 5.0 g min^{-1}, resulting in absorption rates of $m_{abs,tube}$ = 0.184 – 0.194 g min^{-1}. However, reduction to $m_{L,in,tube}$ = 0.5 g min^{-1} significantly limits absorption ($m_{abs,tube}$ = 0.106 g min^{-1}). This analysis indicates that uneven liquid inlet distribution may result in effectively inactive tubes. One challenge with the proposed absorber design is thus to design a distributor header or drip-tray that delivers similar liquid flow rates to all tubes.

Absorption rates are predicted to vary approximately linearly with solution inlet concentration, increasing from 0.61 – 2.24 g min^{-1} for $\psi_{L,in}$ = 0.51 – 0.60. Thus, slightly improved absorber performance could be achieved by increasing the NaSCN charge in experimental systems. However, it is important to ensure that the crystallization

concentration is not exceeded ($\psi_{crsyt}(25°C)$ = 0.645). Additionally, increased solution concentrations may necessitate higher source temperatures for BPG operation.

A number of investigations have demonstrated the deleterious effects of non-absorbable gas ingress or production on absorber performance in two-pressure absorption systems (Grossman and Gommed, 1997; Yang and Wood, 1993). In the DAR cycle, a significant charge of non-absorbable auxiliary gas (helium here) is required for operation of the evaporator. Thus, an acceptable working-fluid balance must be identified to meet the competing needs of these two components. For example, increasing the absorber gas-phase inlet helium concentration from the baseline assumed value of $\xi_{abs,in}$ = 0.28 to 0.42 (+50%) reduces the total ammonia absorption rate from 1.9 to 0.6 g min^{-1}. However, increasing the evaporator inlet helium concentration was shown to increase cooling capacity (Section 6.2.5). Changing operating conditions in the absorber and evaporator may also cause second-order effects, such as variations in the passive gas circulation rate. These results again highlight the highly coupled nature of DAR systems. Practical factors and effects on all other components must be considered when adjusting design or operating conditions.

6.2.6 Gas loop passive circulation

The auxiliary gas stream circulates through the gas loop, which is comprised of the evaporator, gas heat exchanger (GHX), and absorber. Flow is driven by hydrostatic pressure differences between the cold sinking leg and warm rising leg. In this analysis, the gas circulation rate is predicted by applying simplified momentum balances over all the components in the gas loop. The considered component geometries and operating conditions are the same as those analyzed in the preceding sections. The GHX is modeled

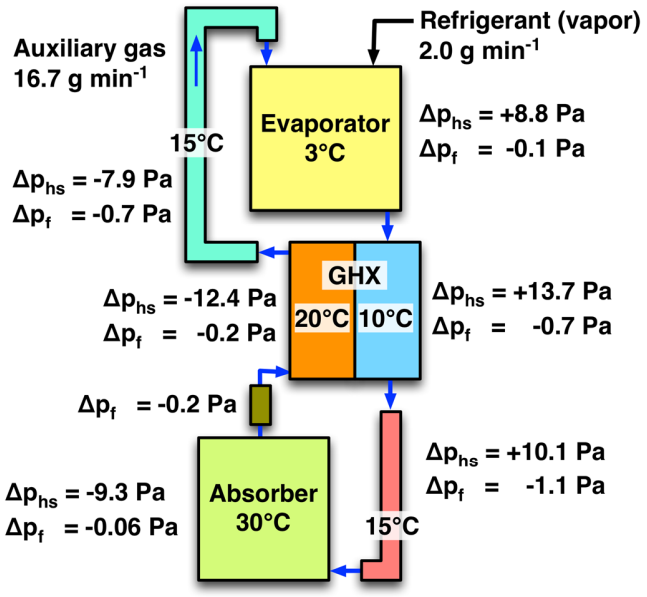

Figure 16 – Schematic of gas loop passive circulation analysis

as a vertical shell-and-tube heat exchanger. No baffles are employed on the shell side to reduce pressure drop in the passive circulation loop. The cool gas stream flows downwards through seven parallel circular tubes (ID_i = 10.9 mm, OD_i = 12.7 mm, H = 0.45 m). The warm auxiliary gas stream rises (counter-flow) through the shell side of the GHX (ID_o = 52.5 mm). A summary of the gas loop passive circulation analysis is presented in Figure 6.16.

The analysis begins in the evaporator, wherein cold refrigerant-gas mixture (m = 18.7 g min^{-1}, ξ = 0.268, T = 3°C) flows downwards. This results in a hydrostatic pressure gain of 8.8 Pa and a frictional pressure loss of 0.1 Pa. The gas stream continues through the tube side of the GHX at an average temperature of 10°C. A hydrostatic pressure gain of 13.7 Pa is predicted. The pressure decreases due to frictional resistance in the tubes (0.5

Pa), and sudden expansions and contractions in the component inlet and outlet headers (0.2 Pa). A section of tube connects the GHX cold stream outlet to the absorber inlet (ID = 17.3 mm, L = 0.61 m, T = 15°C). The hydrostatic gain in this component is 10.1 Pa. Pressure losses are experienced due to channel-flow resistance (1.0 Pa) and a 90° bend (0.05 Pa).

The gas stream is assumed to rise through the absorber at 30°C and intermediate flow rate (17.7 g min^{-1}) and concentration (ξ = 0.284). Hydrostatic pressure change results in a loss of 9.3 Pa in the component. Frictional flow in the absorber tubes (0.05 Pa) and header expansion and contraction losses (0.01 Pa) further reduce the pressure. The auxiliary gas stream (16.7 g min^{-1}, ξ = 0.30, T = 30°C) continues through a connecting tube from the absorber to the GHX shell-side inlet, resulting in a pressure drop of 0.2 Pa. Flow through the gas cooler shell side is assumed to be at an intermediate temperature (20°C). Predicted hydrostatic and frictional flow resistances are 12.4 and 0.2 Pa, respectively. Finally, the auxiliary gas stream flows through a vertical tube (ID = 17.3 mm, L = 0.38 m) to return to the evaporator inlet. The model accounts for pressure drops in this tube due to hydrostatic forces (7.9 Pa), frictional resistance (0.6 Pa), and minor losses in the U-bend connection to the evaporator inlet (0.1 Pa).

Overall, the proposed model predicts a net hydrostatic pressure difference of 3.0 Pa between the sinking cold leg and rising warm leg of the gas loop. This results in an auxiliary gas flow of 16.7 g min^{-1}, which causes the balancing frictional flow resistance. Based on this analysis, gas density changes due to temperature as well as helium concentration (ξ_G) both contribute significantly to motive forces in the gas loop. At the considered operating conditions, the average ~10 K difference between the cold and

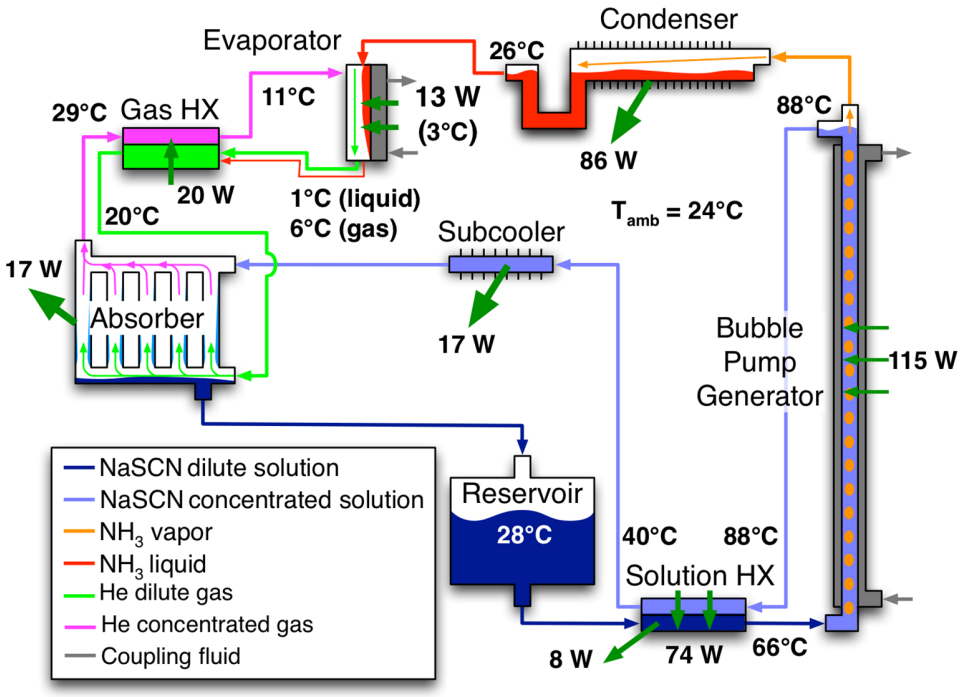

Figure 6.17 – Schematic of full DAR cycle model. All reported heat transfer rates are overall component values.

warm legs of the gas loop results in a 4% change in fluid density. Similarly, the helium concentration swing (0.268 – 0.300) yields a further 6% change in fluid density. This gas loop model yields an "order of magnitude" estimate of gas flow rates. While a more detailed analysis could be performed, it is difficult to precisely predict minor losses from tube bends, fittings, heat exchanger headers, etc., *a priori* for an actual DAR system.

6.3 Full System Analysis

A complete cycle level model is formulated to analyze the DAR system for low-source-temperature operation. Results from the individual component level analyses (Section 6.2) are incorporated for closure. Mass, species, and energy balances are applied to each component to obtain the state points indicated in Figure 6.17. UA-LMTD models

are formulated for the single-phase heat exchanger components (solution heat exchanger (SHX), solution subcooler, gas heat exchanger (GHX)) as follows.

The SHX is assumed to be a tube-in-tube counter-flow heat exchanger, with the warm stream (H) flowing in the inner channel and the cool stream (C) flowing through the outer channel. The heat transfer rate from the warm stream to the cool stream is:

$$Q_{\mathrm{SHX}} = \mathrm{UA}_{\mathrm{SHX}} \frac{\left(T_{\mathrm{SHX,H,in}} - T_{\mathrm{SHX,C,out}}\right) - \left(T_{\mathrm{SHX,H,out}} - T_{\mathrm{SHX,C,in}}\right)}{\ln\left(\dfrac{T_{\mathrm{SHX,H,in}} - T_{\mathrm{SHX,C,out}}}{T_{\mathrm{SHX,H,out}} - T_{\mathrm{SHX,C,in}}}\right)} \tag{6.42}$$

Additionally, the outer channel flow loses heat to the ambient as:

$$Q_{\mathrm{SHX,Loss}} = \mathrm{UA}_{\mathrm{SHX,Loss}} \frac{\left(T_{\mathrm{SHX,C,in}} - T_{\mathrm{amb}}\right) - \left(T_{\mathrm{SHX,C,out}} - T_{\mathrm{amb}}\right)}{\ln\left(\dfrac{T_{\mathrm{SHX,C,in}} - T_{\mathrm{amb}}}{T_{\mathrm{SHX,C,out}} - T_{\mathrm{amb}}}\right)} \tag{6.43}$$

The solution subcooler precools the warm solution stream flowing from the SHX outlet to the absorber inlet by rejecting heat to the ambient. It is modeled as:

$$Q_{\mathrm{sub}} = \mathrm{UA}_{\mathrm{sub}} \frac{\left(T_{\mathrm{sub,in}} - T_{\mathrm{amb}}\right) - \left(T_{\mathrm{sub,out}} - T_{\mathrm{amb}}\right)}{\ln\left(\dfrac{T_{\mathrm{sub,in}} - T_{\mathrm{amb}}}{T_{\mathrm{sub,out}} - T_{\mathrm{amb}}}\right)} \tag{6.44}$$

The gas heat exchanger (GHX) is modeled as a counter-flow heat exchanger. The evaporator working-fluid outlet stream (C) may have the two phases exiting in inequilibrium with each other (see Section 6.2.4). However, for simplicity, heat transfer is modeled assuming no phase change, that the driving temperature differences are

between the two gas streams (C and H), and that the cool stream (C) exits in thermal equilibrium ($T_{L,C,out} = T_{G,C,out}$).

$$Q_{GHX} = UA_{GHX} \frac{\left(T_{GHX,H,in} - T_{GHX,C,out}\right) - \left(T_{GHX,H,out} - T_{GHX,C,in}\right)}{\ln\left(\frac{T_{GHX,H,in} - T_{GHX,C,out}}{T_{GHX,H,out} - T_{GHX,C,in}}\right)} \tag{6.45}$$

Additionally, the following closure models and parameters are applied:

- The condenser closest approach temperature is: $CAT_{cond} = T_{cond,out} - T_{amb} = 2$ K
- The evaporator-to-CF stream (T_{cool}) closest approach temperature is: $CAT_{evap} = T_{cool} - T_{evap,out} = 2$ K
- Unevaporated refrigerant liquid from the evaporator flows through the GHX without additional evaporation. The stream mixes adiabatically with the absorber solution outlet stream
- The evaporator mass transfer conductance is: $UA^*_{evap} = 0.8 \times 10^{-10}$ kg Pa^{-1} s^{-1}
- The gas flow exiting the evaporator is warmer than the outlet liquid refrigerant stream by a $CAT_{evap,G,L} = 5$ K. This mixture is assumed to reach thermal equilibrium at the SHX outlet.
- The gas heat exchanger (GHX) overall conductance is: $UA_{GHX} = 2.0$ W K^{-1}
- The solution heat exchanger (SHX) overall conductance is: $UA_{SHX} = 5.0$ W K^{-1}
- The SHX heat loss conductance is: $UA_{SHX,amb} = 0.5$ W K^{-1}
- The solution subcooler overall conductance is: $UA_{sub} = 1.6$ W K^{-1}
- Absorber gas and liquid outlet closest approach temperatures are: $CAT_{abs} = T_{abs,G,out} - T_{amb} = T_{abs,L,out} - T_{amb} = 5$ K

- The absorber mass transfer conductance is: $UA^*_{abs} = 1.6 \times 10^{-10}$ kg Pa^{-1} s^{-1}

Sample calculations of this cycle model are presented in Appendix Section A.3.

Representative cycle-level model results are presented in Figure 6.17 for operating conditions of: $\psi_{DS} = 0.538$, $p_{sys} = 1.15$ MPa, $Q_{BPG} = 115$ W, $T_{cool} = 3$°C, and $T_{amb} = 24$°C. For these conditions, the refrigerant generation rate is 3.9 g min^{-1}. Concentrated solution and auxiliary gas flow rates are assumed to be 39.0 g min^{-1} ($10 \times m_{ref}$) and 19.5 g min^{-1} ($5 \times m_{ref}$), respectively. These values are representative of results from the first-principles based BPG and gas loop models formulated in Section 6.2.

At these conditions, the evaporator delivers 13.1 W of cooling to the coupling fluid at $T_{cool} = 3$°C (COP = Q_{evap} / $Q_{BPG} = 0.114$), which is sufficient for preservation of many temperature sensitive pharmaceuticals and foodstuffs (~5°C required). The concentrated solution (CS) concentration is $\psi_{CS} = 0.592$, which is well below the crystallization point at the ambient temperature ($\psi_{cryst}(24°C) = 0.646$). Thus, the system operates within working-fluid constraints. The BPG outlet temperature is predicted to be 88.2°C, which is comparable to results predicted in Section 6.2.2 for BPG coupling fluid inlet temperatures of 110 – 130°C. Thus, the proposed DAR system can deliver cooling suitable for refrigeration with low thermal input temperatures, meeting the proposed design objectives.

A sensitivity study was conducted to assess the performance of the investigated DAR system at varying operating conditions. For this analysis, baseline conditions and closure models (summarized above) are employed except where specified otherwise. The predicted system COP increases with cold delivery temperature, reaching 0.282 at

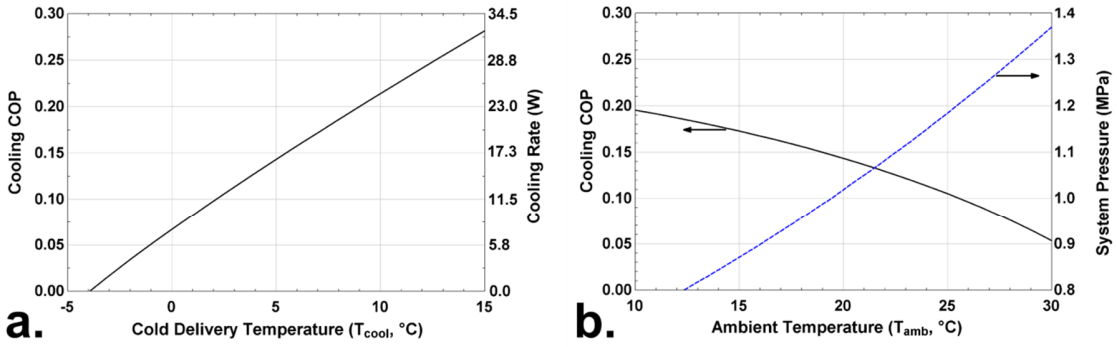

Figure 6.18 – Predicted DAR system performance at varying **a**. cooling delivery temperature (T_{cool}) and **b**. ambient temperature (T_{amb})

representative A/C conditions (T_{cool} = 15°C) (Figure 6.18a). The cooling delivery temperature can also be reduced slightly below the (water) freezing point, with a COP of 0.034 at T_{cool} = -2°C. System performance decreases with increasing ambient temperature (Figure 6.18b). For these cases, the system pressure is varied such that $T_{sat,NH3}(p_{sys}) - T_{amb}$ = 5.5 K (to ensure proper condenser operation). A COP of 0.054 can be maintained at T_{amb} = 30°C. However, the BPG source temperature may also have to be increased ($T_{BPG,out}$ = 95.8°C) to ensure proper operation at these conditions.

In the preceding component-level analyses, transport rates in the evaporator and absorber components were highlighted as potential performance limitations. The two component mass transfer conductances (UA^*_{evap}, UA^*_{abs}) were thus varied to determine effects on overall system performance (Figure 6.19). Cooling capacity is predicted to sharply decrease with UA^*_{evap}. COP decreases to < 0.05 for UA^*_{evap} values below ~0.5×10^{-10} kg Pa^{-1} s^{-1}. Component performance tends to vary more smoothly with UA^*_{abs} values, indicating that evaporator performance may be a more severe limitation near baseline system conditions. If UA^*_{evap} and UA^*_{abs} can be increased to 1.6 and 2.4×10^{-10}

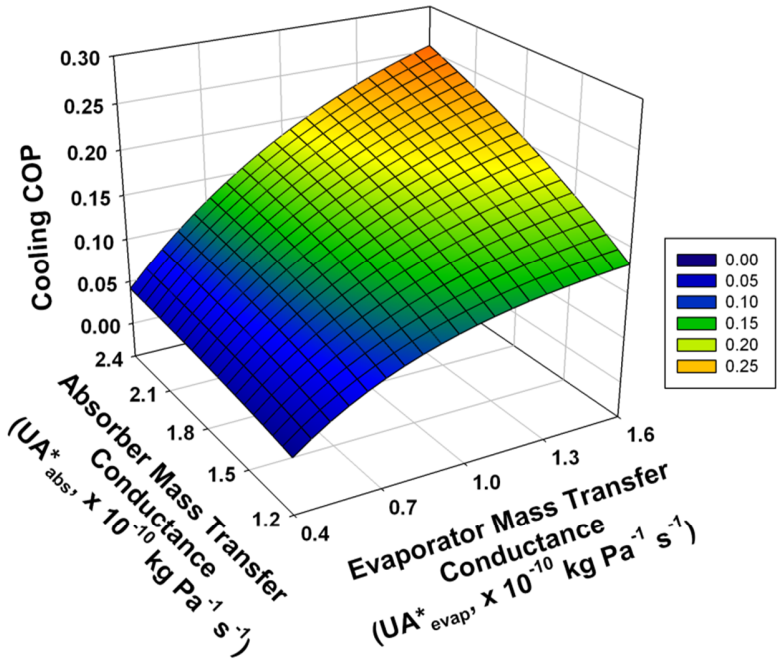

Figure 6.19 – Effects of absorber and evaporator mass transfer conductances on overall DAR system performance

kg Pa^{-1} s^{-1}, respectively, then the predicted system COP reaches 0.256. Thus, future system design investigations should focus on mass transfer enhancement of the evaporator and absorber.

The effects of relative auxiliary gas (m_{aux}/m_{ref}) and solution flow rates (m_{CS}/m_{ref}) are summarized in (Figure 6.20). An optimal auxiliary gas-to-refrigerant refrigerant flow rate ratio of 1.85 is identified for the baseline conditions (COP = 0.162). At higher m_{aux}, the parasitic gas cooling load in the evaporator limits overall performance. At lower flow rates, the gas stream becomes saturated with vapor refrigerant, limiting evaporation. DAR system performance is predicted to decrease with greater relative solution flow rates (m_{CS}/m_{ref}). This occurs because a larger portion of input heat (Q_{BPG}) is used for sensible

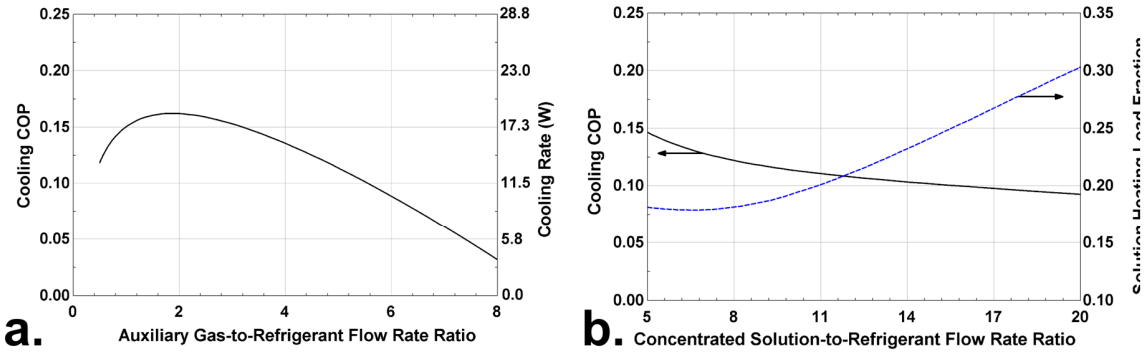

Figure 6.20 – Predicted DAR system performance at varying relative (**a**) auxiliary gas and (**b**) solution flow rates

solution heating, and the driving vapor pressure difference is reduced in the absorber. For the representative operating conditions, solution flow rates cannot be reduced below ~5 × m_{ref} due to NaSCN crystallization concerns. Additionally, absorber solution distribution and film wetting may be poor at low flow rates, limiting practical component performance.

6.4 Conclusions

In this investigation, detailed component models were formulated for all cycle components in a low-source-temperature ($T_{source} \leq 130°C$), passively cooled DAR refrigeration ($T_{cool} \sim 5°C$) system with NH_3-NaSCN-He working fluids. This study presented the first detailed design models for the DAR coupling-fluid heat bubble-pump generator (with actual working fluids), condenser, evaporator, and passive circulation gas loop. A new, enhanced absorber design that addresses major limitations of conventional implementations was analyzed. Simplified descriptions of the component sub-models were integrated into a complete system-level model, which was applied to analyze performance over varying operating conditions.

The investigated DAR system was predicted to achieve a COP of 0.11 at baseline conditions, assuming complete film wetting in the evaporator and absorber. Parametric studies suggested that much higher COPs could be achieved at elevated cooling temperatures (~0.28 for A/C applications). Bubble-pump generator model results indicated that stable operation could be achieved with thermal input at 110 – 130°C, which could be delivered from low-grade sources such as solar collectors or engine exhaust. Low-velocity ambient air circulation (~0.1 m s^{-1}) was predicted to be necessary for proper condenser operation at design conditions. Significant system modifications or higher source temperatures may be required if no such flow is present.

An improved COP of 0.26 was predicted if evaporator and absorber mass transport conductances were significantly increased. These two parameters (UA^*_{evap} and UA^*_{abs}) were found to be the key factors limiting system performance. However, enhanced inter-phase transport may be difficult to achieve with the limited pressure drop budgets available in passive DAR systems. Incomplete film wetting or liquid distribution can dramatically decrease absorber and evaporator capacities. In practice, these may be more severe concerns at reduced solution and refrigerant flow rates. Thus, future investigations should focus on enhancement of these two components.

This investigation highlighted the strongly coupled nature of DAR cycle components. For example, reduced BPG solution pumping rates could enable increased refrigerant generation (reduced parasitic solution heating load). However, this could lead to poor liquid distribution and film wetting in the absorber, limiting cooling capacity. Similarly, the passive gas loop circulation analysis (Section 6.2.6) demonstrated how the behavior of the evaporator, gas heat exchanger, absorber, and plumbing connections affect gas

circulation rates. Modifications to any individual component can thus dramatically affect overall system performance. By providing a set of detailed component level models, this investigation enables integrated system design, which accounts for such effects. Validation of this model was not discussed in this paper. In Chapter 7, these models are assessed and validated with results from an experimental investigation of a DAR system.

CHAPTER 7. LOW-SOURCE-TEMPERATURE DIFFUSION ABSORPTION REFRIGERATION: EXPERIMENTS AND MODEL ASSESSMENT

7.1 Introduction

In Chapter 6, fully passive low-source-temperature ($T_{source} \leq 130°C$) diffusion absorption refrigeration (DAR) at $T_{cool} \lesssim 5°C$ was identified to have considerable potential for a wide range of applications, such as solar-thermal-energy driven vaccine preservation in developing countries and off-grid refrigeration using engine waste heat. Some experimental low-source-temperature DAR systems have been demonstrated (Ben Ezzine *et al.*, 2010b; Jakob *et al.*, 2008; Wang, 2012). However, most have required forced liquid flow for absorber and condenser cooling, employed mechanically pumped internal fluid circulation, or operated at elevated evaporator temperatures that are not suitable for refrigeration. Additionally, few component-level design resources are available for DAR components, except for the bubble-pump generator (BPG). Limited experimental validation or assessment has been performed for reported component models.

A detailed design for a fully passive low-source-temperature DAR refrigeration system was proposed in Chapter 6. The proposed system employs an alternate working-fluid mixture (NH_3-NaSCN-He, conventional systems employ NH_3-H_2O-H_2/He), a distributed coupling-fluid (CF) heated BPG, and an enhanced absorber. These three modifications enable operation at reduced source temperatures. Additionally, detailed models were formulated for the bubble-pump generator (BPG), condenser, evaporator, absorber, passive circulation gas loop, and overall system.

The objective of the present investigation is to apply the models from Chapter 6 to develop a complete demonstration-scale DAR system that satisfies the target operating conditions and constraints. The experimental system is evaluated over a range of source temperatures, input heating rates, cooling delivery temperatures, ambient temperatures, ambient air-flow velocities, and system pressures. Results from this investigation are employed to assess the component- and system-level models described in Part I. Additionally, insights gained from this experimental study are applied to identify model refinement approaches, fundamental research needs, and pathways to enhance low-source-temperature DAR technology.

7.2 Experimental Facility and Procedure

7.2.1 Overview

The complete experimental DAR system developed and fabricated in this study is presented in Figure 7.1. Heat input to the BPG is supplied from a mineral oil coupling-fluid (CF) loop, which simulates a low grade thermal source, such as a passive solar thermosyphon. Cooling is delivered from the evaporator to a water CF loop. This configuration is different than would be employed in a conventional refrigeration system in which an insulated compartment is cooled. The CF loop is employed here to enable precise measurement of cooling capacity. The entire facility is stationed inside a ventilation hood with a variable-speed fan drive. This was employed to contain potential working fluid leaks and permit control of ambient air-flow velocity and temperature (with portable space heaters).

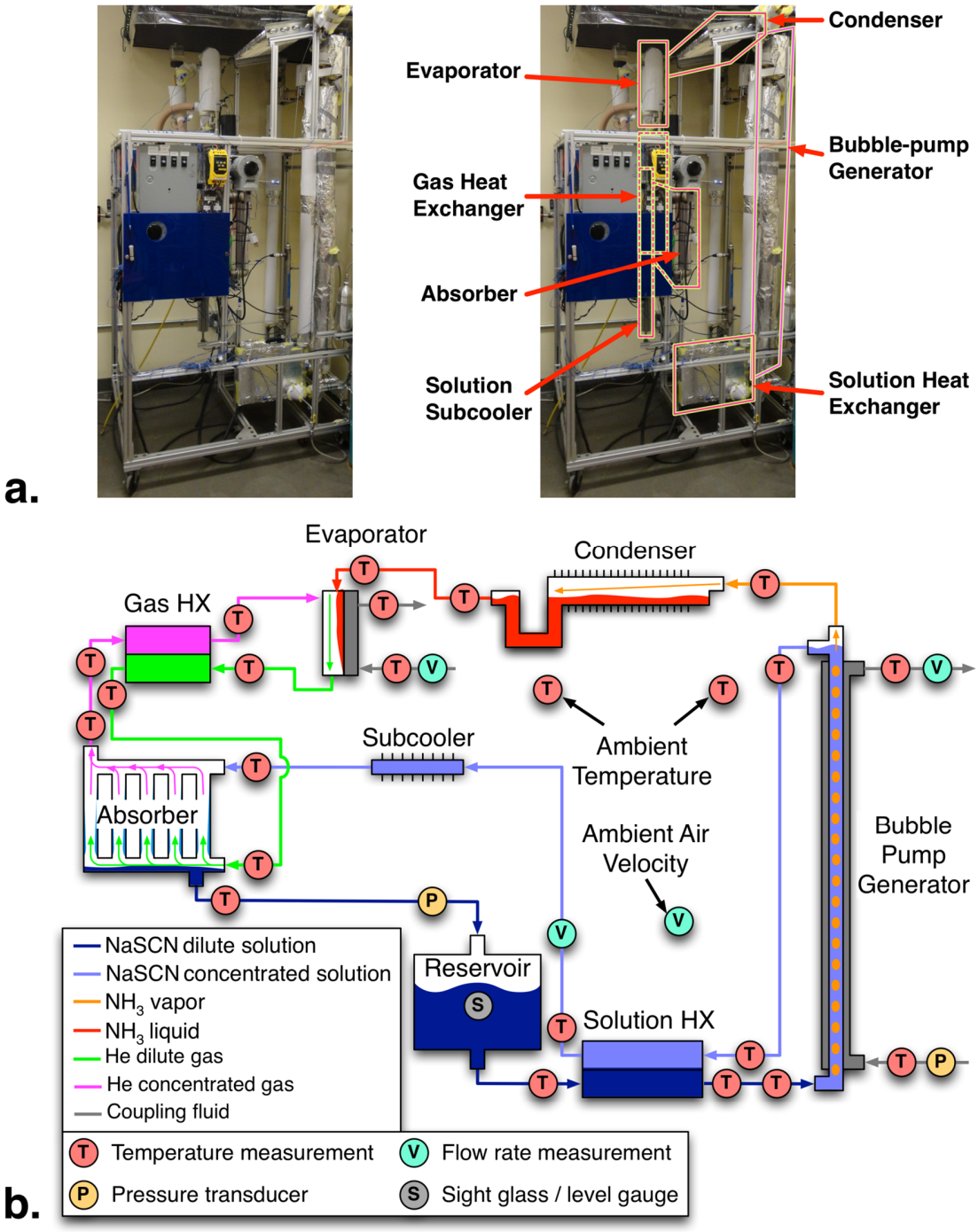

Figure 7.1 – **a**. Complete fully passive low-source-temperature diffusion absorption refrigeration system, **b**. Flow diagram of experimental facility and instrumentation

Tests were conducted over a primary test matrix for varying BPG heat input rates (Q_{BPG} = 90 and 120 W, nominal), BPG CF inlet temperatures ($T_{BPG,CF,in}$ = 110, 120, 130°C, nominal), and evaporator CF inlet-to-outlet temperature glides ($T_{evap,CF}$ = 18 → 14°C, 12 → 8°C, 6 → 3°C). The middle evaporator temperature glide (12 → 8°C) corresponds approximately to air-conditioning or chiller operation. The lower temperature glide (6 → 3°C) is representative of maximum acceptable refrigeration temperatures. For this primary test matrix, the system pressure was p_{sys} ~ 1.15 MPa, dilute solution (DS) concentration was ψ_{DS} ~ 0.52, and ambient air temperature was ~25°C. The upward ambient air velocity varied over ~0.2 – 0.8 m s^{-1} in the ventilation hood (~0.5 m s^{-1} near the condenser and absorber), as measured with a handheld turbine anemometer. Tests were also conducted over smaller auxiliary test matrices to assess off-design system performance with varying ambient temperatures (T_{amb} = 25, 27, 29°C, nominal), ambient air-flow rates (U_{amb} = 0.2 – 0.8 m s^{-1}, 0.0 – 0.4 m s^{-1}, ~0 m s^{-1}), and system pressures (p_{sys} = 1.15, 1.27, 1.39 MPa). These off-design cases were evaluated with Q_{BPG} ~ 120 W, $T_{BPG,CF,in}$ ~ 120°C (130°C for elevated p_{sys} cases), and $T_{evap,CF}$ ~ 12 → 8°C. The test matrices are summarized in Table 7.1.

The ambient temperature range employed in this investigation (25 – 29°C) was selected to be representative of typical operating conditions (e.g., room temperature), and is lower than some residential refrigerator rating protocols (T_{amb} = 32°C (United States Department of Energy, 2012)). This ambient temperature range is also similar to those employed in other low-source-temperature experimental DAR studies (27 – 31°C (Jakob *et al.*, 2008), 20°C (Ben Ezzine *et al.*, 2010b), 10 – 28°C (Wang, 2012)), enabling comparison with related systems.

Table 7.1 – Summary of system experimental conditions

Primary Test Matrix		
p_{sys} = 1.15 MPa, ψ_{DS} = 0.52, T_{amb} = 25°C, U_{amb} = 0.2 – 0.8 m s^{-1}		
Evaporator Coupling Fluid Temperature ($T_{evap,CF}$)	**Bubble Pump Generator Input Heat (Q_{BPG})**	**Heat Source Temperature ($T_{BPG,CF,in}$)**
6 → 3°C	90 W, 120 W	110, 120, 130°C
12 → 8°C	90 W, 120 W	110, 120, 130°C
18 → 14°C	90 W, 120 W	110, 120, 130°C
Varying Ambient Temperature		
p_{sys} = 1.15 MPa, ψ_{DS} = 0.52, U_{amb} = 0.2 – 0.8 m s^{-1}, $T_{evap,CF}$ = 12 → 8°C, Q_{BPG} = 120 W, $T_{BPG,CF,in}$ = 120°C		
T_{amb} = 24, 27, 29°C		
Varying Ambient Air Vertical Velocity		
p_{sys} = 1.15 MPa, ψ_{DS} = 0.52, T_{amb} = 25°C, $T_{evap,CF}$ = 12 → 8°C, Q_{BPG} = 120 W, $T_{BPG,CF,in}$ = 120°C		
U_{amb} = 0.2 – 0.8, 0.0 – 0.4, 0 m s^{-1}		
Varying System Pressure		
ψ_{DS} = 0.52, T_{amb} = 25°C, U_{amb} = 0.2 – 0.8 m s^{-1}, $T_{evap,CF}$ = 12 → 8°C, Q_{BPG} = 120 W, $T_{BPG,CF,in}$ = 130°C		
p_{sys} = 1.15, 1.27, 1.39 MPa		

For each case, the DAR system was first operated at steady state conditions for about 15 – 30 minutes. Measurements were then collected every 30 seconds for 15 minutes and averaged to serve as inputs for the data reduction procedures. Descriptions of the individual system components, instrumentation, and data reduction procedures are provided in the following sections.

7.2.2 Bubble-pump generator

The bubble pump generator is a tube-in-tube co-flow heat exchanger (Figure 7.2). Working fluid (NH_3-NaSCN solution and NH_3 vapor) flows vertically upward in an inner stainless steel tube (ID_i = 4.9 mm, OD_i = 6.4 mm, L = 1.74 m). Heating coupling fluid (CF) (Paratherm NF® mineral oil (Paratherm Corporation, 2013)) flows through an outer annulus (ID_o = 7.0 mm, OD_o = 9.5). The lower 1.60 m portion of the BPG is heated by the CF, and the upper 0.14 m penetrates into a settling vessel that separates the liquid and

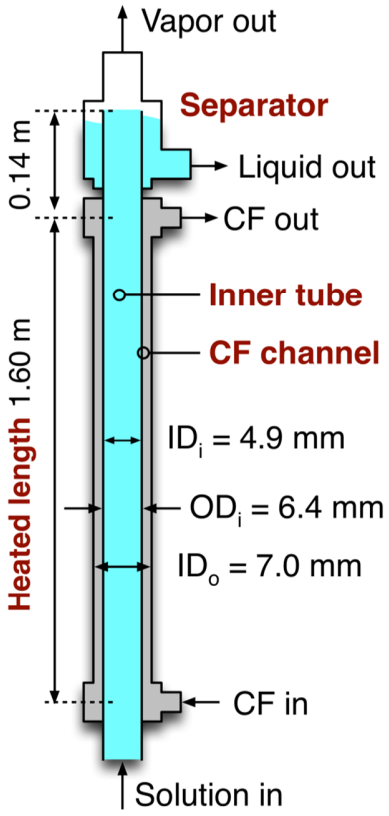

Figure 7.2 – Schematic of bubble-pump generator

vapor streams. The full component is wrapped with fiberglass insulation to reduce heat loss to the surroundings. Based on experiments conducted with the inner tube evacuated, the overall thermal resistance from the coupling fluid stream to the ambient ranges over $R_{BPG,CF,amb}$ = 2.0 – 2.3 K W^{-1}, depending on the ambient air velocity in the ventilation hood. A conservative uncertainty of ± 25% is assumed for this thermal resistance.

The solution reservoir level was measured visually with a sight glass. The solution level oscillated during system operation; therefore a conservative uncertainty of ± 10 mm is employed to account for these variations. This corresponds to an uncertainty in the submergence ratio (S_r) of ± 0.006 (± 90 Pa driving pressure at representative operating

conditions). For all cases, S_r was maintained in the range: 0.255 – 0.280. The measured submergence ratio does not account for pressure loss in the plumbing and dilute solution side of the solution heat exchanger. Therefore, effective BPG driving pressures are slightly less than $\rho_L \, g \, S_r \, H_{BPG}$.

Concentrated solution flow rates are measured downstream of the solution heat exchanger (SHX) with an ultrasonic time-of-flight volumetric flow meter (Titan Atrato 700 Series, uncertainty of ± 1.0% of readings). Working fluid inlet and outlet temperatures are measured with calibrated T-type insertion thermocouples (± 0.25 K uncertainty). The DAR system operating pressure is measured with a Rosemount 2088A absolute pressure transducer (uncertainty ± 5.5 kPa).

The CF volumetric flow rate is measured with a gear flow meter (AW Lake JVM-12KG, ± 0.3 ml min^{-1} uncertainty). CF inlet and outlet temperatures are measured with calibrated insertion thermocouples (± 0.25 K). CF properties are determined using data from the Paratherm Corporation (2013b). The total heat transfer rate from the CF stream is:

$$Q_{BPG,CF} = \frac{V_{BPG,CF,out}}{\rho_{BPG,CF}\left(T_{BPG,CF,out}\right)}\left[i_{BPG,CF}\left(T_{BPG,CF,in}\right) - i_{BPG,CF}\left(T_{BPG,CF,out}\right)\right] \tag{7.1}$$

Measured CF heat transfer rates vary over 124 – 161 W with relatively low propagated uncertainties (± 1.1 – 3.6 W). Heat transfer to the working fluid is determined, accounting for heat loss from the coupling fluid to the ambient.

$$Q_{BPG} = Q_{BPG,CF} - Q_{BPG,loss} \tag{7.2}$$

$$Q_{\mathrm{BPG,loss}} = \frac{\left(T_{\mathrm{BPG,CF,in}} + T_{\mathrm{BPG,CF,out}}\right)/2 - T_{\mathrm{amb}}}{R_{\mathrm{BPG,CF,amb}}} \tag{7.3}$$

Here, $(T_{\mathrm{BPG,CF,in}} + T_{\mathrm{BPG,CF,out}})/2$ is the estimated average coupling fluid channel temperature, and T_{amb} is the ambient air temperature (averaged over two thermocouples in the enclosing ventilation hood). Measured heat transfer rates to the working fluid (Q_{BPG}) range over 89 – 122 W ($Q_{\mathrm{BPG,loss}}$ = 36 – 47 W). Corresponding uncertainties range over 9 – 12 W, and are less than 12% of Q_{BPG} for all cases. The greater uncertainties for Q_{BPG} than for $Q_{\mathrm{BPG,CF}}$ are due to the relatively large uncertainty applied to the heat-loss thermal resistance (± 25%).

Concentrated solution flow rates range over 26 – 45 ml min^{-1} ± 1% (27 – 45 g min^{-1}) for the main test matrix. Flow rates tend to increase with CF inlet source temperatures. This occurs because greater portions of input heat are transferred near the BPG base with elevated $T_{\mathrm{CF,in}}$, increasing average channel void fraction and reducing hydrostatic pressure drop. Flow rates are lower for the two elevated pressure cases (25 ml min^{-1} at 1.25 MPa, 19 ml min^{-1} at 1.39 MPa). This occurs because of the greater sensible heating load at elevated pressure (higher T_{sat}) and reduced driving temperature difference near the BPG inlet.

The BPG liquid outlet flow is assumed to be saturated solution. Therefore, the concentrated solution (CS) NaSCN concentrations (ψ_{CS}) are determined using the saturation curve formulated by Infante Ferreira (1984) for NH_3-NaSCN solutions ($p_{\mathrm{sys}} = p_{\mathrm{v,NH3\text{-}NaSCN}}(T_{\mathrm{BP,out}}, \psi_{\mathrm{CS}})$). The resulting values of ψ_{CS} range over 0.559 – 0.622 ± 0.001. ψ_{CS} tends to decrease slightly with increasing solution flow rate. This occurs because less

refrigerant is generated in these cases for fixed heating rates (greater portions of Q_{BPG} are used for sensible heating of the solution).

Assuming that the inlet flow to the BPG is subcooled liquid, the dilute solution flow rate (m_{DS}), dilute solution concentration (ψ_{CS}), and refrigerant vapor generation rate (m_{ref}) can be determined by applying mass, species, and energy balances over the BPG.

$$m_{DS} = m_{CS} + m_{ref} \tag{7.4}$$

$$\psi_{DS} m_{DS} = \psi_{CS} m_{CS} \tag{7.5}$$

$$m_{DS} i_{NH_3\text{-}NaSCN}\left(T_{BPG,in}, \psi_{DS}\right) - m_{CS} i_{NH_3\text{-}NaSCN}\left(T_{BPG,out}, \psi_{CS}\right) - m_{ref} i_{NH_3}\left(T_{BPG,out}, p_{sys}\right) = Q_{BPG} \tag{7.6}$$

The dilute solution flow rates are found to range over 24 – 49 ± 0.5 – 0.6 g min^{-1}. Dilute solution concentrations range over 0.513 – 0.538 ± 0.006 – 0.013. Refrigerant flow rates range over m_{ref} = 2.5 – 4.2 ± 0.5 g min^{-1}. The high uncertainty for m_{ref} (10 – 20%) is due to the relatively large uncertainty in heat loss from the BPG to the ambient. BPG inlet temperatures ($T_{BPG,in}$) range over 58 – 70°C, and outlet temperatures ($T_{BPG,out}$) over 77 – 94°C (except for the elevated pressure cases: 98.2°C at 1.27 MPa, 106.3°C at 1.39 MPa).

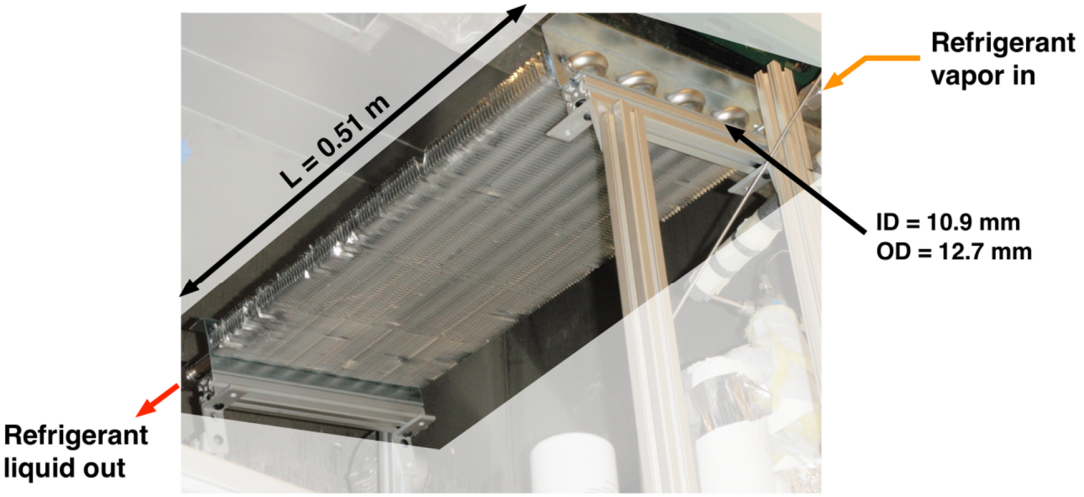

Figure 7.3 – Serpentine finned-tube condenser

7.2.3 Condenser

A serpentine finned-tube condenser was employed in the DAR system (Figure 7.3). The component has 9 rows of stainless steel tubes (ID = 10.9 mm, OD = 12.7 mm, L_{row} = 0.51 m, L_{tot} = 4.57 m). Tube rows are spaced by p_{row} = 31.8 mm. The tubes are enhanced with press-fit smooth rectangular fins of thickness 0.19 mm, height 27.5 mm, and pitch 4.2 mm. The condenser is inclined slightly downward (towards the refrigerant outlet) such that condensate drains into the evaporator. A U-tube gas-trap is installed at the condenser outlet to prevent non-condensable helium ingress.

During system start-up, some amount of helium is expected to be present in the condenser. Vapor refrigerant flow from the BPG is expected to quickly displace this helium, permitting effective condensation with minimal mass transfer resistance from the non-condensable gas. However, it is also possible that some helium may be contained in the condenser, between the inlet stream from the BPG and the gas trap at the outlet. This

effect was not clearly observed during operation of the experimental DAR system, but could be significant in other implementations. One potential strategy to address this issue is to oversize the gas-trap tube diameter in order to ensure that all helium is purged from the condenser before the gas trap fills with liquid. Related approaches to reducing condensation and absorption mass transfer resistance by advecting away non-condensable gases have been proposed by Lee and Rose (1984) and Medrano *et al.* (2003).

The condenser refrigerant flow rates are determined from the BPG analysis (m_{ref} = 2.5 – 4.2 ± 0.5 g min^{-1}). Condenser inlet temperatures are assumed to be equal to BPG outlet temperatures ($T_{cond,in} = T_{BPG,out}$ = 77 – 94°C for the main test matrix cases). Condenser outlet temperatures range over $T_{cond,out}$ = 23.0 – 27.3°C, and are generally slightly lower than the average ambient temperatures (~1 K difference). The slightly low condenser outlet temperatures could be due to variations in local ambient temperature or heat transfer to the cool downstream evaporator. The condenser heat transfer is evaluated as:

$$Q_{cond} = m_{ref}\left[i_{NH_3}\left(T_{BPG,out}, p_{sys}\right) - i_{NH_3}\left(T_{cond,out}, p_{sys}\right)\right] \tag{7.7}$$

Condenser heat transfer rates vary over 36 – 93 ± 11 W. The uncertainty in Q_{cond} is primarily due to the uncertainty in m_{ref}. In all measured cases, $T_{cond,out}$ was less than T_{sat} ($T_{sat} - T_{cond,out}$ = 2 – 6 K for the primary test matrix), indicating complete condensation.

7.2.4 Evaporator

A tube-in-tube evaporator was used in this investigation (Figure 7.4). The liquid refrigerant and auxiliary gas contact in a Tee above the evaporator, and drain through the stainless steel evaporator tube (ID_i = 17.3 mm, OD_i = 19.1 mm, L = 0.30 m). Coupling fluid (water) flows upward (counter-flow) through an annular channel around the

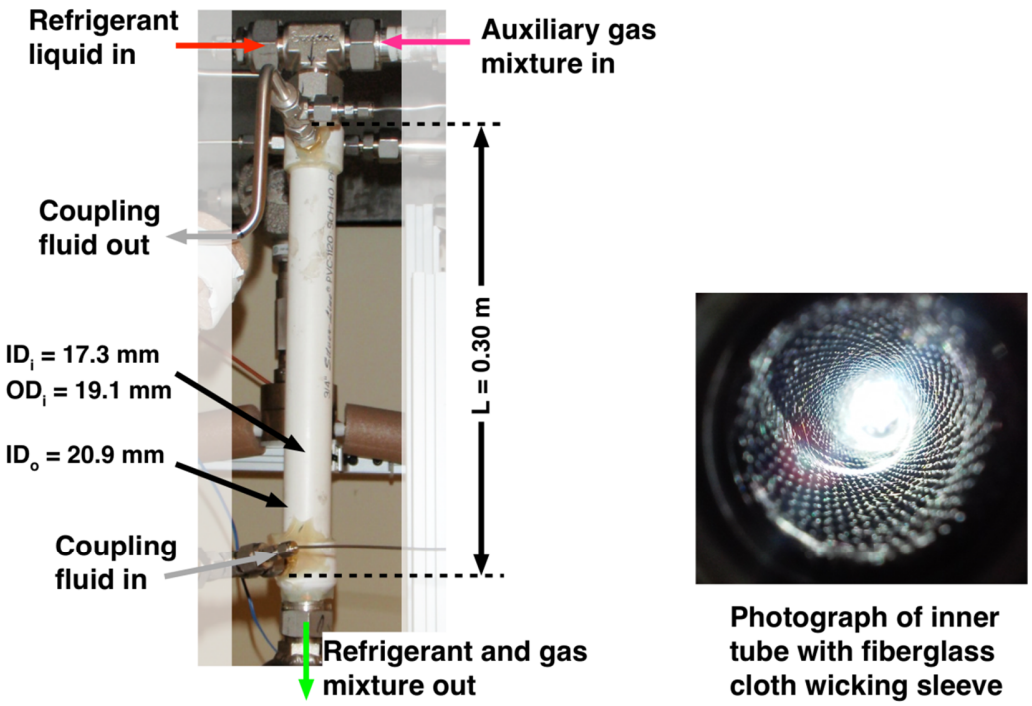

Figure 7.4 – Tube-in-tube evaporator

evaporator tube (ID_o = 20.9 mm). The full component is insulated with ~25 mm of fiberglass wrap. A woven fiberglass sleeve (~0.7 mm thick) is inserted inside the evaporator inner tube to improve film wetting. Heat gain from the ambient is assumed negligible because of the relatively small component size (L = 0.30 m) and low average temperature difference ($T_{amb} - T_{evap,CF}$ ~ 10 – 20 K).

Working fluid and CF temperatures are measured at the component inlets and outlets with T-type insertion thermocouples (± 0.25 K). The coupling fluid is circulated with a diaphragm metering pump (Pulsatron Pulsafeeder LMH6TA-PTC3). The pump was calibrated to ensure accurate CF flow rates during operation (± 5% uncertainty). An electric immersion heater and a chiller-coupled tube-in-tube heat exchanger were

installed upstream of the evaporator to control CF inlet temperatures. The CF flow rate was adjusted during operation to maintain intended temperature glides (18 → 14°C, 12 → 8°C, 6 → 3°C). The delivered cooling rate is evaluated as:

$$Q_{\text{evap}} = V_{\text{evap,CF}} \rho_{\text{evap,CF}} c_{\text{p,evap,CF}} \left(T_{\text{evap,CF,in}} - T_{\text{evap,CF,out}} \right) \tag{7.8}$$

Evaporator cooling rates varied over 5 – 21 W for most cases, with propagated uncertainties of ± 1 – 2 W.

Evaporator inlet auxiliary gas composition is challenging to determine, and was not measured directly in these experiments. An absorber approach ammonia vapor pressure difference was assumed (CAVP_{abs} = 150 kPa) to estimate the composition ($p_{\text{v,aux}} = p_{\text{v,NH3-NaSCN}}(T_{\text{abs,L,in}}, \psi_{\text{CS}}) + \text{CAVP}_{\text{abs}}$). This value is slightly more conservative than predicted in Section 6.2.5 (111 kPa) to account for non-uniform flow distribution and incomplete film wetting. The resulting inferred auxiliary gas helium fractions range over ξ_{aux} = 0.273 – 0.462. In future investigations, techniques such as gas chromatography or ultrasonic time-of-flight measurement could be employed to directly measure gas mixture composition. Auxiliary gas flow rates are inferred from the gas heat exchanger analysis (GHX) described in the next section. The resulting values are determined to range over m_{aux} = 25 – 41 g min^{-1} for the different experimental cases.

7.2.5 Gas heat exchanger

A stainless steel shell-and-tube gas heat exchanger was employed in the experimental DAR system (Figure 7.5). No baffles were installed on the shell side to minimize pressure drop in the passive circulation loop. The evaporator outlet stream flows downward through seven parallel circular tubes (ID_{i} = 10.9 mm, OD_{i} = 12.7 mm, L =

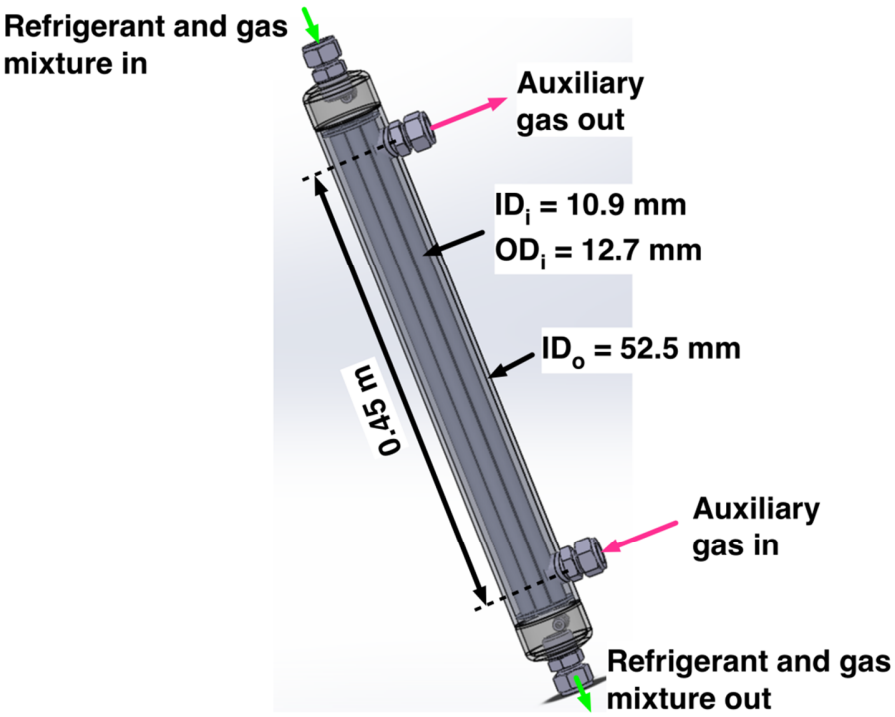

Figure 7.5 – Shell-and-tube gas heat exchanger

0.45 m). The warm auxiliary gas stream rises counterflow through the shell side of the GHX (ID_o = 52.5 mm). Temperature measurements were collected at all four GHX ports (T-type thermocouples, ± 0.25 K uncertainty).

No flow meters were commercially available to measure the auxiliary gas stream that satisfied requirements for total working pressure (1.1 – 1.4 MPa), low pressure drop (natural circulation flow), material compatibility (NH_3 gas), and anticipated low velocities (~0.2 m s^{-1}). In future experiments, special-purpose insertion-type thermal anemometers could be employed to accurately measure auxiliary gas flow rates with acceptable pressure drops. Commercially available thermal anemometers are generally configured for higher flow rates, relatively low working pressure (1.0 MPa max), and

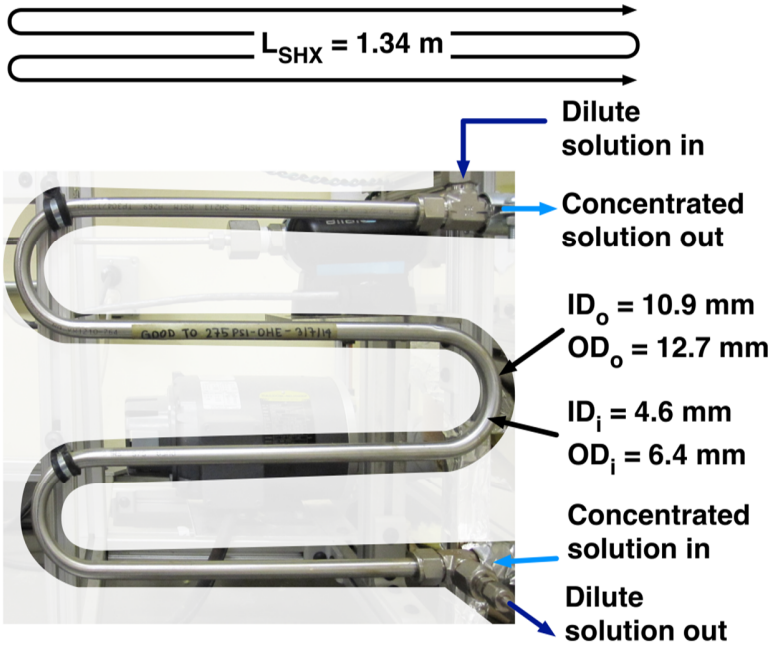

Figure 7.6 – Serpentine tube-in-tube counterflow solution heat exchanger

expose circuitry to the working fluid. The auxiliary gas flow rate (m_{aux} = $m_{abs,G,out}$ = $m_{evap,G,in}$) was inferred based on the design GHX overall conductance (UA_{GHX} = 2.0 W K^{-1}) and inlet and outlet temperature measurements (i.e., $LMTD_{GHX}$).

$$Q_{GHX} = UA_{GHX} \frac{\left(T_{GHX,o,in} - T_{GHX,i,out}\right) - \left(T_{GHX,o,out} - T_{GHX,i,in}\right)}{\ln\left(\frac{T_{GHX,o,in} - T_{GHX,i,out}}{T_{GHX,o,out} - T_{GHX,i,in}}\right)} \tag{7.9}$$

$$m_{aux} = \frac{Q_{GHX}}{c_{p,aux}\left(T_{GHX,o,in} - T_{GHX,o,out}\right)} \tag{7.10}$$

Inferred GHX heat transfer rates range over 13 – 29 W, yielding auxiliary gas flow rates of 25 – 41 g min^{-1}.

7.2.6 Solution heat exchanger

A stainless steel serpentine counterflow tube-in-tube solution heat exchanger (SHX) is employed in the experimental system (Figure 7.6). The hot concentrated solution (CS) stream flows through an inner tube (ID_i = 4.6 mm, OD_i = 6.4 mm, L_{SHX} = 1.34 m). The cooler dilute solution (DS) stream flows through the annular channel (ID_o = 10.9 mm, OD_o = 12.7 mm). Inlet and outlet temperatures are measured for both streams (T-type insertion thermocouples, ± 0.25 K uncertainty). The component is insulated with fiberglass panels (~50 mm thick) to reduce heat loss. The component is rated based on heat transfer to the cooler DS stream.

$$Q_{SHX} = m_{DS}\left[i_{NH_3\text{-}NaSCN}\left(T_{DS,out},\psi_{DS}\right) - i_{NH_3\text{-}NaSCN}\left(T_{DS,in},\psi_{DS}\right)\right] \tag{7.11}$$

Component heat transfer rates range over Q_{SHX} = 32 – 56 ± 1 W for the experimental cases. Heat loss from the component is determined based on the overall energy balance.

$$Q_{SHX,loss} = \begin{array}{l} m_{DS}\left[i_{NH_3\text{-}NaSCN}\left(T_{DS,in},\psi_{DS}\right) - i_{NH_3\text{-}NaSCN}\left(T_{DS,out},\psi_{DS}\right)\right] \\ +m_{CS}\left[i_{NH_3\text{-}NaSCN}\left(T_{CS,in},\psi_{CS}\right) - i_{NH_3\text{-}NaSCN}\left(T_{CS,out},\psi_{CS}\right)\right] \end{array} \tag{7.12}$$

SHX heat loss rates range over 8 – 18 ± 1 W.

7.2.7 Solution subcooler

A solution subcooler was installed between the SHX CS outlet and absorber solution inlet (Figure 7.7). The component design includes a bare horizontal inlet tube section (ID = 4.6 mm, OD = 6.4 mm, L = 0.46 m), a main vertical finned section (ID = 10.9 mm, OD = 12.7 mm, L = 0.71 m), and a bare horizontal outlet tube section (ID = 4.6 mm, OD = 6.4 mm, L = 0.23 m). The main portion is wrapped with 18 H_{fin} = 25 mm tall, δ_{fin} = 0.35 mm thick, smooth corrugated aluminum fins. This configuration results in 18 open (outward-facing) channels with average width δ_o = 5.5 mm and 18 closed (inward-facing)

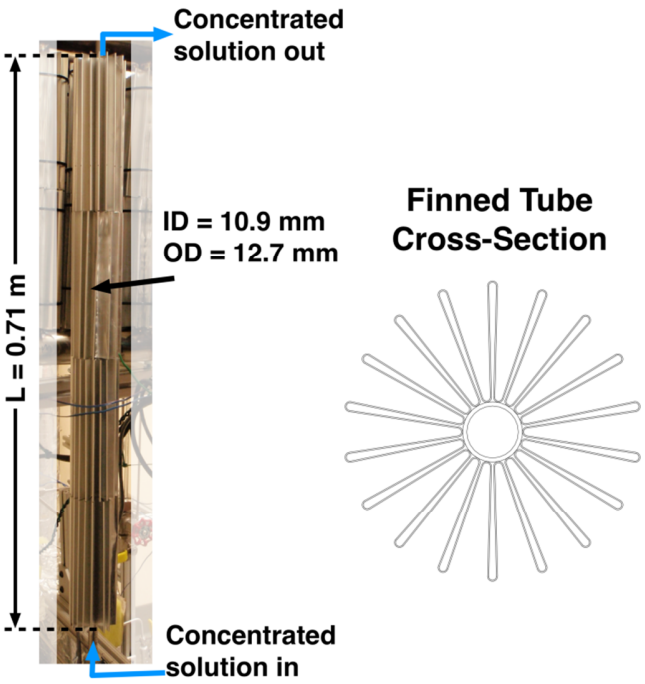

Figure 7.7 – Passive solution subcooler, main finned section

channels with average width 3.0 mm. The fins were affixed to the subcooler with an epoxy resin (Loctite 608 Hysol, reported thermal conductivity ~ 0.21 W m^{-1} K^{-1} (Loctite Corporation, 2001)). In a separate set of passively air-cooled water-flow experiments, this was found to increase overall heat transfer by 5 – 20% compared with affixing fins only with external compression bands. In future investigations, fins could be brazed to the subcooler to further reduce thermal contact resistance. Temperature measurements were collected at the component inlet (SHX CS outlet) and outlet (absorber solution inlet). The overall component heat transfer rate and conductance are:

$$Q_{sub} = m_{CS}\left[i_{NH_3\text{-}NaSCN}\left(T_{sub,in},\psi_{CS}\right) - i_{NH_3\text{-}NaSCN}\left(T_{sub,out},\psi_{CS}\right)\right] \tag{7.13}$$

$$UA_{sub} = Q_{sub}/LMTD_{sub,amb} \tag{7.14}$$

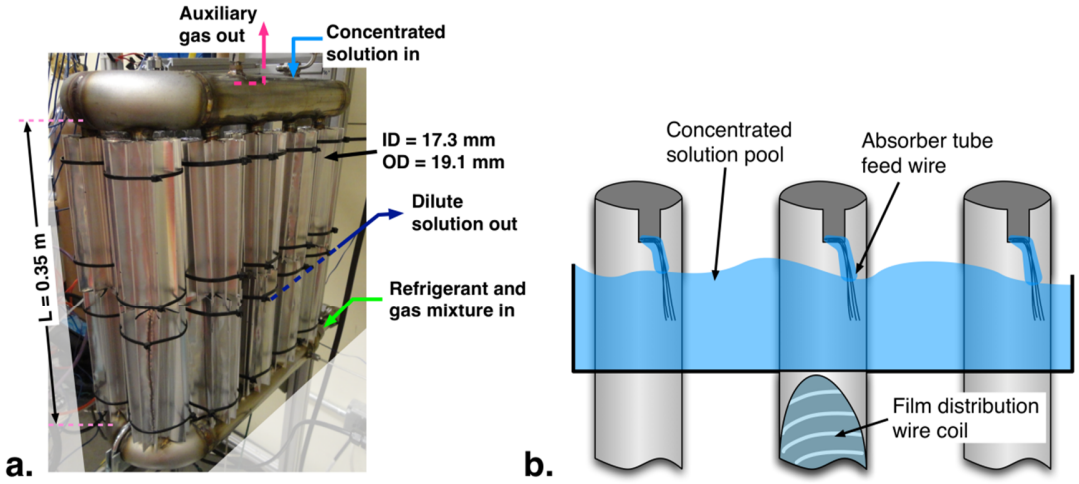

Figure 7.8 – **a**. Enhanced parallel finned-tubed counter-flow absorber, **b**. Solution distribution mechanism

Here $LMTD_{sub,amb}$ is the log-mean temperature difference between the subcooler solution stream and ambient air. The component heat transfer rate varies over 7.4 – 21.7 ± 0.7 W. The corresponding conductance range is UA_{sub} = 1.5 – 2.1 ± 0.1 W K^{-1}.

7.2.8 Absorber

The absorber configuration proposed in Section 6.2.5 was implemented in the experimental facility. In this design, downward flowing NH_3-NaSCN solution contacts rising NH_3-He gas in 10 parallel vertical tubes (ID = 17.3 mm, OD = 19.1 mm, L = 0.35 m) (Figure 7.8a). Each tube is wrapped with twelve 25 mm tall, 0.35 mm thick, smooth corrugated aluminum fins. The fins are affixed to the absorber with epoxy resin, as in the solution subcooler. Liquid is distributed to the absorber tubes from a horizontal U-tube header. The absorber tubes penetrate 12.7 mm into the header. Each tube top is slotted, and stranded stainless steel "feed wires" are installed to wick liquid from the solution pool in the header (Figure 7.8b). This design was experimentally evaluated with ambient

pressure water flow, and was found to result in more uniform liquid distribution than with plain tubes. To improve internal film wetting, helical wire coils were inserted into the absorber tubes (wire diameter 0.6 mm).

T-type insertion thermocouples (± 0.25 K uncertainty) were installed in all four absorber inlet and outlet ports. However, the auxiliary gas flow rate and concentration (absorber gas outlet) could not be directly measured in experiments (see Sections 7.2.4 – 7.2.5). Similarly, the refrigerant-gas mixture may enter the absorber in a two-phase state with unknown quality. Therefore, the absorber heat rejection rate (Q_{abs}) is determined from an energy balance applied over the entire gas loop (evaporator, GHX, absorber, and connective plumbing).

$$Q_{abs} = \begin{matrix} m_{CS} i_{NH_3\text{-NaSCN}}\left(T_{abs,L,in}, \psi_{CS}\right) - m_{DS} i_{NH_3\text{-NaSCN}}\left(T_{abs,L,out}, \psi_{CS}\right) \\ + m_{ref} i_{NH_3}\left(T_{evap,L,in}, p_{sys}\right) + Q_{evap} \end{matrix} \tag{7.15}$$

In this energy balance, heat transfer between the ambient and the gas-loop plumbing and exterior of the GHX is included in Q_{abs}. However, the flows contained in these volumes are typically close to the ambient temperature; therefore, such contributions to Q_{abs} are expected to be small. The resulting absorber heat transfer rates range over Q_{abs} = -6.3 – 12.4 ± 1 – 2 W. These values are relatively low in magnitude, and are negative in some cases due to sensible heating of the refrigerant-gas mixture and solution.

7.2.9 Complete DAR system

The full DAR system is rated using the cooling coefficient of performance (COP). An external COP is defined with respect to total heat transfer from the BPG CF.

$$COP_{ext} = Q_{evap} / Q_{BPG,CF} \tag{7.16}$$

Representative external COP values for the main test matrix are: ~0.05 ± 0.006 ($T_{evap,CF}$ = 6 → 3°C), ~0.09 ± 0.01 (12 → 8°C), ~0.11 ± 0.01 (18 → 14°C).

Internal COPs are evaluated based on only accounting for heat transferred to the working fluid in the BPG (i.e., Q_{BPG}). These values still account for heat loss from the SHX and warm solution lines.

$$COP_{int} = Q_{evap} / Q_{BPG} \tag{7.17}$$

Internal COP values are higher, with representative main test matrix values of: ~0.06 ± 0.01 ($T_{evap,CF}$ = 6 → 3°C), 0.14 ± 0.02 (12 → 8°C), 0.17 ± 0.02 (18 → 14°C). Uncertainties for COP_{int} are slightly greater than those for COP_{ext} due to the high (25%) uncertainty applied to $R_{BPG,CF,amb}$, as discussed previously.

Overall energy balances are applied to the DAR system.

$$Q_{net} = Q_{BPG,CF} - Q_{BPG,loss} - Q_{cond} + Q_{evap} - Q_{BPG\text{-}SHX,loss} - Q_{SHX,loss} - Q_{sub} - Q_{abs} \tag{7.18}$$

Here, $Q_{BPG\text{-}SHX,loss}$ is the heat loss in the connective plumbing from the BPG CS outlet to SHX CS inlet (7.8 – 13.1 ± 0.3 – 0.7 W). Net heat transfer rates in the entire system are 0 W to within solver precision ($|Q_{net}| < 10^{-9}$ W), which provides verification for the overall analysis approach.

7.3 Component and Model Assessment

7.3.1 Bubble-pump generator

Stable bubble-pump generator (BPG) solution pumping was observed in all experimental cases; $V_{BP,L,out}$ = 27 – 45 ml min^{-1} for the primary test matrix. Additionally, submergence ratios of only 0.255 – 0.280 were employed for these cases. This ensured adequate vertical space for the gas-loop components (condenser, evaporator, GHX,

absorber), and yielded a liquid head of approximately 1.3 m to drive flow through the SHX and absorber. Liquid pumping rates ($V_{BPG,L,out}$) generally increased with vapor refrigerant flow rates ($V_{BPG,V,out}$) for the primary test matrix, varying ambient temperature cases, and varying ambient air velocity cases (Figure 7.9). The varying ambient pressure cases were not included in Figure 7.9 because solution saturation temperatures were significantly higher at those conditions. On average, solution flow rates increased slightly with source temperature ($T_{BPG,CF,in}$) as predicted in Section 6.2.2, but variations in submergence ratios between cases (0.255 – 0.280) made it difficult to isolate this effect. Still, these results indicate that low source temperatures (~110°C) can be employed without significantly degrading BPG performance.

The major limitation of the proposed BPG design is the relatively high heat loss rate (~40 ± 10 W). For the experimental cases, this results in a 25 – 30% external COP penalty. The OD_o = 9.5 mm BPG was insulated with OD ~ 100 mm of fiberglass wrap. Modeling results suggest that only minimal heat loss reductions could be achieved with additional insulation. More compact designs for other components could enable a shorter BPG, and thus, decreased heat loss rates ($Q_{Loss} \sim L_{BPG}$). In a packaged system, relatively hot components, such as the BPG, SHX, and reservoir could also be integrated to reduce exterior area and heat loss from plumbing.

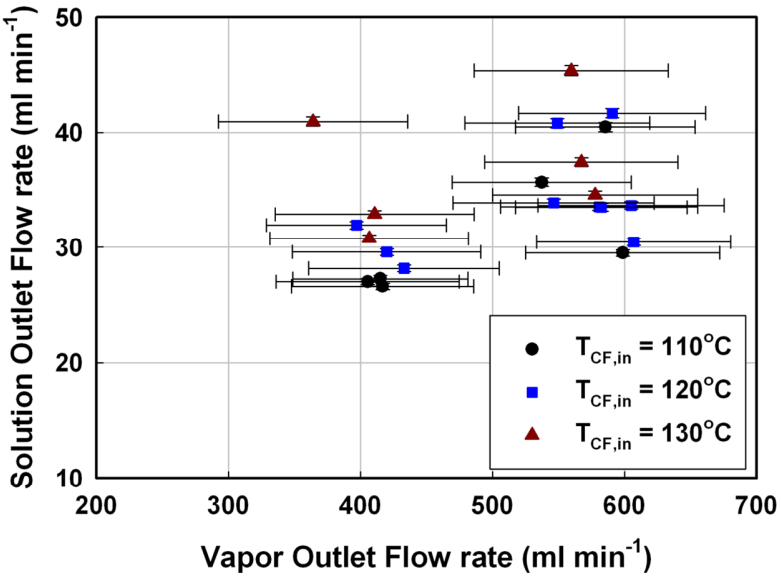

Figure 7.9 – Bubble-pump generator concentrated solution and vapor outlet flow rates for the primary test matrix, varying ambient temperature cases, and varying ambient air velocity cases

Experimental data from all cases were employed as inputs for the BPG model described in Section 6.2.2. If measured solution outlet flow rates are specified (m_{CS}), model predictions for submergence ratios (S_r) agree with experimental results with an average absolute deviation of 11% ($AAD = (1/N)\sum_{N}\left(S_{r,mod} - S_{r,exp}\right)/S_{r,exp}$). In general, the proposed model under-predicts S_r (average of 0.029 under-prediction of S_r, or equivalently ~270 Pa in BPG driving pressure). This may be due to pressure drops in the solution heat exchanger and connective plumbing from the reservoir to the BPG inlet (not accounted for in the model). Additionally, material property correlations for NH_3-NaSCN are based on a limited database of measurements (Infante Ferreira, 1984). No solution viscosity data are available for the conditions in the BPG, and no surface tension data are

available for the mixture. The overall model performance is acceptable considering these factors.

On average, the proposed BPG model predicts refrigerant flow rates to within 0.1 g min^{-1} of experimental values (m_{ref} = 2.5 – 4.2 ± 0.5 g min^{-1}). Average errors for the outlet coupling fluid ($T_{BPG,CF,out}$) and working fluid ($T_{BPG,\ out}$) temperatures are 0.8 K and 2.1 K, respectively. Average concentrated solution concentration (ψ_{CS}) errors are 0.007 (experimental uncertainty ± 0.001). Average errors for total CF heat transfer ($Q_{BPG,CF}$) and BPG heating rates (Q_{BPG}) are 4.8 W and 3.4 W, respectively. Corresponding experimental uncertainties are 1 – 4 W and 9 – 12 W, respectively. This indicates that the proposed model captures the overall behavior of the BPG, in addition to the liquid pumping performance. For some parameters, discrepancies are significantly less than experimental uncertainties. This is primarily an artifact of the BPG heat loss model, for which the same assumptions for $R_{BPG,CF,amb}$ and $Q_{BPG,loss}$ are employed in the model and experimental data reduction procedure.

If submergence ratios are supplied to the proposed model as inputs (rather than m_{CS}), then predictions for solution pumping rates significantly exceed experimental measurements (AAD = 56%). This large discrepancy is a result of the numerical conditioning of the BPG design problem, for which small changes in S_r yield large changes in m_{CS}. Improved model performance may not be possible at present due to the limited fluid property data available in the literature. As indicated above, predicted and measured liquid pumping rates can be brought into agreement with submergence ratio (S_r) adjustments of only 0.03 on average. From the perspective of DAR system design,

the proposed model is acceptable because only minor charge adjustments are required during system commissioning to achieve target flow rates.

7.3.2 Condenser

It is difficult to rigorously assess the condenser performance using available experimental data (m_{ref}, $T_{cond,in}$, $T_{cond,out}$). In all cases, complete condensation (T_{sat} – $T_{cond,out}$ = 4.4 K on average) and close approach to ambient temperatures (CAT_{cond} = $T_{cond,out}$ – T_{amb} = -1.0 K on average) were observed. As indicated in Section 7.2.3, negative CAT_{cond} values may be due to local ambient air-temperature variations or proximity of the condenser outlet thermocouple to the evaporator core. This indicates that the proposed condenser design is acceptable, or even oversized for this application.

Local upward ambient air velocities were measured with a handheld anemometer, and varied over U_{amb} = 0.2 – 0.8 m s^{-1} in the ventilation hood (0.5 m s^{-1} near the condenser) for the primary test matrix. The model formulated in Section 6.2.3 predicts complete condensation for almost all of these cases with ambient velocities of 0.10 – 0.45 m s^{-1} (two cases require greater U_{amb}). These results indicate general validity of the proposed model. At reduced ventilation rates (50%), measured velocities varied over 0.0 – 0.4 m s^{-1} (0.4 m s^{-1} near the condenser). The condenser model predicts a required ambient air circulation rate of 0.52 m s^{-1} for the experimental case measured at these conditions. No velocity readings registered on the anemometer when the hood fan was turned off. The condenser model predicts a required ambient air velocity of 0.13 m s^{-1} for the experimental case evaluated at this condition, which is close to the instrument minimum reading of 0.1 m s^{-1}. Overall, these results suggest that the proposed condenser model is

suitable for overall component sizing. In future studies, additional instrumentation could enable more detailed model assessment and refinement.

7.3.3 Evaporator

Evaporator cooling rates were generally in the range of Q_{evap} = 5 – 20 W for the primary test matrix. These results correspond to only 17 – 35% evaporation of refrigerant. It may be possible to increase system performance with a larger (longer) evaporator or improved refrigerant film wetting-promotion techniques. The evaporator was sized to fit between the condenser and GHX, while yielding acceptable gas-phase flow resistance. Therefore, in future design iterations, these components may also have to be modified to accommodate changes in the evaporator configuration.

The evaporator model presented in Section 6.2.4 requires inputs of *WF* (the portion of the tube area effectively wetted by refrigerant liquid), auxiliary gas flow rate, and auxiliary gas concentration. It is not possible to rigorously assess the proposed model because these three parameters could not be directly measured. However, the evaporator model can still be applied to qualitatively assess the experimental component performance. If the measured evaporator cooling rate is provided as a model input, the effective value of *WF* can be determined. For the experimental cases, on average, the inferred wetting factor is 24%, and cooling capacity indicates only 30% evaporation of refrigerant. Inferred *WF* values are plotted against refrigerant flow rates (m_{ref}) in Figure 7.10. The effective film wetting area tends to increase with liquid refrigerant flow rate, as would be expected for the transition from rivulet to falling-film flow. Based on these results, the evaporator is mass-transfer area limited, and performance could be

significantly improved by refining the liquid film distribution mechanism (currently a woven fiberglass sleeve) or increasing the component length as suggested above.

Employing the same approach, the design model can be used to quantify the evaporator mass transfer conductance (UA^*_{evap}). This quantity is defined as $UA^*_{evap} = \dot{m}_{evap}/LMPD_{evap}$, where $LMPD_{evap}$ is the log-mean vapor pressure difference between the gas mixture and liquid refrigerant streams. For the lower (Q_{BPG} ~ 90 W) and higher (Q_{BPG} ~ 120 W) heating rate cases in the main test matrix, UA^*_{evap} ranges over $3.5 – 5.0 \times 10^{-11}$ kg Pa^{-1} s^{-1} and $5.0 – 7.5 \times 10^{-11}$ kg Pa^{-1} s^{-1}, respectively (units of mass flow/vapor pressure difference). These values are approximately 30 – 60% of those predicted for complete film-wetting ($WF = 1$) in Section 6.2.4.

If Q_{evap} is provided as a model input, the predicted outlet gas-to-liquid temperature difference ($CAT_{evap,G,L} = T_{evap,G,out} - T_{\_evap,L,out}$) varies with cooling temperature approximately as: $CAT_{evap,G,L}(T_{evap,CF} = 6 \rightarrow 3°C)$ ~ 15 K, $CAT_{evap,G,L}(T_{evap,CF} = 12 \rightarrow 8°C)$ ~ 12 K, $CAT_{evap,G,L}(T_{evap,CF} = 18 \rightarrow 14°C)$ ~ 9 K. This non-equilibrium behavior causes the low-cooling-temperature performance penalty to be less severe, because only a portion of the maximum gas sensible cooling load ($\dot{m}_G c_{p,G} (T_{evap,G,in} - T_{evap,L,out})$) is incurred (see Section 6.2.4). For example, for the case with Q_{BPG} = 90 W, $T_{BPG,CF,in}$ = 130°C, $T_{evap,CF} = 6 \rightarrow 3°C$, and Q_{evap} = 6.5 W, the model predicts $T_{evap,G,out}$ = 18.5°C and $T_{evap,L,out}$ = 3.1°C. The evaporator outlet thermocouple measured 9.9°C for this case, which is between these two values. However, if the evaporator outlet flow was actually in equilibrium at 9.9°C, then it would not be possible for $T_{evap,out} > T_{evap,CF,in}$, $T_{evap,in} > T_{evap,CF,in}$, and for net cooling to be delivered.

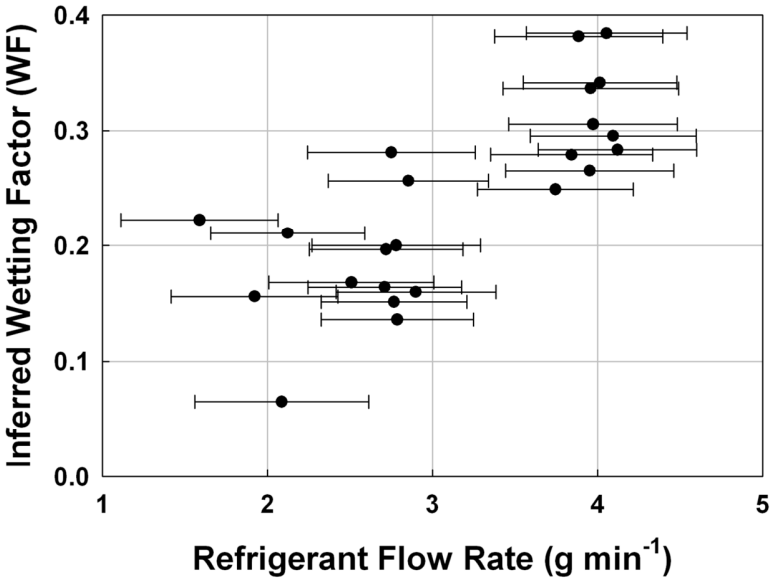

Figure 7.10 – Effect of refrigerant flow rate on inferred evaporator wetting factor (*WF*)

7.3.4 Gas heat exchanger

The gas heat exchanger (GHX) meets the design objective of achieving a significant reduction in the auxiliary gas stream temperatures. Measured auxiliary gas temperature drops ($T_{GHX,o,in} - T_{GHX,o,out}$) range over 7.6 – 14.5 K. Cold-side stream temperature rises (6.5 – 9.9 K) are slightly lower, but of similar order to corresponding warm-side values. This indicates that if two-phase flow enters the cold-side of the GHX (as discussed in Section 7.3.3), only a minor amount of additional evaporative cooling occurs in this component.

Based on overall system results, the gas heat exchanger may in fact be oversized, even with a measured heat exchanger effectiveness of only 31 – 51%. The evaporator and GHX are installed coaxially between the absorber gas outlet and condenser outlet. If the GHX length is reduced, a larger evaporator could be employed, which may yield an

increased refrigerant evaporation fraction (only 17 – 35% in this investigation). This approach would increase the evaporator gas inlet temperature, and potentially increase parasitic cooling load. However, based on model results and the discussion in Section 7.3.3, gas-to-interface thermal resistance is relatively high in the evaporator. Thus, only a small portion of the additional potential parasitic gas cooling load may be incurred.

7.3.5 Solution heat exchanger

The measured solution heat exchanger effectiveness ranges over ε_{SHX} = 62 – 73% ± 2% ($\varepsilon_{SHX} = Q_{SHX} \Big/ \left\{ m_{CS} \left[i_{NH_3\text{-}NaSCN}\left(T_{SHX,CS,in}, \psi_{CS}\right) - i_{NH_3\text{-}NaSCN}\left(T_{SHX,DS,in}, \psi_{DS}\right) \right] \right\}$). Here Q_{SHX} is the net heat gain in the cooler DS stream (i.e., accounting for heat loss to the ambient). The corresponding overall conductances range over UA_{SHX} = 2.7 – 4.8 ± 0.2 W K^{-1}.

Even with relatively thick insulation (~50 mm thick fiberglass panels), a significant amount of heat is lost from the SHX ($Q_{SHX,loss}$ = 8 – 18 W, 16 – 40% of Q_{SHX}). This corresponds to an effective heat loss coefficient of $UA_{SHX,amb}$ = 0.5 – 1.0 ± 0.1 W K^{-1} based on the log-mean temperature difference between the SHX annulus side and ambient.

Increased component length may improve UA_{SHX}, but would also result in approximately proportional increases in heat loss. Thus, while there is some potential to increase SHX performance (ε_{SHX} = 0.62 – 0.73), it may be more productive to focus on improving component packaging and insulation to reduce $UA_{SHX,amb}$ rather than increasing SHX size and UA_{SHX}.

7.3.6 Solution subcooler

The solution subcooler yields CS temperature reductions of 9 – 11 K for the experimental cases, corresponding to 7.4 – 21.7 W of heat removal and heat transfer conductances of UA_{sub} = 1.5 – 2.1 W K^{-1}. This significantly reduces the required absorber heat rejection capacity, and lowers the absorber inlet solution vapor pressure by 53 – 118 kPa. These results suggest that the inclusion and fin enhancement of the solution subcooler section may improve overall DAR system performance.

7.3.7 Absorber

Measured absorber heat transfer rates vary over Q_{abs} = -6.3 – 12.4 ± 1 – 2 W for the main test matrix. These values are relatively low because of sensible heating of gas and solution in the absorber. As discussed in Section 7.2.8, negative absorber heat transfer rates occur in some cases due to sensible heating of the cool gas mixture inlet stream (15 – 23°C at the GHX outlet). If sensible solution and gas stream (at $m_{abs,G}$ and ξ_{abs}) loads are accounted for, then absorber latent heat transfer rates of 24 – 45 W are inferred. This range corresponds to absorption of 1.2 – 2.5 g min^{-1} of ammonia ($i_{LV,NH3}$ = 1140 kJ kg^{-1}), about twice the inferred evaporator evaporation rates. This suggests that additional phase change occurs in the GHX and connecting plumbing to the absorber gas inlet. However, it is difficult to perform more detailed analysis without precise auxiliary gas flow rate and concentration data and specification of the state of the potentially non-equilibrium two-phase inlet gas-refrigerant matrix.

The absorber and evaporator performances are tightly coupled. In the primary experimental test matrix, cooling rates indicate only 17 – 35% evaporation of refrigerant. Some additional evaporation occurs between the evaporator outlet and absorber inlet. The remaining refrigerant is assumed to enter the absorber in the liquid state, and mix with the

outlet solution stream. If the evaporation rate could be increased, the absorber inlet gas ammonia vapor pressure would rise, resulting in increased absorption. Similarly, if the absorption rate could be increased, the driving vapor pressure difference for evaporation in the evaporator would increase, resulting in greater cooling capacity. Given the relatively low cooling rates (corresponding to 17 – 35% of $m_{ref} \times i_{LV,NH3}$), the evaporator and absorber can be identified as the primary limitations on system performance. Future investigations should thus focus on refining these two components.

If inferred auxiliary gas inlet and outlet states are specified as model inputs (assuming $m_{abs,G,in} = m_{evap,G,out}$, $\xi_{abs,G,in} = \xi_{evap,G,out}$ and equal flow in all 10 tubes), then inferred film wetting factors range over WF = 0.21 – 0.61 (0.46 on average). This suggests that incomplete film wetting could be limiting absorber performance. Similarly, if WF is set to 1.0, then the number of active tubes (i.e., N_{tubes} such that $Q_{abs,mod} = Q_{abs,exp}$) ranges over 2.1 – 6.8 (4.7 average). The number of active tubes represents those that receive sufficient liquid from the inlet header. From this perspective, increasing the number of absorber tubes may not improve component performance if working fluid distribution is not also improved. The actual absorber performance is probably limited by a combination of these two factors. Poor liquid distribution may result in liquid rivulet ($WF < 1$) or no-flow ($WF = 0$) in some tubes.

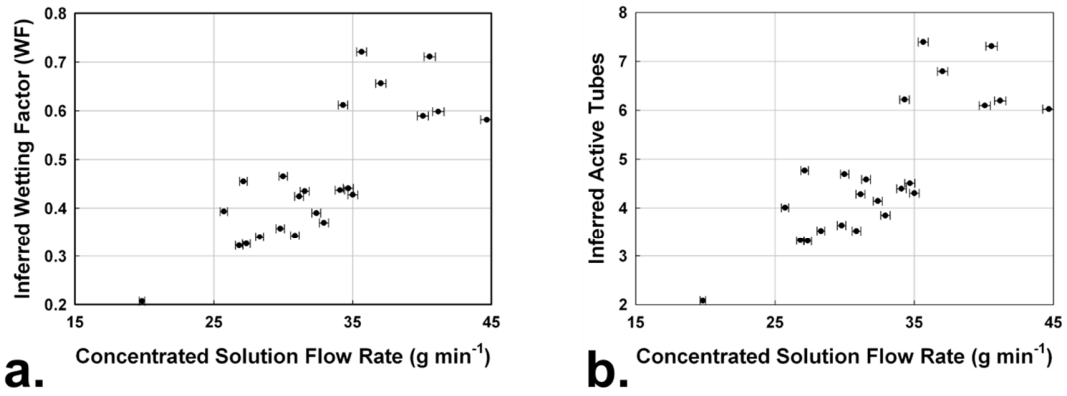

Figure 7.11 – Effect of concentrated solution flow rate on inferred (**a**) absorber film wetting factor (WF) and (**b**) number of active absorber tubes (N_{tubes})

Inferred *WF* and active tube counts are presented with measured CS flow rates in Figure 7.11. These plots indicate that component performance improves with increased solution flow rates. This supports the proposed explanations of limited absorber performance, as increased solution flow in each tube would improve liquid film wetting (WF). Similarly, increased solution flow to the upper header would improve liquid distribution between tubes (i.e., not only feeding liquid to tubes closest to the inlet port).

Gas-to-solution mass transfer conductances (UA^*_{abs}) for the main test matrix for low and high heating rates (Q_{BPG} = 90 W, 120 W) range over $0.7 – 1.0 \times 10^{-10}$ kg Pa^{-1} s^{-1} and $0.9 – 1.6 \times 10^{-10}$ kg Pa^{-1} s^{-1}, respectively. The values are about 30 – 60% of those predicted in the design model for uniform solution distribution and film wetting (2.4×10^{-10} kg Pa^{-1} s^{-1}, Section 6.2.5). System performance could potentially be improved by raising the BPG reservoir level to increase solution flow rates. However, in the current experimental system configuration, this would flood the lower absorber header,

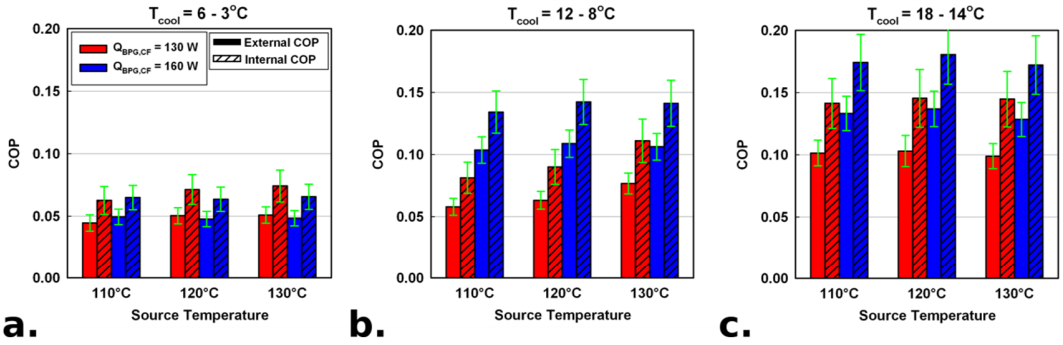

Figure 7.12 – Internal and external system COP values for the primary test matrix (p_{sys} ~1.15 MPa, ψ_{DS} ~ 0.52, T_{amb} ~ 25°C, U_{amb} = 0.2 - 0.8 m s^{-1}) for evaporator coupling fluid temperatures of $T_{evap,CF}$ = (**a**) 6 → 3°C, (**b**) 12 → 8°C, (**c**) 18 → 14°C

preventing gas circulation. This approach can be explored in future studies with minor modifications to the experimental facility.

7.4 Complete DAR System

External and internal system COP results from the main test matrix are presented in Figure 7.12. For these cases, the system pressure was p_{sys} ~1.15 MPa, dilute solution (DS) concentration was ψ_{DS} ~ 0.52, ambient air temperature was T_{amb} ~ 25°C, and the ambient air-flow velocity varied over U_{amb} = 0.2 – 0.8 m s^{-1} in the ventilation hood. Representative internal cooling COPs are: 0.06 ($T_{evap,CF}$ = 6 → 3°C), 0.14 (12 → 8°C), and 0.17 (18 → 14°C). The intermediate evaporator CF temperature results are comparable with those from another fully passive low-source-temperature DAR system reported in the literature (COP = 0.10 – 0.14 for $T_{evap,CF}$ = 9°C (Ben Ezzine *et al.*, 2010b)). However, it is difficult to make one-to-one comparisons between experimental DAR systems in general, because relative component sizes (and costs) and operating conditions can vary significantly.

System cooling capacity and COPs decrease at lower evaporator temperatures. This occurs because (1) the driving vapor pressure difference for evaporation decreases ($p_{sat,NH3}(T_{evap}) - P_{v,aux}$), and (2) the parasitic liquid refrigerant and auxiliary gas cooling load increases. A minimum evaporator outlet temperature of -2°C was measured with no evaporator CF circulation. This suggests that the proposed system can also be used for freezing at low COPs.

The system performance was found to be nearly independent of BPG CF inlet temperature (T_{source}), provided that a minimum temperature for stable operation was exceeded (~110°C). This result demonstrates the suitability of the proposed DAR system for solar- or waste-heat activated applications, for which source temperatures may vary during operation. It is difficult to isolate the effects of source temperature on system performance. At increased T_{source}, heat loss rates to the ambient increase slightly. Additionally, the solution flow rate in the BPG increases. This leads to greater sensible heating load and reduced refrigerant generation. However, increased solution flow was found to yield improved absorber performance in Section 7.3.7. Conversely, refrigerant generation rates increased with decreased T_{source}. This was found to improve evaporator performance in Section 7.3.3. These competing effects may cause the relatively low sensitivity of COP to T_{source}.

In this investigation, system performance was found to consistently decrease with lower input heating rates. This result may initially seem counter-intuitive, because thermal system efficiencies usually decrease with increasing load as the individual heat and mass exchangers become effectively "under-sized". However, in the proposed system, flow distribution and film wetting in the evaporator and absorber have been

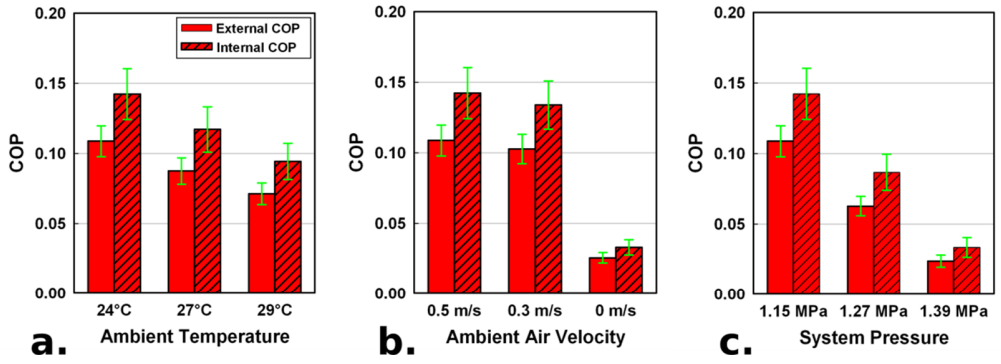

Figure 7.13 – Internal and external system COP values for the off-design condition test matrices ($T_{BPG,CF,in}$ = 120°C (130°C for elevated p_{sys} cases), $Q_{BPG,CF}$ = 160 W, and $T_{evap,CF}$ = 12 → 8°C) with (**a**) Varying ambient temperature, (**b**) Varying ambient air vertical velocity, (**c**) Varying system pressure

identified as key limitations on system performance. Based on results from Sections 7.3.3 and 7.3.7, reduced flow rates can severely inhibit operation of these components. For example, at very low solution flow rates, almost all DS may flow through the absorber tubes closest to the liquid inlet, yielding minimal interfacial area. Additionally, in the proposed system, heat loss rates primarily depend on operating temperatures and not heat transfer rates. Thus, relative heat loss rates from the solution plumbing and SHX and heat gain rates in the evaporator and GHX may be more significant at reduced system capacity. Similarly, the relative internal-to-external COP penalties are more severe at reduced thermal input rates ((COP_{int} – COP_{ext})/COP_{int} ~ 40% at $Q_{BPG,CF}$ ~ 120 W, and ~30% at $Q_{BPG,CF}$ = 160 W).

Results from the off-design-condition test matrices (varying T_{amb}, U_{amb}, p_{sys}) are presented in Figure 7.13. For these cases, $T_{BPG,CF,in}$ = 120°C (130°C for elevated p_{sys} cases), $Q_{BPG,CF}$ = 160 W, and $T_{evap,cf}$ = 12 → 8°C. System performance is found to

steadily decrease with increasing average ambient temperature (Figure 7.13a), with COP_{int} = 0.142 → 0.094 for T_{amb} = 24 → 29°C. This trend is commonly found in cooling systems, and is due to a combination of factors. Elevated ambient temperatures cause increased condenser outlet/evaporator refrigerant inlet temperatures (23.0, 24.2, 26.5°C for these cases). This leads to increased parasitic refrigerant cooling load. As noted in Section 7.2.3, condenser outlet temperatures were found to be slightly below measured average ambient temperatures in many cases, possibly due to fluctuations in air temperature or proximity to the cold evaporator core. Additionally, elevated ambient temperatures cause reduced driving temperature differences for solution subcooler and absorber heat rejection. For these three increasing T_{amb} cases, the subcooler outlet temperatures were 27.9, 32.9, and 33.8°C, respectively. Finally, the elevated system pressure at high T_{amb} resulted in reduced solution flow in the BPG (T_{amb} = 24°C: p_{sys} = 1.15 MPa and m_{CS} = 34.8 g min^{-1}, T_{amb} = 29°C: p_{sys} = 1.18 MPa and m_{CS} = 30.5 g min^{-1}). This could cause reduced absorber performance.

Reduced ambient air-velocity (Figure 7.13b) was found to have a minor effect on system performance from U_{amb} = 0.2 – 0.8 m s^{-1} to 0 – 0.4 m s^{-1} (COP_{int} = 0.142 → 0.134). However, further reduction to negligible ambient air flow severely reduced performance (COP_{int} = 0.033). This behavior is consistent with results from the condenser model, which predicts low threshold U_{amb} values (~0.1 – 0.2 m s^{-1}) below which condensation will be incomplete. Reduced air flow also caused increased ambient temperatures (24.0, 25.5, 26.1°C) for these cases because the experimental facility was operated inside a closed ventilation hood. As discussed previously, the resulting elevation in ambient temperature further reduces system performance.

As discussed in Section 6.2.3, increased system pressure may be required to ensure complete condensation if ambient cooling is limited. The effect of system pressure (p_{sys}) on performance is presented in Figure 7.13c. Elevated p_{sys} is found to sharply reduce COPs, with: COP_{int}(1.15 MPa) = 0.142, COP_{int}(1.27 MPa) = 0.087, and COP_{int}(1.39 MPa) = 0.034. The system charge was not varied during this parametric study. Thus, solution saturation temperatures increased with p_{sys}. For these three cases, the BPG solution outlet temperature increased from 89.1 → 98.2 → 106.3°C. This resulted in increased sensible heating load, increased heat loss rates (greater temperature difference to the ambient), and reduced solution pumping rates because $T_{BPG,CF,in}$ was fixed at 130°C (V_{CS} = 45.4 → 25.0 → 18.9 ml min^{-1}). These factors may have all contributed to reduced system performance. Elevated system pressure increases the driving vapor pressure difference for absorption ($p_{v,abs,G} - p_{v,NH3\text{-}NaSCN}(T_{abs,L}, \psi_{abs,L})$), but also reduces the driving vapor pressure for evaporation ($p_{sat,NH3}(T_{evap,L}) - p_{v,evap,G}$). Thus, the evaporator and absorber effects may compensate for each other.

The full DAR cycle model proposed in Section 6.3 is assessed with experimental results from the main and elevated ambient temperature test matrices. For this analysis, the following measured parameters are provided as model inputs: BPG heat input (Q_{BPG}), dilute solution concentration (ψ_{DS}), system pressure (p_{sys}), average cooling delivery temperature ($T_{cool} = (T_{evap,CF,in} + T_{evap,CF,out})/2$), average ambient temperature (T_{amb}), CS flow rate (m_{CS}), and auxiliary gas flow rate (m_{aux}).The solution and auxiliary gas flow rates could be predicted as part of the cycle analysis using proposed sub-models. However, these quantities are very sensitive to system configuration and operating conditions (e.g., solution reservoir level, minor losses in gas-loop plumbing). Therefore,

Table 7.2 – Closure parameters for full system model

Parameter	Definition	Value
CAT_{cond}	$T_{cond,out} - T_{amb}$	1 K
CAT_{evap}	$T_{cool} - T_{evap,L,out}$	2 K
UA^*_{evap}	m_{evap} / $LMPD_{evap}$	4.0×10^{-11} kg Pa^{-1} s^{-1} (Q_{BPG} = 90 W) 5.5×10^{-11} kg Pa^{-1} s^{-1} (Q_{BPG} = 120 W)
$CAT_{evap,G,L}$	$T_{evap,G,out} - T_{evap,L,out}$	15 K (T_{cool} = 4.5°C) 12 K (T_{cool} = 10.0°C) 9 K (T_{cool} = 16.0°C)
UA_{GHX}	Q_{GHX} / $LMTD_{GHX}$	2.0 W K^{-1}
UA_{SHX}	Q_{SHX} / $LMTD_{SHX}$	4.0 W K^{-1}
$UA_{SHX,amb}$	$Q_{SHX,loss}$ / $LMTD_{SHX,amb}$	0.7 W K^{-1}
UA_{sub}	Q_{sub} / $LMTD_{sub}$	1.8 W K^{-1}
$CAT_{abs,amb}$	$T_{abs,G,out} - T_{amb}$ $T_{abs,L,out} - T_{amb}$	5 K
UA^*_{abs}	m_{abs} / $LMPD_{abs}$	0.85×10^{-10} kg Pa^{-1} s^{-1} (Q_{BPG} = 90 W) 1.30×10^{-10} kg Pa^{-1} s^{-1} (Q_{BPG} = 120 W)

experimental values were employed for m_{CS} and m_{aux}. Closure parameters are selected based on results from the individual component analyses presented in Section 7.3 (Table 7.2). Absorber and evaporator mass transfer conductances (UA^*_{evap}, UA^*_{abs}) are specified based on the input heating rate (Q_{BPG}) due to the high sensitivities to refrigerant and solution flow rates, respectively. Similarly, the evaporator outlet gas-to-liquid refrigerant approach temperature ($CAT_{evap,G,L}$) is specified as a function of the cooling delivery temperature (T_{cool}).

Predicted and measured system COPs are compared for the main and elevated ambient temperature test matrices in Figure 7.14. An average absolute deviation of 21% is found between predicted and experimental COP (and Q_{evap}) values. Two of the low evaporator temperature case COP values are significantly under-predicted (52%, 62% error). However, these relatively large COP errors only correspond to ~5 W errors in

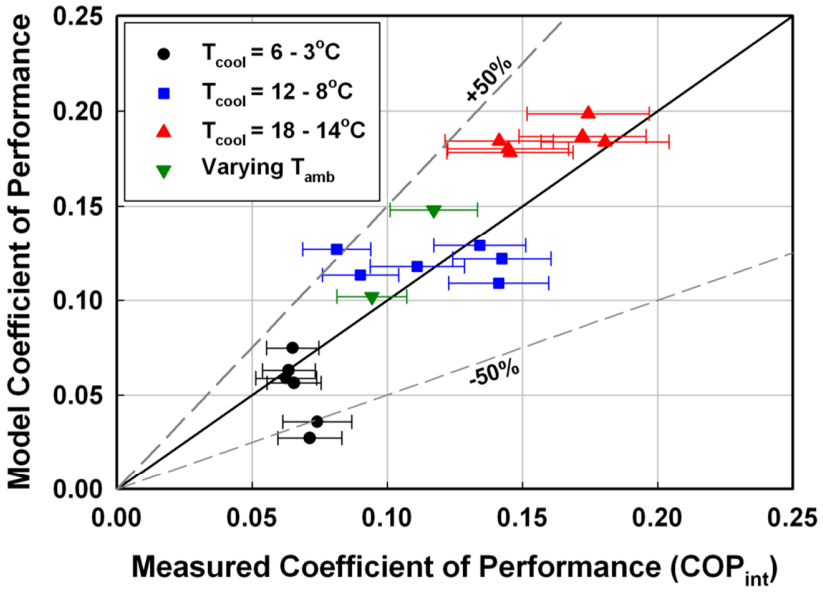

Figure 7.14 – Comparison of predicted and measured system internal COPs for the main test matrix and varying ambient temperature test matrix

Q_{evap}. These results demonstrate general global validation of the proposed cycle model (e.g. for COP, Q_{evap}).

Detailed model and experimental results are compared in Figure 7.15 for a representative low-cooling-temperature case with operating conditions summarized in Table 7.3. For this case, measured and predicted internal COP values are 0.064 (Q_{evap} = 7.6 W) and 0.063 (Q_{evap} = 7.5 W), respectively. Most measured and predicted temperature and component heat transfer rates agree to within 4 K and 15%, respectively. The measured evaporator working fluid outlet temperature is 6.8°C. This is between the predicted liquid refrigerant and gas mixture outlet values of 2.4 and 17.4°C, respectively. However, it is difficult to compare these temperature values more rigorously without knowing the precise two-phase flow pattern over the thermocouple probe. The measured GHX cold stream outlet temperature is lower than the predicted value (15.8°C vs.

Table 7.3 – Operating conditions for representative low-cooling-temperature case

Parameter	Value
T_{cool}	4.5°C
Q_{BPG}	118.9 W
ψ_{DS}	0.534
m_{CS}	34.1 g min^{-1}
m_{aux}	38.6 g min^{-1}
T_{amb}	25.6°C
p_{sys}	1.14 MPa

24.9°C). This could be due to non-equilibrium two-phase flow over the outlet thermocouple or a small amount of post-evaporator refrigerant evaporation, which are not considered in the cycle model. As a result, the measured GHX heat transfer rate is 6 W higher than predicted with the model. The potential additional evaporation could cause the greater measured absorber heat rejection rate (7.9 W vs. -0.1 W). The predicted SHX inlet temperature is higher than the measured value (89.8°C vs. 81.7°C). This is due to a small amount of heat loss (10 W) from the connective plumbing between the BPG CS outlet and SHX CS inlet, which is not considered in the model. The model predicts a SHX heat recovery rate 9 W higher than was measured for the same reason.

Overall, this analysis demonstrates that the proposed cycle model effectively characterizes the overall behavior of the experimental DAR system. Additional sub-models could be incorporated to account for the discrepancies highlighted here. However, the current cycle model already requires many closure parameters to account for multicomponent mixture effects (NH_3-NaSCN-He), coupled inter-phase heat and mass transfer (evaporator and absorber), and non-equilibrium two-phase flow (evaporator outlet). The potential for increased accuracy should thus be weighed against overall model complexity and robustness.

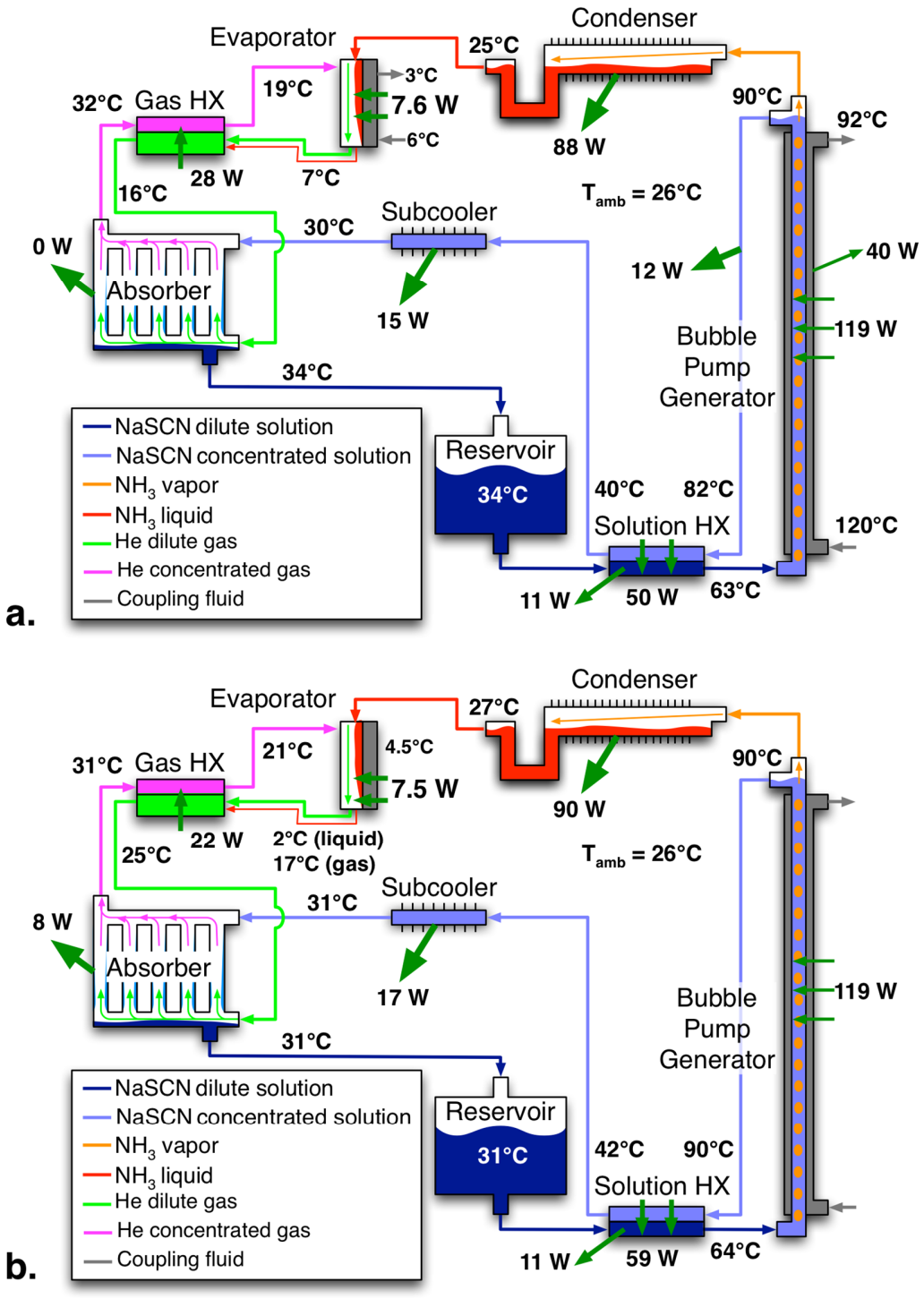

Figure 7.15 – Comparison of (**a**) experimental and (**b**) model results for the representative low-cooling-temperature conditions

7.5 Discussion

In this investigation, a complete passively cooled low-source-temperature (110 – 130°C) DAR system was developed. Cooling was achieved at temperature ranges suitable for refrigeration ($T_{evap,CF}$ = 6 → 3°C, COP_{int} ~ 0.06) and air-conditioning (12 → 8°C, COP_{int} ~ 0.14; 18 → 14°C, COP_{int} ~ 0.17). The DAR system was also evaluated at off-design conditions. A 34% reduction in internal system COP was measured for T_{amb} = 24 → 29°C. Minimal performance penalties were found with reduced ambient air velocity from 0.2 – 0.8 → 0.0 – 0.4 m s^{-1}. However, COP sharply reduced for U_{amb} → 0, indicating that some minimal ambient air circulation is necessary for operation. At such limited external cooling conditions, elevated system pressures may be necessary for condenser operation. However, increased source temperatures are also required for high p_{sys}. Results from this investigation demonstrated reduced COPs at high system pressures. In future studies, it may be possible to mitigate such penalties by reducing NaSCN concentration, thus maintaining solution saturation temperatures and required source temperatures near target values (~90°C and ~110°C, respectively).

The system design was based on detailed component-level models formulated in Chapter 6. BPG measurements generally confirmed sub-model validity (average S_r error = 0.03 (~11%)). The condenser delivered complete refrigeration condensation in all cases, as predicted with the design model for low ambient air velocities (U_{amb} ~0.1 – 0.2 m s^{-1}). However, more rigorous validation of the component model was not possible with available measurements (inlet and outlet temperatures and refrigerant flow rate). Measured evaporator cooling rates were supplied as model inputs, and results indicate

only 17 – 35% evaporation of generated refrigerant. This corresponds to a low average liquid film wetting factor (*WF*) of 24%.

Absorber inlet and outlet gas states were supplied as model inputs, and effective wetting factors (*WF* = 0.46 average) and numbers of active tubes (N_{tubes} = 4.7) were determined. Absorber mass transfer conductances were significantly lower than those inferred for uniform fluid distribution and film wetting (experimental: UA^*_{abs} = 0.7 – 1.6 × 10^{-10} kg Pa^{-1} s^{-1} vs. uniform model: 2.4 × 10^{-10} kg Pa^{-1} s^{-1}). Component UA* improved with solution flow rate, indicating that it may be possible to improve overall system performance by increasing solution flow rates (increasing S_r).

GHX temperature measurements were employed to infer auxiliary gas circulation rates (m_{aux}) and concentrations (ξ_{aux}). Overall, the component yielded large gas stream temperature reductions (7.6 – 14.5 K). Measured SHX overall conductance values were UA_{SHX} ~ 4.0 W K^{-1}, resulting in 32 – 56 W of heat recovery. However, 8 – 18 W of heat were lost from the component at experimental conditions. Solution subcooler conductances were measured to be UA_{sub} ~ 1.8 W K^{-1}, corresponding to concentrated solution temperature reductions of ~10 K.

Component-level results from this experimental study were employed to refine cycle-level model closure parameters. Measured and model COP results generally agreed, with an average absolute deviation of 21% for the primary test matrix and elevated ambient temperature cases. This demonstrates general applicability of the proposed system-level model, provided that closure parameters are appropriate.

In this investigation, relatively low cooling COPs were measured and predicted for the studied DAR system (COP_{int} ~ 0.06 for refrigeration) compared to other technologies, such as vapor compression (COP ~ 2 – 4) and two-pressure absorption refrigeration (~0.5 – 0.8 (Herold *et al.*, 1996)). The low COP can be expected, to some extent, for passive operation with only relatively low exergy thermal input. However, results from this investigation indicate that the system performance is primarily *transport limited*, rather than being limited by fundamental thermodynamic requirements. For the representative model case presented in Figure 7.15b, the predicted cooling capacity is 7.5 W corresponding to a COP of 0.063 and evaporation of only 25% of generated refrigerant. If the evaporator and absorber mass transfer conductances are both increased five-fold to 2.8×10^{-10} and 6.5×10^{-10} kg s^{-1} Pa^{-1}, respectively, with all other input parameters held fixed, then the predicted cooling capacity increases approximately ten-fold to 70.5 W. This corresponds to almost complete refrigerant evaporation (99.5%). The resulting COP (0.593) is comparable to that of two-pressure absorption systems. Thus, there is the potential for major efficiency advances for low-source-temperature DAR technology, but significant engineering challenges must be overcome.

Uncertainties in system operating conditions and fluid properties were significant challenges in this investigation. System instrumentation included solution flow meters, pressure transducers, sight glasses, and thermocouples. However, no instruments were commercially available to measure the auxiliary gas circulation rate. Auxiliary gas concentration could be measured with techniques such as gas-chromatography, but this would significantly increase experimental system costs. In future investigations, special-purpose thermal anemometers and time-of-flight ultrasonic concentration measurement

instruments could be employed to determine these quantities. Such detailed information will enable improved assessment of gas-loop components and models.

Modeling results indicate that the refrigerant and auxiliary gas mixture flowing from the evaporator to the absorber was two-phase and far from thermal equilibrium ($T_G - T_L \sim$ 15 K in some cases). It was therefore difficult to interpret temperature measurements of this stream. In future studies, it may be possible to install multiple thermocouples at different cross-sectional locations in this flow path to collect distinct liquid and gas phase measurements.

Limited transport property data are available for the NH_3-NaSCN solution. No surface tension data have been reported and viscosity measurements are not available for the high temperature conditions in the bubble-pump generator. Thus, additional investigations are needed to determine fluid properties.

Another challenge arose in prediction of coupled natural convection, forced convection, and radiation heat transfer for the corrugated longitudinal vertical fins employed in the solution subcooler and absorber. This heat transfer enhancement geometry may be advantageous for a variety of passively cooled technologies, but has not been well characterized in the literature. Analyses based on canonical heat transfer configurations (e.g., vertical cylinder, parallel plates) led to substantially different heat transfer predictions (see Section 6.2.5). Detailed studies of this heat transfer configuration or other enhancement techniques applicable to DAR systems would be valuable.

7.6 Conclusions

A complete low-source-temperature (110 – 130°C) passively cooled diffusion absorption refrigeration (DAR) system was developed. A new working fluid mixture was employed: NH_3-NaSCN-He. Cooling was achieved at temperature ranges suitable for refrigeration ($T_{evap,CF}$ = 6 → 3C, COP_{int} ~ 0.06) and air-conditioning (12 → 8°C, COP_{int} ~ 0.14; 18 → 14°C, COP_{int} ~ 0.17). This demonstrates the potential of low-source-temperature fully passive DAR operation at refrigeration conditions.

Detailed analyses of individual system components were performed. Results were applied to assess models proposed in Chapter 6, and general agreement was found for the bubble-pump generator and condenser. Component models were applied to assess the evaporator and absorber, and fluid distribution was identified as a potential limiting factor for system performance. Alternative instrumentation techniques could be developed to enable more rigorous analysis of the condenser and gas-loop components.

The refrigeration system achieved stable performance at target operating conditions. Elevated cooling temperature COP was comparable to that reported for another passive low-source-temperature DAR system reported in the literature (Ben Ezzine *et al.*, 2010b). The present investigation highlighted a number of pathways to improve system performance.

- Heat loss from the BPG, SHX, and connective plumbing significantly reduced system performance. On average, internal COP values were ~30% higher than external COP values. It may be possible to achieve significant performance gains by improving system packaging to reduce heat loss from warm components (BPG and SHX) and heat gain to cool components (evaporator and GHX).

- Absorber performance was found to increase significantly with solution flow rate. By adjusting component sizes and configuration, the solution reservoir level (S_r) could be raised to increase solution flow rate.
- Results from this study indicate that the evaporator was under-sized. It may be possible to improve DAR performance by increasing the evaporator length, and reducing that of the GHX.
- Liquid distribution and film-wetting in the evaporator and absorber were identified as potential factors limiting system performance, especially at low flow rates. By refining fluid distribution techniques, improved system performance could be obtained over a wide range of operating conditions.

Thus, while DAR technology has existed for approximately 90 years, there is still potential for new low-source-temperature implementations and substantial efficiency gains.

CHAPTER 8. CONCLUSIONS AND RECOMMENDATIONS

8.1 Overview

Detailed investigations of diffusion absorption refrigeration (DAR) technology from the underlying multicomponent two-phase flow transport phenomena, to component design and analysis, and to full system integration were performed. A comprehensive description was developed for the Taylor flow pattern in the intermediate Bond number regime. This model was validated with detailed experimental (air-water) and volume-of-fluid (VOF) based simulation data. This formulation was extended to describe a new distributed-heated bubble-pump generator (BPG) design. The resulting model was validated with measurements of steam-water and ammonia vapor-ammonia-sodium thiocyante solution flows. A new, mechanistically consistent, geometric-interface-reconstruction-free, phase-change simulation model was developed and validated. This formulation was applied to assess the distributed heated BPG model data in detail. This BPG configuration was integrated with novel absorber and other component designs to develop a complete low-source-temperature (T_{source} = 110 – 130°C) diffusion absorption refrigeration system with a new working fluid mixture (NH_3-NaSCN-He). Detailed design models were formulated for key system components and processes (e.g., natural buoyancy-driven circulation). These models were assessed with data from DAR system operation. A complete DAR cycle-level model was formulated based on these component-level analyses, and was experimentally validated over a range of operating conditions (varying Q_{BPG}, T_{source}, T_{cool}, T_{amb}). This effort resulted in a low-source-temperature ($T_{source} \leq 130$°C), fully thermally activated passive DAR system that can deliver cooling at temperatures suitable for refrigeration. Key results and

recommendations for future work are presented in the following sections for each stage of this investigation.

8.2 Taylor Flow in the Intermediate Bond Number Regime

8.2.1 Summary

The Taylor flow two-phase flow pattern can occur over a large span of channel diameters (μms to cms), flow rates, and fluid properties (water to heavy oils). This flow regime has been extensively studied at the large Bond number limit ($Bo = (\rho_L - \rho_G)\, g\, D^2 / \sigma > 40$) (Fernandes *et al.*, 1983; Sylvester, 1987; Taitel and Barnea, 1990) and small Bond number/capillary limit ($Bo < 5$) (Angeli and Gavriilidis, 2008; Garimella, 2004; Liu *et al.*, 2005; Thulasidas *et al.*, 1995). However, Taylor flow has not been well characterized in the transitional, intermediate Bond number regime ($5 < Bo < 40$), which is particularly applicable to bubble pumps. Additional classes of forces and phenomena may be considered with flows at either limit as the bases.

In Chapter 2, experimental air-water studies were reported for vertical upward Taylor flows in the intermediate Bond number regime. Measurements spanned the range of $4.9 < Bo < 12.2$, $480 < Re_j < 4460$ ($Re_j = \rho_L j D/\mu_L$), $0.0008 < Ca < 0.009$ ($Ca = \mu_L j/\sigma$), $1500 < N_f < 3000$ ($N_f = (\rho_L g D^3/\mu_L^2)^{1/2}$). High-speed photography was employed to measure flow parameters including Taylor bubble velocity, liquid film thickness, void fraction, and Taylor bubble and liquid slug length. A new universal model was validated for the Taylor bubble rise velocity in flowing liquids. Additionally, a correlation was developed for Taylor bubble lengths in intermediate bond number flows. Laminar falling-film results were demonstrated to apply for liquid films around Taylor bubbles in intermediate Bond number flows. An analytical unit-cell model was formulated, and demonstrated to

accurately predict void fraction and average liquid slug length. This effort resulted in a complete kinematic description of intermediate Bond number Taylor flows.

In Chapter 3, direct VOF simulations were employed to independently validate hydrodynamic closure models for Taylor Flow in the intermediate Bond number regime. A number of flow models have been proposed for similar conditions (de Cachard and Delhaye, 1996; Delano, 1998; Reinemann *et al.*, 1990), but individual hydrodynamic closure models have not been assessed. Many simulations of Taylor flow have been performed (Akbar and Ghiaasiaan, 2006; Bugg *et al.*, 1998; Irandoust and Andersson, 1989; Kang *et al.*, 2010; Kawaji *et al.*, 1997; Marschall *et al.*, 2014; Taha and Cui, 2006). However, most have focused on kinematic flow measurements. In this study, special-purpose VOF formulations were developed to study Taylor flows. Single unit-cell simulations were performed for $6.6 < (L_b + L_s) / D < 15$, $0.540 < \beta < 0.650$, $5 < \mathrm{Bo} < 20$, $250 < N_f < 1000$, and $20 < \mathrm{Re}_j < 1500$. Results from this study demonstrated best agreement with an analytical model for bubble-region frictional pressure gradient (AAD = 1.9%), the fully developed channel flow correlation of Churchill (1977) for slug-region frictional pressure drop (AAD = 28%), and the flow transition pressure loss model of Kreutzer *et al.* (2005) (AAD = 53%). Full channel-length developing Taylor flow simulations were also performed, but results were somewhat less conclusive. These hydrodynamic sub-model results (with a modified transition pressure loss model) were integrated with kinematic flow model results from Chapter 2 to formulate a comprehensive description of intermediate Bond number Taylor flows. The resulting overall model predicted bubble-pump liquid flow rates more accurately ($\mathrm{AAD}_{\log} = 0.10$)

for conditions considered here than other Taylor flow models from the literature (AAD_{log} = 0.21 – 0.48 (de Cachard and Delhaye, 1996; Liu *et al.*, 2005; Sylvester, 1987)).

8.2.2 Recommendations for future research

- Prediction of entrance lengths for intermediate scale Taylor flows was identified as an open research challenge. This is particularly relevant for measurement and prediction of bubble and slug lengths, which can significantly affect the frequency and flow-transition pressure losses. Average bubble and slug lengths increase in the flow direction, up to stable values, as trailing bubbles merge with leading ones (Dukler *et al.*, 1985). Taitel *et al.* (1980) proposed an entrance-length correlation for large Bo turbulent flows, but applicability to other flow conditions is unclear. Future investigations focusing on Taylor-flow entrance lengths for different Bo and Re_j ranges are therefore warranted.
- A capillary-to-large scale transitional model was proposed for predicting Taylor bubble rise velocity (Equation 2.23). A similar approach could assist in developing a universal Taylor bubble length model. However, insufficient data were available in the literature. A distinct bubble-length intermittency phenomenon was observed for air-water flow in the D = 6.0 mm test sections (Bo = 4.9 mm, see Section 2.3.1), which corresponds, approximately, to the capillary-to-intermediate scale transition. At this flow condition, successive rising short bubbles merged periodically, resulting in long, high velocity bubbles. This effect is representative of the significant variations in Taylor flow behavior that can occur at different scales. Future investigations focusing on the transition from the capillary-to-large scale limits would thus be of great value. The governing regime scale is primarily a function of Bond

number, which only depends on tube diameter and fluid properties. It is more difficult to perform experiments over a continuous range of Bond numbers than for other parameters, which can be varied simply with flow rate. This is thus an attractive avenue for simulation-based studies.

- Higher resolution full-channel-length simulations could significantly improve understanding of developing Taylor flow hydrodynamics in the intermediate Bond number regime. However, even for 2D axisymmetric studies, computational costs scale rapidly as $O(j\Delta r^{-3})$. Advances in two-phase flow simulation efficiency may be needed.
- Further investigations are needed to characterize and formulate modeling approaches for developing flow effects in short liquid slugs in the intermediate Bond number regime. The challenge arises from the complex annular inlet pattern from liquid film to liquid slug regions, which is affected by Taylor bubble tail profiles (e.g., convex, flat, or skirted tails, see Figure 3.9) and wake region flow patterns (see Figure 3.12).
- A number of mechanisms have been proposed for Taylor flow transition pressure losses, including capillary forces (Bretherton, 1961), combined capillary and inertial effects (Kreutzer *et al.*, 2005), liquid-film flow reversal (Dukler and Hubbard, 1975), and liquid-film flow stagnation (Fukano *et al.*, 1989). An empirical model was proposed to extend the applicability of the Kreutzer *et al.* (2005) model to high mass flux conditions (Equations 3.44 – 3.45). This model performed well in this investigation, but has not been independently validated. Future investigations to clarify the mechanisms of transition pressure losses are needed to formulate a robust and universal approach for predicting Δp_{trans}.

- Intermediate Bond number Taylor flows can occur over a wide range of laminar-to-turbulent flow conditions. Additionally, for many Taylor flows in the intermediate Bond number regime, turbulent conditions may only arise in liquid slug regions. Intermittency transport models have been proposed for single-phase simulations with localized turbulence (Menter *et al.*, 2004), but formulations for two-phase flows are limited. It would be more appropriate to apply LES or DNS techniques for these conditions. Such approaches require 3D simulations, and would necessitate resolution of greater ranges of spatial and temporal scales. Thus, it may be valuable to perform high-resolution 3D simulations of intermediate Bond number Taylor flows.

8.3 Distributed Heated Bubble-Pump Generators

8.3.1 Summary

In the conventional "spot-heated" BPG design, all input heat is transferred through a small region near the base of the component. This enables high pumping efficiencies and relatively simple analysis for the major portion of the BPG length, but necessitates high source temperatures. Recently alternate distributed-heated BPG designs that can operate at significantly lower source temperatures have been proposed (Benhimidene *et al.*, 2011; Dammak *et al.*, 2010; Jakob *et al.*, 2008). However, experimentally validated models have not yet been reported for these configurations. In Chapter 4, detailed experimental investigations for a distributed coupling-fluid (CF) heated BPG with ambient pressure steam-water working fluid were described. Measurements were collected for a range of operating conditions: T_{source} = 110 – 130°C, Q_{BPG} = 25 – 200 W, S_r = 0.2 – 0.4. This configuration can enable operation of single-pressure refrigeration systems using low temperature thermal sources – as low as 11°C above T_{sat} in this study.

A segmented model of this configuration was formulated, accounting for the transitions from bubbly-to-Taylor flow and subcooled-to-saturated flow boiling. This model integrated the comprehensive intermediate Bond number Taylor flow formulation developed in Chapters 2 and 3. Model validation was demonstrated for these conditions, with water and steam flow rates predicted to within 25% of measured values for 90% and 91% of cases, respectively. In Section 6.2.2, this model was extended to support flow-boiling of zeotropic mixtures and account for heat loss from the CF channel. This model was applied to design a BPG, which was installed in an experimental DAR system with NH_3-NaSCN-He working fluids (Section 7.3.1). For specified solution flow rates, predicted S_r values agreed with measurements, with an average absolute deviation of 11%. However, overall model agreement was somewhat poorer than for the steam-water cases. This may be due, in part, to uncertainty in working fluid transport properties (μ_L, k_L, σ).

8.3.2 Recommendations for future research

- As discussed previously, improved characterization of Taylor bubble length and transition pressure losses in the intermediate Bond number region could improve BPG model performance. Additionally, the effects of boiling phase change on the Taylor flow pattern are unknown, and could be significant (e.g., disruption of the liquid film by nucleating bubbles, increased film waviness due to evaporating vapor flux, bubbles in the liquid slugs at low Bond numbers).
- With few exceptions (e.g., NH_3-H_2O, H_2O-LiBr), transport properties of promising absorption system working fluid sets are poorly characterized. For the conditions encountered in the experimental DAR BPG with NH_3-NaSCN working fluid, limited

information is available for liquid viscosity (μ_L) and thermal conductivity (k_L), and no surface tension data (σ) have been measured. Similarly, critical pressures are not known for this mixture, and had to be estimated (employed in the nucleate boiling component of the flow boiling model of Liu and Winterton (1991)). As a result, there are large uncertainties in BPG and other component model predictions. For example, at specified submergence ratios (S_r), the proposed BPG model predicted liquid pumping rates ~50% higher than were measured. These model results were obtained using surface tension data for NH_3-$LiNO_3$ (a similar mixture) from Zacarias *et al.* (2013). For the representative BPG case described in Section 6.2.2, the estimated surface tension value was 0.022 kg s^{-2} (3.0 times the pure ammonia value of 0.007 kg s^{-2}). If a more conservative value of 0.014 kg s^{-2} is assumed, then the predicted liquid flow rate is 37.0 ml min^{-1}, which is comparable to measured values. Given the high model sensitivity to transport properties, additional measurements of the working fluid properties and boiling characteristics are warranted.

- Heat loss from the BPG integrated into the experimental DAR system was identified as a significant limitation on system performance (25 – 30% COP penalty). The relative effect of heat loss could be reduced in future designs by increasing component heat transfer intensity (Q_{BPG}/BPG volume). More compact designs for other components could also enable shorter BPGs (Q_{loss} ~ L_{BPG}). In future system packaging efforts, relatively hot components, such as the BPG, SHX, and reservoir could be integrated to reduce exterior area and heat loss from plumbing. Specifically designed thermal isolation from the colder components would also reduce parasitic heat exchange.

8.4 Phase-Change Flow Simulations

Agreement was found for global quantities (e.g., Q_{BPG}, V_L, V_V) between BPG experimental results and segmented model predictions. However, local quantities (e.g., α, U_b, ∇p_d) could not be evaluated directly. To assess these models in more detail, two-phase flow phase change simulations were performed for a representative condition of the BPG design proposed in Chapter 4 (with increased μ_L and ρ_V).

While relatively mature simulation techniques have been developed to study adiabatic two-phase flows, the field of thermally driven phase-change simulations is still in its infancy. Rate parameter and analytical solution/correlation based phase change models have been adopted in many studies because of the relative ease of implementation (Jeon *et al.*, 2009; Kunkelman and Stephan, 2009; Yang *et al.*, 2008). However, general applicability of more empirical formulations has been limited. Interfacial transport based approaches resolve the governing mechanisms of phase change, and rigorous validation has been demonstrated for some (Esmaeeli and Tryggvason, 2004a, b; Juric and Tryggvason, 1998; Subramaniam and Garimella, 2009). However, such models have relied on geometric interface reconstruction or direct tracking and advection of the interface, which are both computationally expensive and difficult to perform on unstructured meshes. Therefore, a new interface reconstruction-free phase-change formulation was developed in Chapter 4 that is suitable for VOF-based simulations. This approach was demonstrated to achieve mesh independence, and agreement was found with established results for horizontal film condensation and evaporation and smooth and wavy falling-film condensation.

This formulation was applied to the simulation of the saturated flow-boiling portion of the distributed CF-heated BPG. If discrepancies in evaporative heat transfer coefficients and Taylor bubble rise velocities are accounted for, close agreement was found between segmented model and simulation predictions for heat transfer rates (Q_{BPG}), axial phase flow rate profiles (V_L, V_V), void fraction (α), liquid film thickness (δ_f), Taylor bubble and liquid slug lengths (L_b, L_s, β), and hydrodynamic pressure gradient (∇p_d). Taylor bubble wake and thermally developing flow effects were identified as possible causes for the high convective evaporation coefficient values found in the simulation case. A simple convective flow evaporation model was proposed that accounts for the Taylor bubble wake effect as a "reset" of the thermal boundary layer. This model agreed well with simulation results for convective heat transfer coefficients. Finite bubble acceleration rate could explain the relatively low Taylor bubble rise velocities found for the simulation case. Overall, results from this study provided confirmation of the segmented CF-heated BPG model formulated in Chapter 4. Potential approaches were discussed for simulation of target working fluids (e.g., NH_3-NaSCN-He) and operating conditions.

8.4.1 Recommendations for future research

- Some discrepancies were found between simulation results and experimentally derived falling-film condensation heat transfer correlations (<11% for q_{wall}). A number of potential causes were suggested, including 3D effects and spurious currents from the surface tension model. Further investigation of these phenomena could enable development of first-principles based models for wavy-film phase-

change heat transfer. In particular, the effects of surface tension on heat transfer could be assessed, which have been neglected in many previous models.

- For the BPG conditions considered in Chapter 5, simulation results indicated much higher convective flow evaporation coefficients than predicted with representative models from the literature (Liu and Winterton, 1991; Wadekar and Kenning, 1990). A new developing slug flow heat transfer model was proposed that agreed well with simulation data. However, model assessment at other operating conditions is needed, particularly for turbulent flows.
- In flows with distributed phase-change heat transfer, local phase velocities (e.g., U_b) may deviate from fully developed adiabatic values due to finite fluid acceleration rates. This could lead to significant discrepancies in overall two-phase flow model predictions (Section 5.4.6). Additional investigation of such effects is warranted.
- The BPG simulation only accounts for convective evaporation in the saturated flow portion of the domain. It would be valuable to simulate the subcooled boiling portion as well. However, nucleate boiling is an important mode of heat transfer in the subcooled-boiling region. This could be performed with the current formulation at great computational cost by resolving individual bubble nucleation sites (relevant preliminary results can be seen in Figure 8.1). Alternatively, a combined one-/two-fluid simulation formulation could be employed in which small nucleating bubbles are modeled with a subgrid-scale approach (Lahey Jr. and Drew, 2001; Ẑun *et al.*, 1993) until coalescence to grid-scale bubbles occurs.

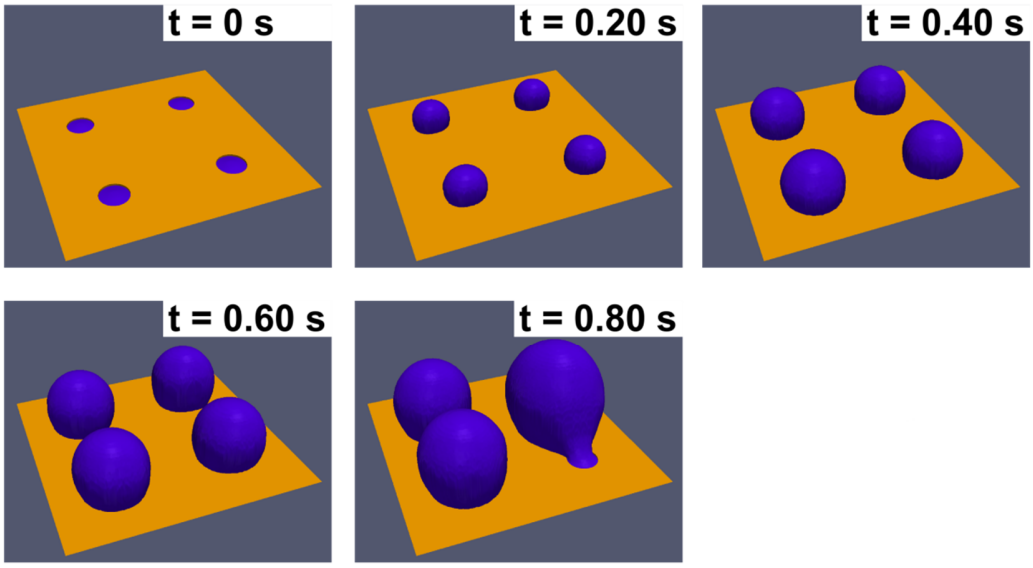

Figure 8.1 – Representative simulation results of nucleate boiling on a heated surface using the phase-change model formulated in Chapter 5

8.5 Low-Source-Temperature Passive Diffusion Absorption Refrigeration

8.5.1 Overview

Diffusion absorption refrigeration (DAR) technology has many promising applications in off-grid settings, such as solar-thermal refrigeration of vaccines in developing countries or stationary generator waste heat recovery at forward operating military bases. However, conventional DAR systems require high source temperatures (150 – 200°C (Jakob *et al.*, 2008; Srikhirin *et al.*, 2001)). Recently, a number of low-source-temperature DAR systems have been demonstrated (Ben Ezzine *et al.*, 2010b; Jakob *et al.*, 2008; Wang, 2012). However, all have required forced liquid flow for absorber and condenser cooling, employed mechanically pumped internal fluid circulation, or operated at elevated evaporator temperatures that are not suitable for refrigeration. In Chapter 6, a design was proposed for a low-source-temperature ($T_{source} \leq$ 130°C) fully passive DAR system that delivers cooling at temperatures suitable for

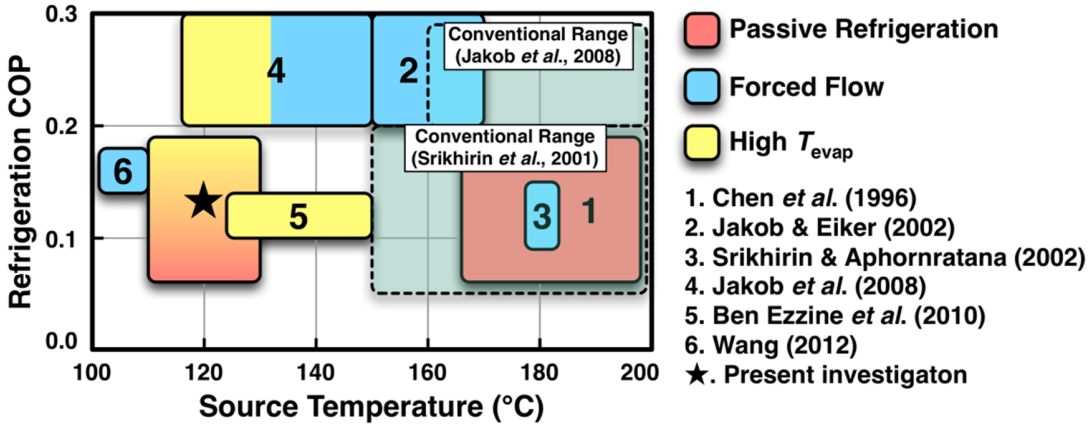

Figure 8.2 – Map of demonstrated diffusion absorption refrigeration cooling COPs including results from present investigation (high T_{evap} at high COP)

refrigeration ($T_{cool} \lesssim 5$°C). This design can operate at low source temperatures due to: (1) the enhanced distributed CF heated BPG design, (2) an enhanced absorber design, and (3) an alternative working fluid mixture (NH_3-NaSCN-He).

In Chapter 6, detailed design models were formulated for the DAR components. While many BPG studies have been published (Dammak *et al.*, 2010; de Cachard and Delhaye, 1996; Delano, 1998; Garma *et al.*, 2014; Pfaff *et al.*, 1998; Reinemann *et al.*, 1990), this study represents the first experimental validation of a distributed-heated BPG model. Only one detailed DAR absorber model has been published before (Rattner and Garimella, 2012). This study presents the first detailed heat and mass transfer models for the DAR condenser, evaporator, and passive-circulation gas loop. Simplified component descriptions were integrated to yield a complete system-level model.

Individual component models proposed in Chapter 6 were applied to the development of a fully passive low-source-temperature experimental DAR system in Chapter 7. Stable

operation was demonstrated at source temperatures of T_{source} = 110 – 130°C with cooling delivery temperatures of T_{cool} = 6 → 3°C, 12 → 8°C, 18 → 14°C. This system thus meets the target operating condition range identified in Section 6.1.4.1 (also, see Figure 8.2). Intermediate cooling temperature performance (COP ~ 0.14) was found to be comparable to that of the one other fully passive low-source-temperature DAR system reported in the literature (COP = 0.10 – 0.14, (Ben Ezzine *et al.*, 2010b)). Additionally, system performance was evaluated at varying ambient temperatures (T_{amb} = 24 – 29°C), ambient air flow rates (U_{amb} = 0 – ~0.5 m s^{-1}), and system pressures (p_{sys} = 1.15 – 1.39 MPa).

Detailed measurements from system level experiments were applied to assess individual component performances and model predictions. BPG, condenser, and solution subcooler performances were acceptable and behavior agreed with model predictions in general. The solution heat exchanger performance was significantly lower than predicted in modeling efforts, possibly due to uncertainties in NH_3-NaSCN solution transport properties (k_L). Precise evaluation of evaporator, gas heat exchanger, and absorber performances was challenging due to limitations in available instrumentation (for gas flow rate and concentration) and highly non-equilibrium flow behavior ($T_L - T_G$ ~ 15 K). Modeling results suggest that liquid maldistribution in the evaporator and absorber may be the most significant factors limiting overall system performance. Future investigations should thus focus on enhancing these components. A refined overall system-level model was proposed, and good agreement with experimental system performance was demonstrated.

8.5.2 Recommendations for future research

- Uncertainties in system operating conditions and fluid properties were significant challenges in this investigation. No instruments were commercially available to measure the auxiliary gas circulation rate. Auxiliary gas concentration could be measured with techniques such as gas-chromatography, but this would significantly increase experimental system costs. In future investigations, special-purpose thermal anemometers and time-of-flight ultrasonic concentration measurement instruments could be employed to determine these quantities. Such detailed measurement would enable improved assessment of gas-loop components and models.
- System COP was found to sharply decrease at low ambient air velocities. At such limited external cooling conditions, elevated system pressures may be necessary for condenser operation. However, increased source temperatures are also required at high p_{sys}. In this investigation, COPs were found to be lower at high system pressures. In future studies, it may be possible to mitigate such penalties by reducing NaSCN concentration, thus maintaining solution saturation temperatures and required source temperatures near target values.
- Heat loss from the BPG, SHX, and connective plumbing significantly reduced system performance. As previously discussed, it may be possible to achieve significant performance gains by improving system packaging to reduce heat loss from warm components (BPG and SHX) and heat gain to cool components (evaporator and GHX).
- Absorber performance was found to increase significantly with solution flow rate. By adjusting component sizes and configuration, the solution reservoir level (S_r) could be raised to increase solution flow rate.

- Results from the experimental investigation indicate that the evaporator was under-sized (17 – 35% refrigerant evaporation). It may be possible to improve DAR performance by increasing the evaporator length, and reducing that of the GHX.

Liquid distribution and film-wetting in the evaporator and absorber were identified as potential factors limiting system performance, especially at low flow rates. By refining fluid distribution techniques, improved system performance could be obtained over a wide range of operating conditions.

APPENDIX A: SAMPLE CALCULATIONS FOR PROPOSED MODELS

A.1 Vertical Upward Taylor Flow Model for Intermediate Bond Number Flows

Sample calculations are presented here for the comprehensive kinematic and hydrodynamic (Chapters 2 – 3) model for Taylor flow in the intermediate Bond number regime. Input parameters that are determined implicitly are highlighted in yellow.

Table A.1: Intermediate Bond number Taylor flow calculation

Conditions: air-water flow (T = 22°C, $p = p_{atm}$), D = 8.0 mm, V_L = 80 ml min^{-1} and V_G = 600 ml min^{-1}		
Inputs	**Equations**	**Results**
Fluid properties		
T = 22°C p = 101 kPa	$\rho_L = \rho_{H2O}(T, p)$ $\mu_L = \mu_{H2O}(T, p)$ $\sigma = \sigma_{H2O}(T)$ $\rho_G = \rho_{air}(T, p)$ $\mu_G = \mu_{air}(T)$	ρ_L = 998 kg m^{-3} $\mu_L = 9.54 \times 10^{-4}$ kg m^{-1} s^{-1} σ = 0.072 kg s^{-2} ρ_G = 1.20 kg m^{-3} $\mu_G = 1.84 \times 10^{-5}$ kg m^{-1} s^{-1}
Kinematic definitions		
V_G = 600 ml min^{-1} V_L = 80 ml min^{-1} $A = 5.03 \times 10^{-5}$ m^2	$j_G = V_G / A$ $j_L = V_L / A$ $j = j_G + j_L$	j_G = 0.199 m s^{-1} j_L = 0.027 m s^{-1} j = 0.2255 m s^{-1}
Dimensionless parameters		
ρ_L = 998 kg m^{-3} $\mu_L = 9.54 \times 10^{-4}$ kg m^{-1} s^{-1} σ = 0.072 kg s^{-2} ρ_G = 1.20 kg m^{-3} j_G = 0.199 m s^{-1} j_L = 0.027 m s^{-1} j = 0.2255 m s^{-1} D = 8.0 mm	$\mathrm{Bo} = (\rho_L - \rho_G) gD^2 / \sigma$ $\mathrm{N_f} = \sqrt{\frac{\rho_L (\rho_L - \rho_G) gD^3}{\mu_L^2}}$ $\mathrm{Re}_j = \frac{\rho_L j D}{\mu_L}$ $\mathrm{Re}_{j,L} = \frac{\rho_L j_L D}{\mu_L}$ $\mathrm{Ca} = \frac{\mu_L j}{\sigma}$	Bo = 8.64 N_f = 2343 Re_j = 1886 $Re_{j,L}$ = 222 Ca = 0.00297

Table A.1: Intermediate Bond number Taylor flow calculation – cont.

Taylor bubble rise velocity		
Bo = 8.64 N_f = 2343 Re_j = 1886 Ca = 0.00297 g = 9.81 m s^{-2} j = 0.2255 m s^{-1} D = 8.0 mm	$$\Gamma = \begin{cases} 0.344\left[1-\exp\left(\frac{-0.01N_f}{0.345}\right)\right] \\ \times\sqrt{1+\frac{20}{Bo}-\frac{93.7}{Bo^2}-\frac{676.5}{Bo^3}+\frac{2706}{Bo^4}} \\ \times\frac{1-0.96\exp(-0.0165Bo)}{1-0.52\exp(-0.0165Bo)} \end{cases} \quad Bo>4.55$$ $$\Gamma = 0 \quad Bo \le 4.55$$ $$C_{0,Ca} = \frac{1}{1-0.61Ca^{0.33}}$$ $$C_{0,LS} = 1.20 + \frac{1.09}{1+(Re_j/805)^4}$$ $$f_{LS} = \left(\frac{1}{1+4840\,Re_j^{-0.163}}\right)^{0.816/Bo}$$ $$C_0 = f_{LS}C_{0LS} + (1-f_{LS})C_{0,Ca}$$ $$U_b = C_0 j + \Gamma\sqrt{gD}$$	Γ = 0.128 $C_{0,Ca}$ = 1.098 $C_{0,LD}$ = 1.235 f_{LS} = 0.034 C_0 = 1.167 U_b = 0.299 m s^{-1}
Kinematic closure (all equations in this section solved implicitly)		
D = 8.0 mm ρ_G = 1.20 kg m^{-3} μ_{G_1} = 1.84 × 10^{-5} kg m^{-1} s^{-1} g = 9.81 m s^{-2} j = 0.2255 m s^{-1} μ_{L_1} = 9.54 × 10^{-4} kg m^{-1} s^{-1} U_b = 0.299 m s^{-1} U_f = 0.251 m s^{-1} δ_f = 0.277 mm Re_b = 266.9 L^*_b = 0.03511 D_b = 7.45 mm L_b = 0.06978 mm	$$U_f = \left\{\frac{4}{\pi\left[D^2-(D-2\delta_f)^2\right]}\times\int_{D/2-\delta_f}^{D/2}(2\pi r)\left\{\frac{g(\rho_L-\rho_G)}{4\mu_L}\left[\left(\frac{D}{2}\right)^2-r^2+2\left(\frac{D}{2}-\delta_f\right)^2\ln\left(\frac{2r}{D}\right)\right]+\frac{\tau_{int}(D/2-\delta_f)}{\mu_L}\ln\left(\frac{2r}{D}\right)\right\}dr\right\}$$ $$f_b = \frac{4}{Re_b}\left\{\frac{3.44}{\sqrt{L_b^*}}+\frac{\left[\frac{1.25}{4L_b^*}+16-\frac{3.44}{\sqrt{L_b^*}}\right]}{\left[1+0.00021\left(L_b^*\right)^{-2}\right]}\right\}$$ $$\tau_{int} = \frac{f_b}{8}\rho_G(U_b+U_f)^2$$ $$Re_b = \frac{\rho_G(U_b+U_f)D_b}{\mu_G}$$ $$L_b^* = \frac{L_b}{Re_b D_b}$$	U_f = 0.251 m s^{-1} f_b = 0.359 τ_{int} = 0.016 Pa Re_b = 266.9 L^*_b = 0.03511

Table A.1: Intermediate Bond number Taylor flow calculation – cont.

D = 8.0 mm j = 0.2255 m s^{-1} U_b = 0.299 m s^{-1} j_G = 0.199 m s^{-1} U_f = 0.251 m s^{-1} δ_f = 0.277 mm β = 0.768 α_b = 0.8662 α = 0.665	$\alpha_b U_b - (1-\alpha_b) U_f = j$ $\delta_f = \frac{D}{2}\left(1-\alpha_b^{1/2}\right)$ $\beta = \frac{j_G}{\alpha_b U_b}$ $\alpha = \alpha_b \beta$ $D_b = D - 2\delta_f$	δ_f = 0.277 mm β = 0.768 α_b = 0.8662 α = 0.665 D_b = 7.45 mm
D = 8.0 mm U_b = 0.299 m s^{-1} j = 0.2255 m s^{-1} β = 0.768 α = 0.665	$\frac{L_b}{D} = 1.813\left\{\begin{array}{l}\exp\left[1.815 - 0.866\left(\frac{U_b}{j}\right)^{2.176}\right] \\ \times\left(\frac{\alpha}{1-\alpha}\right)^{1.637} + 1\end{array}\right\}$ $\beta = L_b / (L_b + L_s)$	L_b = 69.8 mm L_s = 21.1 mm
Bubble region frictional pressure gradient		
ρ_L = 998 kg m^{-3} ρ_G = 1.20 kg m^{-3} D = 8.0 mm D_b = 7.45 mm τ_{int} = 0.016 Pa g = 9.81 m s^{-2}	$\tau_{int}(\pi D_b) - \tau_w(\pi D) =$ $\frac{\pi}{4}\left(D^2 - D_b^2\right)(\rho_L - \rho_G) g$ $\nabla p_{f,b} = \frac{4\tau_w}{D}$	τ_w = 2.601 Pa $\nabla p_{f,b}$ = -1300 Pa m^{-1}
Liquid slug region frictional pressure gradient		
Re_j = 1886 ρ_L = 998 kg m^{-3} j = 0.2255 m s^{-1} D = 8.0 mm g = 9.81 m s^{-2}	$f_{f,s} = 8\left\{\begin{array}{l}\left[\left(\frac{8}{Re_j}\right)^{12} + \right. \\ \left[\left(2.457 \ln\left(\frac{1}{(7/Re_j)^{0.9}}\right)\right)^{16}\right. \\ \left.\left.+\left(\frac{3750}{Re_j}\right)^{16}\right]^{-1.5}\right\}^{1/12}$ $\nabla p_{f,s} = \frac{1}{2}\rho_L j^2 / D$	$f_{f,s}$ = 0.034 $\nabla p_{f,s}$ = 107.6 Pa m^{-1}
Flow transition pressure loss		
ρ_L = 998 kg m^{-3} j = 0.2255 m s^{-1} $Re_{j,L}$ = 222 Ca = 0.00297	$\Delta p_{trans} = \left[\begin{array}{l}\frac{1}{2}\frac{\rho_L j^2}{Re_j^{2/3} Ca^{1/3}} \\ \times\left(10.88 + \frac{60}{1 + (Re_{j,L}/800)^{-2}}\right)\end{array}\right]$	Δp_{trans} = 17.5 Pa

Table A.1: Intermediate Bond number Taylor flow calculation – cont.

Hydrodynamic closure		
ρ_L = 998 kg m^{-3} ρ_G = 1.20 kg m^{-3} α = 0.665 g = 9.81 m s^{-2} β = 0.768 $\nabla p_{f,s}$ = 107.6 Pa m^{-1} $\nabla p_{f,s}$ = 107.6 Pa m^{-1} Δp_{trans} = 17.5 Pa L_b = 69.8 mm L_s = 21.1 mm	$-\frac{dp}{dz} = \left\{ \begin{array}{l} [\alpha\rho_G + (1-\alpha)\rho_L]g \\ +\beta\nabla p_{f,b} + (1-\beta)\nabla p_{f,s} + \frac{\Delta p_{trans}}{L_b + L_s} \end{array} \right\}$ $S_r = -\left(\frac{dp}{dz}\right) \Big/ \rho_L g$	dp / dz = -2495 Pa m^{-1} S_r = 0.255

A.2 Coupling-fluid heated bubble-pump generator model

Sample calculations are presented here for one segment (segment 10 of 21) of the flow-boiling bubble-pump generator model proposed in Chapter 4. Results are reported for the model with operating conditions: S_r = 0.299, $T_{CF,in}$ = 120.5°C, $\dot{v}_{CF}$ = 231.2 ml min^{-1} (Q_{BP} ~ 125 W), and $T_{L,in}$ = 94.8°C. Input parameters that are determined implicitly are highlighted in yellow.

Table A.2: Coupling-fluid heated bubble-pump generator model calculation

Conditions: steam-water flow (T_{sat} = 99.2°C, $p = p_{atm}$), ID_i = 7.75 mm, $D_{a,i}$ = 9.53 mm, $D_{a,o}$ = 10.92 mm, $V_{L,i}$ = 140.036 ml min^{-1}, $V_{V,i}$ = 498.52 ml min^{-1}, $T_{L,i}$ = 98.87°C, V_{CF} = 231.2 ml min^{-1}, $T_{CF,i}$ = 113.6°C, p_i = 2935 Pa (gage)		
Inputs	**Equations**	**Results**
Fluid properties		
T_{sat} = 99.2°C p = 98.6 kPa $T_{L,i}$ = 94.8°C	$\rho_L = \rho_{H2O}(T_{sat}, x = 0)$ $c_{p,L} = c_{p,H2O}(T_{sat}, x = 0)$ $\mu_L = \mu_{H2O}(T_{sat}, x = 0)$ $k_L = \mu_{H2O}(T_{sat}, x = 0)$ $i_{L,i} = i_{H2O}(T_{sat}, p) + (T_{L,i} - T_{sat})c_{p,L}$ $Pr_L = Pr_{H2O}(T_{sat}, x = 0)$ $\sigma = \sigma_{H2O}(T_{sat})$ $\rho_V = \rho_{H2O}(T_{sat}, x = 1)$ $\mu_V = \mu_{H2O}(T_{sat}, x = 1)$ $i_V = i_{H2O}(T_{sat}, x = 1)$ $k_t = k_{ss}(T_{sat})$ $\rho_{CF} = \rho_{paratherm\text{-}NF}(T_{sat})$ $c_{p,CF} = c_{p,paratherm\text{-}NF}(T_{sat})$ $k_{CF} = k_{paratherm\text{-}NF}(T_{sat})$	ρ_L = 958.9 kg m^{-3} $c_{p,L}$ = 4.215 kJ kg^{-1} K^{-1} $\mu_L = 2.84 \times 10^{-4}$ kg m^{-1} s^{-1} k_L = 0.6788 W m^{-1} K^{-1} $i_{L,i}$ = 414.4 kJ kg^{-1} Pr_L = 1.76 σ = 0.059 kg s^{-2} ρ_V = 0.582 kg m^{-3} $\mu_V = 1.22 \times 10^{-5}$ kg m^{-1} s^{-1} i_V = 2674 kJ kg^{-1} k_t = 14.3 W m^{-1} K^{-1} ρ_{CF} = 831.4 kg m^{-3} $c_{p,CF}$ = 2.245 kJ kg^{-1} K^{-1} k_{CF} = 0.101 W m^{-1} K^{-1}
Mass balances		
$m_{L,i}$ = 145.955 g min^{-1} $m_{V,i}$ = 0.290 g min^{-1} $m_{V,i+1}$ = 0.322 g min^{-1}	$\dot{m}_{L,i} + \dot{m}_{V,i} = \dot{m}_{L,i+1} + \dot{m}_{V,i+1}$	$m_{L,i+1}$ = 141.924 g min^{-1}
Thermal energy transport (all equations in this section solved implicitly)		
$m_{L,i}$ = 145.955 g min^{-1} $m_{V,i}$ = 0.290 g min^{-1} $A_i = 8.70 \times 10^{-4}$ m^2 $T_{L,i}$ = 98.87°C $i_{L,i}$ = 414.4 kJ kg^{-1} i_V = 2674 kJ kg^{-1} $m_{V,i+1}$ = 0.322 g min^{-1} $m_{L,i+1}$ = 141.924 g min^{-1} $q_{L,i}$ = 3480 W m^{-2} $q_{V,i}$ = 1351 W m^{-2}	$\dot{m}_{L,i+1} i_{i+1} - \dot{m}_{L,i} i_i = q_{L,i} A_i$ $(\dot{m}_{V,i+1} - \dot{m}_{V,i})(i_V - i_{L,i+1}) = q_{V,i} A_i$ $i_{L,i+1} - i_{L,i} = c_{p,L}(T_{L,i+1} - T_{L,i})$	$i_{L,i+1}$ = 415.8 kJ kg^{-1} $m_{V,i+1}$ = 0.322 g min^{-1} $T_{L,i+1}$ = 99.20°C

Table A.2: Coupling-fluid heated bubble-pump generator model calculation – cont.

$m_{L,i} = 145.955$ g min^{-1} $m_{V,i} = 0.290$ g min^{-1} $A = 4.717 \times 10^{-5}$ m^2 $ID_i = 7.75$ mm $\mu_L = 2.84 \times 10^{-4}$ kg m^{-1} s^{-1} $\rho_L = 958.9$ kg m^{-3} $\rho_V = 0.582$ kg m^{-3} $k_L = 0.6788$ W m^{-1} K^{-1} $Pr_L = 1.76$ $x_i = 0.00215$ $p = 98.6$ kPa $p_{cr} = 22060$ kPa MW = 18.02 kg kmol^{-1} $T_{L,i} = 98.87$°C $T_{wall,i} = 101.71$°C $q_{L,i} = 3480$ W m^{-2} $q_{V,i} = 1351$ W m^{-2}	$G = \left(\dot{m}_{L,i} + \dot{m}_{V,i}\right) / A$ $\mathrm{Re}_{L0} = G\,ID_i / \mu_L$ $h_{L0,i} = \frac{k_L}{ID_i} 0.023\,\mathrm{Re}_{L0}^{0.8}\,\mathrm{Pr}_L^{0.4}$ $h'_{L0,i} = \left[1 + x_i\,\mathrm{Pr}_L\left(\frac{\rho_L}{\rho_v} - 1\right)\right]^{0.35} h_{L0,i}$ $h_{NB,i} = \left\{\begin{array}{l} 55\,(p/p_{cr})^{0.12}\,[\log_{10}(p_{cr}/p)]^{-0.55} \\ \times \mathrm{MW}^{-0.5}\,(q_{L,i} + q_{V,i})^{2/3} \end{array}\right\}$ $h'_{NB,i} = \frac{h_{NB,i}}{\left\{1 + 0.055\left[1 + x_i\,\mathrm{Pr}_L\left(\frac{\rho_L}{\rho_v} - 1\right)\right]^{0.035} \mathrm{Re}_{L0}^{0.016}\right\}}$ $q_{LW,sub,i} = \sqrt{\left[h'_{L0,i}\,(T_{wall,i} - T_{L,i})\right]^2 + \left[h'_{NB,i}\,(T_{wall,i} - T_{sat,i})\right]^2}$ $q_{L,i} = q_{LW,sub,i}\left[\frac{h'_{L0,i}\,(T_{wall,i} - T_{L,i})}{q_{LW,sub,i}}\right]^2$ $q_{V,i} = q_{LW,sub,i}\left[\frac{h'_{NB,i}\,(T_{wall,i} - T_{sat})}{q_{LW,sub,i}}\right]^2$	$G = 50.26$ kg m^{-2} s^{-1} $\mathrm{Re}_{L0} = 1371$ $h_{L0,i} = 817.4$ W m^{-2} K^{-1} $h'_{L0,i} = 1635$ W m^{-2} K^{-1} $h_{NB,i} = 1209$ W m^{-2} K^{-1} $h'_{NB,i} = 1018$ W m^{-2} K^{-1} $q_{LW,sub,i} = 4834$ W m^{-2} $q_{L,i} = 3480$ W m^{-2} $q_{V,i} = 1351$ W m^{-2}
$ID_i = 7.75$ mm $D_{a,i} = 9.53$ mm $D_{a,o} = 10.92$ mm $k_t = 14.3$ W m^{-1} K^{-1} $T_{CF,i} = 113.63$°C $h_{CF,i} = 355{,}1$ W m^{-2} K^{-1} $c_{p,CF} = 2.245$ kJ kg^{-1} K^{-1} $m_{CF} = 192.2$ g min^{-1} $H_{seg,i} = 35.7$ mm $T_{wall,i} = 101.71$°C $T_{CF,i+1} = 113.04$°C $q_{L,i} = 3480$ W m^{-2} $q_{V,i} = 1351$ W m^{-2}	$R'_{CF} = \frac{1}{h_{CF}(\pi D_{a,i})}$ $R'_t = \frac{\ln(D_{a,o}/D_{a,i})}{2\pi k_t}$ $\left(q_{L,i} + q_{V,i}\right)(\pi ID_i) = \frac{T_{CF,i+1} - T_{wall,i}}{R'_{CF} + R'_t}$ $(T_{CF,i} - T_{CF,i+1})(\dot{m}_{CF}\,c_{p,CF}) = H_{seg,i}\,\frac{T_{CF,i+1} - T_{wall,i}}{R'_{CF} + R'_t}$	$R'_{CF} = 0.094$ m K W^{-1} $R'_t = 0.002$ m K W^{-1} $T_{wall,i} = 101.71$°C $T_{CF,i+1} = 113.04$°C

Table A.2: Coupling-fluid heated bubble-pump generator model calculation – cont.

Momentum balances (all equations in this section solved implicitly)		
(V_V and V_L are averaged over segment) $V_{V,i} = 525.34$ ml min^{-1} $V_{L,i} = 148.02$ ml min^{-1} $\rho_L = 958.9$ kg m^{-3} $\rho_V = 0.582$ kg m^{-3} $\sigma = 0.059$ kg s^{-2}	$j_{V,i} = V_{V,i} / A$ $j_{L,i} = V_{L,i} / A$ $\text{IsBubbly}_i = \left\{ \begin{matrix} j_{L,i} - 2.34\, j_{V,i} \\ +1.07 \left[\dfrac{\sigma g (\rho_L - \rho_V)}{\rho_L^2} \right]^{1/4} \end{matrix} \right\} > 0$	$j_V = 0.186$ m s^{-1} $j_L = 0.052$ m s^{-1} IsBubbly_i = False (Taylor flow)
($V_{V,i}$, $V_{L,i}$, α_i are averaged over segment) $V_{V,i} = 525.34$ ml min^{-1} $V_{L,i} = 148.02$ ml min^{-1} $\text{ID}_i = 7.75$ mm $\rho_L = 958.9$ kg m^{-3} $\mu_L = 2.84 \times 10^{-4}$ kg m^{-1} s^{-1} $\sigma = 0.059$ kg s^{-2} $\rho_V = 0.582$ kg m^{-3} $\mu_V = 1.22 \times 10^{-5}$ kg m^{-1} s^{-1} $H_{seg,i} = 35.7$ mm	Apply the Taylor flow model from Appendix A.1 $\Delta p_{d,i} = -\left\{ \beta \nabla p_{f,b} + (1-\beta) \nabla p_{f,s} + \dfrac{\Delta p_{trans}}{L_b + L_s} \right\} H_{seg,i}$	$\Delta p_{d,i} = -0.03$ Pa $\alpha = 0.598$
$\rho_L = 958.9$ kg m^{-3} $\rho_V = 0.582$ kg m^{-3} $A = 4.717 \times 10^{-5}$ m^2 $m_{L,i} = 145.955$ g min^{-1} $m_{V,i} = 0.290$ g min^{-1} $m_{V,i+1} = 0.322$ g min^{-1} $m_{L,i+1} = 141.924$ g min^{-1} $\alpha_i = 0.588$ $\alpha_{i+1} = 0.607$	$U_{L,i} = \dfrac{\dot{m}_{L,i}}{\rho_L (1-\alpha_i) A}$ $U_{L,i+1} = \dfrac{\dot{m}_{L,i+1}}{\rho_L (1-\alpha_{i+1}) A}$ $U_{V,i} = \dfrac{\dot{m}_{V,i}}{\rho_V \alpha_i A}$ $U_{V,i+1} = \dfrac{\dot{m}_{V,i+1}}{\rho_V \alpha_{i+1} A}$ $\Delta p_{acc,i} = \left\{ \begin{matrix} \rho_L \left[U_{L,i+1}^2 (1-\alpha_{i+1}) - U_{L,i}^2 (1-\alpha_i) \right] \\ +\rho_V \left[U_{V,i+1}^2 \alpha_{i+1} - U_{V,i}^2 \alpha_i \right] \end{matrix} \right\}$	$U_{L,i} = 0.124$ m s^{-1} $U_{L,i+1} = 0.130$ m s^{-1} $U_{V,i} = 0.305$ m s^{-1} $U_{V,i+1} = 0.326$ m s^{-1} $\Delta p_{acc,i} = 0.3$ Pa

Table A.2: Coupling-fluid heated bubble-pump generator model calculation – cont.

$\alpha = 0.598$ $\rho_L = 958.9$ kg m^{-3} $\rho_V = 0.582$ kg m^{-3} $g = 9.81$ m s^{-2} $H_{seg,i} = 35.7$ mm $\Delta p_{d,i} = -0.03$ Pa $\Delta p_{acc,i} = 0.3$ Pa $p_i = 2935$ Pa	$\Delta p_{hs,i} = [(1-\alpha_i)\rho_L + \alpha\rho_V]\, gH_{seg,i}$ $p_i - p_{i+1} = \Delta p_{hs,i} + \Delta p_{acc,i} + \Delta p_{d,i}$	$\Delta p_{hs,i} = 135.3$ Pa $p_{i+1} = 2799$ Pa

A.3 Diffusion absorption refrigeration cycle model

Sample calculations are presented here for the diffusion absorption refrigeration cycle model proposed in Chapters 6 and 7. State points locations are indicated in the cycle schematic (Figure A.1). Here, state points 12 and 13 represent the gas mixture and liquid refrigerant outlet streams from the evaporator, respectively. Similarly, state points 6 and 14 represent the gas mixture and liquid refrigerant outlet streams from the cold side of the gas heat exchanger. Results are reported for the operating conditions with: $T_{cool} = 4.5$°C, $Q_{BPG} = 118.9$ W, $\psi_{DS} = 0.534$, $m_{CS} = 34.1$ g min^{-1}, $m_{aux} = 38.6$ g min^{-1}, $T_{amb} = 25.6$°C, $p_{sys} = 1.14$ MPa. Fluid thermodynamic properties are evaluated following the approaches described in Section 6.2.1 (highlighted in blue). Input parameters that are determined implicitly are highlighted in yellow.

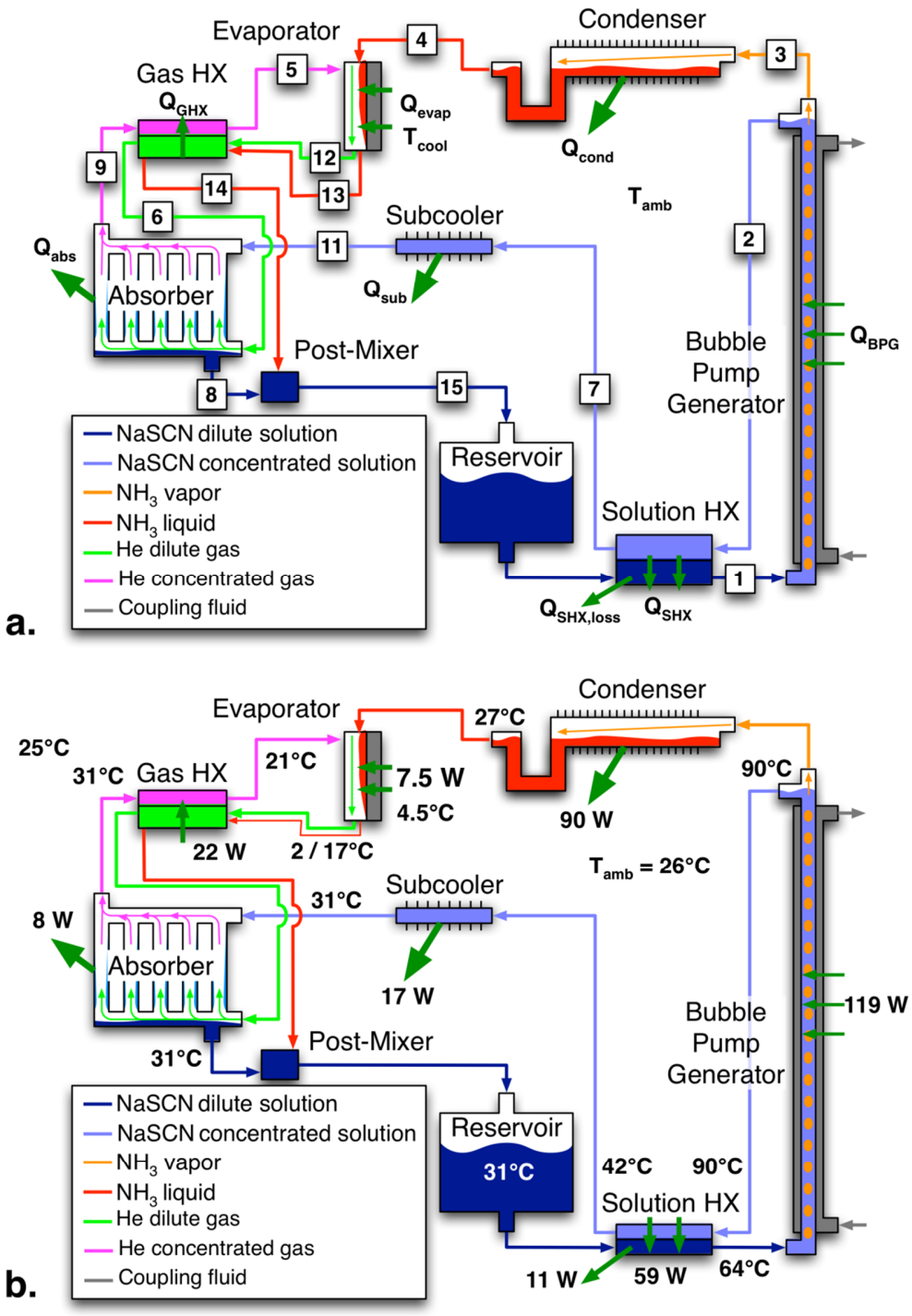

Figure A.1 – **a**. Schematic of DAR cycle with labeled state points, **b**. Temperatures and heat transfer rates predicted with the cycle model

Table A.3: Diffusion absorption refrigeration cycle model calculation

Conditions: T_{cool} = 4.5°C, Q_{BPG} = 118.9 W, ψ_{DS} = 0.534, m_{CS} = 34.1 g min^{-1}, m_{aux} = 38.6 g min^{-1}, T_{amb} = 25.6°C, p_{sys} = 1.14 MPa		
Inputs	**Equations**	**Results**
Bubble-pump generator		
m_2 = 34.1 g min^{-1} ψ_1 = 0.534 p_{sys} = 1.14 MPa Q_{BPG} = 118.9 W T_1 = 64.4°C i_1 = 174.7 kJ kg^{-1} i_2 = 231.8 kJ kg^{-1} i_3 = 1453 kJ kg^{-1}	$m_1 = m_2 + m_3$ $m_1\psi_1 = m_2\psi_2$ $T_2 = T_3$ $p_{sys} = p_{v,NH_3\text{-}NaSCN}(T_2, \psi_2)$ $m_1 i_1 + Q_{BPG} = m_2 i_2 + m_3 i_3$	m_1 = 38.1 g min^{-1} m_3 = 4.06 g min^{-1} ψ_2 = 0.598 T_2 = 89.8°C T_3 = 89.8°C
Condenser		
m_3 = 4.1 g min^{-1} T_3 = 89.8°C CAT_{cond} = 1 K T_{amb} = 25.6°C i_3 = 1453 kJ kg^{-1} i_4 = 125.5 kJ kg^{-1}	$m_4 = m_3$ $T_4 = T_{amb} + CAT_{cond}$ $Q_{cond} = m_3 i_3 - m_4 i_4$	m_4 = 4.1 g min^{-1} T_4 = 26.6°C Q_{cond} = 89.8 W
Evaporator		
UA^*_{evap} = 5.5 × 10^{-11} kg Pa^{-1} s^{-1} CAT_{evap} = 2 K $CAT_{evap,GL}$ = 15 K T_4 = 26.6°C m_4 = 4.1 g min^{-1} m_5 = 38.6 g min^{-1} p_{sys} = 1.14 MPa ξ_{12} = 0.330 (ξ^*_{12} = 0.677) T_5 = 20.5°C ξ_5 = 0.339 (ξ^*_5 = 0.686) T_{13} = 26.6°C i_4 = 125.5 kJ kg^{-1} i_5 = 908.7 kJ kg^{-1} i_{12} = 908.6 kJ kg^{-1} i_{13} = 12.9 kJ kg^{-1}	$p_{v,4} = p_{sat,NH_3}(T_4)$ $p_{v,13} = p_{sat,NH_3}(T_{13})$ $p_{v,12} = (1-\xi^*_{12})\, p_{sys}$ $p_{v,5} = (1-\xi^*_5)\, p_{sys}$ $\mathrm{LMPD}_{evap} = \dfrac{(p_{v,4} - p_{v,5}) - (p_{v,13} - p_{v,12})}{\ln\left(\dfrac{p_{v,4} - p_{v,5}}{p_{v,13} - p_{v,12}}\right)}$ $m_{evap} = UA^*_{evap} \mathrm{LMPD}_{evap}$ $m_{12} = m_5 + m_{evap}$ $m_{13} = m_4 - m_{evap}$ $m_{12}\xi_{12} = m_5\xi_5$ $T_{12} = T_{cool} - CAT_{evap} + CAT_{evap,GL}$ $T_{13} = T_{12} - CAT_{evap,GL}$ $m_{12} i_{12} + m_{13} i_{13} = m_5 i_5 + m_4 i_4 + Q_{evap}$ $i_{13} = i_4 + c_{p,NH_3,L}(T_{13} - T_4)$	$p_{v,4}$ = 1055 kPa $p_{v,13}$ = 470 kPa $p_{v,5}$ = 358 kPa $p_{v,12}$ = 368 kPa LMPD_{evap} = 309 kPa m_{evap} = 1.0 g min^{-1} m_{12} = 39.6 g min^{-1} m_{13} = 3.0 g min^{-1} ξ_{12} = 0.330 (ξ^*_{12} = 0.677) T_{12} = 17.4°C T_{13} = 2.4°C Q_{evap} = 7.5 W i_{13} = 12.9 kJ kg^{-1}

Table A.3: Diffusion absorption refrigeration cycle model calculation – cont.

Gas heat exchanger		
$m_5 = 38.6$ g min^{-1} $\mathrm{CAT}_{abs} = 5$ K $\mathrm{UA}_{GHX} = 2.0$ W K^{-1} $\xi_5 = 0.339$ $m_{12} = 39.6$ g min^{-1} $\xi_{12} = 0.330$ $(\xi^*_{12} = 0.677)$ $m_{13} = 3.0$ g min^{-1} $\xi_{12} = 0.330$ $T_5 = 20.5$°C $T_{12} = 17.4$°C $T_{13} = 2.4$°C $i_5 = 908.7$ kJ kg^{-1} $i_6 = 933.2$ kJ kg^{-1} $i_9 = 942.3$ kJ kg^{-1} $i_{12} = 908.6$ kJ kg^{-1} $i_{13} = 12.9$ kJ kg^{-1} $i_{14} = 117.3$ kJ kg^{-1}	$m_{12} = m_6 \quad \xi_6 = \xi_{12}$ $m_5 = m_9 \quad \xi_5 = \xi_9$ $m_{14} = m_{13}$ $T_9 = T_{amb} + \mathrm{CAT}_{abs}$ $T_{14} = T_6$ $i_{14} = i_4 + c_{p,\mathrm{NH_3,L}}(T_{14} - T_4)$ $\mathrm{LMTD}_{GHX} = \dfrac{(T_9 - T_6) - (T_5 - T_{13})}{\ln\left(\dfrac{T_9 - T_6}{T_5 - T_{13}}\right)}$ $Q_{GHX} = \mathrm{UA}_{GHX}\mathrm{LMTD}_{GHX}$ $m_{12}i_{12} + m_{13}i_{13} + m_9 i_9 =$ $m_6 i_6 + m_{14}i_{14} + m_5 i_5$ $Q_{GHX} = m_6 i_6 - m_{12}i_{12} + m_{14}i_{14} - m_{13}i_{13}$	$m_6 = 39.6$ g min^{-1} $\xi_6 = 0.330$ $m_9 = 38.6$ g min^{-1} $\xi_5 = 0.339$ $m_{14} = 3.0$ g min^{-1} $T_5 = 20.5$°C $T_6 = 24.9$°C $T_9 = 30.6$°C $T_{14} = 24.9$°C $i_{14} = 117.3$ kJ kg^{-1} $\mathrm{LMTD}_{GHX} = 10.8$ K $Q_{GHX} = 21.6$ W
Solution heat exchanger		
$\mathrm{UA}_{SHX} = 4.0$ W K^{-1} $\mathrm{UA}_{SHX,loss} = 0.7$ W K^{-1} $m_2 = 34.08$ g min^{-1} $\psi_1 = 0.534$ $T_{amb} = 25.6$°C $m_1 = 38.1$ g min^{-1} $\psi_2 = 0.598$ $T_1 = 64.4$°C $T_2 = 89.8$°C $T_7 = 42.3$°C $T_{15} = 30.5$°C $i_1 = 174.7$ kJ kg^{-1} $i_2 = 231.8$ kJ kg^{-1} $i_7 = 107.0$ kJ kg^{-1} $i_{15} = 81.2$ kJ kg^{-1}	$m_{15} = m_1 \quad \psi_{15} = \psi_1$ $m_7 = m_2 \quad \psi_7 = \psi_2$ $\mathrm{LMTD}_{SHX} = \dfrac{(T_2 - T_1) - (T_7 - T_{15})}{\ln\left(\dfrac{T_2 - T_1}{T_7 - T_{15}}\right)}$ $Q_{SHX} = \mathrm{UA}_{SHX}\mathrm{LMTD}_{SHX}$ $\mathrm{LMTD}_{SHX,loss} = \dfrac{(T_1 - T_{amb}) - (T_{15} - T_{amb})}{\ln\left(\dfrac{T_1 - T_{amb}}{T_{15} - T_{amb}}\right)}$ $Q_{SHX,loss} = \mathrm{UA}_{SHX,loss}\mathrm{LMTD}_{SHX,loss}$ $m_2 i_2 + m_{15}i_{15} = m_1 i_1 + m_7 i_7 + Q_{SHX,loss}$ $Q_{SHX} = m_2 i_2 - m_7 i_7$	$m_{15} = 38.1$ g min^{-1} $\psi_{15} = 0.534$ $m_7 = 34.1$ g min^{-1} $\psi_7 = 0.598$ $\mathrm{LMTD}_{SHX} = 17.7$ K $Q_{SHX} = 59.5$ W $\mathrm{LMTD}_{SHX,loss} = 16.3$ K $Q_{SHX,loss} = 11.4$ W $T_7 = 42.3$°C $T_1 = 64.4$°C

Table A.3: Diffusion absorption refrigeration cycle model calculation – cont.

Solution subcooler		
$UA_{sub} = 1.8$ W K^{-1} $T_{amb} = 25.6$°C $m_7 = 34.1$ g min^{-1} $\psi_7 = 0.598$ $T_7 = 42.3$°C $T_{11} = 30.5$°C $i_7 = 107.0$ kJ kg^{-1} $i_{11} = 76.5$ kJ kg^{-1}	$m_{11} = m_7 \quad \psi_{11} = \psi_7$ $\mathrm{LMTD}_{sub} = \dfrac{(T_7 - T_{amb}) - (T_{11} - T_{amb})}{\ln\left(\dfrac{T_7 - T_{amb}}{T_{11} - T_{amb}}\right)}$ $Q_{sub} = \mathrm{UA}_{sub}\mathrm{LMTD}_{sub}$ $Q_{sub} = \mathrm{m}_7 i_7 - \mathrm{m}_{11} i_{11}$	$m_{11} = 34.1$ g min^{-1} $\psi_{11} = 0.598$ $\mathrm{LMTD}_{sub} = 9.6$ K $Q_{sub} = 17.3$ W $T_{11} = 30.5$°C
Absorber		
$T_{amb} = 25.6$°C $UA^*_{abs} = 1.3 \times 10^{-10}$ kg Pa^{-1} s^{-1} $T_6 = 24.9$°C $T_{11} = 30.6$°C $T_9 = 30.5$°C $\psi_{11} = 0.598$ $\psi_8 = 0.581$ $\xi_6 = 0.330$ $(\xi^*_6 = 0.677)$ $\xi_6 = 0.339$ $(\xi^*_6 = 0.686)$ $m_6 = 39.6$ g min^{-1} $m_9 = 38.6$ g min^{-1} $m_8 = 35.1$ g min^{-1} $m_{11} = 34.1$ g min^{-1} $i_6 = 933.2$ kJ kg^{-1} $i_8 = 78.0$ kJ kg^{-1} $i_9 = 942.3$ kJ kg^{-1} $i_{11} = 76.5$ kJ kg^{-1}	$p_{v,11} = p_{v,\mathrm{NH_3\text{-}NaSCN}}(T_{11}, \psi_{11})$ $T_8 = T_{amb} + \mathrm{CAT}_{abs}$ $p_{v,8} = p_{v,\mathrm{NH_3\text{-}NaSCN}}(T_8, \psi_8)$ $p_{v,6} = (1 - \xi^*_6)\, p_{sys}$ $p_{v,9} = (1 - \xi^*_9)\, p_{sys}$ $\mathrm{LMPD}_{abs} = \dfrac{(p_{v,9} - p_{v,6}) - (p_{v,6} - p_{v,8})}{\ln\left(\dfrac{p_{v,9} - p_{v,6}}{p_{v,6} - p_{v,8}}\right)}$ $m_{evap} = \mathrm{UA}^*_{abs}\mathrm{LMPD}_{abs}$ $m_6 i_6 + m_{11} i_{11} = m_8 i_8 + m_9 i_9 + Q_{abs}$	$p_{v,11} = 214$ kPa $T_8 = 30.6$°C $p_{v,8} = 250$ kPa $p_{v,6} = 368$ kPa $p_{v,9} = 358$ kPa $\mathrm{LMPD}_{abs} = 131$ kPa $\xi_9 = 0.339$ $Q_{abs} = 7.9$ W
Absorber post-mixer (mixes unevaporated refrigerant and solution		
$m_8 = 35.1$ g min^{-1} $\psi_8 = 0.581$ $T_8 = 30.6$°C $m_{14} = 3.0$ g min^{-1} $T_{14} = 24.9$°C $m_{15} = 38.1$ g min^{-1} $\psi_{15} = 0.534$ $T_{15} = 30.5$°C $i_8 = 78.0$ kJ kg^{-1} $i_{14} = 117.3$ kJ kg^{-1} $i_{15} = 81.2$ kJ kg^{-1}	$m_{15} = m_{14} + m_8$ $m_{15}\psi_{15} = m_8\psi_8$ $m_{15} i_{15} = m_8 i_8 + m_{14} i_{14}$	$m_8 = 35.1$ g min^{-1} $\psi_8 = 0.581$ $T_{15} = 30.5$°C

APPENDIX B: JOURNAL PAPER REPRODUCTION PERMISSIONS

Thesis Chapters 2, 4, and 5 use, as starting points, published journal papers authored by Alexander S Rattner and Srinivas Garimella. Citations for these journal papers are provided here and in the References section.

Chapter 2:
Rattner, A.S., Garimella, S., 2015. Vertical upward intermediate scale Taylor flow: experiments and kinematic closure, International Journal of Multiphase Flow (in press).

Chapter 4:
Rattner, A.S., Garimella, S., 2015. Coupling-fluid heated bubble pump generators: experiments and model development, UHVC Science and Technology for the Built Environment (In press).

Chapter 5:
Rattner, A.S., Garimella, S., 2014. Simple mechanistically consistent formulation for volume-of-fluid based computations of condensing flows, Journal of Heat Transfer 136.

Permissions for reproduction of these articles have been granted by the original publishers. These permission statements are reproduced in the following pages.

Subject: RE: Obtain Permission – Journal request
From: "Shridhar, Lakshmi Priya (ELS-CHN)" <l.shridhar@elsevier.com>
Date: 3/17/15 5:54 AM
To: "Alex.Rattner@gatech.edu" <Alex.Rattner@gatech.edu>

ELSEVIER

Dear Alexander S Rattner
Thank you for your email.
Please note that as one of the authors of this article, you retain the right to include the journal article, in full or in part, in a thesis or dissertation. You do not require permission to do so.
For full details of your rights as a Journal Author, please visit: http://www.elsevier.com/wps/find/authorsview.authors/copyright#whatrights
Your retained rights allow you to submit your article in electronic format and to post this Elsevier article online if it is embedded within your thesis. You are also permitted to post your Author Accepted Manuscript online; however posting of the final published article is prohibited.
Please refer to Elsevier's Posting Policy for further information: http://www.elsevier.com/wps/find/authors.authors/postingpolicy
Feel free to contact me if you have any queries.

Regards

Lakshmi Priya
Global Rights Department
Elsevier
(A division of Reed Elsevier India Pvt. Ltd.)

International Tech Park | Crest – 12th Floor | Taramani Road | Taramani | Chennai 600 113 | India
Tel: +91 44 42994660 | Fax: +91 44 42994701
E-mail: l.shridhar@elsevier.com | url: www.elsevier.com

From: Alex.Rattner@gatech.edu [mailto:Alex.Rattner@gatech.edu]
Sent: Friday, March 13, 2015 7:33 AM
To: Rights and Permissions (ELS)
Subject: Obtain Permission - Journal request

Title:	Mr
First name:	Alexander
Last name:	Rattner

Institute/company:	Georgia Institute of Technology
Address:	390 17th St NW, Unit 4009
Post/Zip Code:	30363
City:	Atlanta
Country:	United States
Telephone:	410-533-0017
Email:	Alex.Rattner@gatech.edu
Please select the type of publication:	Journal
Journal - Title:	International Journal of Multiphase Flow
Journal - ISSN:	0301-9322
Journal - Volume:	X
Journal - Issue:	X
Journal - Year:	2015
Journal - Pages from:	X
Journal - Pages to:	XX
Journal - Author:	Alexander S Rattner, Srinivas Garimella
Journal - Article Title:	Vertical upward intermediate scale Taylor flow: Experiments and kinematic closure
I would like to use (please select one of the following options):	Full article/chapter
If using figures/tables or illustrations please specify the quantity:	Full article
Are you the author of the material?:	Yes
If not, is the author involved with your project:	Yes
In what format will you use the material?:	Electronic
Will you be translating the material?:	No
Information about your proposed use:	thesis
Proposed use text:	posting on library website repository, only accessible with university affiliation or through the library

Additional comments/Information:	I am the first author of IJMF-D-14-00257, and plan to include it in my PhD thesis. The review process has been slow. If accepted, it might not be possible to request permissions through Rightslink in time for my thesis submission. Would it be possible to receive permission in advance? Thanks!

Taylor & Francis
Taylor & Francis Group

Permissions

T & F Reference Number: P040115-04

4/1/2015

Alexander S Rattner
390 17th St NW, Unit 4009
Atlanta GA 30363
Alex.Rattner@gmail.com

Dear Mr. Rattner,

We are in receipt of your request to reproduce your article

> Alexander S Rattner & Srinivas Garimella (2015)
> Coupling-Fluid Heated Bubble Pump Generators: Experiments and Model Development
> *Science and Technology for the Built Environment* (Online)

for use in your thesis

You retain the right as author to post your Accepted Manuscript on your departmental or personal website with the following acknowledgment: "This is an Accepted Manuscript of an article published in *Science and Technology for the Built Environment* online [February 19, 2015], available online: http://www.tandfonline.com/doi/full/10.1080/10789669.2015.1004978#abstract

This permission is all for print and electronic editions.

For the posting of the full article it must be in a secure, password-protected intranet site only. An embargo period of twelve months applies for the Accepted Manuscript to be posted to an institutional or subject repository.

We will be pleased to grant you permission free of charge on the condition that:

This permission is for non-exclusive English world rights. This permission does not cover any third party copyrighted work which may appear in the material requested.

Full acknowledgment must be included showing article title, author, and full Journal title, reprinted by permission of Taylor & Francis LLC (http://www.tandfonline.com).

Thank you very much for your interest in Taylor & Francis publications. Should you have any questions or require further assistance, please feel free to contact me directly.

Sincerely,

Mary Ann Muller
Permissions Coordinator
Telephone: 215.606.4334
E-mail: maryann.muller@taylorandfrancis.com

530 Walnut Street, Suite 850, Philadelphia, PA 19106 • Phone: 215-625-8900 • Fax: 215-207-0050
Web: www.tandfonline.com

RE: Requesting permissions to include my ASME Journal paper...

Subject: RE: Requesting permissions to include my ASME Journal paper in my PhD thesis
From: Beth Darchi <DarchiB@asme.org>
Date: 3/13/15 1:51 PM
To: 'Alex Rattner' <Alex.Rattner@gatech.edu>

Dear Prof. Rattner,
It is our pleasure to grant you permission to publish **any part or all of** the ASME paper "Simple Mechanistically Consistent Formulation for Volume-of-Fluid Based Computations of Condensing Flows," by Alexander S. Rattner; Srinivas Garimella J. Heat Transfer. 2014; 136(7), as cited in your letter in the PhD Thesis entitled Single-pressure absorption refrigeration systems for low-source-temperature applications to be published by Georgia Institute of Technology.

Permission is granted for the specific use as stated herein and does not permit further use of the materials without proper authorization. Proper attribution must be made to the author(s) of the materials. **Please note**: if any or all of the figures and/or Tables are of another source, permission should be granted from that outside source or include the reference of the original source. ASME does not grant permission for outside source material that may be referenced in the ASME works.

As is customary, we request that you ensure proper acknowledgment of the exact sources of this material, the authors, and ASME as original publisher. Acknowledgment must be retained on all pages printed and distributed.

Many thanks for your interest in ASME publications.

Sincerely,

asmeLogo_Lin

Beth Darchi
Publishing Administrator
ASME
2 Park Avenue, 6th Floor
New York, NY 10016-5990
Tel 1.212.591.7700
darchib@asme.org

REFERENCES

ANSYS CFX, ANSYS, Inc.

ANSYS FLUENT, ANSYS, Inc.

STAR-CD, CD-adapco.

2001. Hysol Product 608 Product Description Sheet. Loctite Corporation, Rocky Hill, CT.

2012. Electronic Code of Federal Regulations, Title 10, Chapter II, Subchapter D, Part 430. United States Department of Energy, Washington, DC.

2013a. COMSOL Multiphysics, 4.3a, COMSOL.

2013b. Paratherm NF Heat Transfer Fluid. Paratherm Corporation, http://www.paratherm.com, accessed 2/1/2014.

2014. OpenFOAM, 2.2.0, The OpenFOAM Foundation.

Acuña, A., Velázquez, N., Cerezo, J., 2013. Energy analysis of a diffusion absorption cooling system using lithium nitrate, sodium thiocyanate and water as absorbent substances and ammonia as the refrigerant, Applied Thermal Engineering 51, 1273-1281.

Akbar, M.K., Ghiaasiaan, S.M., 2006. Simulation of Taylor flow in capillaries based on the volume-of-fluid technique, Industrial and Engineering Chemistry Research 45, 5396-5403.

Akers, W.W., Deans, H.A., Crosser, O.K., 1958. Condensing heat transfer within horizontal tubes, Chemical Engineering Progress 54.

Aland, S., Lehrenfeld, C., Marschall, H., Meyer, C., Weller, S., 2013. Accuracy of two-phase flow simulations: The Taylor flow benchmark, Proceedings in Applied Mathematics and Mechanics 13, 595-598.

Almen, C.G., 2007. Gas Absorption Refrigeration, http://www.absreftec.com, accessed 3/15/2012.

Anderson, R., Zhang, L., Ding, Y., Blanco, M., Bi, X., Wilkinson, D.P., 2010. A critical review of two-phase flow in gas flow channels of proton exchange membrane fuel cells, Journal of Power Sources 195, 4531-4553.

Angeli, P., Gavriilidis, A., 2008. Hydrodynamics of Taylor flow in small channels: A Review, Proceedings of the Institution of Mechanical Engineers, Part C: Journal of Mechanical Engineering Science 222, 737-751.

Anglart, H., Podowski, M.Z., 2002. Fluid mechanics of Taylor bubbles and slug flows in vertical channels, Nuclear Science and Engineering 140, 165-171.

Argyropoulos, P., Scott, K., Taama, W.M., 1999. Carbon dioxide evolution patterns in direct methanol fuel cells, Electrochimica Acta 44, 3575-3584.

Asadolahi, A.N., Gupta, R., Fletcher, D.F., Haynes, B.S., 2011. CFD approaches for the simulation of hydrodynamics and heat transfer in Taylor flow, Chemical Engineering Science 66, 5575-5584.

Bar-Cohen, A., Rohsenow, W.M., 1984. Thermally optimum spacing of vertical, natural convection cooled, parallel plates, Journal of Heat Transfer 106, 116-123.

Barnea, D., Brauner, N., 1985. Holdup of the liquid slug in two phase intermittent flow, International Journal of Multiphase Flow 11, 43-49.

Barnea, D., Taitel, Y., 1993. A model for slug length distribution in gas-liquid slug flow, International Journal of Multiphase Flow 19, 829-838.

Beattie, D.R.H., Whalley, P.B., 1982. A simple two-phase frictional pressure drop calculation method, International Journal of Multiphase Flow 8, 83-87.

Behafarid, F., Jansen, K.E., Podowski, M.Z., 2015. A study on large bubble motion and liquid film in vertical pipes and inclined narrow channels, International Journal of Multiphase Flow (In press).

Belman-Flores, J.M., Rodrigues-Munoz, J.L., Rubio-Maya, C., Ramirez-Minguela, J.J., Perez-Garcia, V., 2014. Energetic analysis of a diffusion-absorption system: A bubble pump under geometrical and operational conditions effects, Applied Thermal Engineering 71, 1-10.

Ben Ezzine, N., Garma, R., Bellagi, A., 2010a. A numerical investigation of a diffusion-absorption refrigeration cycle based on R124-DMAC mixture for solar cooling, Energy 35, 1874-1883.

Ben Ezzine, N., Garma, R., Bourouis, M., Bellagi, A., 2010b. Experimental studies on bubble pump operated diffusion absorption machine based on light hydrocarbons for solar cooling, Renewable Energy 35, 464-470.

Bendiksen, K.H., 1984. An experimental investigation of the motion of long bubbles in inclined tubes, International Journal of Multiphase Flow 10, 467-483.

Bendiksen, K.H., 1985. On the motion of long bubbles in vertical tubes, International Journal of Multiphase Flow 11, 797-812.

Benhimidene, A., Chaouachi, B., Gabsi, S., 2010. A review of bubble pump technologies, Journal of Applied Sciences 10, 1806-1813.

Benhimidene, A., Chaouachi, B., Gabsi, S., 2014. Effect of tube diameter on the performance of the bubble pump, International Journal of Control, Energy and Electrical Engineering 2.

Benhimidene, A., Chaouachi, B., Gabsi, S., Bourouis, M., 2011. Modelling of heat flux received by a bubble pump of absorption-diffusion refrigeration cycles, Heat and Mass Transfer 47, 1341-1347.

Benjamin, T.B., 1957. Wave Formation in Laminar Flow down an Inclined Plane, Journal of Fluid Mechanics 2, 554-574.

Berberovic, E., 2008. interFoamKistler.

Boger, M., Schlottke, J., Munz, C., Weigand, B., 2010. Reduction of parasitic currents in the DNS VOF code FS3D, 12th Workshop on two-phase flow predictions, Halle (Saale), Germany.

Bothe, D., Warnecke, H.J., 2005. VOF-simulation of rising air bubbles with mass transfer to the ambient liquid, 10th Workshop on Transport Phenomena in Two-phase Flow, pp. 61-72.

Brackbill, J.U., Kothe, D.B., Zemach, C., 1992. A Continuum Method for Modeling Surface-Tension, Journal of Computational Physics 100, 335-354.

Bretherton, F.P., 1961. The motion of long bubbles in tubes, Journal of Fluid Mechanics 10, 166-188.

Brill, J.P., Schmidt, Z., Coberly, W.A., Herring, J.D., Moore, D.W., 1981. Analysis of two phase tests in large diameter flow lines in Prudhoe bay field, Society of Petrochemical Engineering Journal 271, 363-378.

Brotz, W., 1952. Uber die Vorausberedinung der Absorptions geschwineig von Gayen instromenden flussig kectsschichten, Chem. Ing. Tech. 26, 470-478.

Bugg, J.D., Mack, K., Rezkallah, K.S., 1998. A numerical model of Taylor bubbles rising through stagnant liquids in vertical tubes, International Journal of Multiphase Flow 24, 271-281.

Bugg, J.D., Saad, G.A., 2002. The velocity field around a Taylor bubble rising in a stagnant viscous fluid: numerical and experimental results, International Journal of Multiphase Flow 28, 791-803.

Butterworth, D., 1983. Heat Exchanger Design Handbook. Hemisphere, Washington, DC.

Chan, K.W., McCulloch, M., 2013. Analysis and modelling of water based bubble pump at atmospheric pressure, International Journal of Refrigeration 36, 1521-1528.

Chaouachi, B., Gabsi, S., 2007. Design and simulation of an absorption diffusion solar refrigeration unit, American Journal of Applied Sciences 4, 85-88.

Chen, J., Kim, K.J., Herold, K.E., 1996. Performance enhancement of a diffusion-absorption refrigerator, International Journal of Refrigeration 19, 208-218.

Chen, S.L., Gerner, F.M., Tien, C.L., 1987. General film condensation correlations, Experimental Heat Transfer 1, 93-107.

Chisholm, D., 1967. A theoretical basis for the Lockhart-Martinelli correlation for two-phase flow, International Journal of Heat and Mass Transfer 10, 1767-1778.

Churchill, S.W., 1977. Friction-factor equation spans all fluid-flow regimes, Chemical Engineering 84, 91-92.

Clarke, A., Issa, R.I., 1997. A numerical model of slug flow in vertical tubes, Computers & Fluids 26, 395-415.

Collins, R., Moraes, F.F.D., Davidson, J.F., Harrison, D., 1978. The motion of a large gas bubble rising through liquid flowing in a tube, Journal of Fluid Mechanics 89, 497-514.

Dammak, N., Chaouachi, B., Gabsi, S., Bourouis, M., 2010. Optimization of the geometrical parameters of a solar bubble pump for absorption-diffusion cooling systems, American Journal of Engineering and Applied Sciences 3, 693-698.

Dassault Systems, 2013. PhotoView 360, Waltham, MA.

Davies, R.M., Taylor, G.I., 1950. The mechanics of large bubbles rising through extended liquids and through liquids in tubes, Proceedings of the Royal Society A 200, 375-390.

de Cachard, F., Delhaye, J.M., 1996. A slug-churn flow model for small-diameter airlift pumps, International Journal of Multiphase Flow 22, 627-649.

Delano, A.D., 1998. Design and analysis of the Einstein refrigeration cycle, PhD Thesis, Georgia Institute of Technology, Atlanta, GA.

Deshpande, S.S., Anumolu, L., Trujillo, M.F., 2012. Evaluating the performance of the two-phase flow solver interFoam, Computational Science and Discovery 5.

Dukler, A.E., Hubbard, M.G., 1975. A model for gas-liquid slug flow in horizontal and near horizontal tubes, Industrial Engineering Chemical Fundamentals 14, 337-347.

Dukler, A.E., Maron, D.M., Brauner, N., 1985. A physical model for predicting the minimum stable slug length, Chemical Engineering Science 40, 1379-1385.

Dumetriscu, D.T., 1943. Strömung an einer Luftblase im senkrechten Rohr, ZAMM - Journal of Applied Mathematics and Mechanics 23, 139-149.

Einstein, A., Szilard, L., 1930. Refrigeration, Patent 1,781,541.

El-Genk, M.S., Saber, H.H., 2001. Minimum thickness of a flowing down liquid film on a vertical surface, International Journal of Heat and Mass Transfer 44, 2809-2825.

Elenbaas, W., 1942. Heat dissipation of parallel plates by free convection, Physica 9, 1-28.

Enteria, N., Yoshino, H., Mochida, A., 2013. Review of the advances in open-cycle absorption air-conditioning systems, Renewable and Sustainable Energy Reviews 28, 265-289.

Eskin, D., Mostowfi, F., 2012. A model of a bubble train flow accompanied with mass transfer through a long microchannel, International Journal of Heat and Fluid Flow 33, 147-155.

Esmaeeli, A., Tryggvason, G., 2004a. Computations of film boiling. Part I: numerical method, International Journal of Heat and Mass Transfer 47, 5451-5461.

Esmaeeli, A., Tryggvason, G., 2004b. Computations of film boiling. Part II: multi-mode film boiling, International Journal of Heat and Mass Transfer 47, 5463-5476.

Fairbrother, F., Stubbs, A.E., 1935. Studies in electro-endosmosis. Part VI. The "Bubble-tube" method of measurement, Journal of the Chemical Society, 527-529.

Fang, C., David, M., Rogacs, A., Goodson, K., 2010. Volume of fluid simulation of boiling two-phase flow in a vapor venting microchannel, Frontiers in Heat and Mass Transfer 1.

Fenghour, A., Wakeham, W.A., Vesovic, V., Watson, J.T.R., Millat, J., Vogel, E., 1995. The viscosity of ammonia, Journal of Physical and Chemical Reference Data 24, 1649-1667.

Fernandes, R.C., 1981. Experimental and theoretical studies of isothermal upward gas-liquid flows in vertical tubes, PhD Thesis, University of Houston, Houston, TX.

Fernandes, R.C., Semiat, R., Dukler, A.E., 1983. Hydrodynamic model for gas-liquid slug flow in vertical tubes, AIChE Journal 29, 981-989.

Figueroa-Espinoza, B., Fabre, J., 2011. Taylor bubble moving in a flowing liquid in vertical channel: transition from symmetric to asymmetric shape, Journal of Fluid Mechanics 679, 432-454.

Friedel, L., 1979. Improved friction pressure drop correlations for horizontal and vertical two-phase pipe flow, European Two-Phase Flow Group Meeting, Ispra, Italy.

Fujita, T., Ueda, T., 1978. Heat transfer to falling liquid films and film breakdown I: Subcooled liquid films, International Journal of Heat and Mass Transfer 21, 97-108.

Fukano, T., Kariyasaki, A., Kagawa, M., 1989. Flow patterns and pressure drop in isothermal gas-liquid concurrent flow in a horizontal capillary tube, ANS National Heat Transfer Conference, Philadelphia, PA, pp. 153-161.

Funada, T., Joseph, D.D., Maehara, T., Yamashita, S., 2005. Ellipsoidal model of the rise of a Taylor bubble in a round tube, International Journal of Multiphase Flow 31, 473-491.

Gao, Z.K., Jin, N.D., 2012. Characterization of chaotic dynamic behavior in the gas–liquid slug flow using directed weighted complex network analysis, Physica A: Statistical Mechanics and its Applications 391, 3005-3016.

Garimella, S., 2000. Microchannel components for absorption space-conditioning systems ASHRAE Transactions Symposia 106, 453-462.

Garimella, S., 2003. Innovations in energy efficient and environmentally friendly space-conditioning systems, Energy 28, 1593-1614.

Garimella, S., 2004. Condensation flow mechanisms in microchannels: basis for pressure drop and heat transfer models, Heat Transfer Engineering 25, 104-116.

Garimella, S., Killion, J.D., Coleman, J.W., 2002. An experimentally validated model for two-phase pressure drop in the intermittent flow regime for circular microchannels, Journal of Fluids Engineering 124, 205-214.

Garma, R., Stiriba, Y., Bourouis, M., Bellagi, A., 2014. Numerical investigations of the heating distribution effect on the boiling flow in bubble pumps, International Journal of Hydrogen Energy 39, 15256-15260.

Ghiaasiaan, S.M., 2008. Two-Phase Flow, Boiling, and Condensation in Conventional and Miniature Systems. Cambridge University Press, New York, NY.

Ghidersa, B.E., Wörner, M., Cacuci, D.G., 2004. Exploring the flow of immiscible fluids in a square vertical mini-channel by direct numerical simulation, Chemical Engineering Journal 101, 285-294.

Griffith, P., Wallis, G.B., 1961. Two-phase slug flow, Journal of Heat Transfer 83, 307-320.

Groß, S., Peters, J., Reichelt, V., Reusken, A., 2002. The DROPS package for numerical simulations of incompressible flows using parallel adaptive multigrid techniques. Institut fur Geometrie und Praktische Mathematik, Aachen, Germany.

Grossman, G., 2002. Solar-powered systems for cooling, dehumidification and air-conditioning, Solar Energy 72, 53-62.

Grossman, G., Gommed, K., 1997. Heat and mass transfer in film absorption in the presence of non-absorbable gases, International Journal of Heat and Mass Transfer 40, 3595-3606.

Guo, F., Chen, B., 2009. Numerical study on Taylor bubble formation in a micro-channel T-junction using VOF method, Microgravity Science and Technology 21, 51-58.

Gupta, R., Fletcher, D.F., Haynes, B.S., 2009. On the CFD modelling of Taylor flow in microchannels, Chemical Engineering Science 64, 2941-2950.

Hardt, S., Wondra, F., 2008. Evaporation model for interfacial flows based on a continuum-field representation of the source terms, Journal of Computational Physics 227, 5871-5895.

Harvie, D.J.E., Davidson, M.R., Rudman, M., 2006. An analysis of parasitic current generation in Volume of Fluid simulations, Applied Mathematical Modelling 30, 1056-1066.

Hassanvand, A., Hasemabadi, S.H., 2012. Direct numerical simulation of mass transfer from Taylor bubble flow through a circular capillary, International Journal of Heat and Mass Transfer 55, 5959-5971.

Herold, K.E., Radermacher, R., Klein, S.A., 1996. Absorption Chillers and Heat Pumps. CRC Press, Boca Raton, FL.

Hirt, C.W., Nichols, B.D., 1981. Volume of Fluid (VOF) Method for the Dynamics of Free Boundaries, Journal of Computational Physics 39, 201-225.

Hornbeck, R.W., 1965. An all-numerical method for heat transfer in the inlet of a tube, American Societry of Mechanical Engineers 88, Paper 65-WA/HT-36.

Hussaini, I.S., Wang, C.Y., 2009. Visualization and quantification of cathode channel flooding in PEM fuel cells, Journal of Power Sources 187, 444-451.

Infante Ferreira, C.A., 1984. Thermodynamic and physical property data equations for ammonia-lithium nitrate and ammonia-sodium thiocyanate solutions, Solar Energy 32, 231-236.

Irandoust, S., Andersson, B., 1989. Simulation of flow and mass transfer in Taylor flow through a capillary, Computers & Chemical Engineering 13, 519-526.

Issa, R.I., 1982. Solution of the implicit discretized fluid flow equations by operator splitting. Imperial College, London, UK.

Jakob, U., Eicker, U., 2002. Solar cooling with diffusion absorption principle, in: Sayigh, A.A.M. (Ed.), World Renewable Energy Congress VII, Cologne, Germany.

Jakob, U., Eicker, U., Schneider, D., Taki, A.H., Cook, M.J., 2008. Simulation and experimental investigation into diffusion absorption cooling machines for air-conditioning applications, Applied Thermal Engineering 28, 1138-1150.

Jayanti, S., Hewitt, G.F., 1992. Prediction of the slug-to-churn flow transition in vertical two-phase flow, International Journal of Multiphase Flow 18, 847-860.

Jayanti, S., Hewitt, G.F., 1996. Hydrodynamics and heat transfer of wavy thin film flow, International Journal of Heat and Mass Transfer 40, 179-190.

Jeon, S.S., Kim, S.J., Park, G.C., 2009. CFD simulation of condensing vapor bubble using VOF model, World Academy of Science, Engineering and Technology 60, 209-215.

Jo, S.W., Sherif, S.A., Lear, W.E., 2014. Numerical simulation of saturated flow boiling heat transfer of ammonia/water mixture in bubble pumps for absorption–diffusion refrigerators, Journal of Thermal Science and Engineering Applications 6.

Juric, D., Tryggvason, G., 1998. Computations of boiling flows, International Journal of Multiphase Flow 24, 387-410.

Kang, C.W., Quan, S., Lou, J., 2010. Numerical study of a Taylor bubble rising in stagnant liquids, Physical Review E 81.

Kaushik, S.C., Kauinya, J.V., 1989. Open cycle absorption cooling - a review, Energy Conversion and Management 29, 89-109.

Kawahara, A., Chung, P.M.Y., Kawaji, M., 2002. Investigation of two-phase flow pattern, void fraction and pressure drop in a microchannel, International Journal of Multiphase Flow 28, 1411-1435.

Kawaji, M., DeJesus, J.M., Tudose, G., 1997. Investigation of flow structures in vertical slug flow, Nuclear Engineering and Design 175, 37-48.

Khandekar, S., Panigrahi, P.K., Lefèvre, F., Bonjour, J., 2010. Local hydrodynamics of flow in a pulsating heat pipe: A review, Frontiers in Heat Pipes 1.

Kim, S.J., Park, G.C., 2008. Interfacial heat transfer of condensing bubble in subcooled boiling flow at low pressure, Fifth International Conference on Transport Phenomena In Multiphase Systems, Bialystok, Poland.

Kissling, K., Springer, J., Jasak, H., Schutz, S., Urban, K., Piesche, M., 2010. A coupled pressure based solution algorithm based on the volume-of-fluid approach for two or more immiscible fluids, V European Conference on Computational Fluid Dynamics, Lisbon, Portugal.

Kistler, S.F., 1993. Hydrodynamics of wetting, in: Berg, J. (Ed.), Wettability. Marcel Dekker, Inc, New York, pp. 311-420.

Klein, S.A., 2014. Engineering Equation Solver, 9.721, F-Chart Software.

Koncar, B., Krepper, E., 2008. CFD simulation of convective flow boiling of refrigerant in a vertical annulus, Nuclear Engineering and Design 238, 693-706.

Kothe, D.B., Mjolsness, R.C., 1992. RIPPLE: A new model for incompressible flows with free surfaces, AIAA Journal 30, 2694-2700.

Koyfman, A., Jelinek, M., Levy, A., Borde, I., 2003. An experimental investigation of bubble pump performance for diffusion absorpti on refrigeration system with organic working fluids, Applied Thermal Engineering 23, 1881-1894.

Krepper, E., Koncar, B., Egorov, Y., 2007. CFD modelling of subcooled boiling - concept, validation and application to fuel assembly design, Nuclear Engineering and Design 237, 716-731.

Kreutzer, M.T., Kapteijn, F., Moulijn, J.A., Kleijn, C.R., Heiszwolf, J.J., 2005. Inertial and interfacial effects on pressure drop of Taylor flow in Capillaries, AIChE Journal 51, 2428-2440.

Kreutzer, M.T., Wei, W., Kapteijn, F., Moulijn, J.A., Heiszwolf, J.J., 2003. Pressure drop of Taylor flow in capillaries: impact of slug length, International Conference on Microchannels and Minichannels, Rochester, New York.

Kunkelman, C., Stephan, P., 2009. CFD simulation of boiling flows using the volume-of-fluid method within OpenFOAM, Numerical Heat Transfer 56, 631-646.

Laborie, S., Cabassud, C., Durand-Boulier, L., Laine, J.M., 1999. Characterisation of gas–liquid two-phase flow inside capillaries, Chemical Engineering Science 54, 5723-5735.

Lafaurie, B., Nardone, C., Scardovelli, R., Zaleski, S., Zanetti, G., 1994. Modelling merging and fragmentation in multiphase flows with SURFER, Journal of Computational Physics 113, 134-147.

Lahey Jr., R.T., Drew, D.A., 2001. The analysis of two-phase flow and heat transfer using a multidimensional, four field, two-fluid model, Nuclear Engineering and Design 204, 29-44.

Lee, W.C., Rose, J.W., 1984. Forced convection film condensation on a horizontal tube with and without non-condensing gases, International Journal of Heat and Mass Transfer 27, 519-528.

Legius, H.J.W.M., Akker, H.E.A.v.d., Narumo, T., 1997. Measurements on wave propagation and bubble and slug velocities in cocurrent upward two-phase flow, Experimental Thermal and Fluid Science 15, 267-278.

Lel, V.V., Al-Sibai, F., Kneer, R., 2009. Thermal entry length and heat transfer phenomena in laminar way falling films, Microgravity Science and Technology 21, 215-220.

Lien, F.S., Chen, W.L., Leschziner, M.A., 1996. Low-Reynolds-number eddy-viscosity modelling based on non-linear stress-strain/vorticity relations, Engineering turbulence modelling and experiments 3, 91-100.

Liu, H., Vandu, C.O., Krishna, R., 2005. Hydrodynamics of Taylor flow in vertical capillaries: flow regims, bubble rise velocity, liquid slug length, and pressure drop, Industrial Engineering Chemical Research 44, 4884-4897.

Liu, Z., Winterton, R.H.S., 1991. A general correlation for saturated and subcooled flow boiling in tubes and annuli, based on a nucleate pool boiling equation, International Journal of Heat and Mass Transfer 34, 2759-2766.

Llewellin, E.W., Del Bello, E., Taddeucci, J., Scarlato, P., Lane, S.J., 2011. The thickness of the falling film of liquid around a Taylor bubble, Proceedings of the Royal Society A.

Lu, X., Prosperetti, A., 2009. A Numerical Study of Taylor Bubbles, Industrial & Engineering Chemistry Research 48, 242-252.

Mandal, T.K., Das, G., Das, P.K., 2007. Prediction of rise velocity of a liquid Taylor bubble in a vertical tube, Physics of Fluids 19, 2007.

Mao, Z.S., Dukler, A.E., 1990. The motion of Taylor bubbles in vertical tubes. I. A numerical simulation for the shape and rise velocity of Taylor bubbles in stagnant and flowing liquid, Journal of Computational Physics 91, 132-160.

Marschall, H., Boden, S., Lehrenfeld, C., Falconi D, C.J., Hampel, U., Reusken, A., Wörner, M., Bothe, D., 2014. Validation of interface capturing and tracking techniques with different surface tension treatments against a Taylor bubble benchmark problem, Computers & Fluids 102, 336-352.

Marschall, H., Hinterberger, K., Schuler, C., Habla, F., Hinrichsen, O., 2012. Numerical simulation of species transfer across fluid interfaces in free-surface flows using OpenFOAM, Chemical Engineering Science 78, 111-127.

Medrano, M., Bourouis, M., Perez-Blanco, H., Coronas, A., 2003. A simple model for falling film absorption on vertical tubes in the presence of non-absorbables, International Journal of Refrigeration 26, 108-116.

Mejbri, K., Ben Ezzine, N., Guizani, Y., Bellagi, A., 2006. Discussion of the feasibility of the Einstein refrigeration cycle, International Journal of Refrigeration 29, 60-70.

Menter, F.R., Langtry, R.B., Likki, S.R., Suzen, Y.B., Huang, P.G., Volker, S., 2004. A correlation-based transition model using local variables - Part I: model formulation, Journal of Turbomachinery 128, 413-422.

Milkie, J.A., 2014. Condensation of hydrocarbon and zeotropic hydrocarbon/refrigerant mixtures in horizontal tubes, PhD Thesis, Georgia Institute of Technology, Atlanta, GA.

Mishima, K., Hibiki, T., 1996. Some characteristics of air-water two-phase flow in small diameter vertical tubes, International Journal of Multiphase Flow 22, 703-712.

Mitrović, J., 1988. Der Wärmeaustausch am Berieselungskühler, Brennstoff-Wärme-Kraft 40, 243-249.

Moissis, R., Griffith, P., 1962. Entrance effects in two-phase slug flow, Journal of Heat Transfer 84, 29-39.

Mukherjee, A., Kandlikar, S.G., 2005. Numerical simulation of growth of a vapor bubble during flow boiling of water in a microchannel, Microfluid Nanofluid 1, 137-145.

Müller-Steinhagen, H., Heck, K., 1986. A simple friction pressure drop correlation for two-phase flow in pipes, Chemical Engineering and Processing: Process Intensification 20, 297-308.

Nellis, G., Klein, S.A., 2009. Heat Transfer. Cambridge University Press, New York, NY.

Nguen, K., Daw, C.S., Chakka, P., Cheng, M., Bruns, D.D., Finney, C.E.A., Kennell, M.B., 1996. Spatio-temporal dynamics in a train of rising bubbles, The Chemical Engineering Journal and the Biochemical Engineering Journal 64, 191-197.

Nicklin, D.J., Wilkes, J.O., Davidson, J.F., 1962. Two-phase flow in vertical tubes, Transactions of the Institution of Chemical Engineers 40, 61-68.

Nogueira, S., Riethmuler, M.L., Campos, J.B.L.M., Pinto, A.M.F.R., 2006a. Flow in the nose region and annular film around a Taylor bubble rising through vertical columns of stagnant and flowing Newtonian liquids, Chemical Engineering Science 61, 845 - 857.

Nogueira, S., Riethmuler, M.L., Campos, J.B.L.M., Pinto, A.M.F.R., 2006b. Flow patterns in the wake of a Taylor bubble rising through vertical columns of stagnant and flowing Newtonian liquids: An experimental study, Chemical Engineering Science 61, 7199-7212.

Nusselt, W., 1916. The surface condensation of steam., Z Ver Dtsch Ing 60, 569-575.

Özkan, F., Wörner, M., 2007. Critical evaluation of CFD codes for interfacial simulation of bubble-train flow in a narrow channel, International Journal for Numerical Methods in Fluids 55, 537-564.

Patankar, S.V., 1980. Numerical Heat Transfer and Fluid Flow. Taylor & Francis Group, New York, NY.

Petukhov, B.S., Irvine, T.F., Hartnett, J.P., 1970. Advances in Heat Transfer. Academic Press, New York.

Pfaff, M., Saravanan, R., Maiya, M.P., Murthy, S.S., 1998. Studies on bubble pump for a water-lithium bromide vapour absorption refrigerator, International Journal of Refrigeration 21, 452-462.

Pinto, A.M.F.R., Coelho-Pinheiro, M.N., Campos, J.B.L., 2001. On the interaction of Taylor bubbles rising in two-phase co-current slug flow in vertical columns: turbulent wakes, Experiments in Fluids 31, 643-652.

Premoli, A., Francesco, D., Prina, A., 1971. A dimensionless correlation for determining the density of two-phase mixtures, Termotecnica 25, 17-26.

Quan, S., 2011. Co-current flow effects on a rising Taylor bubble, International Journal of Multiphase Flow 37, 888-897.

Raeini, A.Q., Blunt, M.J., Bijeljic, B., 2012. Modelling two-phase flow in porous media at the pore scale using the volume-of-fluid method, Journal of Computational Physics 17, 5653-5668.

Rattner, A.S., Garimella, S., 2011a. Coupled component- and system-level simulation of a diffusion absorption refrigeration system for residential applications, International Sorption Heat Pump Conference, Padua, Italy.

Rattner, A.S., Garimella, S., 2011b. Energy harvesting, reuse and upgrade to reduce primary energy usage in the USA, Energy 36, 6172-6183.

Rattner, A.S., Garimella, S., 2012. Design and analysis of the absorber component in waste-heat-driven diffusion absorption refrigeration systems, ASME Heat Transfer Conference, Puerto Rico.

Rattner, A.S., Garimella, S., 2014. Simple mechanistically consistent formulation for volume-of-fluid based computations of condensing flows, Journal of Heat Transfer 136.

Rattner, A.S., Garimella, S., 2015a. Coupling-fluid heated bubble pump generators: experiments and model development, UHVC Science and Technology for the Built Environment (In press).

Rattner, A.S., Garimella, S., 2015b. Vertical upward intermediate scale Taylor flow: experiments and kinematic closure, International Journal of Multiphase Flow (in press).

Reinemann, D.J., Parlange, J.Y., Timmons, M.B., 1990. Theory of small-diameter airlift pumps, International Journal of Multiphase Flow 16, 113-122.

Rider, W.J., Kothe, D.B., 1998. Reconstructing volume tracking, Journal of Computational Physics 141, 112-152.

Rodríguez-Muñoz, J.L., Belman-Flores, J.M., 2014. Review of diffusion-absorption refrigeration technologies, Renewable and Sustainable Energy Reviews 30, 145-153.

Rohsenow, W.M., 1952. A method of correlating heat transfer data for surface boiling of liquids, Transactions of the ASME 74, 969-975.

Ros, N.C.J., 1961. Simultaneous flow of gas and liquid as encountered in well tubing, Journal of Petroleum Engineers 13, 1037-1049.

Rusche, H., 2002. Computational Fluid Dynamics of Dispersed Two-Phase Flows at High Phase Fractions, PhD Thesis, Imperial College of Science, Technology & Medicine, London, UK.

Sabisch, W., Wörner, M., Grötzbach, G., Cacuci, D.G., 2001. 3D volume-of-fluid simulation of a wobbling bubble in a gas-liquid system of low Morton number, Proceedings of the 4th International Conference on Multiphase Flow, New Orleans, LA.

Saravanan, R., Maiya, M.P., 2003. Experimental analysis of a bubble pump operated H2O–LiBr vapour absorption cooler, Applied Thermal Engineering 23, 2383-2397.

Schaefer, L.A., 2000. Single pressure absorption heat pump analysis, PhD Thesis, Georgia Institute of Technology, Atlanta, GA.

Schmidt, Z., 1977. Experimental study of two-phase slug flow in a pipeline-riser pipe system, PhD Thesis, University of Tulsa, Tulsa, AZ.

Sethian, J.A., Smereka, P., 2003. Level set methods for fluid interfaces, Annual Review of Fluid Mechanics 35, 341-372.

Shah, R.K., London, A.L., 1978. Laminar Flow Forced Convection in Ducts. Academic Press, New York.

Shao, N., Gavriilidis, A., Angeli, P., 2011. Effect of inlet conditions on Taylor bubble length in microchannels, Heat Transfer Engineering 32, 1117-1125.

Shelton, S.V., Delano, A.D., Schaefer, L.A., 1999. Second law analysis of the einstein refrigeration cycle, Renewable and Advanced Energy Systems for the 21st Century`, Maui, Hawaii.

Son, G., Dhir, V.K., 2008. Numerical simulation of nucleate boiling on a horizontal surface at high heat fluxes, International Journal of Heat and Mass Transfer 51, 2566-2582.

Srikhirin, P., Aphornratana, S., 2002. Investigation of a diffusion absorption refrigerator, Applied Thermal Engineering 22, 1181-1193.

Srikhirin, P., Aphornratana, S., Chungpaibulpatana, S., 2001. A review of absorption refrigeration technologies, Renewable and Sustainable Energy Reviews 5, 343-372.

Stenning, A.H., Martin, C.B., 1968. An analytical and experimental study of air-lift pump performance, Journal for Engineering for Power 90, 106-110.

Subramaniam, V., Garimella, S., 2009. From measurements of hydrodynamics to computation of species transport in falling films, International Journal of Refrigeration 32, 607-626.

Sussman, M., Smereka, P., Osher, S., 1994. A level set approach for computing solutions to incompressible two-phase flow, Journal of Computational Physics 114, 146-159.

Sylvester, N.D., 1987. A mechanistic model for two-phase vertical slug flow in pipes, Journal of Energy Resources Technology 109, 206-213.

Taha, T., Cui, Z.F., 2006. CFD modelling of slug flow in vertical tubes, Chemical Engineering Science 61, 676-687.

Taitel, Y., Barnea, D., 1990. Two-phase slug flow, Advances in Heat Transfer 20, 83-132.

Taitel, Y., Barnea, D., Dukler, A.E., 1980. Modelling flow pattern transitions for steady upward gas-liquid flow in vertical tubes, AIChE Journal 26, 345-354.

Talebi, S., Abbasi, F., Davilu, H., 2009. A 2D numerical simulation of sub-cooled flow boiling at low-pressure and low-flow rates, Nuclear Engineering and Design 239, 140-146.

Tao, Y.J., Huai, X.L., Li, Z.G., 2009. Numerical simulation of vapor bubble growth and heat transfer in a thin liquid film, Chinese Physics Letters 26.

Taylor, G.I., 1961. Deposition of a viscous fluid on the wall of a tube, Journal of Fluid Mechanics 10, 161-165.

Thiele, R., 2010. Modeling of Direct Contact Condensation With OpenFOAM, Masters thesis, Royal Institute of Technology, Stockholm, Sweden.

Thulasidas, T.C., Abraham, M.A., Cerro, R.L., 1995. Bubble-train flow in capillaries of circular and square cross section, Chemical Engineering Science 50, 183-199.

Tillner-Roth, R., Harms-Watzenberg, F., Baehr, H.D., 1993. Eine neue fundamentalgleichung für ammoniak, DKV TAGUNGSBERICHT 20, 67.

Triplett, K.A., Ghiaasiaan, S.M., Abdel-Khalik, S.I., LeMouel, A., McCord, B.N., 1999. Gas–liquid two-phase flow in microchannels: Part II: void fraction and pressure drop, International Journal of Multiphase Flow 25, 395-410.

Tuković, Ž., Jasak, H., 2012. A moving mesh finite volume interface tracking method for surface tension dominated interfacial fluid flow, Computers & Fluids 55, 70-84.

Unverdi, S.O., Tryggvason, G., 1992. A front-tracking method for viscous, incompressible, multi-fluid flows, Journal of Computational Physics 100, 25-37.

van Baten, J.M., Krishna, R., 2004. CFD simulations of mass transfer from Taylor bubbles rising in circular capillaries, Chemical Engineering Science 59, 2535-2545.

van Baten, J.M., Krishna, R., 2005. CFD simulations of wall mass transfer for Taylor flow in circular capillaries, Chemical Engineering Science 60, 1117-1126.

van der Walt, S., 2012. The Design and Optimization of a Bubble Pump for an Aqua-Ammonia Diffusion Absorption Heat Pump, M.Eng. Thesis, North-West University, Potchefstroom, South Africa.

van Hout, R., Barnea, D., Shemer, L., 2001. Evolution of statistical parameters of gas-liquid slug flow along vertical pipes, International Journal of Multiphase Flow 27, 1579-1602.

van Hout, R., Barnea, D., Shemer, L., 2002. Translational velocities of elongated bubbles in continuous slug flow, International Journal of Multiphase Flow 28, 1333-1350.

Viana, F., Pardo, R., Yánez, R., Trallero, J.L., Joseph, D.D., 2003. Universal correlation for the rise velocity of long gas bubbles in round pipes, Journal of Fluid Mechanics 494, 379-398.

von Platen, B.C., Munters, C.G., 1928. Refrigerator, Patent U.S. 1,685,764.

Wadekar, V.V., Kenning, D.B.R., 1990. Flow boiling heat transfer in vertical slug and churn flow region, International Heat Transfer Conference, Jerusalem, Israel.

Wang, H., 2012. A new style solar-driven diffusion absorption refrigerator and its operating characteristics Energy Procedia 18, 681-692.

Wang, Q., Gong, L., Wang, J.P., Sun, T.F., Cui, K., Chen, G.M., 2011. A numerical investigation of a diffusion absorption refrigerator operating with the binary

refrigerant for low temperature applications, Applied Thermal Engineering 31, 1763-1769.

Wang, S., Zhang, H., Wang, J., 2009. Cryogenic liquid slug and Taylor bubble length distributions in an inclined tube, Chinese Journal of Chemical Engineering 17, 20-26.

Weller, H.G., 2002. Derivation modelling and solution of the conditionally averaged two-phase flow equations. Nabla Ltd.

Weller, H.G., Tabor, G., Jasak, H., Fureby, C., 1998. A tensorial approach to computational continuum mechanics using object-oriented techniques, Computers in Physics 12, 620-631.

White, E.T., Beardmore, R.H., 1962. The rise velocity of single cylindrical air bubbles through liquids contained in vertical tubes, Chemical Engineering Science 17, 351-361.

White, S.J., 2001. Bubble pump design and performance, MS Thesis, Georgia Institute of Technology, Atlanta, GA.

Winkler, J., Killion, J., Garimella, S., 2012. Void fractions for condensing refrigerant flow in small channels. Part II: Void fraction measurement and modeling, International Journal of Refrigeration 35, 246-262.

Woldesemayat, M.A., Ghajar, A.J., 2007. Comparison of void fraction correlations for different flow patterns in horizontal and upward inclined pipes, International Journal of Multiphase Flow 33, 347-370.

Wörner, M., Ghidersa, B., Onea, A., 2007. A model for the residence time distribution of bubble-train flow in a square mini-channel based on direct numerical simulation results, International Journal of Heat and Fluid Flow 28, 83-94.

Yang, R., Wood, B.D., 1993. Experimental study for heat and mass transfer in wavy film absorption with the presence of non-absorbable gases, Chemical Engineering Communications 125, 77-90.

Yang, Z., Peng, X.F., Ye, P., 2008. Numerical and experimental investigation of two phase flow during boiling in a coiled tube, International Journal of Heat and Mass Transfer 51, 1003-1016.

Youngs, D.L., 1982. Time-dependent multi-material flow with large fluid distortion, Numerical Methods for Fluid Dynamics, 273-285.

Zacarias, A., Venegas, M., Lecuona, A., Ventas, R., 2013. Experimental evaluation of ammonia adiabatic absorption into ammonia-lithium nitrate solution using a fog jet nozzle, Applied Thermal Engineering 50, 781-790.

Zhang, S.P., Ni, M.J., Ma, H.Y., 2011. VOF Method for simulation of multiphase incompressible flows with phase change, Sixth International Conference on Fluid Mechanics. American Institute of Physics, pp. 579-581.

Zigrang, D.J., Sylvester, N.D., 1982. Explicit approximations to the solution of Colebrook's friction factor equation, AIChE Journal 28, 514-515.

Zohar, A., Jelinek, M., Levy, A., Borde, I., 2005. Numerical investigation of a diffusion absorption refrigeration cycle, International Journal of Refrigeration 28, 515-525.

Zohar, A., Jelinek, M., Levy, A., Borde, I., 2007. The influence of diffusion absorption refrigeration cycle configuration on the performance, Applied Thermal Engineering 27, 2213-2219.

Zohar, A., Jelinek, M., Levy, A., Borde, I., 2008. The influence of the generator and bubble pump configuration on the performance of diffusion absorption refrigeration (DAR) system, International Journal of Refrigeration 31, 962-969.

Zohar, A., Jelinek, M., Levy, A., Borde, I., 2009. Performance of diffusion absorption refrigeration cycle with organic working fluids, International Journal of Refrigeration 32, 1241-1246.

Žun, I., Kljenak, I., Mo̕e, S., 1993. Space-time evolution of the nonhomogeneous bubble distribution in upward flow, International Journal of Multiphase Flow 19, 151-172.